# High-repetition rate CEP-stable Yb-doped fiber amplifier for high harmonic generation

Michele Natile



université PARIS-SACLAY

NNT : 2019SACLS149

Thèse de doctorat

# High-repetition rate CEP-stable Yb-doped fiber amplifier for high harmonic generation

Thèse de doctorat de l'Université Paris-Saclay
préparée à l'Université Paris-Sud

Ecole doctorale n°572 Ondes et Matière (EDOM)
Spécialité de doctorat : Lasers, molécules, rayonnement atmosphérique

Thèse présentée et soutenue à Palaiseau, le 7 Juin 2019, par

**MICHELE NATILE**

Composition du Jury :

| | |
|---|---|
| Mme Sophie Kazamias<br>Professeur, Université Paris-Sud (LPGP) | Présidente |
| M. Giuseppe Sansone<br>Professeur, University of Freiburg | Rapporteur |
| M. Eric Cormier<br>Professeur, Université Bordeaux (CELIA) | Rapporteur |
| Mme Agnès Desfarges-Berthelemot<br>Professeur, Université de Limoges (XLIM) | Examinatrice |
| M. Willem Boutu<br>Chargé de recherche, CEA Saclay (LIDYL) | Directeur de thèse |
| M. Florent Guichard<br>Ingenieur, Amplitude Laser Group | Invité |
| M. Marc Hanna<br>Chargé de recherche, CNRS (Laboratoire Charles Fabry) | Invité |

# French summary

Depuis une vingtaine d'années, la physique attoseconde, via le phénomène de génération d'harmoniques d'ordres élevés (HHG), a permis de nombreuses avancées dans la compréhension des phénomènes de dynamique ultra-rapide sur des échelles jusqu'à l'attoseconde. Les lasers femtoseconde émettant des impulsions de fortes énergies et de durées de quelques cycles optiques sont les outils indispensables à cette physique. Pour des durées d'impulsions si courtes, le contrôle de la phase entre la porteuse et l'enveloppe (CEP) est nécessaire pour pouvoir contrôler l'interaction entre le laser et le gaz à la base du phénomène HHG. Récemment les lasers basés sur les fibres dopées ytterbium ont permis de transposer les expériences d'HHG à haute cadence. La stabilisation de la CEP pour ce type de systèmes constitue la brique manquante au développement de sources à haute cadence pleinement compatibles avec ces applications.

Cette thèse a été consacrée à la stabilisation CEP d'un laser à fibre dopée ytterbium pour une application à la génération de rayonnement cohérent dans l'XUV à fort flux de photon. Cette source permettra la réalisation des expériences d'imagerie cohérente avec une résolution nanométrique et temporelle de l'ordre de la femtoseconde.

Dans la première partie nous présentons l'architecture d'une source à un taux de répétition de 100 kHz stable en CEP émettant des impulsions de 30 μJ et 96 fs. Ce système constitue une preuve de principe pour les futures sources haute énergie basées sur un amplificateur à fibre dopé Yb suivi par un étage de compression non linéaire. La stabilisation de CEP est assurée par une architecture hybride composée d'un injecteur stabilisé passivement suivi d'un amplificateur de puissance stabilisé activement. L'architecture de l'injecteur est basée sur un amplificateur paramétrique optique (OPA) qui permet de produire des impulsions d'environ 150 fs de durée à 1030 nm avec 400 nJ d'énergie par impulsion. L'architecture d'amplification par dérive de fréquence (CPA) utilise une fibre rod-type dopée Yb. L'étage de compression non linéaire par élargissement spectral est une cellule multi-passage incluant une lame mince de silice.

Une caractérisation complète du système en terme de bruit CEP a été menée. L'étude, réalisée par trois méthodes différentes de détection, a permis une analyse sur des durées d'opération allant de la seconde à une heure. Pour les mesures sur l'échelle de la seconde, une nouvelle méthode développée au sein de la thèse a permis de montrer une stabilité CEP de 325 mrad, mesuré tir à tir à 100 kHz. Une mesure de bruit CEP de 375 mrad sur 66 minutes a confirmé le fonctionnement du système sur le long terme. L'influence majeure du bruit d'intensité du laser de pompe de l'injecteur stabilisé passivement a été mise en évidence par une étude du bruit d'intensité et son impact sur la chaine laser stabilisée en CEP.

Dans la seconde partie nous présentons la mise au point d'une ligne HHG XUV optimisée à 13 nm pour les paramètres d'un laser à fibre, pour des applications à l'imagerie par diffraction cohérente. La ligne est composée de trois éléments fondamentaux : une chambre de génération, une partie dédiée au filtrage de l'infra-rouge résiduel et une dernière partie utilisée à la fois comme spectromètre pour la caractérisation des HHG et comme montage pour l'expérience d'imagerie. La gestion des plus faibles énergies par impulsion et la plus forte puissance moyenne par rapport au cas plus classique des lasers Ti:Sa sont les éléments centraux considérés pour la conception. La partie génération est basée sur un capillaire de très petit diamètre interne rempli de gaz comme milieu d'interaction pour la génération d'harmoniques d'ordre élevés. Cette configuration permet des intensités dans le capillaire supérieures à $10^{14}$ W/cm^2.

La ligne XUV conçue est également bien adaptée à d'autres applications telles que les expériences de spectroscopie électronique de photoémission (PEES/ARPES) ou pour la réalisation de mesures en coïncidence (COLTRIMS).

# Contents

# Chapter I

# Introduction

In the IV century BC, Aristotle in the sixth book of his *Physics* cited Zeno's paradoxes about motion. One of the most famous is the arrow paradox. The paradox considers the motion of an arrow along a distance. Zeno says that if we look at the arrow at discrete time instants, it appears constantly occupying the same portion of space corresponding to its proper length. His conclusion was that the arrow is not actually moving because motion is an illusion given by the sum of each instantaneous position of the arrow. Since then, science and physics have never stopped asking questions about objects moving in space and think about the way of freezing it. At the end of the XIX century, Eadweard Muybridge decomposed the motion of a galloping horse using several cameras for acquiring the different horse positions. At this time, artists used to represent the horse galloping with four feet off the ground extended to the front and to the back. Muybridge refuted this depiction, showing that during horse galloping, the four feet off the ground are all grouped together under the horse body.
In Zeno and Muybridge cases, one clear thing is that we need a tool to freeze the motion to be able to understand its dynamics. The faster the camera, the higher is our ability to resolve the different positions composing the motion of the studied object.
In modern physics, ultrafast laser sources are the cameras allowing to detect dynamics at time scales as short as $10^{-18}$ s, an *attosecond*. On this time scale, the motion of very small element of nature such as an electron can be analyzed. The development of ultrashort sources is the key enabling the discovery of more and more detailed parts of the microcosm. To obtain these short time pulse durations, a mode-locked femtosecond laser (1 fs= $10^{-15}$ s) is focused in a gas medium to induce a phenomenon known as *High harmonic generation (HHG)*. This phenomenon was first observed in 1987 by Mcphersson et al. [McPherson *et al.* , 1987] and in 1988 by Ferray et al. [Ferray *et al.* , 1988]. A 30 ps long laser in the first case and a 350 fs one, respectively emitting in the ultra-violet (UV) and infrared (IR), were converted via HHG process producing spectra in the extreme UV range. At that time it was not clear yet that this high frequency conversion via a nonlinear effect could be seen as the generation of an attosecond pulse train. To simply understand the process, we can imagine that a high intensity femtosecond laser pulse excites a gas atom which oscillation become the source of an attosecond pulse. The constructive interference of all these atoms emissions generates the pulse train. It is interesting to point out that one attosecond pulse occurs each half-optical cycle of the fs driving laser. We therefore understand that the turning point of managing an attosecond source is controlling a fs laser on a single optical cycle precision. The control knob is the *Carrier-Envelope Phase* (CEP). This phase is directly linked to the real behavior of the fs few-cycle electric field. In multi-optical cycle mode-locked laser regimes we can consider a pulse as the envelope of a fast oscillating electric field. Approaching few-optical cycle pulse durations, this approximation is meaningless: two pulses with the same envelope present two different oscillating electric field behaviors. The CEP of a fs laser is a random value in the range $[0; 2\pi]$, different for each pulse. Particular strategies must be adopted to stabilize the

CEP of each pulse of the train to a certain value and then control it.
In the last decades, high energy few cycle CEP-stable fs sources have been realized using titanium-doped sapphire (Ti:S) lasers [Krausz, 2016, Haworth *et al.* , 2007] for driving HHG. This kind of laser allows the amplification of fs laser pulse to high peak power up to the PW level [Li *et al.* , 2018, Aoyama *et al.* , 2003]. This high peak power can be obtained in Ti:S laser chain thanks to the *Chirped Pulse Amplification* (CPA) technology [Strickland & Mourou, 1985]. For the impact of this technique in vast domains of laser physics, D. Strickland and G. Mourou have been awarded the physics Nobel prize in 2018. Ti:S lasers can provide few-cycle pulses thanks to the broad amplification spectra.
Nowadays several HHG applications require to have a high flux of generated photons and/or high repetition rate. A first example are experiments using coincidence detection scheme in complex atomic systems such as COLTRIMS [Jahnke *et al.* , 2004, Reduzzi *et al.* , 2015]. For these experiments it is important to generate only few photons per laser shot. The measurable coincidence events occur rarely, making the experiment acquisition time very long to obtain a good signal-to-noise ratio.
Other than the dedicated tool to study ultrafast dynamics, the HHG process is particularly useful as a table-top source for XUV imaging applications. *Coherent Diffraction Imaging* (CDI) is a major example, in this sense, allowing to probe matter with a resolution of the order of wavelength [Ravasio *et al.* , 2009, Robinson & Harder, 2009, Seaberg *et al.* , 2011]. In this technique, a large number of photons have to be acquired in the shortest possible time in order to have a perfectly retrieved resolved image.
This high photon flux requirement directly translates to the need for a high repetition rate, high power, fs pump laser source. The average power is limited for Ti:S CPA technology because of the thermals effects in the crystal. For this reason, HHG ready CPA Ti:S lasers have been reported with a maximum repetition rate of 10 kHz [Golinelli *et al.* , 2017]. The solution for driving HHG at repetition rates higher than 10 kHz has been using the Optical Pulse Chirped Pulse Amplification (OPCPA) [Krebs *et al.* , 2013, Rudawski *et al.* , 2015]. This kind of systems is particularly advantageous because of a large emission wavelength tunability. The price to pay is a low conversion efficiency ($\leq 15$ %) and a high system complexity.
Ytterbium-doped fiber has emerged in last years as one of the few laser technologies well suited to high average power, high repetition rate sources. The big difference with respect to the Ti:S case is a low quantum defect. Pumped at 915 nm or at 976 nm, this laser emits around 1030 nm [Agrawal, 2000]. Energy up to the mJ with repetition rate higher than 500 kHz has been demonstrated recently [Müller *et al.* , 2016]. The long-term stability and robustness make these sources adequate for an ever-increasing number of applications. The limit with respect to the Ti:S or the OPCPA techniques is the narrower amplification bandwidth. The narrower bandwidth implies longer pulse duration. To overcome this limit, nonlinear effects (*post-compression*) can be used to broaden the Yb-doped source spectrum allowing to reach very short pulse duration. Few-cycle, high energy and repetition rate HHG driver laser based on this technology have been recently demonstrated [Lavenu *et al.* , 2019, Lavenu *et al.* , 2017, Hädrich *et al.* , 2013, Hädrich *et al.* , 2011]. High flux HHG driven by few-cycle Yb-doped system has opened the way for a new generation of high repetition rate experiments [Gonzalez *et al.* , 2018, Hädrich *et al.* , 2016].
The remaining bottleneck for the high repetition rate Yb-doped fiber driven HHG source is the CEP stabilization and control.
The context of development of this thesis work is related to the ANR project HELLIX. This project aims at the development of a CEP-stable high repetition rate Yb-doped fiber driven sub-20 nm HHG source for lens-less CDI experiments. In particular, this thesis has been centered on two main goals:

- The achievement of CEP-stabilization on the Yb-doped fiber laser.
- The development of sub-20 nm optimized HHG line designed on a sub-10 fs, 150 $\mu$J, 166

kHz laser developed in the project [Lavenu *et al.* , 2019].

HELLIX is a collaborative project involving Amplitude Laser Group[1], the Laboratoire Interaction Dynamique et Lasers (LYDIL), the Laboratoire Charles Fabry (LCF) and the Laboratoire de l'Accelerateur Lineaire (LAL). This thesis is the result of the synergistic collaboration between the four projects partners. The thesis works have been carried out at LCF for the laser source development, and at LIDYL for the HHG beamline development.

The thesis has been funded by a Marie Curie Sklodowska International Training Network (ITN) fellowship called *MEDEA*[2]. MEDEA stands for Molecular Electron Dynamics driven by intense laser field (E) and Attosecond pulses. The scope of the network, grouping two laser companies and five research laboratories, is to provide a training platform and consolidate the connections between laser development and application in attosecond community.
The manuscript is organized in two thematic parts. In the first part we discuss the fundamentals, the methods and the experimental realization of a proof-of-principle CEP-stable all-Yb-doped amplified source delivering 30 $\mu$J, 100 fs long pulses at 100 kHz. The second part concerns the design of sub-20 nm HHG line optimized on the fiber laser driver developed in the HELLIX project.

**Chapter 2**: The theoretical principles of ultra-short pulse propagation are introduced and the corresponding technological applications are presented. First, we consider the case of a linearly responding medium. The CPA working principles are described highlighting the amplification scheme for an Yb-doped fiber amplifier as technological application. Second, the ultrashort pulse interaction with a nonlinear responding medium is described. Optical Parametric Amplification is discussed as an application of this interaction.

**Chapter 3**: In this chapter we discuss a crucial parameter to be measured in our thesis work: the Relative Intensity Noise (RIN). We first define this parameter and the commonly used measurement techniques. We introduce our measurement setup, discussing the possible issues. The commercial laser representing the first block of our proof-of-principle system is studied using the presented setup. RIN performance improvement is finally shown modifying the commercial laser components.

**Chapter 4**: This chapter is dedicated to the description of the setup and to the characterization of the Yb-based passively stabilized CEP-seeder for our laser chain. We start defining the CEP and discussing the CEP-stabilization most used technique for laser oscillators. We describe the setup of the CEP-stable seeder and the CEP measurement adopted techniques. The high repetition rate CEP measurement detection problem is discussed. The complete characterization in terms of CEP is presented using three different detection techniques. The RIN characterization of the CEP-stable seeder is discussed as well. The influence of the RIN of the commercial pump laser on the CEP of the CEP-stable seeder is evidenced showing the importance of the RIN measurement in CEP-stable systems.

**Chapter 5**: The CEP-stable amplified system is presented in this chapter. We discuss the difficulties of preserving CEP stability in CPA amplification chain. We describe, then, our system composed by a CPA Yb-doped fiber amplifier and a nonlinear post-compression step delivering pulse at 100 kHz having 100 fs time duration and 30 $\mu$J energy. The CEP-stability is ensured thanks to a feedback loop. A complete CEP characterization measuring in-loop and out-of loop cases is realized.

**Chapter 6**: The second part of this manuscript is presented in this chapter. We first rapidly

[1] amplitude-laser.com
[2] www.medea-horizon2020.eu

remind some theoretical principle of the HHG process. We present, then, our design considerations for the interaction medium for HHG sub-20 nm optimized process. The realized complete HHG line and the technical choices adopted are finally discussed highlighting the application ready setup.

# Chapter II

# Theory and Background

## Objectifs

This first chapter is divided in two main parts: theory, technology and application. In the the first section the theoretical concepts concerning ultra-short pulse propagation in media are generally introduced. In the second part, specific examples of realization and application of the theory are presented. A particular interest is given to the fiber propagation case and to frequency conversion configurations.

## Contents

# 1 Theory

In this section we will present the main concepts concerning ultra-short pulse propagation in media having linear and non-linear responses. The first part will concern the introduction of dispersion and dispersion compensation applications. The second one will analyze 2nd and 3rd order nonlinear effects, focusing on relevant examples for the work presented hereafter.

## 1.1 Linear pulse propagation

In order to define the evolution of an electric field $\overrightarrow{E}$ and magnetic field $\overrightarrow{H}$ linearly with a generic medium, we start treating Maxwell [Weiner, 2011] equations in free-space. Naming $\overrightarrow{D}$ and $\overrightarrow{B}$ the electric and magnetic flux densities; $\overrightarrow{J}$ and $\overrightarrow{P}$, the current density and the polarization vectors; $\mu_0$ and $\varepsilon_0$ the permeability and the permittivity of free space, we can write:

$$\nabla \bullet \overrightarrow{D} = 0, \tag{II.1}$$

$$\nabla \bullet \overrightarrow{B} = 0, \tag{II.2}$$

$$\nabla \times \overrightarrow{E} = -\frac{\partial \overrightarrow{B}}{\partial t}, \tag{II.3}$$

$$\nabla \times \overrightarrow{B} = \mu_0(\overrightarrow{J} + \frac{\partial \overrightarrow{D}}{\partial t}). \tag{II.4}$$

Where:

$$\overrightarrow{D} = \varepsilon_0 \overrightarrow{E} + \overrightarrow{P}, \tag{II.5}$$

$$\overrightarrow{B} = \mu_0(\overrightarrow{H} + \overrightarrow{M}). \tag{II.6}$$

We can neglect for the first treatment the magnetization of the material $\overrightarrow{M}$. We can re-arrange Maxwell equations to establish propagation of the electro-magnetic field with only one equation[Weiner, 2011]:

$$\nabla^2 \overrightarrow{E} = \mu_0 \varepsilon_0 \frac{\partial^2 \overrightarrow{E}}{\partial t^2} + \mu_0 \frac{\partial^2 \overrightarrow{P}}{\partial t^2}. \tag{II.7}$$

If we consider the polarization vector as a scalar and we neglect all the transverse variation of the electric field [1], according to the plane wave approximation, we will have:

$$\frac{\partial^2 \mathrm{E}}{\partial z^2} = \frac{1}{c^2}\frac{\partial^2 \mathrm{E}}{\partial t^2} + \mu_0 \frac{\partial^2 \mathrm{P}}{\partial t^2}. \tag{II.8}$$

Where we have used the well-known equivalency on the speed of the light in vacuum, $c = 1/\sqrt{\mu_0 \varepsilon_0}$.
This very general equation can be used to obtain the behaviour of a pulse propagating in a medium having a linear response as already anticipated. We can take for this scope, a plane wave defined as:

$$E(z,t) = A'(z,t)\cos[\omega_0 t - k_0 z + \varphi(z,t)]. \tag{II.9}$$

Where the $A'(z,t)$ is the pulse envelope, $\omega_0$ is the angular frequency, $k_0$ is the wavevector, defined as $k_0 = \frac{2\pi}{\lambda_0}$ [2], and $\varphi(z,t)$ is the phase term. We want, then, to solve equation (II.8) for the so-defined pulse. For doing this, the pulse can be rewritten using a complex envelope:

$$A(z,t) = A'(z,t)e^{i\varphi(z,t)}. \tag{II.10}$$

We can re-write (II.9) as:

[1] This assumption is justified in the cases studied in this manuscript. The beam propagating in fibers and in free space are Gaussian and collimated where the transverse variation of the electric fields can be neglected.

[2] where $\lambda_0$ is the wavelength for the electric field.

$$E\left(z,t\right)=\frac{1}{2}\left[A\left(z,t\right)e^{i(\omega_0 t-k_0 z)}+c.c.\right]. \tag{II.11}$$

Let us focus on the polarization term in (II.8). We have first to define it as follow:

$$P\left(z,t\right)=Re\{p(z,t)e^{i(\omega_0 t-k_p z)}\}. \tag{II.12}$$

We take for this section only the linear part of the polarization vector of the medium, so that $P\left(z,t\right)=P_L(z,t)$ and $k_p=k_0$.
To solve (II.8), we use the Fourier transform for passing to the frequency domain. The electric field and the polarization will become:

$$\tilde{E}\left(z,\omega\right)=Re\{e^{-i(k_0 z)}\int_{-\infty}^{+\infty}A\left(z,t\right)e^{-i(\omega-\omega_0)t}dt\}=\tilde{A}(z,\omega-\omega_0)e^{-i(k_0 z)}, \tag{II.13}$$

$$\widetilde{P_L}\left(z,\omega\right)=Re\{\widetilde{P_L}(z,\omega-\omega_0)e^{-i(k_0 z)}\}. \tag{II.14}$$

The new written terms of (II.13) and (II.14) can be used, then, in the equation (II.8), as follow:

$$\frac{\partial^2\tilde{E}}{\partial z^2}=-\frac{\omega^2}{c^2}\widetilde{\mathrm{E}}-\mu_0\omega^2\widetilde{P_L}. \tag{II.15}$$

And explicating the carrier and envelope terms, we get:

$$\frac{\partial^2\tilde{E}}{\partial z^2}=\underbrace{e^{-i(k_0 z)}}_{\text{carrier}}\underbrace{\left[\frac{\partial^2\tilde{A}}{\partial z^2}-2ik_0\frac{\partial\tilde{A}}{\partial z}-{k_0}^2\tilde{A}\right]}_{\text{envelope}}. \tag{II.16}$$

We can use the slowly varying envelope approximation [Weiner, 2011], neglecting the first term in the square brackets, considering:

$$\frac{\partial^2\tilde{A}}{\partial z^2}\ll k_0\tilde{A}, \tag{II.17}$$

and solving the simplified (II.16), we find:

$$-2ik_0\frac{\partial\tilde{A}}{\partial z}+\left(\frac{\omega^2}{c^2}-{k_0}^2\right)\tilde{A}=-\mu_0\omega^2\widetilde{P_L}. \tag{II.18}$$

The polarization term can be referred to the electric field, introducing the electric susceptibility $\chi(\omega)$, such as, for a linearly responding medium:

$$\widetilde{P_L}(\omega)\ =\varepsilon_0\chi(\omega)\ \widetilde{\mathrm{E}}(\omega)\ . \tag{II.19}$$

Where the refractive index $n(\omega)$ is calculated as:

$$n^2\left(w\right)=\chi\left(\omega\right)+1. \tag{II.20}$$

And considering that the carrier $k_0$ and $k(\omega)$ can be written as:

$$k_0=\frac{2\pi}{\lambda_0}=\frac{\omega_0}{c_0}, \tag{II.21}$$

where $c_0$ is the light speed in vacuum.

$$k(\omega)=\frac{\omega}{c_0}n(\omega). \tag{II.22}$$

The propagation equation in (II.18) becomes, then, the very simple:

$$2ik_0\frac{\partial\tilde{A}}{\partial z} = [k^2(\omega) - k_0^2]\tilde{A}. \tag{II.23}$$

It is interesting to notice that the equation (II.23) there are only terms referring to $A$ and $k$. We can recall this propagation variable, $\beta$, and considering it expanded in Taylor series, in the neighborhood of $\omega_0$:

$$\beta(\omega) = \beta_0 + \beta_1(\omega - \omega_0) + \frac{1}{2}\beta_2(\omega - \omega_0)^2 + \frac{1}{6}\beta_3(\omega - \omega_0)^3 + \ldots, \tag{II.24}$$

Where:

$$\frac{\partial\beta}{\partial\omega} = \beta_1, \tag{II.25}$$

$$\frac{\partial^2\beta}{\partial\omega^2} = \beta_2, \tag{II.26}$$

$$\frac{\partial^n\beta}{\partial\omega^n} = \beta_n. \tag{II.27}$$

We [Agrawal, 2000], define, $\beta_1 = \frac{1}{v_g}$, where $v_g$ is the *group velocity*, because it represents the velocity of propagation of the envelope. $\beta_2$ is the *group velocity dispersion (GVD)* and $\beta_3$ the *third order dispersion* (TOD). If the treatment of the interaction with the medium requires to take higher terms of the series, until the $n-th$ term we have a $n-th$ order dispersion. These terms represent the different types of modification of the pulse due to the dispersive nature of the material.

Considering, then, the Taylor expansion we reformulate the equation (II.23), coming back to the time domain and passing to the *pulse frame*, considering $t' = t - \frac{1}{v_g}$, as [Weiner, 2011]:

$$\frac{\partial\tilde{A}}{\partial z} = \sum_n \frac{i^n}{n!}\beta_n\omega^n\tilde{A}. \tag{II.28}$$

The very general equation in (II.28) can be simplified to the following:

$$\frac{\partial\tilde{A}}{\partial z} - \frac{i}{2}\beta_2\omega^2\tilde{A} = 0, \tag{II.29}$$

where the Taylor series is stopped to the second order, for this discussion[1]. Equation (II.29) allows to treat the problem of the propagation of the pulse in a linearly responding medium, and will give a solution in the form:

$$\tilde{A}(z,\omega) = \tilde{A}(0,\omega)\, e^{i\frac{1}{2}\beta_2\omega^2 z}. \tag{II.30}$$

The last two equations are very useful for introducing the dispersion. This is a central topic for pulse propagation in free-space and in fibers as will be clear in the next pages of this manuscript.

We can introduce the definition of the instantaneous frequency, as follows:

$$\omega_i = -\frac{\partial\phi}{\partial t}, \tag{II.31}$$

we now describe as *chirp*. It is said to be positive when the reddest components of the spectrum travel faster than the bluest ones. In this case, the propagation is said in normal dispersion regime, with $\beta_2 > 0$.

[1]This choice is justified for a simple analysis. In most of the cases of pulse propagation in this thesis only the second and TOD are involved.

The interaction of an ultrashort pulse with a medium follows equation (II.29). The simplest example we can consider is pulse propagation in vacuum. The vacuum is by definition a *non-dispersive medium*. This means that we can re-write equation (II.29) neglecting the second term, $\beta_2$, to the result of a constant $A(z,t)$. This indicates the fact that no changes on the pulse envelope are occurring considering propagation over an arbitrary length $z = L$ in vacuum.

For all the others media, the dispersion will have an impact and carrier and envelope will change. In particular, if we consider a generic added spectral phase $\psi(\omega)$ for a pulse, $E(t)$, in the propagation in a transparent medium:

$$E_{out}(t) = \frac{1}{2\pi}\int_{-\infty}^{+\infty} E_{in}(\omega)e^{i\psi(\omega)}e^{i\omega t}d\omega, \tag{II.32}$$

where the spectral phase is related to $\beta(\omega)$ as $-\psi(\omega)/L$.

To give a more concrete physical meaning what happens to a pulse passing through the medium we consider only the GVD and neglect the TOD. It is common to call *group delay* the first derivative in frequency of $\beta$. This definition is more representative of the physical meaning for the pulse propagation. This term, in fact, is the time at which a determined group of frequency around $\omega_0$ arrives at the end of the propagation. If there is no dispersion of order two in the material, all the frequencies spend the same time for travelling through it.

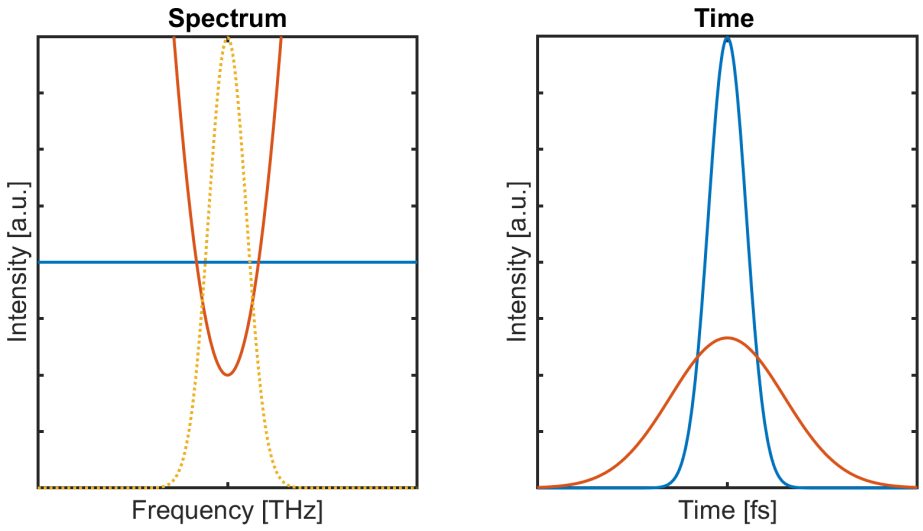


Figure II.1 – Pulse frequency and time domain evolution in a dispersive medium.

In figure II.1 we can see on the right, yellow-dotted curve, the spectrum of a Gaussian pulse. A constant phase and a parabolic one for this spectrum are respectively shown in blue and red on the same graph. On the right graph, the resulting pulse in the time domain is shown. In blue the Gaussian pulse carrying a constant spectral phase and in red the same pulse having a parabolic phase term. We will define the first case pulse as *Fourier Transform-Limited* (TL) pulse because it represents the shortest possible pulse for the given spectrum. The second case, instead, corresponds to a longer pulse for the same spectral width because of the not constant phase. If we take a TL pulse travelling in the medium of length L with only second order dispersion, it exits as the pulse of figure II.1. We talk about positive or negative dispersion depending on the sign of $\beta_2$. If we consider a common case of a pulse in the visible range passing through a piece of glass, the dispersion experienced by the pulse is positive. This is the case for most transparent materials in the visible.

## 1.2 Non-linear pulse propagation

We want, now, to introduce some concepts of non-linearly responding light-medium interaction. The assumption we have done in the first section of this chapter, of taking a polarization term varying linearly with $E$, is no more applicable. In a more general treatment, we will have in fact:

$$P = P_L + P_{NL} = \varepsilon_0\chi_1(\omega)E(\omega) + \varepsilon_0\chi_2(\omega)E^2(\omega) + \varepsilon_0\chi_3(\omega)E^3(\omega) + \ldots. \tag{II.33}$$

We talk about *second order effects* if only the second term has to be considered and of *third order effect* if the cubic field term counts.

### 1.2.1 Second order effects

**General Equation** We consider a new formulation of the general equation (II.29) for the nonlinear case [1] [Weiner, 2011]:

$$\frac{\partial A}{\partial z} + \frac{1}{v_g}\frac{\partial A}{\partial t} - i\beta_2\frac{\partial^2 A}{\partial t^2} = -i\frac{\mu_0 c_0 \omega_0}{2n_0}P_{NL}e^{-i\Delta kz}, \tag{II.34}$$

where $\Delta k = k_p - k_0$ is the difference between the wave vectors.
The more general effect is the sum of two electric fields $E(t) = E_1(t) + E_2(t)$, so that:

$$P_{NL} = \frac{\varepsilon_0\chi_2(\omega)}{4}\{A_1^2 e^{i(2\omega_1 t - 2k_1 z)} + A_2^2 e^{i(2\omega_2 t - 2k_2 z)} + c.c. + \tag{II.35}$$

$$2A_1A_2e^{i[(\omega_1+\omega_2)t-(k_1+k_2)z]} + c.c. + \tag{II.36}$$

$$2A_1{}^*A_2e^{i[(\omega_2-\omega_1)t-(k_2-k_1)z]} + c.c. + \tag{II.37}$$

$$+ 2A_1{}^*A_1 + 2A_2{}^*A_2\}. \tag{II.38}$$

Each line of the equation above will be the basis for a specific second order process. The first (II.35) is *Second Harmonic Generation* (SHG), the second (II.36) is *Sum Frequency Generation* (SFG), the third one, (II.37) is *Difference Frequency Generation* (DFG), and the last one (II.38) is *Optical Rectification* (OR). We will discuss in more detail the SHG and DFG effects.
The second order effects are often referred to as *three wave mixing* (3WM). We can consider them, in fact, as the interaction of two entrance wave and a resulting one. We will consider the three electric fields at $\omega_1, \omega_2, \omega_3$ such that $\omega_1 + \omega_2 = \omega_3$. We have three coupled equations, that can be obtained from (II.34), to solve:

$$\begin{cases} \frac{\partial A_1}{\partial z} + \frac{1}{v_{g_1}}\frac{\partial A_1}{\partial t} - i\beta_2\frac{\partial^2 A_1}{\partial t^2} = -i\frac{d_{eff}\omega_1}{2n_1c_0}A_3A_2{}^*e^{-i\Delta kz}, \\ \frac{\partial A_2}{\partial z} + \frac{1}{v_{g_2}}\frac{\partial A_2}{\partial t} - i\beta_2\frac{\partial^2 A_2}{\partial t^2} = -i\frac{d_{eff}\omega_2}{2n_2c_0}A_3A_1{}^*e^{-i\Delta kz}, \\ \frac{\partial A_3}{\partial z} + \frac{1}{v_{g_3}}\frac{\partial A_3}{\partial t} - i\beta_2\frac{\partial^2 A_3}{\partial t^2} = -i\frac{d_{eff}\omega_3}{2n_3c_0}A_1A_2e^{i\Delta kz}. \end{cases} \tag{II.39}$$

Where $d_{eff} = \frac{\chi_2(\omega)}{2}$ and $\Delta k = k_3 - k_2 - k_1$.
It is not so easy to solve analytically these equations. However, some qualitative considerations can be done on the physical meaning of each term. As we already discussed in paragraph 1.1, the third term represents pulse broadening due to the dispersion. The $2^{nd}$ term implies that the three pulses have different group velocities. In a first approximation we neglect the terms containing the $\beta_2$ considering only the ones related the group velocities. This approximation is

[1] For simplicity in the next we call the envelope A(z,t)=A

justified considering the GVD due to propagation in the crystal is not relevant for the second-order effect [1]. We can introduce the *group velocity mismatch* (GVM) as the difference of the inverse of the group velocity one or two with respect to the third one, as follow:

$$\delta_{13} = \frac{1}{v_{g1}} - \frac{1}{v_{g3}}, \delta_{23} = \frac{1}{v_{g2}} - \frac{1}{v_{g3}}. \tag{II.40}$$

And referring all to the pulse $E_3$, we obtain:

$$\begin{cases} \frac{\partial A_1}{\partial z} + \delta_{13}\frac{\partial A_1}{\partial t} = -i\frac{d_{eff}\omega_1}{2n_1c_0}A_3{A_2}^*e^{-i\Delta kz}, \\ \frac{\partial A_2}{\partial z} + \delta_{23}\frac{\partial A_2}{\partial t} = -i\frac{d_{eff}\omega_2}{2n_2c_0}A_3{A_1}^*e^{-i\Delta kz}, \\ \frac{\partial A_3}{\partial z} = -i\frac{d_{eff}\omega_3}{2n_3c_0}A_1A_2e^{i\Delta kz}. \end{cases} \tag{II.41}$$

**SHG Process** Second harmonic generation is the simplest example of effect we can analyze using the above equations. In this case, the three waves satisfy $\omega_1 = \omega_2 = \omega = \omega_3/2$. Let us rename the electrics fields as $E_1 = E_2 = E_\omega/\sqrt{2}$ and $E_3 = E_{2\omega}$. Furthermore, we make the strong approximation of considering monochromatic waves. This allows to omit the GVM impact and look only at the effect of SHG on the fields. Starting from the equation (II.41) we can write:

$$\begin{cases} \frac{dA_\omega}{dz} = -i\frac{d_{eff}\omega}{2n_\omega c_0}A_{2\omega}{A_\omega}^*e^{-i\Delta kz}, \\ \frac{dA_{2\omega}}{dz} = -i\frac{d_{eff}\omega}{n_{2\omega}c_0}\frac{{A_\omega}^2}{2}e^{i\Delta kz}. \end{cases}$$

We make the assumption of *no depletion* assuming a constant $A_\omega(z)$, allowing to solve the equation in terms of the evolution of the field $2\omega$ along $z$. We obtain:

$$A_{2\omega}(z) = -i\left(\frac{d_{eff}\omega}{n_{2\omega}c_0}\frac{{A_\omega}^2}{\Delta k}\right)e^{i\Delta kz}\sin\left(\frac{\Delta kz}{2}\right) .$$

Considering the intensity definition [Weiner, 2011], for a plane wave case, we have:

$$I_{2w}(z) = \frac{1}{2}\varepsilon_0 c_0 n_{2\omega}|A_{2\omega}|^2 = \frac{1}{2}\varepsilon_0 c_0 n_{2\omega}\left(\frac{d_{eff}\omega}{n_{2\omega}c_0}\frac{{A_\omega}^2}{\Delta k}\right)sin^2\left(\frac{\Delta kz}{2}\right) .$$

We obtain that the intensity of the doubled field (SHG) along the interacting crystal is varying as a quadratic sinus. This means that the intensity of conversion is maximum for $\Delta kz = 0, \pi, 3\pi, \ldots$ . This condition satisfaction, $\Delta k = 0$, is called *phase matching*. The relation can be rewritten for the SHG case, referring to the refractive index as $n(2\omega) = n(\omega)$. We can easily understand that, because of dispersion, the index for $\omega$ and $2\omega$ is clearly different. Several solutions can be adopted for solving this problem and efficiently generate the SHG. The most common and simplest is to use the so-called *birefringent phase matching*, that will be subject of discussion in the second part of this chapter.

**DFG process** The difference frequency generation can be seen as the equation (II.39), where the three central pulse frequencies are different. It is important to say that it is common to link this phenomenon to the so-called *Optical Parametric Amplification* (OPA) [Minck *et al.* , 1966]. In the scheme in figure II.2 we can see the 3 waves denomination as pump, signal and idler respectively for $\omega_3, \omega_2, \omega_1$.

[1] This is true if we consider pulse duration longer than 300 fs and crystal interaction length of some mm. These are the conditions where the second-order nonlinear effects occur in this manuscript cases.

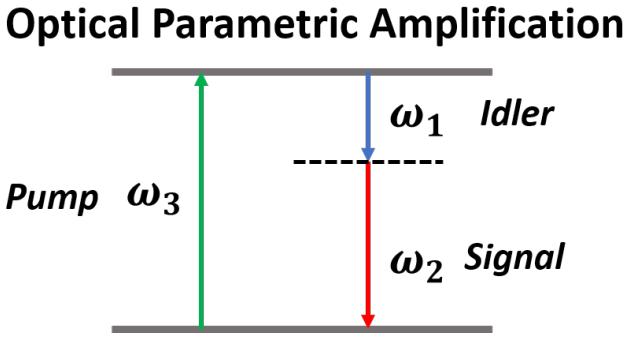


Figure II.2 – Optical Pararametric Amplification (OPA) principle

This scheme can be understood as follows: one photon coming from the beam called pump is converted in a signal and an idler one. In order to understand how this phenomenon works we start again from the general equation (II.41), considering some approximations. First, we consider monochromatic waves in order to neglect the GVM terms. We assume, then, that the pump is undepleted $A_3 = A_3(0)$. Last, we consider that the phase matching condition is satisfied. We get, in this way, two coupled equations:

$$\begin{cases} \frac{dA_1}{dz} = -i\frac{d_{eff}\omega_3}{2n_1c_0}A_3{A_2}^*, \\ \frac{dA_2}{dz} = -i\frac{d_{eff}\omega_2}{2n_2c_0}A_3{A_1}^*. \end{cases} \tag{II.42}$$

We solve it, focusing on $A_2$ behaviour so that:

$$\frac{dA_2}{dz} = k_1k_2|A_3|^2A_2. \tag{II.43}$$

Where: $k_1 = \frac{d_{eff}\omega_3}{2n_1c_0}$ and $k_2 = \frac{d_{eff}\omega_2}{2n_2c_0}$ We can see in the equation (II.43), that $k_1k_2|A_3|^3 = const = \Gamma^2$. The equation will have a solution as follows:

$$A_2(z) = c_1e^{\Gamma z} + c_2e^{-\Gamma z}. \tag{II.44}$$

We can choose boundary conditions so that at the beginning there is no idler $A_1(0) = 0$ and an initial signal defined as a constant $A_2(0) = A_{20}$. In this sense, the constants $c_1, c_2$ in the equation are given by $c_1 = c_2 = \frac{A_{20}}{2}$:

$$A_2(z) = A_{20}\frac{e^{\Gamma z} + e^{-\Gamma z}}{2} = A_{20}\cosh\Gamma z. \tag{II.45}$$

We can, at this point, assume that the amplification is significantly high, such that $\Gamma z >> 1$. In this way we can write[Weiner, 2011]:

$$A_2(z) = A_{20}\cosh\Gamma z \approx A_{20}\frac{e^{\Gamma z}}{2}. \tag{II.46}$$

Since we are considering a plane wave, the intensity of the field at z, is:

$$I_2(z) = \frac{1}{2}c_0n\varepsilon_0|A_2|^2 = I_2(0)\frac{e^{2\Gamma z}}{4} = GI_2(0). \tag{II.47}$$

Where we call the $G$ *Parametric gain.* If we repeat this procedure for $A_1$, we obtain:

$$I_1(z) = \frac{\omega_1}{\omega_2}I_2(z). \tag{II.48}$$

We obtain as a result, that the number of photons of idler is equal to the number of photons of signal at $z$. We have confirmed the scheme in figure II.2: one pump photon gives one signal photon and an idler one.

### 1.2.2 Third Order Effects

**Non-linear Schrodinger Equation** In the case of third-order effects we need to consider the polarization vector $P_{NL}$:

$$P_{NL}(z,t) = \varepsilon_0 \chi_3 E^3(z,t). \tag{II.49}$$

If in the second-order effects we have generalized the possible effects as a three-wave mixing process, for the third-order ones, we can approach it as a mixing of four waves (FWM).We can proceed in the same way and get four coupled equations. In this treatment, we choose to analyze the simplest case, concerning the degenerate FWM, where:

$$\omega_1 = \omega_2 = \omega_3 = \omega_4 = \omega; A_1 = A_2 = A_3 = A_4 = A; k_1 = k_2 = k_3 = k_4 = k. \tag{II.50}$$

In this way, the polarization can be rewritten as:

$$P_{NL}(z,t) = \frac{3}{4}\varepsilon_0 \chi_3 |A|^2 A e^{i\omega t - k_p z}. \tag{II.51}$$

We have to notice that we are in a special case where we are auto phase matched to have $k_p = k$. So that, starting from equation (II.33), we get [Agrawal, 2000]:

$$\frac{\partial A}{\partial z} + \frac{1}{v_g}\frac{\partial A}{\partial t} - \frac{i}{2}\beta_2 \frac{\partial^2 A}{\partial t^2} = -i\frac{3\varepsilon_0 \mu_0 c_0 \omega_0}{8n}\chi_3 |A|^2 A. \tag{II.52}$$

We can define the coefficient, on the right side of the equal, as a generic constant $\gamma$, and make a change of variable for $t' = t - \frac{1}{v_g}$

$$\frac{\partial A}{\partial z} = \frac{i}{2}\beta_2 \frac{\partial^2 A}{\partial t^2} - i\gamma |A|^2 A. \tag{II.53}$$

This equation is denoted as *non-linear Schrondiger equation* (NLSE) because it is the same form as the well-known formulation for a free particle under a potential $V$ [Eisberg & Resnick, 1974]:

$$i\hbar \frac{\partial \Psi}{\partial t} = -\frac{\hbar^2}{2m}\frac{\partial \Psi}{\partial x^2} + V\Psi. \tag{II.54}$$

Where in our case we have a potential $V = \gamma |A|^2$.

**Self-Phase Modulation and spatial Kerr-effect** Let us assume that we are in a medium for which the second order dispersion term, $\beta_2$, is null. Equation (II.53) can be simply solved in the form:

$$A(z,t) = A(0,t)e^{i\Delta\phi_{NL}(z,t)}. \tag{II.55}$$

Where we can see that in a generic position $z$, the field is the envelope at the beginning of the propagation plus a new accumulated phase term $\Delta\phi_{NL}(z,t) = \gamma |A|^2 z$. We can notice that the new added phase is dependent on the square modulus of the input field. This means it will be dependent on the intensity $I(t)$ of the field. The physical meaning of this added phase, can be seen looking at the instantaneous frequency $\omega_i(t)$, as follows:

$$\omega_i(t) = \omega_0 + \delta\omega = \omega_0 - \gamma z \frac{d|A(t)|^2}{dt}. \tag{II.56}$$

This means that the spectrum broadens during pulse propagation. This effect is called *Self-Phase Modulation* (SPM) [Alfano & Shapiro, 1970] and it is of high importance in fibers, we will discuss in more details in the next section of this chapter.
Originated from the same treatment of the SPM, another effect takes place modifying the

spatial profile of the beam [Stolen & Ashkin, 1973]. This effect goes under the name of spatial Kerr-effect, or simply Kerr-lens. Consider what we have said for the SPM added phase term because of the third order susceptibility. We can see that this is linked to a change in the refractive index $n(t)$:

$$n(t) = n_0 + n_2|A(t)|^2. \tag{II.57}$$

Where index is, in this case $n_2 = \frac{3\chi_3}{8n_0}$. This means that for a Gaussian beam impinging on a material of $n_2 > 0$[1], it will experience a $n$ at the center of the beam where the intensity is higher. In particular, this produces a lens with a focal $f$ calculated as follows:

$$f = \frac{\pi R^4}{4n_2 dP}, \tag{II.58}$$

where: R is the beam radius, $d$ is the material thickness and $P$ is the peak power of the pulse.

## 1.3 Fiber applications

Fibers will be one of the media mostly used in this manuscript. For this reason, it is interesting to analyze in detail how the presented dispersion phenomena on ultra-short pulses give rise to specific modification of the propagating pulses in this guiding medium.

### 1.3.1 Linear propagation in fibers

The properties of pulse dispersion discussed in paragraph 1.1 work in the same way for the propagation in fibers. It is important to notice that some notation details and nomenclature could change between bulk and fiber propagation case. In particular, let us recall that a fiber is constituted by a core and a cladding respectively having a refractive index $n_{cladding} < n_{core}$, satisfying the guiding condition. For this reason, it is important to redefine the electric field propagation properties for the fiber case with an effective area $A_{eff}$ and an effective index $n_{eff}$. For understanding what happens in fibers we restart from the general equation (II.15). We have up to now, considered in one dimension, extending it to an $(x, y)$ field case [Agrawal, 2000]. In this way we have:

$$\nabla^2{}_{x,y} u + (\omega^2 \mu_0 \epsilon_1 - \beta^2)u = 0. \tag{II.59}$$

This equation is the starting point for getting the reformulation of the NLSE for the fiber case, as follows:

$$i\frac{\partial A}{\partial z} = -i\frac{\alpha A}{2} + \frac{\beta_2}{2}\frac{\partial^2 A}{\partial T^2} - \gamma|A|^2 A. \tag{II.60}$$

Where A is the amplitude of the pulse envelope normalized so that $|A|^2$ is the power measured in [W]. We make the usual change of variables $T = t - z/v_g$, referring to the pulse frame. The first term on the right side of the equation describes the effect of propagation losses through the coefficient $\alpha$. It has to be noticed that the nonlinear parameter $\gamma$, is different from the one used in the formulation in (II.53). The new $\gamma$ is defined by:

$$\gamma(\omega) = \frac{n_2(\omega_0)\omega_0}{c_0 A_{eff}}. \tag{II.61}$$

Where $A_{eff}$ is the effective area for the guided mode, defined as follows:

$$A_{eff} = \frac{(\int\int |u|^2 dxdy)^2}{\int\int |u|^4 dxdy}. \tag{II.62}$$

With $u$ being the fundamental mode distribution in $(x, y)$. It has to be added that in equation (II.60) only the second order dispersion term, $\beta_2$ is taken into account.

[1] All the media used in this work satisfy this condition.

### 1.3.2 Non-linear Propagation in fibers

It is useful to introduce two characteristic lengths $L_D$ and $L_{NL}$ linked to the dispersion and non-linear propagation effects [Agrawal, 2000].

$$L_D = \frac{{T_0}^2}{|\beta_2|}; L_{NL} = \frac{1}{\gamma P_0}. \tag{II.63}$$

Where $T_0$ is the input pulse width in this case and $P_0$ is the input pulse peak power. We can distinguish 2 different fiber propagation regimes depending on the different values of the ratio $L_D/L_{NL} = N^2$.

- For N$\ll$1, the effects due to the dispersion in the fiber dominate over the non-linear ones. In this case the linear treatment discussed in the previous paragraph is valid.
- For N$\gg$1, the propagation is dominated by the non-linear effects. In this paragraph, we concentrate the analysis considering the SPM as the only effect taking place.

The discussion of section 1.2.2 is applicable in the same way for the fiber case, considering negligible fiber losses. In this case, a temporal non-linear phase term due to the SPM is added to the initial field. The pulse experiences a frequency chirping $\delta\omega$. The maximum phase shift is given by:

$$\phi_{max} = \gamma z P_{peak}. \tag{II.64}$$

Where $P_{peak}$ is the peak power, measured in [W] of the pulse. The input TL pulse is spectrally broadened upon propagation. It has been shown [Agrawal, 2000] that the structure of the broaden spectrum is modulated, presenting some peaks. In figure II.3 shows how SPM acts on the input pulse spectrum as $\phi_{max}$ increase.

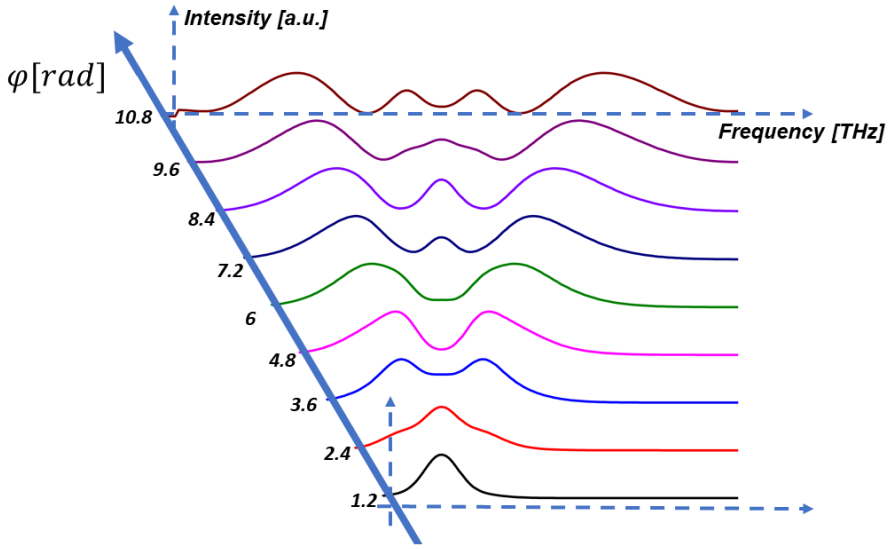


Figure II.3 – Self-Phase Modulation effect on an initially TL pulse propagating in a fiber

In particular, it can be shown that the number of generated spectrum peaks $M$ is linked to $\phi_{max}$ , following[1]:

$$\phi_{max} \approx (M - 1/2)\pi. \tag{II.65}$$

[1]This is true in the case of a Gaussian, TL input pulse.

We have previously seen, also, how the Kerr lensing effect acts on the propagating beam in a medium. For the fiber case, this brings to an even deeper conclusion. We take our beam profile experiencing a converging lens through the Kerr-effect. At some point the lens dominates the natural diffraction of the beam, destroying the medium itself.
We can define a critical power $P_{crit}$ such that for:

- $P_{peak} > P_{crit}$ Self-focusing dominates and the medium is damaged.
- $P_{peak} < P_{crit}$ The beam propagates experiencing negligible Kerr lens effect.

$P_{crit}$ is proportional to $\frac{\lambda}{n_2}^2$. For example, in fused silica fibers $P_{crit}$ is of the order of 4 MW at 1030 nm wavelength. We always work with peak pulse powers lower than $P_{crit}$ in order to avoid the self-focusing phenomenon.

# 2 Technology and Applications

What we have presented in the previous section is a general approach to pulse propagation in media. In this section, we will use the presented concepts with a more technology oriented approach. We will start discussing the impact of the presented effects for high peak power fiber-based amplifier. We will, then, describe the implementation of parametric amplification.

## 2.1 Chirped Pulse Amplification in Yb-Doped Fiber Amplifiers (YDFA)

Yb-doped fibers play a central role as amplifiers for ultrashort pulses at 1030 nm. In particular, they are the only type of laser amplifiers used in this thesis. Considering what we have said about critical power, we find a bottleneck for the amplification linked to the peak power. In order to overcome this problem, the chirped pulse amplification (CPA) [Strickland & Mourou, 1985] has been proposed. For this work and its impact, D. Stricland and G. Mourou have received the Nobel prize in 2018. The CPA scheme exploits the properties of dispersion we have presented in the theory section to enhance the amplification medium capabilities. Figure II.4 shows the working principle. It consists of three steps: pulse stretching, amplification , pulse compression. At the beginning, a high peak power (short and energetic) pulse cannot be amplified directly because of the optical damage it causes to the amplification medium. For this reason, the pulse is chirped and stretched in time in the first step. In this way, the spectrum of the pulse is preserved but the peak power is lowered by several orders of magnitude depending on the positive dispersion added in the stretcher step. The pulses can be, then, amplified in a single or in several stages. Finally, the positive dispersion added in the first step can be compensated in a pulse compressor. At the output this allows amplified high peak power pulses. Each of the three steps are discussed in details in the next three paragraphs.

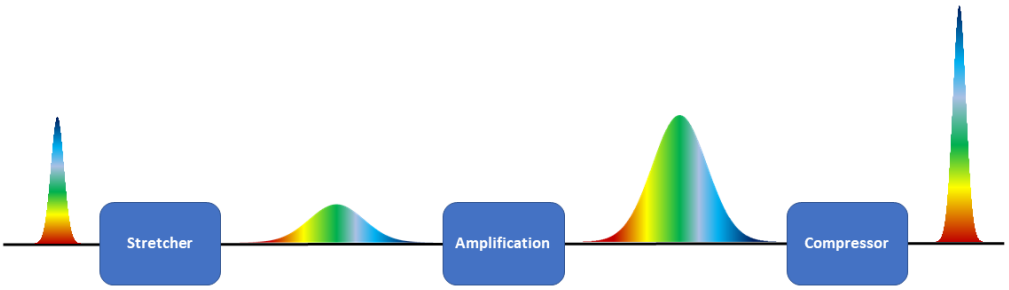


Figure II.4 – Chirped Pulse Amplification scheme.

### 2.1.1 Pulse stretching

We have said that, at $\lambda = 1\mu m$, positive dispersion is typically added to an ultra-short pulse passing through a transparent medium like fused silica. We can easily understand, then, that a passive fiber is the most simple stretcher we can imagine. More sophisticated setups can be realized, as for the pulse compression case, in order to manage more or less precisely the

dispersion added. The most simple and used case relies on the scheme depicted in figure II.5.

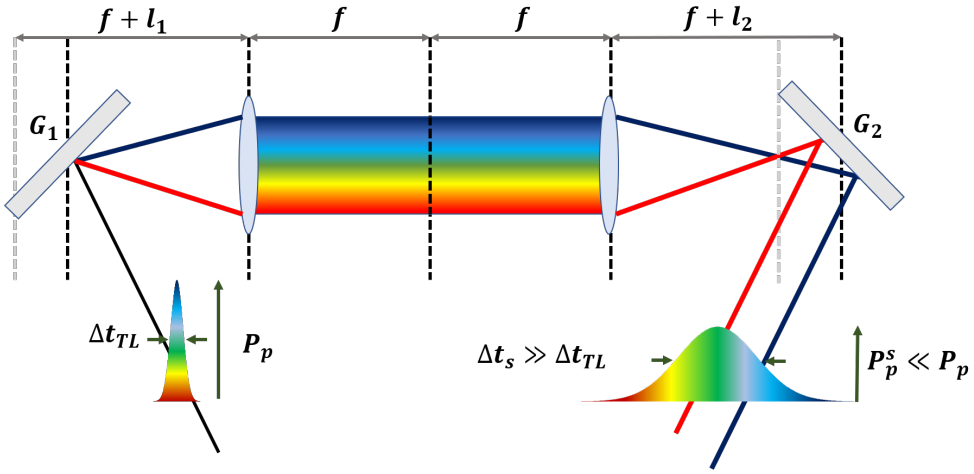


Figure II.5 – 4f stretcher scheme. $G_1$: grating 1, $G_2$: grating 2. $f$: lens focal length, $l_1$: distance between lens focal plane and grating $G1$, $l_2$: distance between lens focal plane and grating $G2$. $P_p$: input peak power; $P_p^s$: stretched pulse peak power; $\Delta t_{TL}$: pulse duration in TL condition; $\Delta t_s$: stretched pulse duration.

We can see that the TL pulse at the entrance is dispersed by the first grating $G1$ and then passes through the lens to be collimated and then refocused on the second grating $G2$ by means of a second identical lens. If the distance between the lens and $G2$ is longer than the focal length $f$, the arrangement introduces negative dispersion. It has been shown that, at the output the pulse will take a second-order phase due to the stretcher that is, for the first order $m = -1$ of the gratings [Rulliere, 2005]:

$$\beta_2 = \frac{\lambda^3 (l_1 + l_2)}{2\pi c^2 d^2 \cos\theta_D}. \tag{II.66}$$

Where $\lambda$ is the central laser wavelength. $l_1$ is the distance of the grating $G1$ respect to the focal plane of the lens and it is equal to zero in the scheme in figure II.5 . Analyzing the equation we understand that the sign and quantity of dispersion $\beta_2$ added by the stretcher is dependent on the sign and modulus of the sum $l_1 + l_2$. This means that the above-described setup can be used either as compressor or stretcher depending on the distance between grating and lens. Moreover, for $l_1 + l_2 = 0$ we will obtain a dispersion-less system. This stretcher setup is usually called *4f-scheme* [Martinez *et al.* , 1984].

### 2.1.2 Amplification in Yb-doped fibers

One of the limitation in fibers is the critical power as we have already said. The core diameter is another central issue for amplification. It introduces important SPM spectrum modulation effects for high peak power, that we want to avoid in amplification. In this sense, in the last decades, several efforts have been spent to obtain large core amplifier fibers. In order to maintain a good spatial quality for the beam profile, we want propagation in the fundamental mode of the fiber. To have a single-mode fiber, indeed, the $\Delta n$ of difference between the core and the cladding has to be low enough to satisfy the equation below [Agrawal, 2000]:

$$V = \frac{2\pi}{\lambda} a \sqrt{(n_{core}^2 - n_{cladding}^2)} < 2,405, \tag{II.67}$$

where $a$ is the radius of the fiber core. The lowest possible $\Delta n$ that can be nowadays realized is of the order of $10^{-3}$, this means that we will have core diameters of maximum 15 $\mu$m. For

getting larger core diameters and preserving a good beam quality, different strategies have been adopted. We can cite two of them:

- One of the first ideas has been to slightly bend a multi-mode fiber in order to systematically introduce losses in the high order modes [Koplow *et al.* , 2000]. On the other hand, this technique has been shown [Nicholson *et al.* , 2007] to reduce the $A_{eff}$.

- Another solution is to use *core coupled fibers*. This technique allows to obtain core sizes up to 60 $\mu$m. It consists of a classical doped core and a second one [Swan *et al.* , 2008] (or several [Ma *et al.* , 2014]) not-doped making a helix structure around the first. The second core has a smaller diameter and allows leakage of the higher order modes leaving only the fundamental propagating through the bigger core.

A different type of fiber with respect to the classical, step-index one, has permitted a very important up-scaling of the *Large Mode Area* (LMA) fibers. The *Photonic Crystal Fibers* (PCF)[Birks *et al.* , 1997] allow to theoretically get core of 80 $\mu$m of diameter. The key point is to completely change the step index classical fiber structure. A section of a PCF is shown in fig II.6.

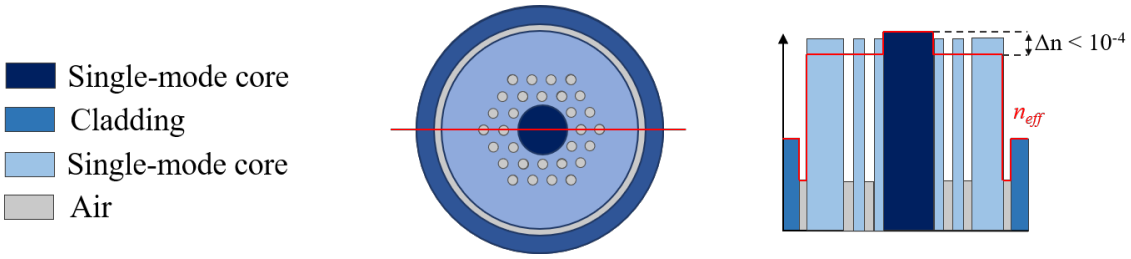


Figure II.6 – Photonic Crystal Fiber structure.

In the middle there is the large doped core. Around it several air-filled holes are fabricated. With this geometry a very low effective index contrast can be obtained $\Delta n \sim 10^{-4}$. The presence of the pump cladding prevents this type of fibers to be strictly single-mode. Nevertheless the amplification of the fundamental mode can be dominant thanks to a specific design. Flexible fibers with core diameter up to 40 $\mu$m [Limpert *et al.* , 2004] have been demonstrated to be single-mode using this kind of structure. For larger core diameter, the flexible nature of the fibers limits the guiding quality. For this reason, rigid fibers going under the name of *rod-type fibers*, have been introduced [Limpert *et al.* , 2005]. With this kind of technology fibers with diameters up to 100 $\mu$m have been realized [Limpert *et al.* , 2012].

### 2.1.3 Pulse compression

We can generally define *pulse compressor*, a setup where the positive dispersion added for stretching the pulse in the first step of the CPA is corrected. Considering what theoretically discussed in 1.1, the principle of this tool is to make again all the pulse instantaneous frequencies, $\omega$, arriving at the same time. This allows to recover a TL limited pulse. Several methods can be used for this, depending on the amount and type of dispersion we need to manage. One example is using the 4-f scheme presented for the stretcher case, with the condition $(l_1 + l_2) < 0$.

**Grating Pair** This is the most simple and common case of compressor existing [Rulliere, 2005], simplifying the setup of the 4f-scheme. It consists of two gratings with the same periodicity as depicted in the scheme in figure II.7.

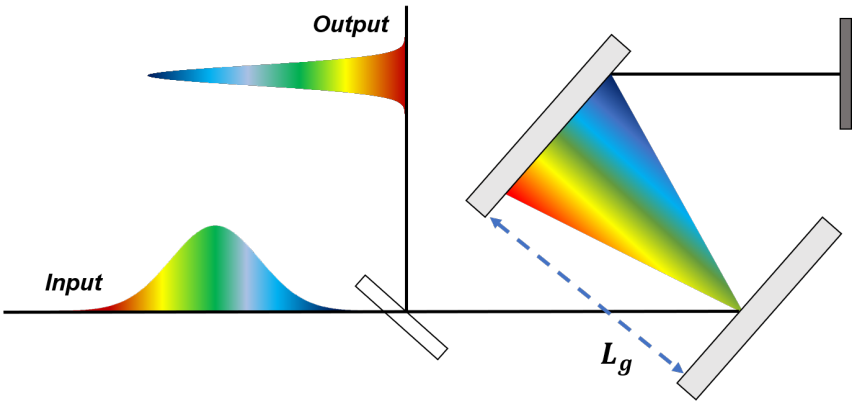


Figure II.7 – Grating pair compressor scheme.$L_g$: grating distance.

The doubled passage in through the grating pair avoids the spatial chirp in the output beam. Looking at the grating equation [Hutley, 1982], the lower frequencies are diffracted with a bigger angle with respect to the higher ones. This produces a different pathlength for the different frequency components. More commonly we talk in terms of wavelength instead of frequency. At the output of the compressor the dispersion will be [Treacy, 1969]:

$$\beta_2 = -\frac{\lambda^3 L_g}{\pi c^2 d^2}\sqrt{1-\left(\frac{\lambda}{d}-\sin\theta_i\right)^2}. \tag{II.68}$$

Where: $L_g$ is the distance between the gratings, $\lambda$ is the central wavelength, $d$ is the grating periodicity, $\theta_i$ is the incident angle on the grating.
From the formula we can appreciate that the dispersion is negative, and it depends on the distance between the gratings as well as on the groove density. This device is useful because it can correct large amounts of $\beta_2$. Nevertheless it can be shown [Treacy, 1969] that it introduces also a positive TOD. Consider a concrete situation of the propagation of an initially TL pulse in a medium with only $\beta_2$. We could compensate the second order dispersion coming from the material using this compressor, but the output pulse cannot be TL because of the added TOD. We understand, then, that we need a compressor allowing to manage TOD on our optical pathlength.

**Prism Pair** One possible solution for having a $\beta_2 < 0$ is the prism pair. The figure II.8 depicts the simple scheme. It can be demonstrated [Kafka & Baer, 1987] that at the output the pulse has experienced negative $\beta_{2,}\beta_3 \propto L_p$. $L_p$ is the distance between the prisms, as shown in figure II.8. The amount of introduced dispersion, also, depends on the material refractive index at the laser central wavelength. Generally, the prism pair can correct very finely small amounts of $\beta_{2,}\beta_3$, where the previous shown grating pair is preferred for large second order dispersion compensation. A classical scheme of pulse compression after a medium introducing $\beta_{2,}\beta_3$ can be a cascade of these two types of compressors [Cruz *et al.* , 1988].

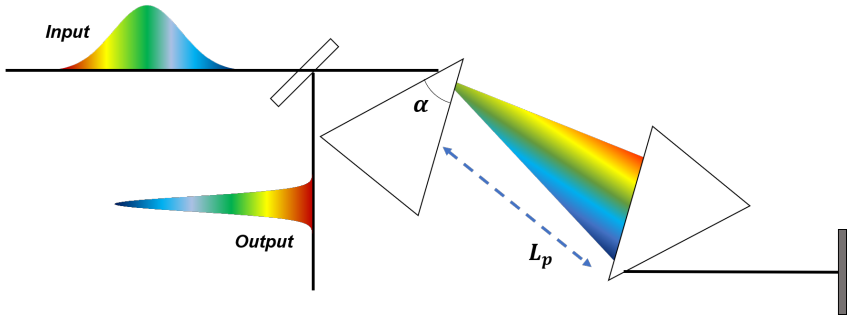


Figure II.8 – Prism pair compressor scheme. $L_p$: distance between the prisms

**Chirped mirrors** Nowadays there exists other techniques to compensate the dispersion more or less precisely on the different orders. Chirped mirrors are an example in this sense. They consist of multi-layered dielectric[Szipöcs *et al.* , 1994]. A principle scheme is shown in figure II.9.

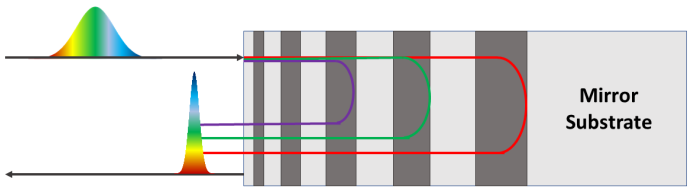


Figure II.9 – Chirped mirrors principle scheme.

Each layer is designed to have different thickness and refractive index that will be the knobs for acting on the phase correction. A specifically designed series of high and low refractive index is used in order to have a constructive interference of all the reflected components. The big advantage of the chirped mirrors is that the phase $\beta(\omega)$ we want to correct can be directly added, engineering the choice of the layers materials and thicknesses. They can be very expensive because of the complexity of the design and fabrication and generally can correct only small dispersion quantities.

**Compression** It is interesting to detail something about how to choose stretcher and compressor in a CPA scheme. Considering what we have said about the different types of compressors, it should be clear that the grating pair will be preferred because of the large amount of dispersion compensation possible. The already treated problem of this compressor is that besides important $\beta_2$ contribution, it carries an opposite sign TOD. As an example, consider a CPA composed by a fiber stretcher and a grating compressor. In this case, the TOD added by the fiber and grating pair accumulates. This added third-order phase in the pulse means a reduction of the peak power because of the appearance of an oscillatory structure. For this reason, it is often preferred to use a stretcher-compressor pair both grating based[Martinez, 1987].

## 2.2 OPA and OPCPA

In this part we want to describe the application of the concepts we introduced for optical parametric amplification. We will first talk about the birefringent phase matching for the OPAs and the most common geometries for this kind of amplification. We will, then, quickly overview a mixing of the CPA amplification scheme and the OPA, the so-called *Optical Parametric Chirped Pulse Amplification* (OPCPA) scheme.

**Birefringent phase matching for OPAs** The evocated birefringent phase matching allows phase-matching condition for a specific crystal. The basic idea is to match the three wave-vectors $k_1, k_2, k_3$ for getting $\Delta k = 0$, thanks to the different refractive indices experienced in the crystal for different polarization axes of the incoming electric field. Table II.1 summarizes the three types of phase matching for a negative uniaxial birefringent crystal ($n_o > n_e$).

| Birifrangent Phase Matching | | | |
|---|---|---|---|
| **Type name** | **Pump** | **Signal** | **Idler** |
| ***Type I*** | ext. | ord. | ord. |
| ***Type II*** | ext. | ext. | ord. |
| ***Type II*** | ext. | ord. | ext. |
| ***Type 0*** | ord. | ord. | ord. |

Table II.1 – Birefringent Phase Matching. ext.: extraordinary axis, ord.: ordinary axis.

Now, we can take a more realistic situation with respect to the one presented in the theoretical part, relaxing the approximation of perfect phase matching. If we consider, then, a non-zero $\Delta k$ , we will add a phase term in equation (II.44) for the signal:

$$A_2(z) = A_2(0)[c_1 e^{gz} + c_2 e^{-gz}]e^{-i\frac{\Delta k z}{2}}. \tag{II.69}$$

The exponential terms in the square brackets have been changed because of the $\Delta k \neq 0$, from $\Gamma$ to $g$, according to:

$$g = \sqrt{(\Gamma^2 - (\frac{\Delta k}{2})^2)}. \tag{II.70}$$

The OPA gain, then, becomes:

$$G(\Delta k, z) = \frac{I_2(z)}{I_2(0)} = \frac{\Gamma^2}{4g^2} e^{2gz}. \tag{II.71}$$

We can see that this expression for the gain is coherent with the equation found for the perfect phase-matching condition, $\Delta k = 0$. We, now, want to define a bandwidth for the OPA. To do this, we can consider the gain such that the $G(\omega) = \frac{G_0}{2}$, as depicted in II.10.

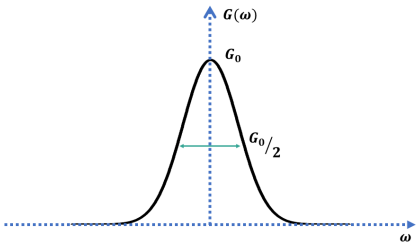


Figure II.10 – Gain definition for OPA bandwidth.

We need to relax the approximation of monochromatism we have done in the previous treatment. In particular, we will introduce an interval of frequencies $\Delta\omega$ around the $\omega_1, \omega_2$ previously considered. We consider still a monochromatic pump $\omega_3$, for simplicity. The GVM is given by $\delta_{12} = (\frac{1}{v_{g1}} - \frac{1}{v_{g2}})$. The phase matching bandwidth of the OPA in this assumption can be shown [Baumgartner & Byer, 1979] to be:

$$\Delta\nu = \frac{2}{\pi}(\log(2))^{1/2}(\frac{\Gamma}{L})^{1/2}\frac{1}{\delta_{12}}. \tag{II.72}$$

In the case of short pulses we will have to manage large spectra. The GVM between the components in the OPA will be crucial for amplifying all the pulse bandwidth and avoid dispersion spreading [Weiner, 2011]. As we have discussed before, this will mean loosing frequencies of the spectrum generating a longer TL pulse.

**Broadband OPAs** We generally wish to have an OPA phase matching BW as large as possible for amplifying ultra-short pulses. An appropriate, and very simple, method to obtain this, is the so-called *Degeneration OPA*. We take, in fact, a type I crystal configuration and signal and idler at the same central frequency $\omega_1 = \omega_2$. In this way the GVM is equal to zero because signal and idler are degenerate. This case is very simple but it is limited in terms of possible frequencies that can be amplified to half the pump central frequency.
We can look for a new degree of freedom for getting a large phase matching for the more common case $\omega_1 \neq \omega_2$. Let us look at the scheme in picture II.11, depicting the three wave vectors.

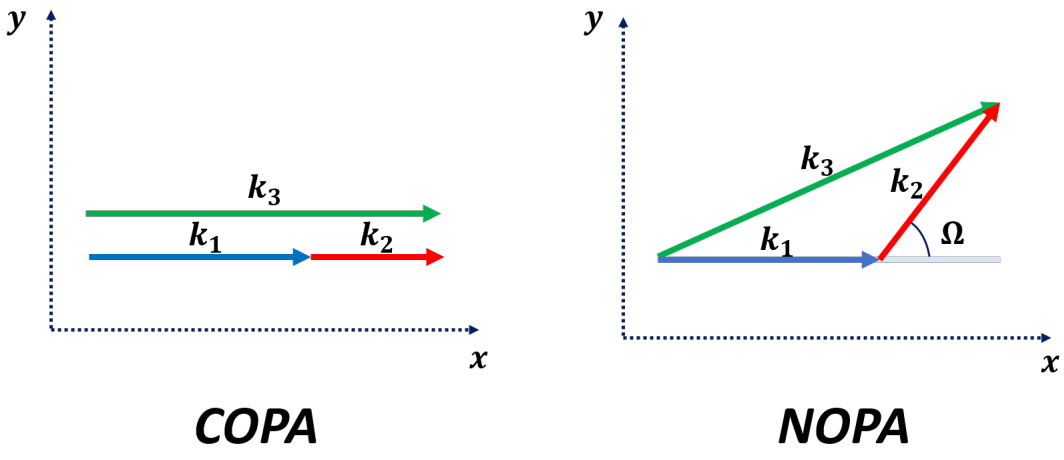


Figure II.11 – Collinear and Non-Collinear phase-matching OPA schemes.

On the left, we can see the discussed case until now. On the right, instead, we will see the case of a pump beam and signal beam that are not collinear. In the latter case, we have two phase matching conditions $\Delta k_{perp}, \Delta k_{par}$ that must be satisfied. These phase matching conditions represent the wave-vectors relations along the perpendicular and parallel axes with respect to the propagation one. It can be shown that both relations are satisfied when [Weiner, 2011]:

$$v_{g2} = v_{g1} cos(\Omega). \tag{II.73}$$

Where $\Omega$ is the angle in figure II.11. We will talk about *Collinear OPA (COPA)* for the first case of discussion, depicted in figure II.11 on the left and *Non-Collinear OPA (NOPA)* in the second one on the right [Shirakawa *et al.* , 1999]. In the NOPA case, the non-seeded wave is spatially chirped. In this work we will choose a COPA geometry because we will interested in the utilization of the idler.

**Optical Parametric Chirped Pulse Amplification (OPCPA)** The mixing of the CPA technique with OPA crystals as amplifier gives origin to the OPCPA. The first demonstration [Dubietis *et al.* , 1992], in 1992, just came some years after the CPA demonstration [Strickland & Mourou, 1985]. At that time, a BBO-based OPA allowed to amplify with a $G{\sim}10^4$, 70 fs long pulses, reaching 0.9 GW of peak power. Since then, the applications of OPCPAs have grown up intensively and tens of systems have been presented [Cerullo & De Silvestri, 2003, Butkus *et al.* , 2004]. A key point of OPCPA sources is the flexibility in wavelength allowing to have sources with output in the UV [Wnuk *et al.* , 2010] or in the Mid-IR [Mayer *et al.* , 2014]. Moreover, considering what we have said about the broadband OPA concepts, extremely broadly tunable sources can be realized [Baudisch *et al.* , 2016]. The output wavelength availability is linked to the laser that can be used as pump and signal. The conversion pump-to-output power ratio is lower than 30 %. Having high output power will depend on having high power pump laser at the right wavelength for the parametric conversion required. The signal, instead, is not required to be very powerful, considering the already-mentioned very strong gain of the process. The important features, in this sense, would be: central wavelength, spectrum and time duration. These three parameters, in fact, allow to optimize the gain stages and the output pulses characteristics. A very common and simple way to provide a signal at a specific wavelength with an arbitrary large spectrum is the *White-Light Generation (WLG)* process.This strongly $\chi_3$ dependent process allows to obtain a very large bandwidth focusing a small energy amount from a pump laser in a crystal [Dubietis *et al.* , 2017]. In this way a large number of wavelengths can be used as seed for the OPCPA chains. This phenomenon is broadly used and will be the theme of deeper discussions in the remaining of this thesis.

# Chapter III

# Relative Intensity Noise in femtosecond amplified laser sources

## Objectifs

In this chapter we will discuss the intensity noise of a mode-locked femtosecond laser. In the first two sections, the motivation for this kind of characterization for femtosecond sources, and a theoretical formalism are respectively discussed. The setup used for the measurement and its issues are analyzed in the third section. In the last part, the results in terms of characterization and improvement of a case-study femtosecond source are finally presented.

## Contents

# 1 Context: RIN measurements for femtosecond mode-locked lasers

Since the first laser demonstration, in the sixties, the laser intensity noise characterization has been crucial for laser feature understanding and performance improvement [McCumber, 1966]. The *Relative Intensity Noise* (RIN) has been introduced as a criterion for these scopes. *Continuous Wave* (CW) emitting diode laser domain has particularly pushed the research on this topic [Petermann, 1991]. For this kind of laser it is of particular interest to have the lowest possible intensity noise for several applications in metrology [Arditi & Picqué, 1980]. For mode-locked lasers, it is relevant to inspect amplitude and RF phase noise. The interest of evaluating the noise performances has acquired a strong importance since the frequency-comb and its applications were pointed out by Hansch [Hänsch, 1972]. In this case, the nature of ML lasers is, for example, used for precision spectroscopy [Hänsch, 2006].
Considering what we have said, we could deduce that the laser noise analysis and consequent reduction to the lowest possible noise is a subject of study only for very precise situations. Nevertheless even commercial pulsed lasers require a characterization of the intensity fluctuations performances. The shot-to-shot stability (or pulse-to-pulse stability), defined as the *root-mean-square* (rms) of photodiode measured pulse energies is the standard [ISO 11554:2017, 2017]. It will be usual to find in product data-sheets that the laser stability is less than some percent rms.
In the last decades, commercial high energy class lasers have been used as strong field physics drivers. For this kind of utilization, ultra-stable laser chain are required, thrusting the limits of the intensity stability features. It is asked, for instance, a laser with a pulse intensity shot-to-shot stability lower than 1%. This opens the discussion about how reproductive and sensitive can be this type of measurement. We believe that femtosecond laser amplified source characterization in terms of RIN brings to a clearer analysis of the system for the desired application with respect to the used shot-to-shot rms. Measuring the RIN of our source provides a frequency spanning fingerprint of the sources of noise contributing to the rms intensity stability. It has to be said that pulse-to-pulse stability is an extremely simple measurement to do, requiring only a photodiode and an oscilloscope. The few studies that have been carried out about RIN measurement for pulsed ultra-short laser require, instead, costly and delicate setup arrangements [Paschotta, 2004, Budunoğlu *et al.* , 2009, Tawfieq *et al.* , 2018]. This complexity is incompatible with the industrial and commercial requirements. In this chapter, we introduce a very simple setup for RIN measurement of femtosecond laser sources explaining details of the measurement and the advantages of the technique.

# 2 Theory and background

In this section, we discuss a theoretical approach for the treatment of intensity noise for femtosecond mode-locked lasers. First the intensity and phase noise is introduced. The RIN is then discussed and some common techniques of measurement are analyzed.

## 2.1 Definition of the RIN

Consider an ideal femtosecond mode-locked laser, without noise. The intensity in the time domain can be described as a sum of Delta functions [Weiner, 2011]:

$$I_0(t) = P\sum\nolimits_n \delta(t - nT), \tag{III.1}$$

where: $P$ is the power of a single pulse, $T$ is the period of the pulse train. In a more realistic situation, we have to consider intensity fluctuations $\Delta I(t)$:

$$I(t) = I_0(t) + \Delta I(t). \tag{III.2}$$

Taking into account amplitude and time fluctuation, we can write:

$$I(t) = P[1 + N(t)] \sum_{n=-\infty}^{+\infty} \delta(t - nT - J(t)). \tag{III.3}$$

Where: $N(t)$ is the normalized power fluctuation, $J(t)$ is the timing jitter. The way to deduce the phase noise and the amplitude noise of the laser usually involves a frequency domain analysis. We remind the definition of the *power spectral density* (PSD) as [Davenport *et al.* , 1958]:

$$S_p(\omega) = F\{\langle I(t)I'(t+\tau)\rangle\}. \tag{III.4}$$

So that, for our train of deltas we get:

$$S_p(\omega) = P^2 \sum_{n=-\infty}^{+\infty} [2\pi\delta(\omega - \omega_n) + S_N(\omega - \omega_n) + n^2{\omega_n}^2 S_J(\omega - \omega_L)]. \tag{III.5}$$

Where: $\omega_L$ is the harmonic mode-locking frequency $\omega_L = \frac{2\pi n}{T}$, $S_N$ is the amplitude noise spectral density and $S_J$ is the phase noise spectral density. We neglect for our treatment the phase spectral noise contribution $S_J$, and focus only on the amplitude one. We take, then, the rms of the amplitude noise fluctuations in time $N(t)$, underlining the equivalence:

$$\sigma_N = \sqrt{\langle N(t)\rangle^2} = \sqrt{\frac{1}{\pi}\int_0^{+\infty} S_N(\omega)d\omega}. \tag{III.6}$$

We introduce a finite bandwidth of frequencies from a $\omega_{min}$ to $\omega_{max}$ to model real measurement conditions.

- $\omega_{max}$ is coming from the bandwidth of the detection system. As we will see in the next section, the detection is limited by the setup elements to a specific frequency, that will be the maximum frequency of the RIN PSD.
- $\omega_{min}$ is strictly linked to the measurement time $\Delta T$, according to $\omega_{min} = \frac{2}{\pi\Delta T}$.

The RIN PSD is simply defined as the amplitude noise $S_N$. It is the above-mentioned power laser spectrum $S_p(\omega)$where we have normalized the average power and neglect the timing jitter contribution. If we take the harmonic $n = 0$ of the pulse train:

$$RIN = \frac{S_P(\omega)}{P^2} = S_N. \tag{III.7}$$

Dimensionally, considering that we are measuring a normalized frequency sample, we have units of $[\frac{1}{Hz}]$. The logarithmic scale is often used for the interpretation of the PSD. We have:

$$RIN_{[dB]} = 10log_{10}(S_N), \tag{III.8}$$

with units of $[dBc/Hz]$. The $c$ in the $dBc$ value is aimed to stress the fact that is a value normalized to a carrier, giving rise to the adimensional term. The integrated value of the RIN (referred as IRIN) is equal to $\sigma_N^2$. We can easily understand that the IRIN value and the shot-to-shot stability (which we have indicated in the context section to be as reference measurement for commercial lasers) are theoretically the same. It will be shown in the next section that even if theoretically the two values should be same, the way they are measured induces different results in practice.

## 2.2 RIN measurements for mode-locked laser

As already said in the context section, the RIN measurement is a well-established characterization tool for CW lasers. For mode-locked lasers there are different details that have to be considered. The simplest way we have to measure a train of pulses is to use a photo-diode (PD) and an *Electrical Spectrum Analyzer*(ESA)[Von der Linde, 1986]. Using this instrument allows to directly access the frequency spectrum of the pulse train. What is particularly interesting is that both phase noise and intensity noise spectra can be retrieved. This can be clarified looking at the figure III.1.

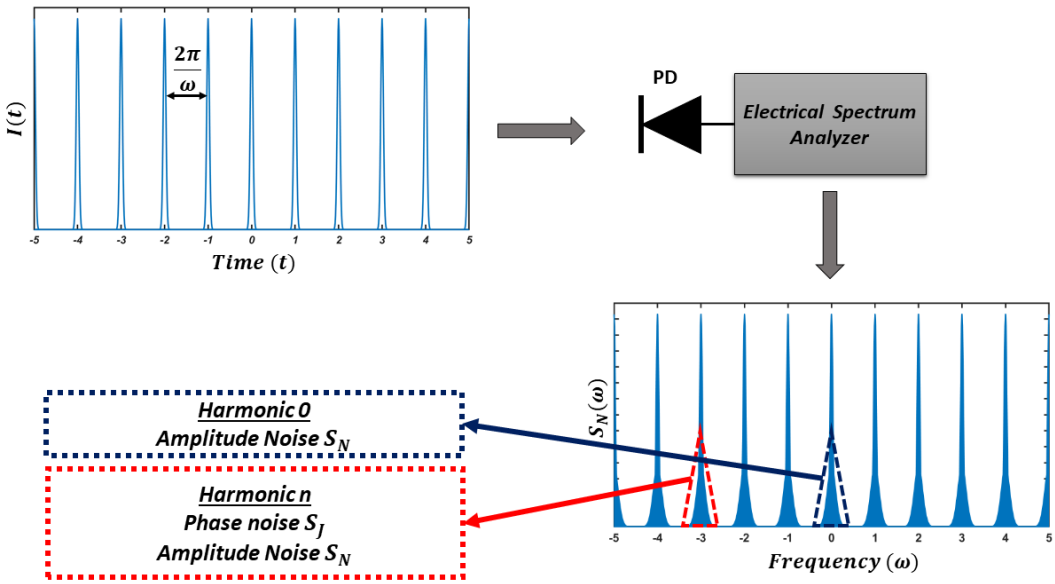


Figure III.1 – Scheme indicating the measurement process with an ESA of a pulse train spectrum. PD: Photodiode.

The figure shows the measurement process following strictly what we have said in the theoretical treatment. At the beginning, a pulse train is illuminating a photo-diode (PD). The intensity of the pulses is proportional to a current $i_n(t)$ generated from the PD. This current is measured by the ESA. The ESA output is the power spectrum of the train in frequency. Each pulse in the RF spectrum has a base structure. For the n-th harmonic the base is due to the $S_N$ and $S_J$ [Scott *et al.* , 2001]. We can notice in the eq.(III.5) that the phase noise spectrum is not present around the 0th order harmonic. In this case we talk about *Baseband*. We can measure the amplitude noise (AN) by filtering out all the laser harmonics different from the

zero-centred one. Considering the symmetry of the power spectrum this means simply isolating the frequency bandwidth from 0 to half the repetition rate laser frequency.

# 3 Measurement setup and issues

We now introduce the setup of RIN measurement we will use. We first discuss how we design it. After, technical details that have to be taken into account for the measurement are pointed out. The setup and the measurement we present in this section has been the result of a learning curve during the thesis period. Some of the RIN results we present in this chapter are realized with slightly modified setup with respect to the optimized one. We ensure the coherence on the results and conclusions we present in the next, using exactly the same setup when we make comparative study between two different laser conditions. It has to be said that the measured IRIN value is overestimated when we use the not optimized setup. These elevated values are meaningful only in the context of the comparative studies. The IRIN corresponding to the real source one is the one obtained using the optimized setup we discuss in this section. This underlines the importance of minimizing measurement noises.

## 3.1 Setup description

We have anticipated that we use a different approach for AN measurement. The main difference is that we are not using the ESA. We measure the pulse signal in time using a PD. While the ESA gives the RF power spectrum we need for analysis of the PSD, we measure, instead, the PD signal using an oscilloscope. We make, then, a post-processing via a *Fast Fourier Transform* (FFT) [Welch, 1967] for getting the RIN PSD. A point to solve still remains for the realization of the time measurement with respect to the spectral one. We have said that we must filter the higher harmonics of the laser for isolating the baseband. We filter the signal of the photodiode using an electrical low-pass high order filter. In particular we choose a filter with a cutting frequency $f_{cut}$ equal or lower than the Nyquist frequency of the laser repetition rate $f_N = \frac{f_{rep}}{2}$.The general RIN measurement setup is the very simple one depicted in figure III.2.

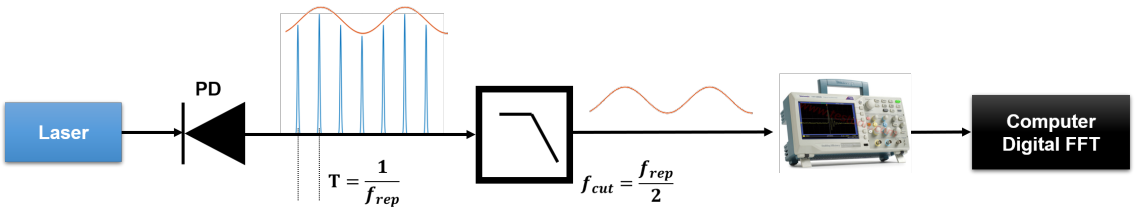


Figure III.2 – Setup of the RIN measurement.

We can see that the filter transmits only the slow variation of the pulse train to the oscilloscope. In the reality of our measurement, we have a noise and not a single modulation as represented in the scheme. Although the setup is very simple, each element of the detection system can distort the laser signal, influencing our RIN measurement. This is something we want to avoid. For this reason, we need to carefully choose each element of the measurement setup as well as their operation parameters.

**Photodiode** The photodiode choice is done considering mainly two aspects: the photodetector noise and the acquisition bandwidth. We use Si photodetector because the responsivity, $R(\lambda)$, is high enough at $1\mu m$, our laser central wavelength. The bandwidth is chosen depending on the repetition rate of the laser we want to measure. The noise quality of the detector is defined by the *Noise Equivalent Power* (NEP) [Hamstra & Wendland, 1972]. This quantity is essentially the minimum detectable power by the detector. To be more precise, it is the minimum detectable power divided per the bandwidth unit, and for this reason is expressed in $[W/\sqrt{Hz}]$. For our measurement, we choose the lowest possible NEP for having the highest

sensitiviy of our RIN. Considering the values that can be found in datasheets of commercial PDs, we must consider the NEP in relation with the bandwidth of the detector and its responsivity. The value normally given is the minimum NEP, that corresponds to the maximum $R(\lambda)$. All this considered, we can reformulate our best possible choice of the photodiode as the lowest NEP, the smallest bandwidth (frequency response), $\lambda$, and the maximum $R(\lambda)$ [Mackowiak *et al.* , 2015].

**Filtering** As already discussed the filter has to be chosen with a cutoff frequency $f_{cut} \leq f_N$, where $f_N$ is the Nyquist frequency. In particular, it is very important for a proper measurement to use a high-order filter. We would use the closest possible $f_{cut}$ to Nyquist. At the same time, we want that the response of the filter is strong enough to really eliminate any residual measurable harmonics signal. If this is not true peaks in our PSD could be measured around the filter cutoff coming from the pulsed character of the laser. We can see that another possibility is to use directly the photodiode bandwidth to filter out the higher frequencies. This is a worst choice respect to a rapid photodiode and an high-order filter because, the bandwidth limit of the photodiode can be seen as a RC first order filter. If we use a photodidode with a BW equal to the $f_N$, the RC filtering still transmits peaks due to the pulsed nature of the laser.

## 3.2 From continuous to discrete: signal sampling and aliasing

In the theory section we have considered our signal as continuous. The nature of the measurement is, instead, discrete. The oscilloscope, moreover, acts as *analog to digital converter* (ADC). It is useful to analyze what impact this conversion could have on the RIN measurement. The oscilloscope is sampling at a determined sampling rate $f_S$ the photocurrent of the PD.

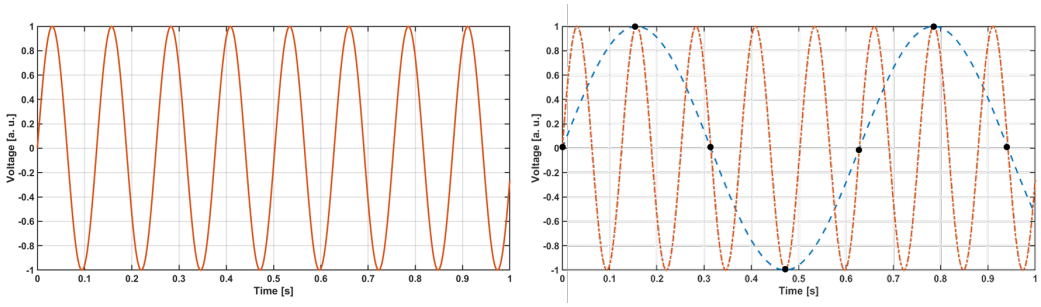


Figure III.3 – Representation of the oscilloscope sampling and aliasing. Left: analog measured sinusoidal signal. Right: oscilloscope undersampling signal (blue-dotted line).

Considering as an example, the sinusoidal oscillating current at a frequency $\omega$ depicted in figure III.3. On the left there is the analog signal in solid orange line. On the right the same signal is dotted in orange. Let us imagine that the $f_S$ is such that a point is measured each $\omega/1.5$, as in figure III.3 on the right is represented by the black dots.

Not only the dotted orange line fit these points but also another modulation with a lower frequency, depicted as a dotted blue line in figure III.3 on the right. This new function is an *alias* of the orange sinus generated by the sampling. This case is referred as *undersampling*. A way to avoid this problem is to sample faster than twice the frequency of the sinus we want to measure [Shannon, 1948].

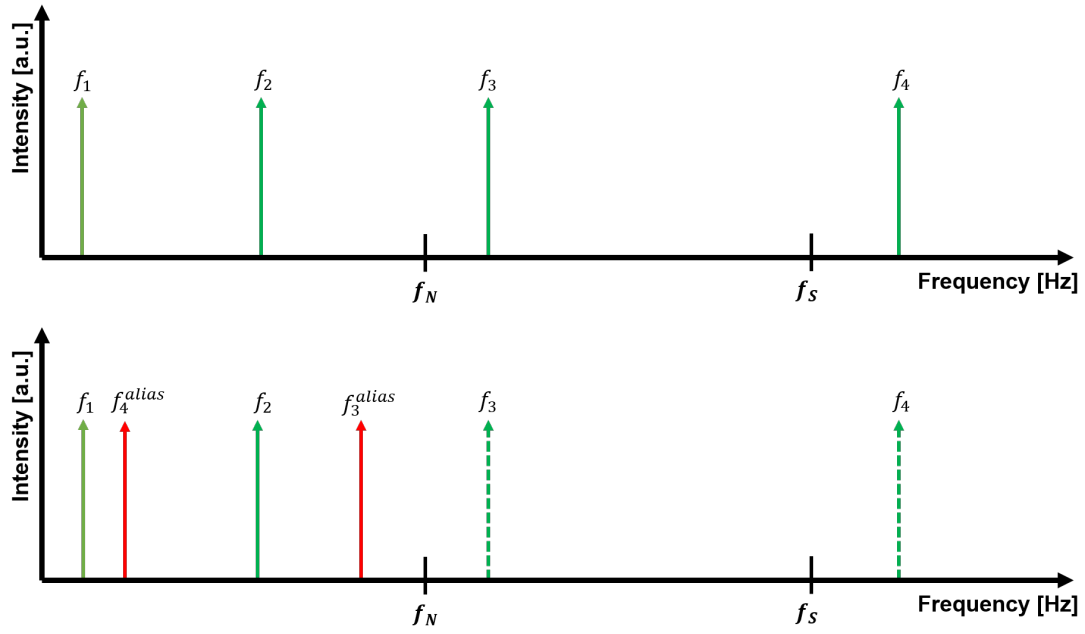


Figure III.4 – Depiction of frequency spectrum aliasing of components higher than $f_N$. Top: real signal. Bottom: aliased signal.

Let us consider that a signal composed of several peaks in the frequency spectrum, like in figure III.4 on the top. The only frequency that are not affected by the aliasing are the ones between zero and the Nyquist frequency $f_N$. If there are components of the signal higher than $f_N$ are aliased. This means that they are transposed at a frequency in the BW $[0;f_N]$. Let us analyze the example in figure III.4 on the top. Consider $f_S = 100$ Hz, $f_1 = 10$ Hz, $f_2 = 30$ Hz, $f_3 = 60$ Hz, $f_4 = 120$ Hz. The frequency of the $f_3$ and $f_4$ are aliased at new frequencies $f_3^{alias}$ and $f_3^{alias}$ that are linked to the $f_S$ according to:

$$f^{alias} = |nf_S - f_x|, \tag{III.9}$$

where $f_x$ is the general original input frequency higher than $f_N$ and $nf_S$ is the closest integer multiple of the sampling frequency. For our example this means:

$$f_3^{alias} = |100 - 60| = 40Hz, \tag{III.10}$$

$$f_4^{alias} = |100 - 20| = 20Hz. \tag{III.11}$$

In our noise signal we can have components higher than $f_N$, that will be aliased in the measurement BW. This is a source of complexity in the data interpretation that have to be considered in our case. It is of particular interest if our sampling rate is not several order of magnitude higher respect to the mode-locked laser frequency. In the next we will see phenomena of aliasing for laser pulse picking schemes.

## 3.3 Shot noise limit

The shot noise limit is the bottom limiting line for RIN PSD. The shot noise is the noise coming directly from the fact that photons are discretely detected by the photodiode [Quimby, 2006]. In particular, we can say that the shot noise variance for the photocurrent is:

$$\langle i_n \rangle^2 = {\sigma_i}^2 = 2qI\Delta f, \tag{III.12}$$

where $i_n$ is the photocurrent of the photodiode, $q$ is the electron charge, $I$ is the average current and $\Delta f$ is the measurement BW. For our treatment, it is useful to have the power spectrum for the shot noise. This is:

$$S(f) = 2qI. \tag{III.13}$$

Considering, now what we have said in the RIN definition section, the spectral power of the shot noise is normalized:

$$S_{RIN}(f) = \frac{\langle i_n \rangle^2}{I^2} = \frac{2q}{I}. \tag{III.14}$$

We can see that the noise value is lower for higher current intensities. For example, for an average photo-current of 1 mA, the RIN is limited to $-159\ dBc/\sqrt{Hz}$ . The assessment above is strictly true for the CW case. The problem for our case is a bit more complex, because it is not so easy to estimate the average current in a pulsed situation. A semi-classical model, introduced by Quinlan et. [Quinlan *et al.* , 2013], gives an approximation for short-pulses. They show that for similar measurement condition to ours, and for ideally Gaussian pulses of around 100 fs of time-length, simply:

$$S_{RIN,pulsed}(f) = \frac{q}{I} = \frac{S_{RIN}}{2}. \tag{III.15}$$

This means that for equivalent average photocurrent $I$, a RIN shot noise limit lower by $-3\ dBc/\sqrt{Hz}$ than in the CW case is obtained. Our estimation of the shot noise limit is done considering the average photocurrent of the detector, calculated as the $R(\lambda)P_{opt}$. $P_{opt}$ is the average optical power impinging on the photodiode. Typical value of $R(\lambda)$ for Si detector at 1 $\mu m$ are 0.6 $A/W$. To have 1.6 mA of average photocurrent, 6 mW of average power should be used for the measurement.

## 3.4 Photodiode saturation

We have realized that we need to have enough average power on the photodiode if we want to keep the shot noise limit low. This becomes important when the noises we want to measure in our under test source are of the order of the calculated shot-noise limit.
We understand that the best solution is to use as much power as possible in order to push down the shot-noise RIN limit. The upper limit to this is the photodiode saturation. When the photocurrent is too high the response of the receiver is no more linear. Considering a CW laser irradiating the PD, the saturation effect depends on the size of the detector, on the load resistance and on the reverse voltage [Quimby, 2006]. The saturation voltage limit grows for bigger load resistance, for smaller detection area and decreasing the inter-electrode resistance. If we, now, concentrate our attention on the pulsed case we can easily understand that this voltage depends on the peak power of our pulses, too [Stuik & Bijkerk, 2002].

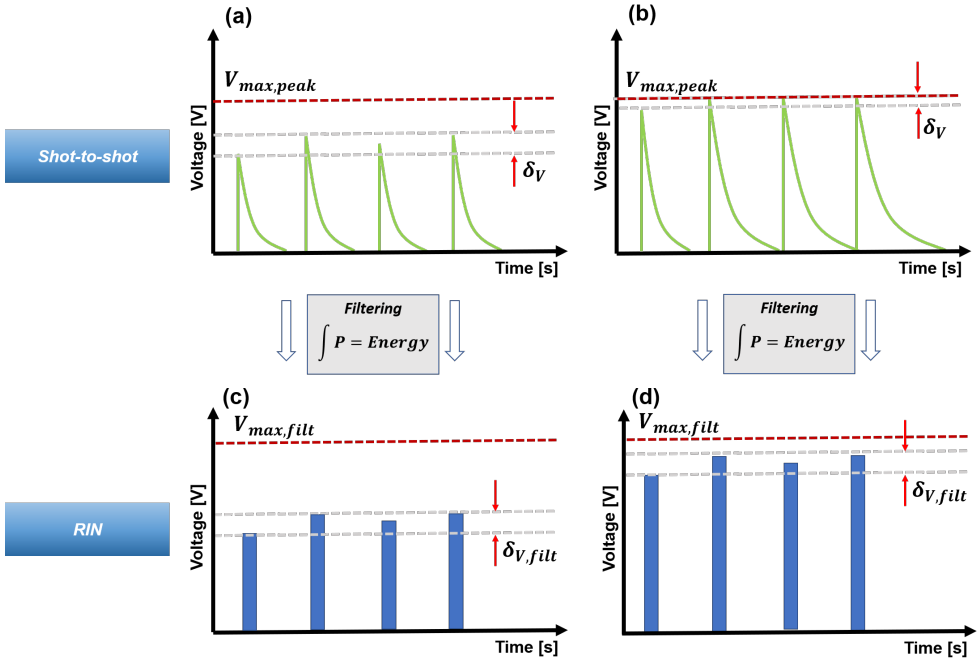


Figure III.5 – (a)PD response in not saturated case, (b) PD response in saturated case, (c) PD response after filtering for case (a), (d) PD response after filtering for case (b).

If we consider the case of an intensity shot-to-shot rms measurement, the saturation voltage limit is directly linked to the $V_{peak}$ measured by the PD for our peaks. Let us analyze the cases depicted in figure III.5(a) and III.5(b). In both cases we are measuring the same source AN but in case (b) the optical power on the PD is bigger than in (a). In the first case we have that the amplitude noise fluctuations corresponds to a certain $\delta_V$ shown in the figure. If the optical power on the photodiode is too high, like in III.5(b), the $V_{peak}$ is no more growing up but the shape of the pulse measured is changed[1]. This means that if we are underestimating the real fluctuations measuring a $\delta_V$ lower than the real one. We can define a $V_{max,peak}$ for which the $V_{peak}$ is no more growing up but the PD response changes. This is the voltage corresponding to the optical power upper limit for a shot-to-shot fluctuation measurement. In the RIN measurement case what is measured is the variation of energy of the successive pulses. The filtering acts as integrator for each pulse. The pulses measured in III.5(a-b) become the integrated value in III.5(c-d). The fluctuations of amplitude $\delta_{V,filt}$ are the same in the two cases, not evidencing the saturation. For even more optical power on the PD, there is saturation of the energy variation. This corresponds to have a $V_{max,filt}$ that is bigger with respect to the previously defined $V_{max,peak}$.
The saturation voltage is evaluated experimentally for each of the measurements we will present in the next pages. In order to have a quick demonstration of what we have said we measure a RIN with two different cases of impinging power on the PD. In figure III.6 we can see the PSDs and the integrated RIN behaviors for a specific laser measurement.

[1]The photocurrent in both these cases is lower than the saturation current $I_{sat}$ of the photodiode. This means that the PD response can be considered linear.

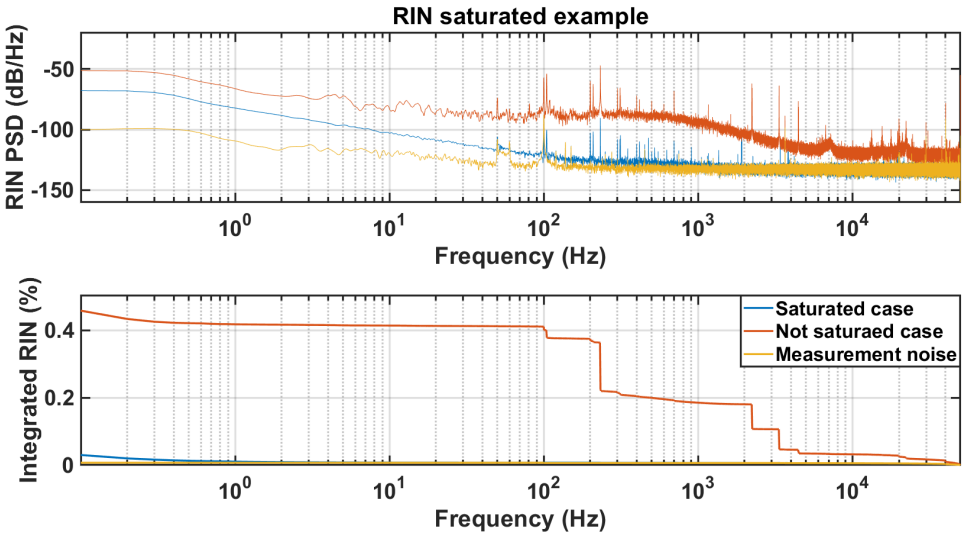


Figure III.6 – PSD RIN (top) and IRIN (bottom) for a saturated example case.

Let us comment this example of saturation. In red the case of the not saturated RIN measurement is depicted. We see in the PSD that a peaked structure is visible. We also observe a continuous floor that naturally goes down for high frequencies. In the saturated case, the floor RIN of the laser is completely missed. It is interesting to remark that the peaks are still clearly visible, even if they are strongly reduced in amplitude. Comparing the IRIN we can see that the effect is dramatic in the underestimation on the laser noise in the saturated case. We get only 0.03 % instead of the real 0.46 %.

## 3.5 Signal-to-Noise Ratio (SNR) optimization

We have already said that each element of our measurement setup has an impact on our measured noise and has to be carefully optimized to have a proper measurement. The oscilloscope itself has, for example, a specific noise that can be dominant on the laser one. The noise characteristic of the oscilloscope relies upon several things such as the quantification error, the input electronic stage of the device and so on. Consider what is depicted in figure III.7. We can see the signal of the oscilloscope after the filter on two different input settings.

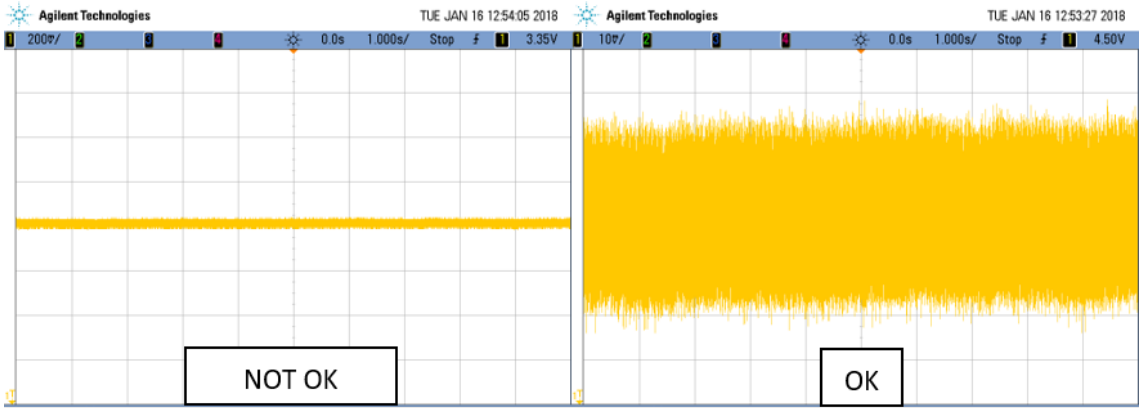


Figure III.7 – Not good and good measurement for electronic noise of the oscilloscope.

In the figure on the left we can see that the oscilloscope trace spans only less than half a division. In the case on the right, instead, the same measurement is zoomed in thereby reducing the quantization error from the input ADC. This is observed also in the oscilloscope noise

provided in the manufacturer data-sheets indicating the noise of the oscilloscope lowering for smaller V/div settings. There are other noise sources in the oscilloscope (and in our detection scheme in general) that we cannot control. We will put all these components under the generic name of electronic noise. As an example, let us analyze the figure III.8. A PSD and the relative integrated RIN are depicted for two different measurement cases of the same laser under test.

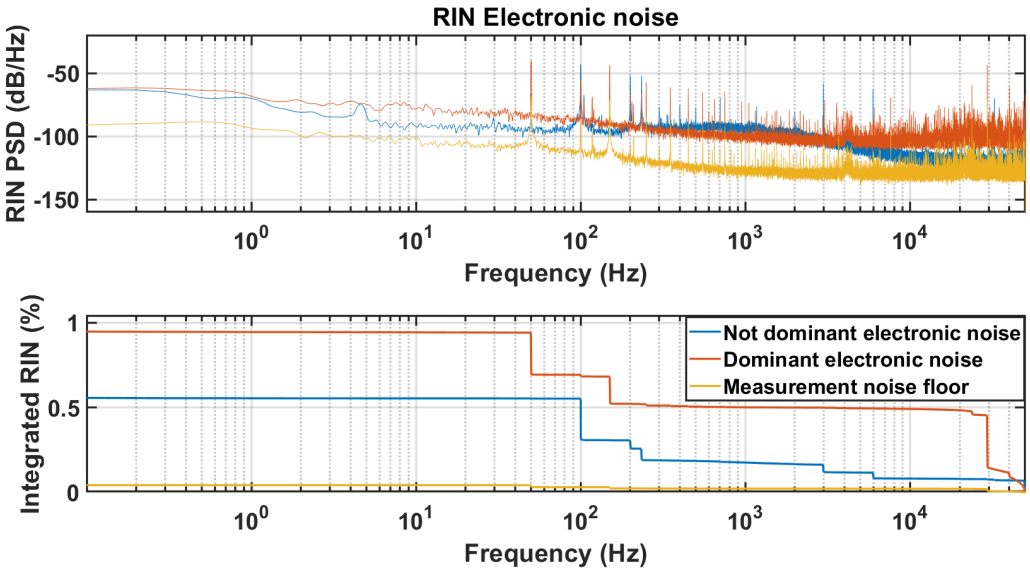


Figure III.8 – PSD(top) and Integrated(bottom) RIN traces.

In the PSD and IRIN curves in red, we have measured a case with low signal on the photodiode corresponding to the worst condition for the oscilloscope. In the case depicted in blue, we have well optimized our oscilloscope to have the smallest input settings and the highest signal before saturation. Finally, in yellow are represented the PSD and the relative integrated measured noise floor, acquired with no light coming on the photodiode. Let us start looking at the IRIN box in the bottom. We can see that the integrated value in the red case is almost twice the one in the blue case. Moreover, not only the total value is different but also the measured structure itself. This appears even clearer if we look at the corresponding PSD. If we look at the peaks in the red and the yellow case we appreciate that they are exactly the same. The blue one, instead, shows different peaks. The red case is completely dominated by the electronic noise evidencing a behavior replicating the measurement noise floor. The real laser RIN is measured in the blue case. In our measurements, we will carefully choose the setup condition to reduce the impact of the electronic noise and optimize the SNR.
Let us imagine, now, that we want to measure a signal with our RIN measurement method but the signal is too low for being optimized on the oscilloscope characteristics as we have just explained. A solution to this problem can be to use an amplifier between the filter and the oscilloscope, enhancing the average voltage. It has to be stressed, once again, the importance of the good choice of the amplifier. This component can, in fact, add noise in the RIN resulting in an altered RIN measurement. An interesting point to emphasize is that the same procedure cannot be applied for lowering the shot noise limit. This limit depends really only on the photodiode. Inserting an amplifier after the detector does not change the shot noise relation.

## 3.6 From pulse-to-pulse stability to RIN

It is finally interesting to show how linked are the RIN measurements and the shot-to-shot intensity stability. To investigate this relation, we take as an example a pulsed laser at 40 MHz. First, we measure the shot-to-shot stability. The measurement setup is a fast photodiode

(DET10A, *Thorlabs*) and a fast oscilloscope (BW $\gg$ 40MHz). We want to avoid the issue described in the previous paragraph about the noise of the oscilloscope. We make a zoom on the pulse measured by the photodiode such that we optimize on the oscilloscope screen only the peak of it. We use the histograms statistics to measure the fluctuations. Since our idea is to compare this measurement to the RIN we take a number of point that will correspond to our RIN measurement time. The result gives a standard deviation of 0.48 %.

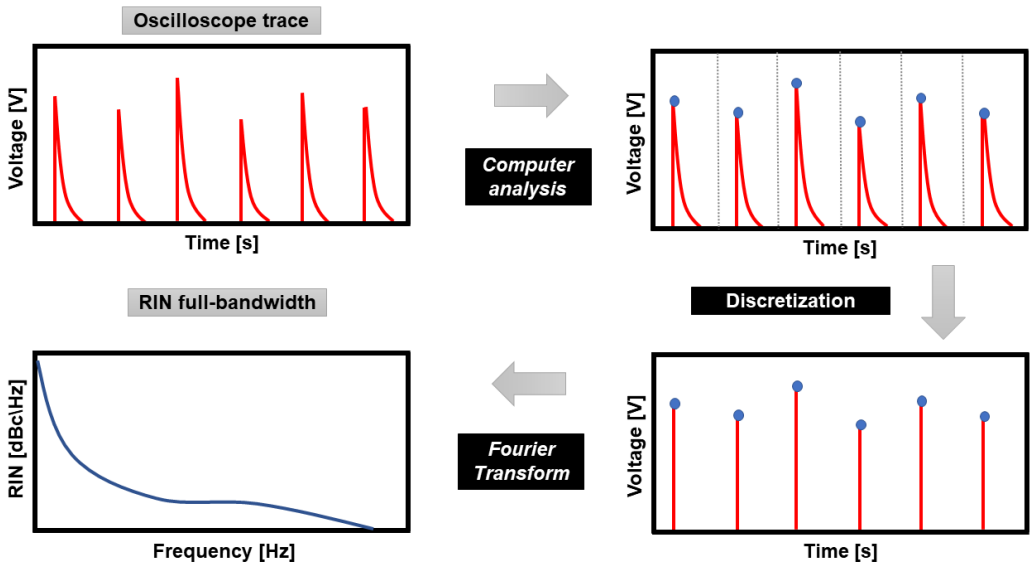


Figure III.9 – Scheme of the process of RIN full-bandwidth

Before making the RIN measurement following the procedure described in the previous part of this section, we decide to make an intermediate measurement. The idea is to use the same setup we have used for the shot-to-shot measurement but post-processing the datas in order to obtain the RIN PSDs and the correspondent IRINs. This is a sort of *RIN full-bandwidth* because of the absence of the filtering step. The principle is explained in figure III.9.

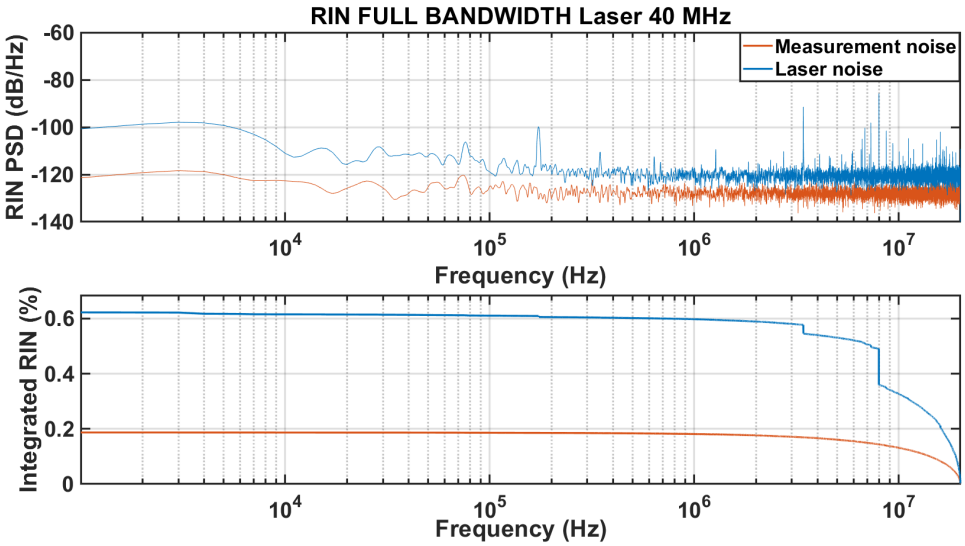


Figure III.10 – Top: RIN full-bandwidth PSD for the laser at 40 MHz Bottom: IRIN full-bandwidth for the laser at 40 MHz

The not filtered signal of the oscilloscope is analyzed on the computer. The trace is dis-

cretized in order to have only one $V_{peak}$ value per pulse, as it is shown by the blue dots in figure III.9. The discretization at this point is a sampling as the one presented before for the oscilloscope. This means that this step is affected by the aliasing. The discretized signal is normalized to the average voltage and Fourier transformed for the calculation of the PSD RIN.

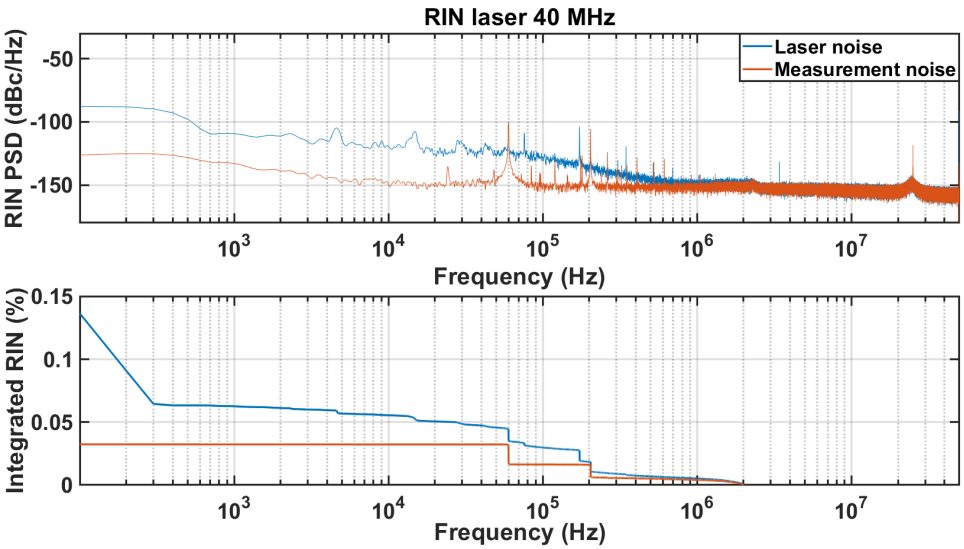


Figure III.11 – Top: RIN PSD for the laser at 40 MHz Bottom: IRIN for the laser at 40 MHz.

The results are depicted in figure III.10. Analyzing the integrated noise we can see that it is 0.62% in the bandwidth between 1 kHz and 20 MHz. We can see that there is an important contribution due to the measurement system itself. The optimization of the SNR described in the previous section is not applicable in the RIN full-bandwidth because the pulses complete response have to be measured. The oscilloscope quantification error is not minimized. We subtract the measurement noise contribution of the RIN full-bandwidth, considering negligible the one of the pulse-to-pulse measurement. We obtain $IRIN = \sqrt{(IRIN^2_{laser} - IRIN^2_{measurement})} = 0.57\%$. This value is very close to the pulse-to-pulse stability found. We pass now to the RIN measurement. We use an amplified photodiode (PDA36-EC, *Thorlabs*), a filter at 2 MHz (LPF1.9+, *mini-circuit*) and an oscilloscope. The results are depicted in figure III.11.

Let us compare them to the RIN full-bandwidth. The IRIN is less than a third, with a value of IRIN=0.14 %. Looking at the IRIN in the full-bandwidth case, we can see that the majority of the contribution is due to two noise peaks at 3.3 MHz and 8 MHz. These peaks are not present in the RIN PSD. The question to answer is if these peaks are real noise or come from the measurement. The frequencies are integer sub-multiples of the laser repetition rate. This is in an indication of an aliasing situation coming from the measurement and not from the noise of the laser [Holst, 1998]. This phenomenon cannot be avoided both in the shot-to-shot measurement and in the RIN full-bandwidth because of the absence of the low-pass filter. The impact of this kind of phenomena as well as the measurement noise itself are completely hidden in the pulse-to-pulse stability. This make this measurement not suitable as a comparison between different system. It can be still useful if it is used as comparison between two situations using exactly the same measurement setup and parameters configuration.

# 4 RIN case study on an amplified FCPA system

In this section we discuss RIN characterization of the pump laser we use for pumping our CEP-stable source, that will be described in the next chapter. In the first part, this industrial amplified laser source is quickly described and a detailed RIN characterization in different laser operation conditions is done. In the second part, the improvement of the laser RIN quality is presented, showing the related results.

## 4.1 RIN characterization of the laser

### 4.1.1 FCPA system description

The laser we use for RIN case study is a commercial source, Satsuma, by *Amplitude Laser*. It delivers 40 $\mu J$, 350 fs width pulses with a repetition rate up to 500 kHz. As already cited, it is a fiber CPA scheme. We do not detail all the characteristics of this laser but we concentrate only on some specific characteristics, looking at the scheme in figure III.12.

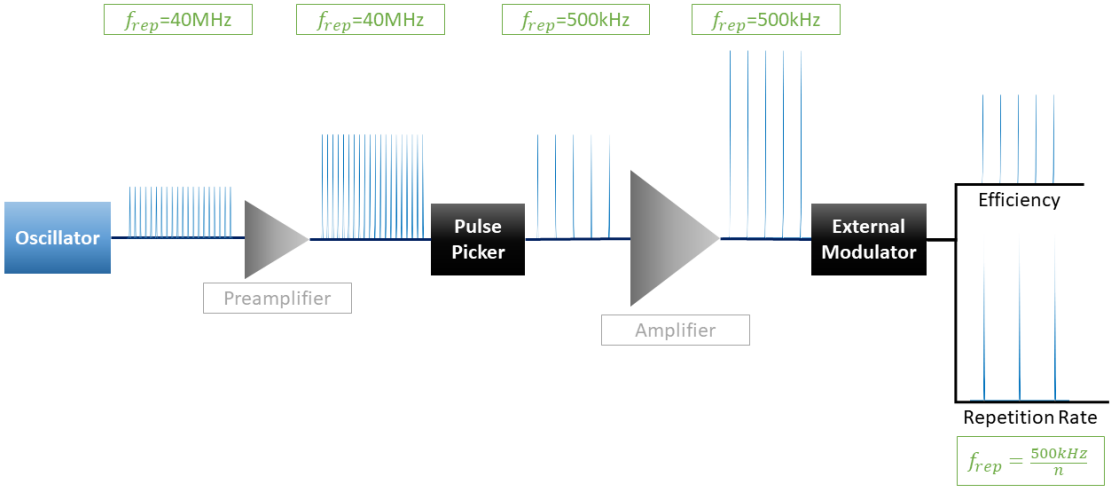


Figure III.12 – Scheme of the pump laser considering only the components acting on the repetition rate.

We can see in the figure III.12 a simplification of the pulses propagation in the laser source. We see that starting from the oscillator, we have in order some single-mode fiber amplifier, a Pulse-picker, the main amplifier and a second element working on the repetition rate called External Modulator (ME). The pulse-picker reduces the oscillator amplified pulses frequency from 40 MHz to 500 kHz in order to allow high energy amplification. The external modulator is an acousto-optic modulator that allows two different things for the laser user. First, the repetition rate of the pulses can be lowered from 500 kHz to its sub-multiples, preserving the pulse energy. Second, the efficiency of the ME can be tuned modifying the energy of the out-coming laser pulses. In practice, this is controlled by a number going from 0 to 100 % in the laser control software. The pulse-picker and the ME will be two main elements we will work on for the RIN characterization and improvement.

### 4.1.2 Pulse-picking noises

The pulse-picking is a sampling operation. It is useful to stress what happens in terms of noise. Consider the scheme of a pulse-picking AOM in figure III.13.

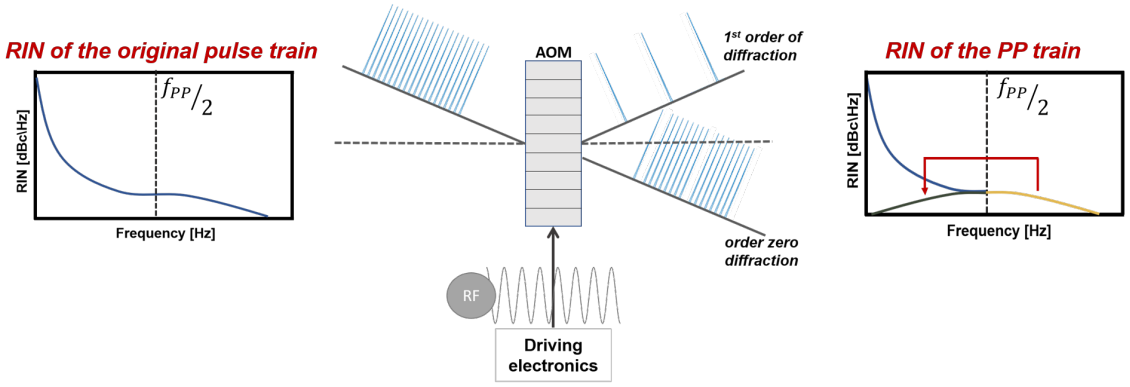


Figure III.13 – Scheme of the pulse-picking AOM on pulses and noise.

Let us now, look at the working principle of the AOM in a simplified idea. A diffraction grating is generated in the crystal thanks to the propagation of an acoustic wave. This wave is generated by a driver. This electronic element is source of noise. This noise is transferred to the acoustic wave and from the acoustic wave to the pulse-picked train. The transfer from the driver to the RF wave and from the RF wave to the optical train depends on the specifics conditions and on the driver electronics. Recalling the principle of operation of the AOM [Saleh *et al.* , 1991], in figure III.13, the original pulse train at $f_{rep}$ is pulse-picked at a lower frequency $f_{PP}$. The noise contribution in the RIN PSD of the initially existing in the bandwidth $[f_{PP}; f_{rep}]$, are aliased in the pulse-picked train in the bandwidth $[0; f_{PP}]$. In the picture a continuous contribution is added in the sampled noise spectrum. For a peak noise at a determined frequency the transfer follows the same principle we have explained in the theory section.
At laser output, the RIN spectrum contains the aliased components of the original 40 MHz train and can have added noise contributions from the pulse-picking electronics.

### 4.1.3 External modulator characterization

As a first test for the laser characterization we decide to see if the action of the ME has an impact on the AN of the laser. This is very important for the application of the laser as seeder of the system we will present in the next chapter. We use it at 100 kHz and with an efficiency of 80 %. First, using the ME, we measure the RINs for different values of the efficiency. We measure for 60, 80 and 100 % with the repetition rate fixed at 100 kHz in the 3 cases. For the realization of the measurement we use a setup slightly different with respect to the one presented in the section 3. We have a switchable amplified photodiode (PDA36-EC, *Thorlabs*) and a filter with $f_{cut} = 20\ kHz$ (EF122, *Thorlabs*).

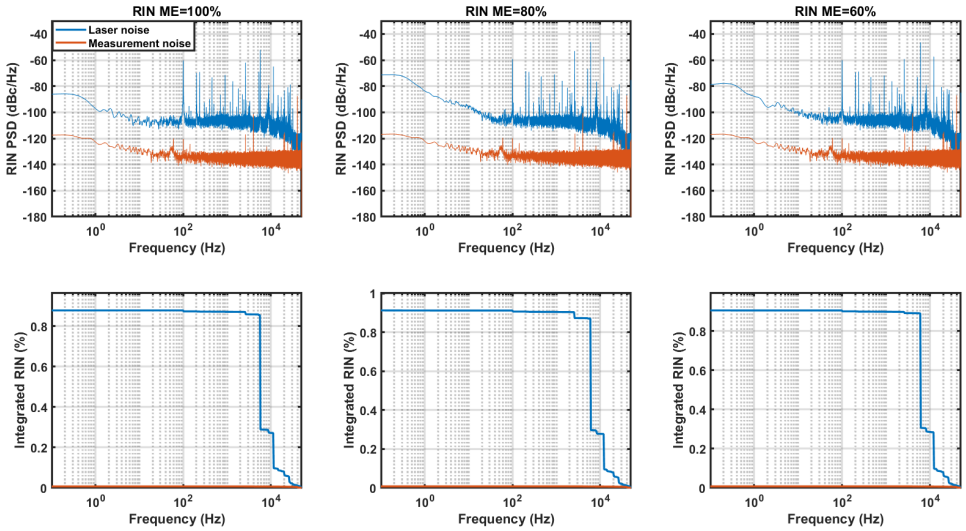


Figure III.14 – Top: PSD RIN for the ME at 100, 80 and 60% efficiency . Bottom: IRIN for the ME at 100, 80 and 60% efficiency.

In figure III.14, we can see the three PSDs in the top and the corresponding integrated noise in the bottom. The bandwidth of the measurement is [0.1Hz; 50kHz], meaning we have take 1 million points in a 10 s oscilloscope trace. For all the measurements we have used the same setup and the same optical power on the photodiode. We have carefully chosen this power to have a shot noise limit lower than our measurement. We have checked we are not saturating the PD. We see basically no impact of the variation of the ME efficiency, evidencing three identical PSDs and IRIN behaviors.
We, then, measure the RIN as a function of repetition rate. We use exactly the same system we have adopted for the efficiency case. In this case, we measure three interesting situations, considering our future applications: 500 kHz, 250 kHz and 100 kHz. We decide to use again the 20 kHz filter and the the same bandwidth [0.1Hz; 50kHz] in order to obtain easily comparable measurements. The efficiency is set to 100% to get the whole energy at the laser output.

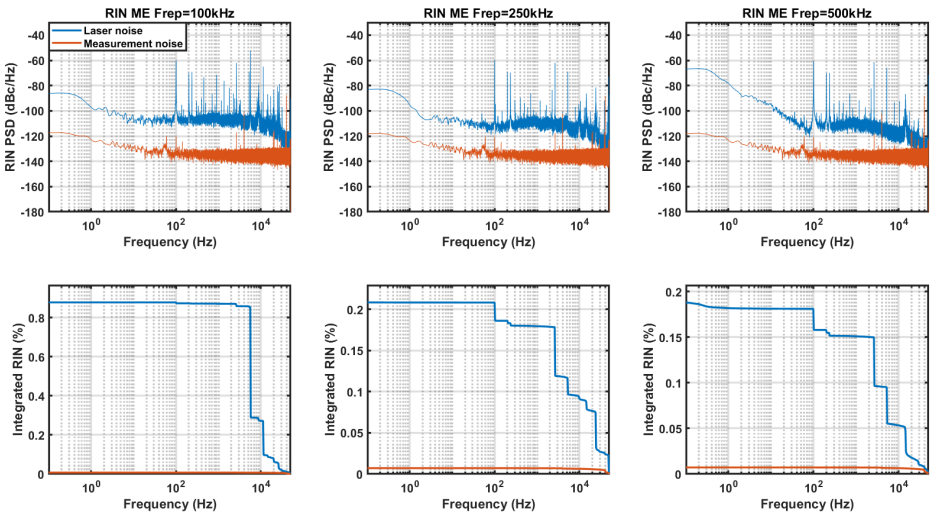


Figure III.15 – Top: PSD RIN for the ME at 500, 250 and 100 kHz of repetition rate. Bottom: IRIN for the ME at 500, 250 and 100 kHz of repetition rate.

Figure III.15 shows the results in the three cases. Let us concentrate on the 100 kHz case on the extreme left. There is a peak around 5.5 kHz that represents more than half of the total IRIN. This peak disappears in the other two cases leading to IRIN values around only 0.2%. If we compare the 500 kHz and 250 kHz behaviors, we observe the same peaks and structures. The origin of the peak in the RIN PSD seems to be linked to the ME operation.
We believe this noise is still present in the complete (going until the Nyquist frequency) PSD for the latter cases. The difference between the $f_{rep}$=100 kHz and the $f_{rep}$=100 kHz, 500 kHz cases lies in the fact that a high frequency noise peak is aliased below or above of the filter cutoff frequency at 20 kHz. To back up this claim, the shot-to-shot intensity stability is found to be the same in the three cases. As we have seen this measurement can be used for a rough estimation of the amplitude noise. In our particular case we have made the three measurements using the same setup of a photodiode and and oscilloscope used in exactly the same conditions. Another confirmation is shown in figure III.16, where we see the intermediate situation corresponding to a ME at 125kHz.

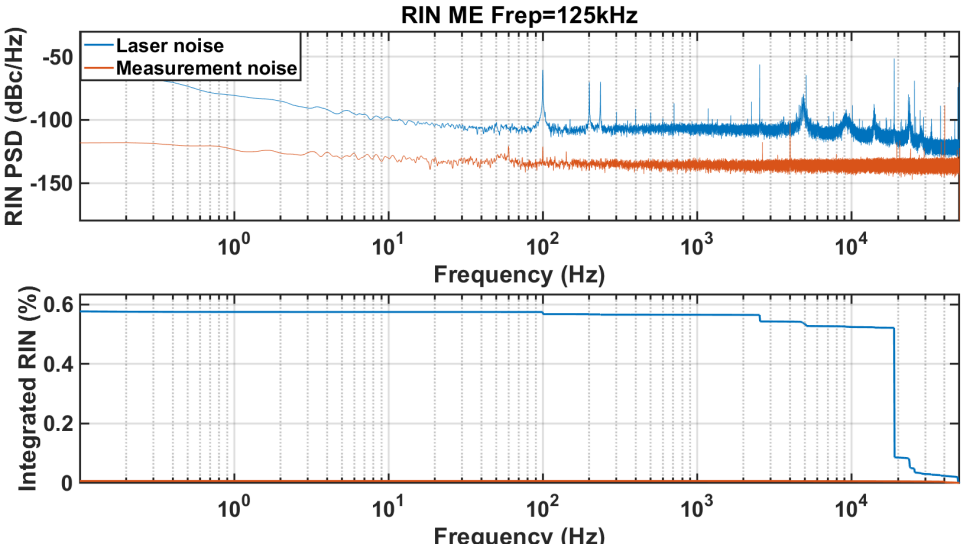


Figure III.16 – Top: PSD RIN for the ME at 125 kHz of repetition rate. Bottom: IRIN for the ME at 125 kHz of repetition rate.

We clearly see a peak contributing to more than half the total IRIN in the measurement bandwidth but is, now, centered around 18 kHz. To be more precise the amplitude of this noise peak is slightly lower with respect to the 100 kHz case. This can be explained by the fact that the filter cut-off frequency is close to the peak position.
We can conclude that the ME operation changing the repetition rate has an impact on the AN of the laser output.

### 4.1.4 Pulse picker characterization

After having tested the influence of the ME on the laser output, we want to analyze the role of the pulse picker. In order to test only this component, we use the ME in alignment mode. In this configuration it transmits all the pulses, at the frequency we set the PP. Let us take two interesting situations: 500 kHz and 40 MHz. The second situation represent the PP alignment mode. We use a not amplified photodiode (DET36A/M, *Thorlabs*) and a filter at 100 kHz (EF502, *Thorlabs*) in the first and a filter at 2MHz (LPF1.9+, *Minicircuit*) in the second case. The results are depicted in figure III.17.

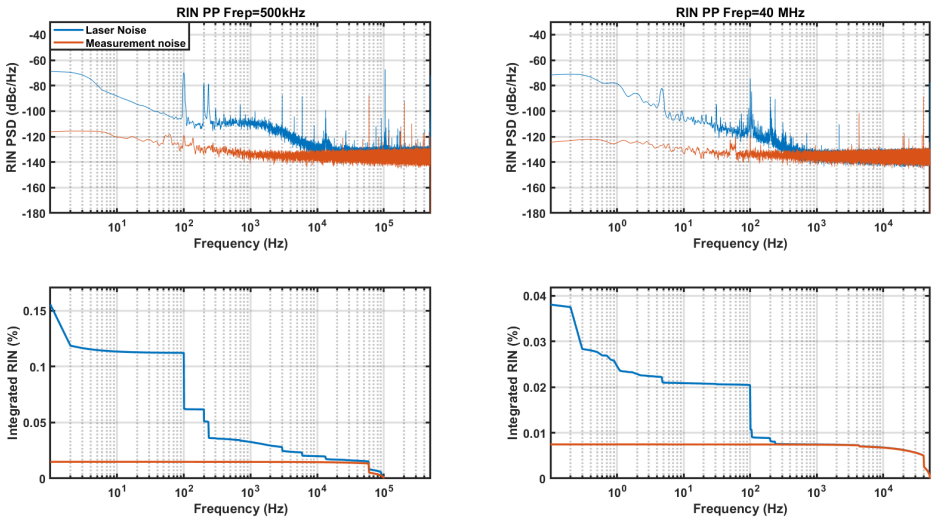


Figure III.17 – RIN PSD (Top) IRIN (bottom) measurement of laser output with ME in alignment mode and PP=500 kHz (Left), 40 MHz (right).

It has to be remarked that the bandwidths of these measurements differ. Focusing on the case at 40 MHz we can see that the noise behavior tends to go below the measurement noise floor around the kHz frequency. For this reason even if the filter we have used in this case goes until 2 MHz we decide to show only the relevant bandwidth. For the case on the left, instead, we have integrated the RIN PSD until the cut-off frequency of the filter. The comparison of the integrated value is meaningful, considering we are neglecting only the bandwidth [0.1 Hz; 1 Hz] in the first case in respect to the second. The conclusion we can make is that the PP has an effect of the RIN. The higher repetition rate case is less noisy than the lower one. For this reason we will modify this component to improve the RIN performances as described in the next paragraph. Another important point of difference emerging looking at these measurement is that the IRIN is in general sensibly lower than the ones for the ME study done in the previous paragraph. Let us compare, in particular, the case at Frep=500 kHz in figure III.15 and the one in figure III.17.

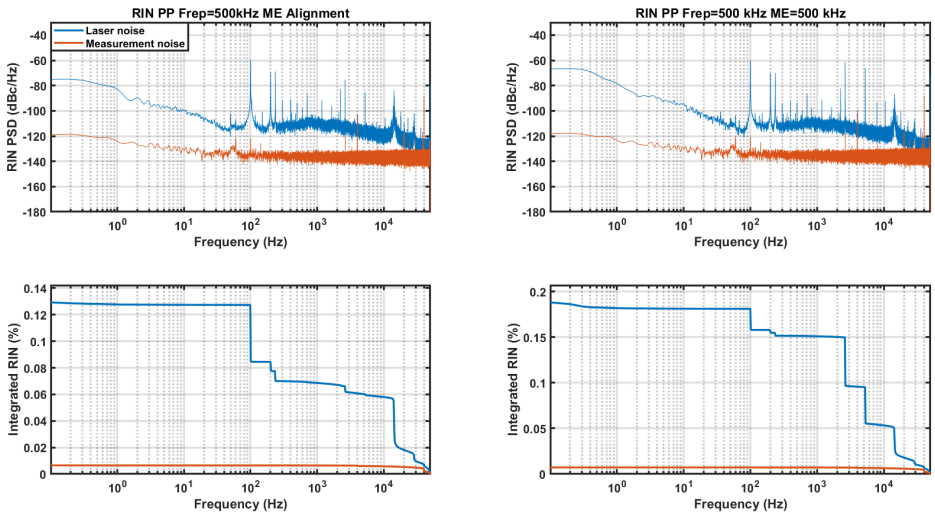


Figure III.18 – PSDs (top) and IRIN (bottom) for PP=500 kHz and ME in alignment mode (left) and ME=500 kHz (right).

Several structures that are present in the first case disappear in the second one. The comparison of these two measurements is delicate because we have used two different measurement setups. For this reason, we make another comparative study at PP=500 kHz with ME=500 kHz and ME in alignment mode. We make the measurement using the setup of the paragraph 4.1.2. Figure III.18 reports the obtained results. We appreciate that there is a difference in the two situations. This certifies again that the ME has an impact on the RIN of the laser. Comparing now figure III.18 and figure III.17 with PP we measure two IRIN values that are reasonably identical (0.13% vs 0.15%). This shows coherence between the results made with two different measurement setups.

## 4.2 RIN performances improvement

In this section we first explain the principle of the technique we have adopted for reducing the amplitude noise of our system working on the PP. We then present the results obtained. Even if we have seen that the ME has an negative impact on the IRIN, we will not act on it. This choice is linked to the difficulty of modifying the ME implementation without changing the whole pump laser architecture.

### 4.2.1 Principle: synchronized pulse-picking

De Vries et al. [de Vries *et al.* , 2015] demonstrated a method for reducing the AN and the PN of the output of a pulse-picking acousto-optic modulator (AOM). The principle main idea is to synchronize the AOM driver RF frequency, normally internally generated, to the repetition rate of the laser we want to pulse-pick. We decide to test this idea for our PP.

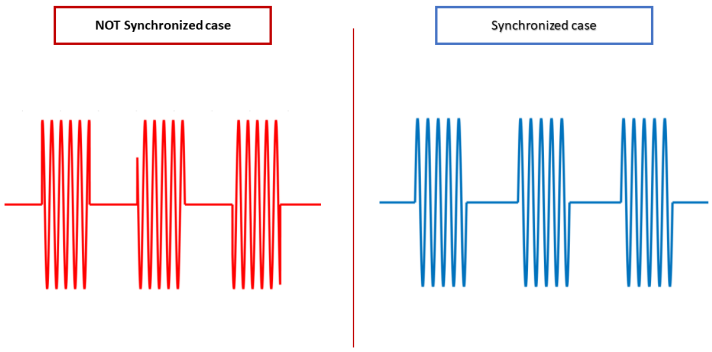


Figure III.19 – Principle of synchronized and not synchronized radiofrequency for driving the pulse-picking AOM.

First we have to clarify how we control the AOM we have called PP until now. For the downsampling of our pulses the driver sends a radiofrequency to the acousto-optic crystal, modulated using a square gating function at the repetition rate we want to obtain at the AOM output. The gating is triggered by the laser pulse train. The driver is, in a simplified depiction, a mixer taking the gating function and a radiofrequency generated internally. The key point of the synchronized PP is to have the RF synthesizer externally synchronized to the laser. For understanding the effect of this, let us have a look at figure III.19. In a qualitative way we can imagine that the type of the signal sent to the AOM crystal has an impact on the pulse picking quality. This means that the first diffracted order of the AOM is switched on/off with the same rising/falling front wave depicted in figure III.19 on the right. In the opposite way, in the non-synchronized case, rising and falling edges are different for each gating period. This effect is more pronounced for fast PP where only few acoustic cycles are used to diffract the

incident beam.
The implementation is depicted in figure III.20. The synchronized scheme clock is generated starting from the oscillator and selecting the 5th harmonic at 200 MHz using a band-pass filter. A 20 dB-gain amplifier is used to increase the signal for the driver entrance. The gating signal is generated from the FPGA electronically controlling of the laser, triggered by the oscillator.

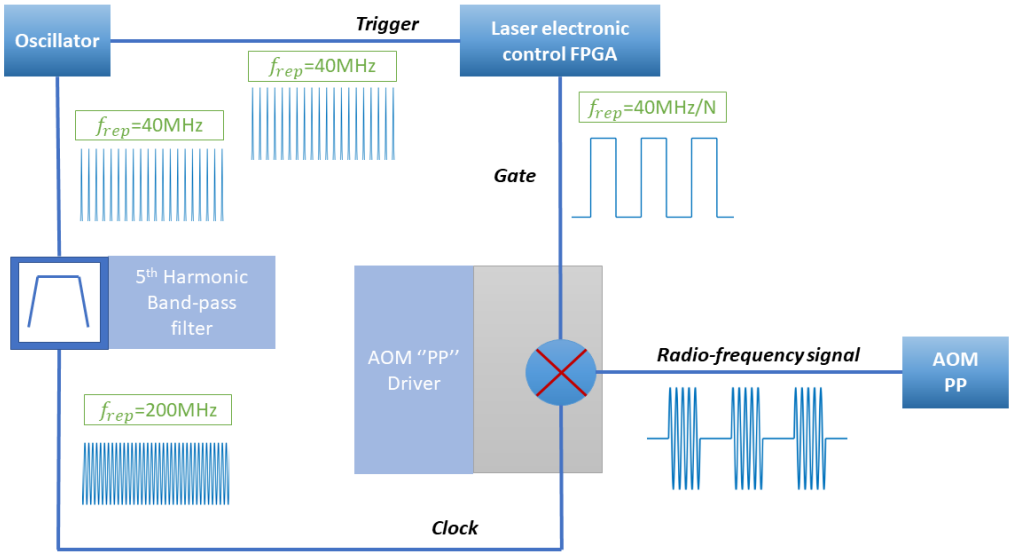


Figure III.20 – Scheme of the PP driver synchronization to the oscillator.

The synchronization acts only on the PP and not on the ME because the first is much more sensitive to the rising and falling edge of the carrier acoustic wave. This is linked to the number of acoustic wave cycles required for the pulse-picking. Let us consider, in a simple depiction, a beam diffracted through the AOM crystal having a diameter $D$ as sketched in figure III.21.

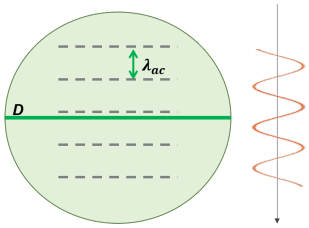


Figure III.21 – Sketch of the transverse beam profile, of diameter $D$, in an AOM.

The acoustic wavelength $\lambda_{ac}$ can be defined as:

$$\lambda_{ac} = \frac{v_{ac}}{f_{ac}}, \tag{III.16}$$

where $v_{ac}$ is the acoustic wave speed and $f_{ac}$ is the acoustic wave frequency. The beam experiences a grating generated by the acoustic wave. The beam diameter can be compared to the acoustic wavelength:

$$D = \lambda_{ac} n, \tag{III.17}$$

where $n$ is the number of acoustic wave cycles. Let us consider, now, that we want to use the pulse picker with a laser repetition rate $f_{rep}$. We can find that the period $T_{rep} = \frac{1}{f_{rep}}$ has to be:

$$T_{rep} > \frac{D}{v_{ac}}. \tag{III.18}$$

From the analysis of (III.17) and (III.18), a maximum number of period for a certain $f_{rep}$ and $f_{ac}$ can be found as:

$$n < \frac{f_{ac}}{f_{rep}}. \tag{III.19}$$

If we consider the PP case, in the equation (III.19), the number of period is only 5. On the other hand, the ME is driven by an acoustic wave at 80 MHz and pulse-picks a 500 kHz repetition rate pulse train. The number of period is, then, n=160. This demonstrates the high sensibitivity of the PP on the rising and falling edges of the carrier acoustic wave and explains why the synchronization effect would not be comparable in the ME case.

### 4.2.2 Results on PP synchronization

To compare the synchronous and non-synchronous systems we use a different measurement system than previously described. In this case we decide to insert an electronic amplifier between the low-pass filter and the oscilloscope. The amplifier is also a substractor in a classical op-amp configuration [Scherz, 2006]. The advantage of having a substractor is to finely tune an offset on the noise trace. This allows us to exploit the dynamic of the oscilloscope, reducing the quantification noise as explained in section 3. We decide to test two situations with PP at 500 kHz. In the first case the ME is in alignment mode and a filter cut-off of 100 kHz is used. In the second one we choose to use the ME at $f_{rep}$ at 167 kHz, and use a filter cut-off of 50 kHz (EF 124, *Thorlabs*). The results are compared in figure III.22.
Let us consider first the 167 kHz situation on the right. We can see that in the bandwidth [0.1 Hz; 50 kHz] we achieve an improvement of about 35 % passing from 0.21 to 0.13 % IRIN. The result is somehow confirmed in the ME alignment mode case, where the IRIN passes from 0.21 % to 0.15 %, providing about 30 % of RIN reduction.

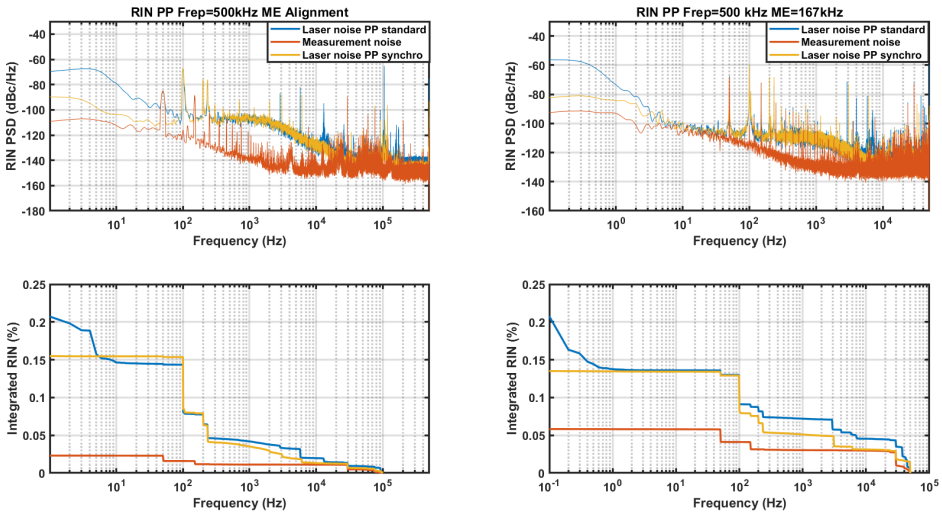


Figure III.22 – PSD and IRIN for synchronized and non-synchronized PP for ME= alignment (left), and ME=167 kHz (right).

It is interesting to compare our results to those found by De Vries et al. [de Vries *et al.* , 2015]. In the publication the AN improvement is shown on the basis of the shot-to-shot measurement. 5000 subsequent pulses at 74 MHz repetition rate, are recorded in the two cases. The standard deviation passes from 2.91% to 0.46%. The big difference stands in the fact that they are pulse-picking at a frequency of 73.8 MHz using a RF wave at 230 MHz. This means that only three acoustic cycles are in pulse-picker driver wave for the

equation (III.19). In our case we have already said that we have 5 acoustic wave cycles. We are, then, less sensitive to the synchronization with respect to their case.

# 5 Conclusions

In this chapter the RIN characterization for a femtosecond laser source has been analyzed. As we have said in the context section, we believe that this kind of characterization is bound to become more important in commercial and industrial lasers. The comparison with the shot-to-shot fluctuations has allowed to prove how this latter is meaningless without a proper comparison of measurement setups. The simplicity of the setup we have presented for RIN allows a broad utilization of this characterization.
We have finally taken, as a case study, the pump laser we will use as pump of our laser chain. The investigation of the pulse-picking system has shown a critical point for the output RIN. This has been the starting point for a performance improvement discussed in the last section. An improvement of 30 % has been measured owing to the optimization of the pulse-picking confirmation. In the next chapters we will see how the RIN measurements will have a strong importance in the whole laser system.
To conclude this chapter it has to be said that other techniques for lowering intensity noise can be adopted on a laser system [Cingöz *et al.* , 2011, Hamm *et al.* , 2000]. In our case, we must keep in mind that we use a commercial laser as a "black box" where we cannot modify freely each element. There is, anyway, a possibility of upgrade even in our case: active RIN stabilization [Huber *et al.* , 2017]. This technique will be implemented in future studies.

# Chapter IV

# Carrier Envelope Phase stable Front-End

## Objectifs

In this chapter the first part of the laser chain, the front-end is introduced. We firstly present the motivations and the context of operations of this source. The carrier envelope phase (CEP) is formally defined and the stabilization in low energy systems (oscillators class) is discussed in the second section. In the third part, the setup is presented and characterized. In the fourth, the CEP measurement setup and the results are discussed. In the fifth, we study the RIN properties and the impact of the AN on CEP noise in our system. Finally, conclusions summarize the chapter in the sixth part.

## Contents

# 1 Context: CEP-stable oscillators and DFG-OPAs

In the first pages of this manuscript we have modeled an ultra-short laser as an electric field composed by a fast oscillating carrier and a slowly varying envelope. We have, indeed, imposed that only the envelope matters for all the treatment we have done. Reducing more and more the pulse duration has lead to an overcoming of this approximation. This means that for pulse duration of only a few-optical cycles and the related applications, not only the envelope but also the carrier of the electric field is important. The *carrier-envelope phase* (CEP) is the parameter allowing to define the relation between the envelope and the carrier for a determined laser. Stabilizing and controlling the CEP means controlling directly the electric field. In the nineties, the strong field physics has seen an exponentially growing interest thanks to progress in femtosecond laser technology [Steinmeyer *et al.* , 1999, Brabec & Krausz, 2000, Nisoli, 1997]. Different sources delivering pulses of only few optical cycles were presented, tracing the road for attosecond science. In this sense, the CEP control is required. The first CEP stable system has been proposed and measured in 1996 by Xu et al. [Xu *et al.* , 1996]. Since then, the phase control of ultrashort laser pulses has interested a broad community of researchers and big efforts to stabilize and measure more precisely have been made. Aiming attention only at CEP-stable low energy lasers [Klenner *et al.* , 2013, Lücking *et al.* , 2012, Rausch *et al.* , 2009], two main applications can be identified. First they are used as seeders for high energy systems, for application in ultrashort strong field physics [Budriūnas *et al.* , 2015, Jullien *et al.* , 2011]. The second application is frequency comb metrology where the control of the CEP allowed unprecedented frequency precision in the optical domain [Kim & Song, 2016].
Let us focus on nowadays existing techniques for CEP stabilization in laser oscillators. We can divide them in two groups: active and passive methods. We define as active all the cases where electronic devices are required for the stabilization, with feedback loops and delicate detection tools. In contrast, passive techniques rely on all-optical methods. The first group includes a large number of detection and actuation systems. This is the historically most adopted way to provide a CEP-seeder. Two of the most relevant techniques will be presented in the next section of this chapter. This approach hold the record of the most stable CEP system [Koke *et al.* , 2010]. The passive stabilization technique exploits nonlinear effect such as DFG for generating phase-stable pulses. We choose this technique for the realization of the front-end. The reasons for this choice are several and will be clarified in this chapter. In particular, we will see that adopting an all-optical setup allows to be completely transparent to the laser repetition rate. This point is of particular interest for the realization of a flexible high repetition rate source. The simplicity of the realization setup and the complete absence of feedback architectures represents a strong advantage to consider in the comparison. We will show this seeder suits the performances requirements for a CEP-stable high repetition rate source for strong field physics applications.

## 2 Theory and background

In this section, we define the CEP in the first part. The two most used active stabilization techniques are described in the second. The CEP stabilization via DFG is, then, introduced.

### 2.1 CEP definition

Let us consider the electric field description of a mode-locked femtosecond laser we have used in section 1 of this manuscript (II.9), it can be rewritten:

$$E(z,t) = A'(z,t)cos[\omega_0 t - k_0 t + \varphi(z,t) + \varphi_{CEP}(z)]. \tag{IV.1}$$

As we have already said, the electric field is described as a slowly varying envelope $A'(z,t)$ and a fast oscillating carrier. The *Carrier-Envelope Phase* (CEP) is the $\varphi_{CEP}(z)$ term in the square brackets of the equation. This term corresponds the difference between the peak of the envelope and the closest carrier peak [Steinmeyer *et al.* , 2013]. Depicted in figure IV.1 we can see a representation of this definition on a few cycle pulse.

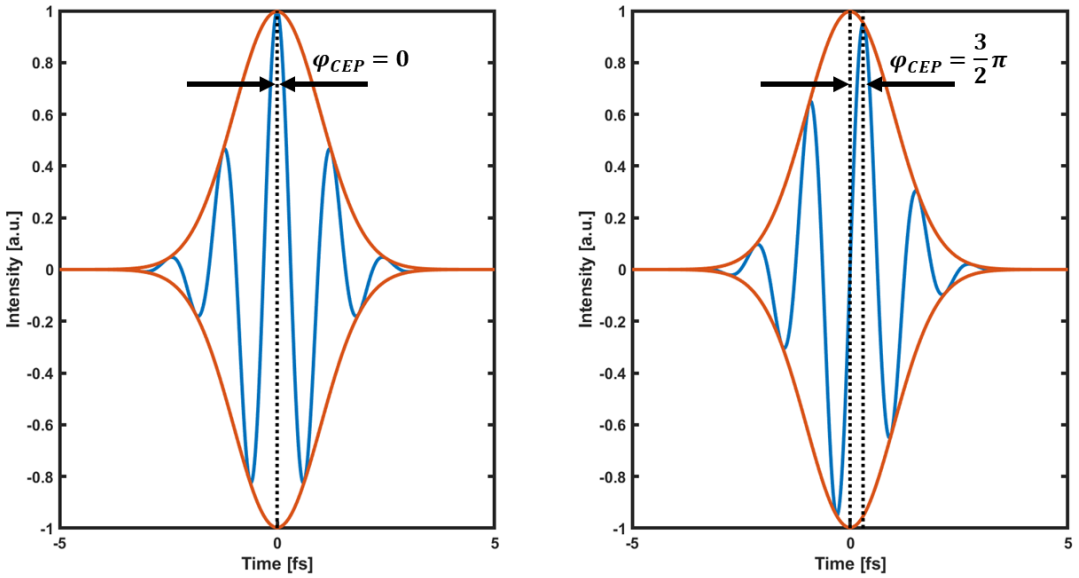


Figure IV.1 – Scheme of the CEP definition on a two-cycles pulse. Left: $\varphi_{CEP} = 0$. Right: $\varphi_{CEP} = 3/2\pi$

We can easily understand looking at the figure that the slowly varying envelope approximation (SVEA) has to be relaxed and the carrier of the electric field has to be taken into account for a very short pulse. Think now that the pulse has a determined $\varphi_{CEP}(0)$ at position $z = 0$. Let the pulse propagate in a medium. The envelope is travelling through the material with a group velocity $v_g$ we have introduced in the chapter II. The carrier, instead, propagates with a *phase velocity* $v_p$. These two speeds are different $v_p \neq v_g$. The CEP of the original pulse is modified because of the different propagation speeds of envelope and carrier in the medium. This produces an added $\Delta\varphi_{CEP}$, defined as [Steinmeyer *et al.* , 2013]:

$$\Delta\varphi_{CEP}(z) = \omega_0 z\left(\frac{1}{v_g(\omega_0)} - \frac{1}{v_p(\omega_0)}\right), \tag{IV.2}$$

showing that the CEP shifts linearly with propagation distance. The phase velocity is dependent on the refractive index, according to $\frac{1}{v_p} = \frac{n(\omega_0)}{c}$. The CEP slippage is strongly

dependent on dispersion in the medium. We can reformulate equation (IV.2) in terms of the chromatic dispersion $\frac{\partial n}{\partial \lambda}$, as follows:

$$\Delta\varphi_{CEP}(z) = -2\pi z \frac{\partial n}{\partial \lambda}. \tag{IV.3}$$

Let us take as an example a laser source emitting at 1030 nm. The chromatic dispersion in air and fused silica is respectively -0.0000028517 $\mu m^{-1}$ and -0.012296 $\mu m^{-1}$. This means that to change the electric field with a CEP shift of $\pi$, the propagation distance in air and glass is:

$$\Delta L_\pi = 35 \quad cm \quad \text{(Air)}. \tag{IV.4}$$

$$\Delta L_\pi = 80 \quad \mu m \quad \text{(Fused Silica)}. \tag{IV.5}$$

These values give us an idea of how sensitive the CEP is to dispersion and how difficult it is to control and stabilize the CEP. In the definition of equation (IV.1) we have considered only a single pulse depiction. Consider, now, a mode-locked oscillator. In the time domain, we have a pulse train equally spaced with $T_R = \frac{1}{f_{rep}}$ where each pulse has its own $\varphi_{CEP}$. In figure IV.2 the pulse train is represented. For each round trip in the oscillator cavity, there is a phase shift $\Delta\varphi_{CEP}$ depending of the elements of the laser cavity. Between two successive pulses of the pulse train there exists this phase shift. In the frequency domain, this origin a frequency like shown in the PSD of the pulse train in figure IV.2 bottom.

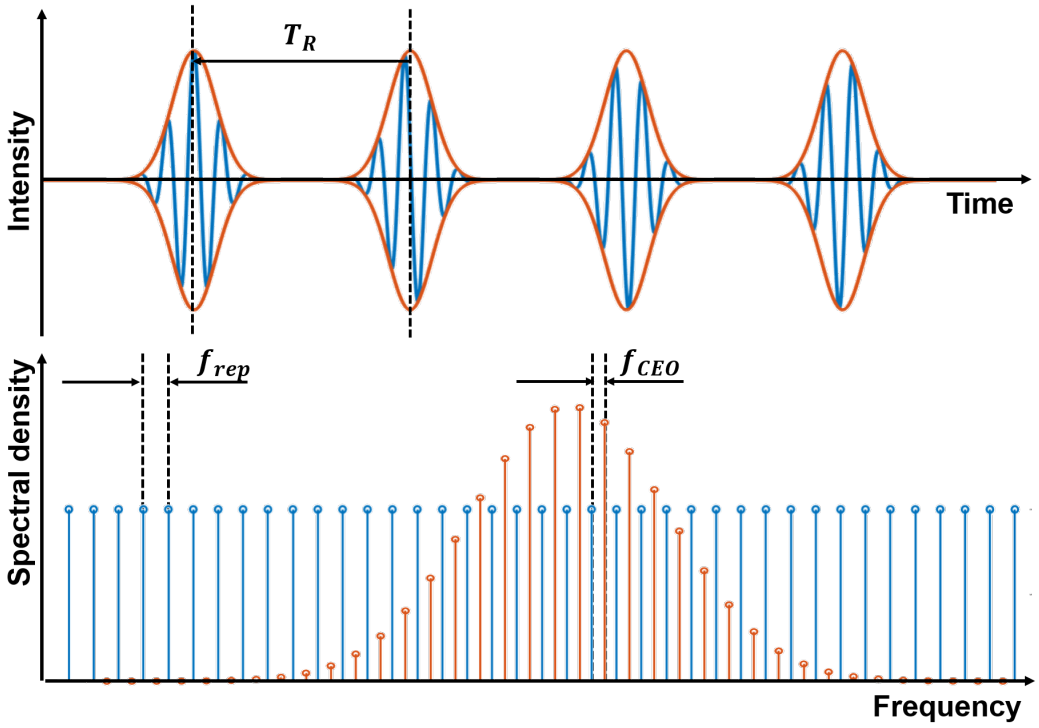


Figure IV.2 – Scheme of the CEP definition on a pulse train.

This frequency referred as *carrier-envelope offset* $f_{CEO}$ defined as in the scheme.

$$f_{CEO} = \frac{1}{2\pi}\Delta\varphi_{CEP} f_{rep}. \tag{IV.6}$$

This frequency represents the offset on the frequency comb in the PSD of the mode-locked laser. If we want to consider the frequency of an arbitrary line $n$ in the scheme, we have:

$$f_n = n f_{rep} + f_{CEO}. \tag{IV.7}$$

Looking again at the scheme in the bottom of the figure IV.2, we see $f_{CEO}$ as the offset of the extrapolated first frequency of the comb with respect to the zero frequency.

## 2.2 Measuring CEP in oscillators

The stabilization of the CEP has clearly progressed in parallel with the ability to precisely measure it. We discuss the main techniques for measuring the CEP in oscillators and the criteria used for the evaluation of the CEP stability of a determined system.

### 2.2.1 Cross-correlation

This is the first proposed measured technique [Xu *et al.* , 1996], and uses a Michelson-type correlator. The interference fringes between two successive pulses of the pulse train are detected using a photo-multiplier tube (PMT). Figure IV.3 shows that the position of the fringe peaks with respect to the origin is directly related to $\Delta\varphi_{CEP}$.

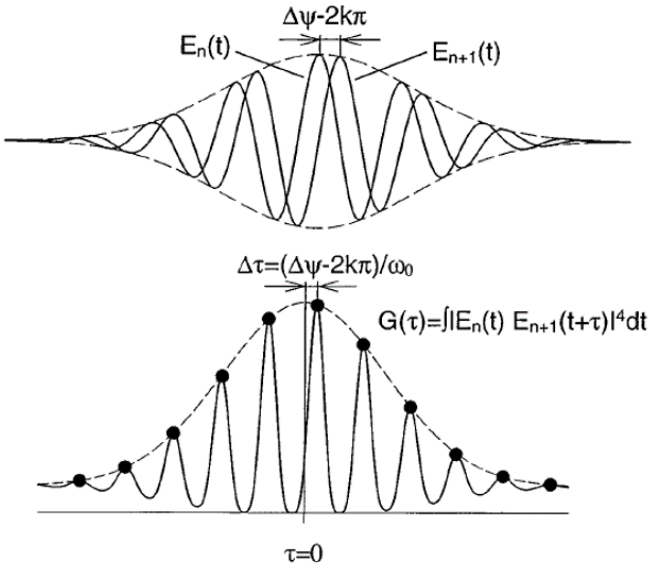


Figure IV.3 – Principle of the cross-correlation technique. Figure taken from [Xu *et al.* , 1996]

A point to clarify is what is interesting to measure. We have said that $\Delta\varphi_{CEP}$ is constant in principle for each roundtrip. This phase shift is affected by small fluctuations. This means for the cross-correlator, and for our pulse depiction in time domain, to measure a jitter. A CEP phase stability r.m.s. can be defined as:

$$\sigma^2_{\varphi_{CEP}} = \langle(\varphi_{CEP}(T) - \varphi_{CEP}(0))^2\rangle. \tag{IV.8}$$

We are measuring a relative phase CEP fluctuation with respect to a an average value $\varphi_{CEP,0}$. The cross-correlation technique for CEP measurement has rapidly shown its limits. First, the accuracy has been shown to be very low, around $\frac{\pi}{10}$. The stability of the interferometer is strongly impacting the measurement. Moreover, it is realized in the frequency domain using an ESA. This forces the measurement being averaged over a large number of pulses, otherwise no frequency corresponding to the jitter can be measured.

### 2.2.2 Heterodyne techniques

Some years after the first CEP phase slip measurement, the heterodyne techniques for CEP measurement have been introduced [Telle *et al.* , 1999, Reichert *et al.* , 1999]. To understand

the is technique we have to start from the definition of $f_{CEO}$ for the frequency comb. In figure IV.4, is represented the most common principle for this type of measurement.

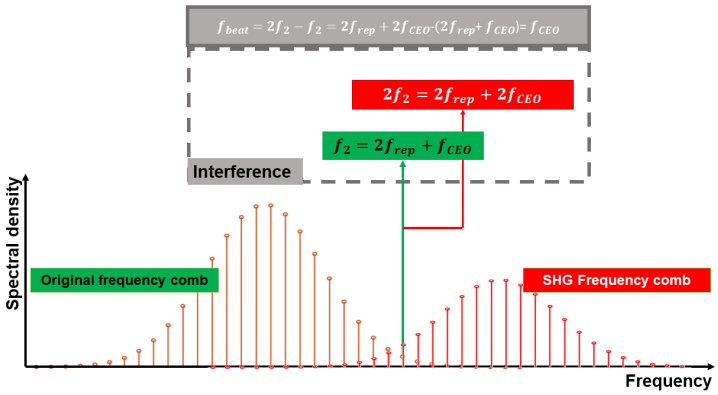


Figure IV.4 – Principle of the f-2f heterodyne CEP detection.

This interferometer configuration is known as *f-2f* [Jones *et al.* , 2000]. The principle is to detect a beat note between the frequency comb under test and its frequency doubled version, that is shifted from the zero frequency by $2f_{ceo}$. In this way, we can directly measuring $f_{CEO}$. Requirement for using this technique is having an octave-spanning fundamental frequency comb, otherwise no interaction with the doubled comb is possible. If we think about an emission spectrum from a mode-locked fs laser, it is very difficult to find such a large spectrum. This problem can be solved by broadening the spectrum using a WLG process. If operation condition of the WLG are such that the SPM is the dominating process, the CEP is preserved. Considering the low-energy available for oscillators, the WLG is realized in a photonic crystal fiber (PCF) [Coen *et al.* , 2001]. Once the broad spectrum is generated, one arm of the interferometer is used for frequency doubling. A polarizer cube is used to project the SHG components and the fundamental ones on the same polarization axis. The detection is done using a filter, that selects the spectral region where both combs overlap, and a photodiode. The $f_{CEO}$ is, then, detected as a beat note frequency using an ESA. This is the most used $f_{CEO}$ detection technique nowadays and different arrangements of the interferometer have been proposed. As for the case of the cross-correlator, the measurement setup impacts on the CEP fluctuations measurement accuracy. Let us imagine, for instance, that there is one mount in one arm of the interferometer vibrating. As a result, the measured $f_{ceo}$ will be modulated. Another critical point can be the stability of the fundamental spectrum from shot to shot. If there is an instability of intensity at the entrance of the PCF, for example, the spectrum at the output has fluctuating values of phase. This adds a phase shift coming from the measurement setup. One of the most efficient scheme proposed to simplify the interferometer and reduce the setup impact on the CEP measurement is the *monolithic* scheme demonstrated by Fuji et al. in 2005 [Fuji *et al.* , 2005]. The spectral broadening of a titanium sapphire laser oscillator is realized in a periodically poled lithium niobate crystal (PPLN). The beat note is not generated from the interaction of the comb line $f$ and $2f$ but from one comb line $f_n$ and the DFG generated frequency from the lower and higher parts of the same spectrum generated in the same crystal [Fuji *et al.* , 2004]. Using the beat note between the DFG and a the corresponding line from the fundamental comb is often referred to as *0-f interferometer*. We can consider the frequency $n$, as $n = n_{high} - n_{low}$. Remembering what we have said for the case of the f-2f, we understand that, in this case:

$$f_{beat} = f_n - f_{DFG} = nf_{rep} + f_{CEO} - (nf_{rep}) = f_{CEO}. \tag{IV.9}$$

We understand that we can use the different nonlinear effects combination for obtaining $f_{CEO}$.

This can be generalized as follow [Steinmeyer *et al.* , 2013]:

$$f_i^N - f_j^M = N f_{CEO} - M f_{CEO} + (i-j) f_{rep}, \tag{IV.10}$$

where N and M are two integers indicating the N-th and M-th harmonics realized with the nonlinear process, and i and j are modes of each frequency combs. We choose the mode for which the condition i=j is satisfied. We can extract the $f_{CEO}$ choosing a combination of M and N. The f-2f case corresponds to taking N=1 and M=2.

## 2.3 CEP stabilization in oscillators

We discuss two stabilization techniques for oscillators. As we have already mentioned, an active feedback loop is required for this scope. Detection and actuation methods define the performances in terms of stabilization. We present two different schemes considering $f_{CEO}$ detected using one of the above described methods.

### 2.3.1 CEP-stabilization on the pump intensity

This stabilization method relies on a fast feedback loop acting on a element inside the cavity: the power of the pump laser [Borchers *et al.* , 2011, Yu *et al.* , 2007, Vernaleken *et al.* , 2012, Poppe *et al.* , 2001]. The idea is simple and is depicted in figure IV.5.

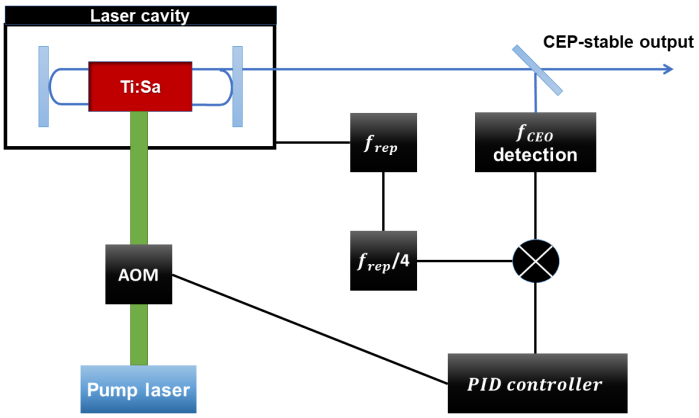


Figure IV.5 – Scheme of the CEP stabilization using a feedback on the pump laser intensity

The $f_{CEO}$ is measured using a heterodyne technique. The $f_{CEO}$ tends to drift upon laser and environment conditions. To obtain CEP-stable pulses at oscillator output we need to lock this frequency [Jones *et al.* , 2000, Apolonski *et al.* , 2000]. A reference frequency is taken as an integer sub-multiple of $f_{rep}$. Usually it is chosen $f_{rep}/4$. A feedback loop stabilizes the error between the reference and the measured $f_{CEO}$. Modulating the pump power on the laser crystal changes the intracavity CEP shift. The transfer dynamics from pump power to CEP output of a Ti:Sa mode-locked laser are well-known [Matos *et al.* , 2006]. An AOM placed between the pump and the crystal is used to modulate and then stabilize the $f_{CEO}$. In this depiction, the laser $f_{rep}$ is drifting. Because the $f_{CEO}$ is locked on a sub-multiple of the laser frequency, this means that $f_{CEO}$ is drifting too. For metrology applications, it is required a completely stabilized frequency comb. In these cases, $f_{rep}$ must be stabilized to the lowest possible jitter [Cundiff, 2002]. The difficulties in these configurations are on the choice on a feedback actuator stabilizing $f_{rep}$ without acting on $f_{CEO}$. Particular electronics and optical architecture have to applied to overcame the problem. The described technique adopted by Borchers et al. [Borchers *et al.* , 2011] allowed to reach a CEP of less than 100 mrad in the bandwidth [0.1 Hz; 100 kHz]. The detection and actuation electronics is the speed limiting

parameter of the correction BW. Commercial CEP-stable lasers based on this technique are available since 2004 (CEP2, Femtolasers).

### 2.3.2 Feed-forward stabilization technique

In 2010 Koke et al. [Koke *et al.* , 2010] introduced a completely different approach to CEP stabilization. It is nowadays the most used technique for commercial CEP-stable oscillators. The novelty of the scheme is using an *Acousto-Optic Frequency Shifter* (AOFS) as actuator placed outside the cavity. The $f_{CEO}$ is detected and, after an amplifying and filtering electronic circuit, is directly sent to the AOFS as RF driving frequency. The pulse train diffracted on the order -1 of the AOFS is outcoming with $f_{CEO} = 0$. The CEO frequency is simply substracted such that the output pulses have $f_n = nf_{rep}$ as depicted in figure IV.6.

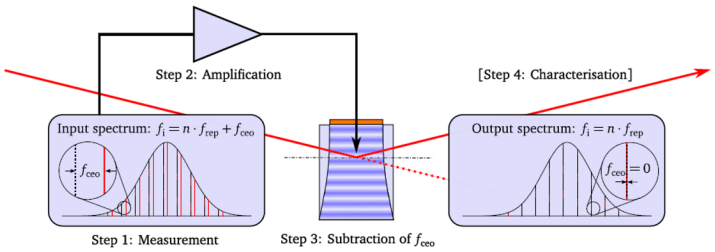


Figure IV.6 – Feed-forward CEP stabilization scheme. Figure taken from [Lücking, 2014]

This scheme goes under the name of *feed-forward stabilization*. Let us compare this approach to the one previously presented. It has the main advantage of simpler electronics and the absence of the feedback loop. This translates to a cheaper system and also a faster one. Bandwidth of operation faster than 500 kHz have been demonstrated [Lücking *et al.* , 2012]. These advantages have allowed to push the limit of CEP noise below 50 mrad in the BW [50 mHz; 500 kHz]. In contrast, the transmission of the AOSF is less than 75% and it adds a slight spatial chirp and dispersion.

## 2.4 Passive CEP stabilization

A completely different way for obtaining a CEP-stable system can be adopted. A nonlinear effect is used after the oscillator for generating self-CEP-stabilized pulses. The first scheme in this sense has been proposed by Baltuska et al. [Baltuška *et al.* , 2002] in 2002. The idea is to use the difference frequency generation between two frequency combs sharing the same $f_{CEO}$. In this way, the CEP phase of the DFG pulses is automatically set to zero. Let us analyze deeper this phenomenon looking at the equations of three-wave mixing in the case of a DFG/OPA we already discussed in section 1. We reformulate the coupled equation for this case adding the term of CE phase such that $B_n = A_n e^{i\varphi_n}$. We define $\Psi = \varphi_3 - \varphi_2 - \varphi_1 - \Delta kz$. We can write, then, the equation for the generalized case, as follows [Cerullo *et al.* , 2011]:

$$\begin{cases} \frac{\partial B_1}{dz} &= k_1 B_2^* B_3 sin\Psi, \\ \frac{\partial B_2}{dz} &= k_2 B_1^* B_3 sin\Psi, \\ \frac{\partial B_3}{dz} &= k_3 B_1 B_2 sin\Psi. \end{cases} \tag{IV.11}$$

Where $k_i$ are the nonlinear coefficient defined in section 1. We consider as before signal at $\omega_1$, pump at $\omega_3$, idler at $\omega_2$. We assume perfect phase matching condition $\Delta k = 0$. We can assume there is no idler at z=0 as boundary condition $B_2(z = 0) = 0$. We can see that the idler is maximized for $\Psi = \pi/2$. The relations of angular frequency and phase for signal, pump

and idler become simply:

$$\begin{aligned} \omega_i &= \omega_p - \omega_s \\ \varphi_i &= \varphi_p - \varphi_s - \pi/2. \end{aligned} \tag{IV.12}$$

In order to obtain a stable CEP idler we want to have $\varphi_{idler}$ constant. The simplest way for doing this is $\varphi_p = \varphi_s$. The generation of coherent and very broad spectra that are necessary to satisfy this condition is always obtained by WLG [Brodeur & Chin, 1999]. Two main ways exist to realize the stabilization: the *intra-pulse* and *inter-pulse* techniques.

### 2.4.1 Inter-pulse CEP stabilization

The idea in this case is to make the DFG between two different pulses, pump and signal, having the same phase $\varphi_{CEP}$. The most used scheme considers a pump and spectrally broadened signal via WLG. The WLG is realized in a PCF [Thai *et al.* , 2011], standard fiber, or more commonly in bulk crystals of sapphire or YAG [Budriūnas *et al.* , 2015]. Let us look at figure IV.7. In the top, there is a depiction example of the inter-pulse stabilization. It can be seen that there is a WLG for generating the signal. A delay line is inserted on the pump arm in order to temporally synchronize for DFG. These two elements can be the source of an added CEP phase shift term $\Delta\varphi_{CEP}$. The interferometer stability acts directly on the output CEP stability. The delay line, by definition, represents a pathlength extensions meaning a naturally more unstable interferometer. The WLG process on the signal arm, instead, could add a CEP term on the signal that does not exist on the pump. Since the WLG is an highly nonlinear effect, intensity fluctuations can be transferred to the phase, thereby degrading the obtained CEP stability [Baltuška *et al.* , 2002]. This is the technique we will use for our setup.

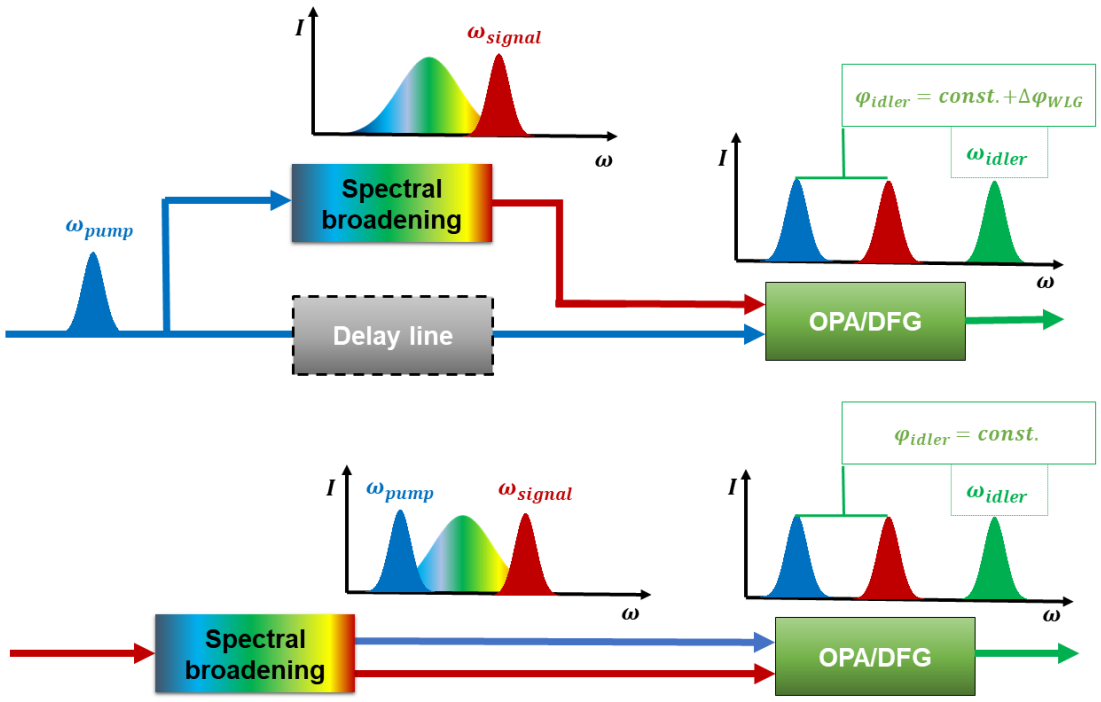


Figure IV.7 – Top: Inter-pulse principle and setup scheme example. Bottom: Intra-pulse principle and setup scheme example.

### 2.4.2 Intra-pulse CEP stabilization

The simplest way we can think for getting a CEP stabilized beam is to make the 3WM between two parts of the same pulse spectrum. We can see in the graph in the bottom figure IV.7 that in this case there is no necessity of the interferometer because pump and signal propagate together. This technique has been often used for Mid-IR range source [Fuji *et al.* , 2006, Moses *et al.* , 2009, Gu *et al.* , 2009]. The first system was realized in 2006 by Fuji et al. [Fuji *et al.* , 2006]. A large spectrum Ti:Sa oscillator was directly used for DFG in a PPLN. This provide a 2.1 $\mu m$ seeder for an OPCPA chain. In several other cases the spectral broadening is achieved through a *filamentation cell*. This allows a very large broadening, accommodating the use of a narrow-spectrum laser [Moses *et al.* , 2009]. It has to be stressed that, as depicted in figure IV.7, there is no added phase term in this case even if a highly nonlinear phenomenon is involved. This is because the term due to the nonlinear effect is canceled out being in the pump and signal components. This is really true if the phases of pump and signal phase of the spectral broadened spectrum are the same. Although the several advantages, intra-pulse techniques lacks of flexibility in terms of obtained wavelength and OPA pumping regime. Pump and signal pumping the OPA/DFG stage, in the intra-pulse scheme are fixed by the input energy for obtaining the most adapted spectral broadening. For the OPA case, this can constitute a limitation to achieve high gain.

# 3 OPA setup for CEP seeder at 1030nm

## 3.1 OPA-CEP output description

We describe now the setup of the passive stabilized seeder of the laser chain. It consists of an OPA pumped by the already presented and RIN characterized commercial laser Satsuma. The pump laser emits 40 $\mu J$, 350 fs long pulses, centered at 1030 nm. For the setup design, it is useful to add that the beam profile is Gaussian with an $M^2$ of 1.1 and a diameter at $1/e^2$ of 1.6 mm. We always operate it using the PP at 500 kHz and the ME at 100 kHz. The system we present here after can be operate to upper repetition rate regime until 500 kHz, simply changing the ME operation.
For the successive amplification we want to realize a CEP-stable seeder still centered at 1030 nm. For doing this we decide to use the scheme in figure IV.8 below.

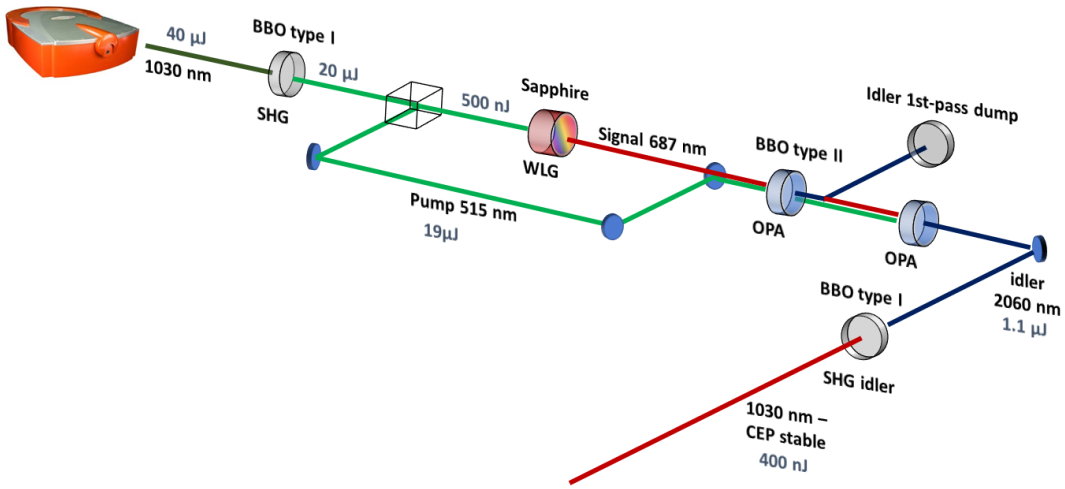


Figure IV.8 – Scheme of principle of the OPA.

Let us analyze in details the scheme. First of all, the pump laser is frequency-doubled to 515 nm. We use a BBO crystal in type I phase matching condition for this. The thickness of the crystal is optimized for conversion efficiency. The best result is found using a 2 mm-thick crystal, reaching 50 % of energy conversion. This is the pump of our OPA. Only 500 nJ of the 20 $\mu J$ obtained are used for spectral broadening through WLG, to generate the signal. The WLG is realized in a sapphire crystal of 10 mm of thickness. The 500 nJ are focused using a lens of 75 mm. The WLG spectrum produced is shown in figure IV.9. We can observe that the signal we want to use for the OPA, at 687 nm, is well optimized in this configuration. A dichroic mirror filtering the 515 nm pump beam has been used to acquire the shown spectrum avoiding saturation of the spectrometer.

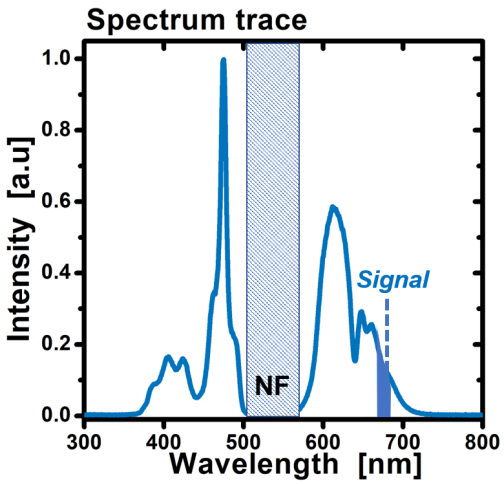


Figure IV.9 – Spectrum of the WLG from a 10 mm thick sapphire crystal pumped by 540 nJ pulses at 515 nm. NF= Notch Filter centered at 515 nm.

As can be seen in the scheme IV.8 we need a signal centered at 687 nm in order to be combined to the 515 nm centered pump for the idler generation at 2060 nm. We are in a collinear OPA (COPA) configuration. This choice is required in order to avoid angular chirp of the idler. The OPA crystal is a BBO in type II phase matching, meaning that the pump and idler are on the same polarization axis and the signal is on the orthogonal one. We use the same crystal for both amplification stages, spatially shifting the first and second pass. The two stages of amplification are important to obtain an idler energy high enough at the output of the system, exploiting all the pump laser energy.
The pump arm is reduced using a telescope to 1 mm beam diameter measured at $1/e^2$. In this configuration, the first OPA pass allows to obtain an amplified signal at 687 nm of the order 12 mW and an idler around 4 mW. The second amplification stage increases these values respectively for signal and idler to 330 mW and 110 mW. Between the first and second pass a delay line is used to re-synchronize temporally signal and pump. This delay line allows, moreover, to select the amplification of the signal and generation of the new idler or the amplification of the idler generated in the first pass. We select the amplification of the first pass signal getting rid of the first pass idler. We can notice that the total conversion efficiency of the system calculated as the ratio between total average power output (signal+idler) on the pump average power is 25.6 %. This is comparable to the efficiency found in the literature [Waxer *et al.* , 2003]. The idler spectrum and autocorrelation trace are shown in figure IV.10.

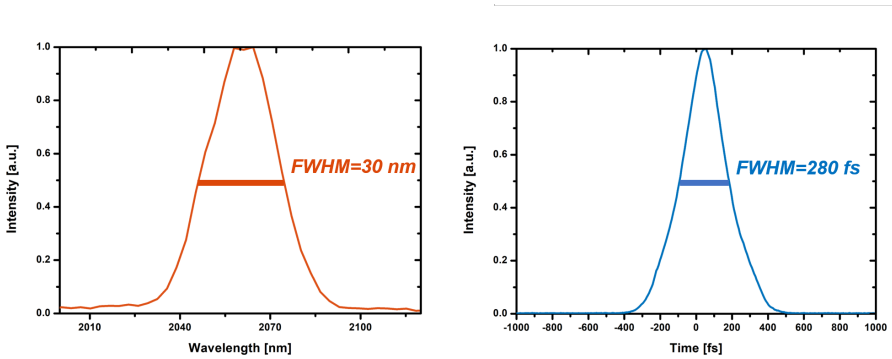


Figure IV.10 – Left: Spectrum of the idler centered at 2060 nm. Right: Autocorrelation trace for the idler centered at 2060 nm.

The autocorrelation trace has a FWHM of 280 fs. For a Gaussian fit, this corresponds to a 200 fs pulse width. The spectrum has a FWHM of 30 nm that translates to a TL pulse of 200 fs for a spectrum centered at 2060 nm.

## 3.2 OPA-CEP output characterization

The idler is frequency doubled in order to obtain the CEP-stable seeder at 1030 nm. The SHG is realized using a 2 mm thick BBO in type I phase matching. The measured power is 43 mW, corresponding to 430 nJ at 100 kHz repetition rate. The spectrum at 1030 nm and the autocorrelation trace are depicted in IV.11. The spectrum FWHM is 8 nm, translating to a TL pulse duration of 195 fs. The SHG essentially preserves the BW of the idler. The autocorrelation FWHM is 270 fs, on the measured signal at 2 $\mu m$.

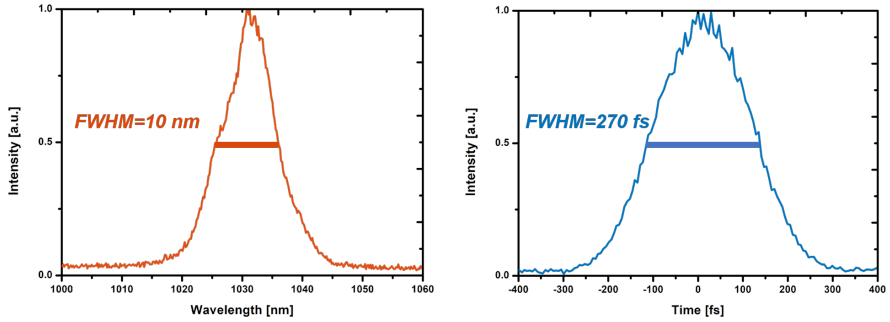


Figure IV.11 – Left: Spectrum of the idler centered at 1030 nm. Right: Autocorrelation trace for the idler centered at 1030 nm.

A crucial point to analyze is the stability of the system. The OPA is very sensitive to the time synchronization between pump and signal as already discussed. The energy of the output can be very fluctuating depending on the arm length and the used mechanical mounts stability. In this sense, the system we have realized has been designed starting from an industrial based OPA (*Amplitude Laser*) to improve the robustness. A picture of the system is shown in figure IV.12 on the left. The size of the OPA described above is only 30 cm x 40 cm. The interferometer arms are of only 40 cm for the first pass and 15 cm for the second one. The whole system is very compact. We have realized a measurement of the long term power stability. The results are depicted in IV.12. The measurement has been realized lowering the repetition rate of the laser at 10 kHz. The standard deviation over 12 h is 0.15 % rms, showing the very high stability of the system.

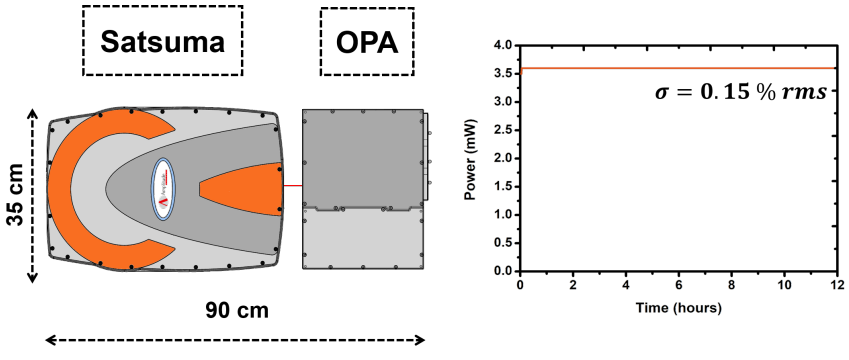


Figure IV.12 – Left: Size of the OPA industrial system and pump laser (*Satsuma*, Amplitude Laser). Right: Output Power stability over 12 h.

The stability of the OPA interferometer, considering robustness and short pathlengths, is a really important point for ensuring stability CEP high performances. In the next parts of this chapter we will see how the choice made on the OPA design minimizes the instabilities of the interferometer directly transferred to the CEP of the output.

# 4 CEP characterization

In this section the realized CEP seeder is characterized in terms of CEP fluctuations. The methods described for the oscillators cannot be used for our setup. The reason is that, in our case, $f_{CEO}$ is automatically set to zero because of the DFG phenomenon. The beat note is therefore not detectable. For this reason we need a different way to make our measurement. We have to look at the measurements methods used for amplified CEP-stable systems. The f-2f scheme is maintained but there are some differences in setup and detection.
For the setup, the energy has to be high enough at the output to allow the spectral broadening by WLG in a bulk crystal instead of using a fiber. Compared to the fiber case, the bulk medium avoids the coupling fluctuations.

## 4.1 Detection techniques for high repetition rate CEP measurement

### 4.1.1 Spectrometer detection

For the detection method, the simplest and most used way is to use a spectrometer. The detection of spectral fringes position at the output of an f-2f interferometer allows to directly calculate the standard deviation on the fluctuation of $\varphi_{CEP}$. We have fringes in the spectral range generated from the interference from f and 2f components. Let us consider the fundamental component electric field of a pulse in the frequency domain:

$$E_f(\omega) = A_f(\omega)e^{i\varphi_{CEP}}, \tag{IV.13}$$

and the corresponding frequency doubled one:

$$E_{2f}(\omega) = A_{2f}(\omega)e^{i(2\varphi_{CEP}+\omega\tau)}, \tag{IV.14}$$

where the 2f component is delayed of a time $\tau$ with respect to the fundamental pulse because of the propagation in the SHG crystal. A spectrometer acquisition measure the intensity of the sum of the two components:

$$I(\omega) = |E_f(\omega) + E_{2f}(\omega)|^2 = I_f(\omega) + I_{2f}(\omega) + 2\sqrt{I_f(\omega)I_{2f}(\omega)}cos(\omega\tau + \varphi_{CEP}) \tag{IV.15}$$

,

where the intensity of the arm $f$ and $2f$ are respectively $I_f(\omega) = |E_f(\omega)|^2$ and $I_2f(\omega) = |E_2f(\omega)|^2$. The last term in the equation (IV.15) represent the fringes that can be see depicted on the left in box 1 in figure IV.13. The fringes width is directly related to the delay $\tau$. The longer is the delay, the smallest is the fringes width. For a delay equal to zero, there are no fringes to measure at all. The position of the fringes is instead linked to the CEP. For measuring the variation of the $\varphi_{CEP}(t)$ in time we acquire several fringe patterns. From the series of fringes in time we can calculate the CEP variation using the *Fourier Transform Spectral Interferometry* (FTSI) [Takeda *et al.* , 1982]. The scheme in figure IV.13 explains the principle of the technique in three steps.

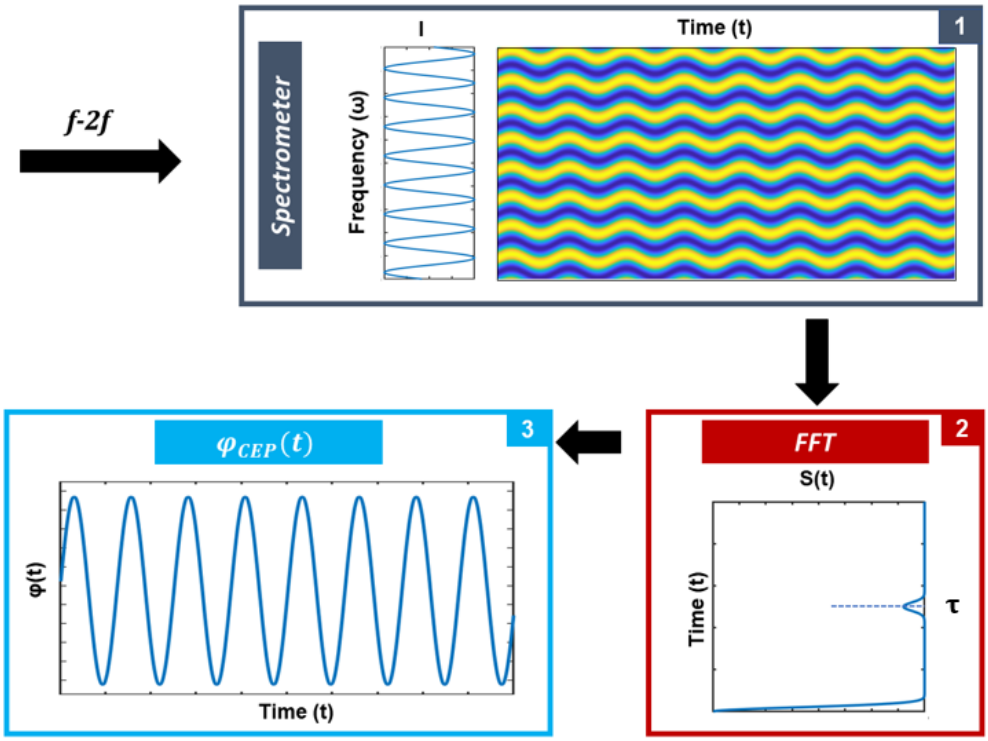


Figure IV.13 – FTSI algorithm depiction for CEP fringes

The signal of the spectrometer from the f-2f allows to acquire the fringes as shown in box 1 of figure IV.13. The evolution of the fringes patterns in time is shown in the two-dimensional plot on the right. For making an easy example, we simulate a sinusoidal modulation of the CEP, corresponding to a sinusoidal modulation of the fringes position in time. Each acquisition of fringes is transformed via *Fast Fourier Transform* (FFT). The magnitude square of the FFT function is in the box of step 2. We can see that there is a peak centered at $\tau$, where $\tau$ is the delay between the two interferometer (f and 2f) arms that we have seen in equation (IV.15). The CEP phase changing in time is retrieved in box three. This is done by selecting the peak centered at $\tau$ and measuring its phase variation in time.
We understand from the procedure explained that the spectrometer acquisition parameters have to be carefully chosen. Two important points have to be considered on this subject: the integration time and the sampling rate. The integration time is the time required for a single fringe pattern acquisition. This means that if we want to take a single CEP value per pulse and obtain a real estimation of the fluctuations $\Delta\varphi_{CEP}$ we need this time to be lower than the period $T_R$ between two pulses. Commercially there exists spectrometer working for the spectral range where we want to detect our f-2f fringes with integration times as low as 3 $\mu s$. This means that the CEP of a single pulse can be measured up to a repetition rate of 333 kHz. The sampling rate is, instead, how fast an acquisition can be done. This time is limited to the order of some ms by the connection spectrometer-computer. Other than the evolution of the phase fluctuation in time we are often interested in looking at their PSD. This is particularly useful to detect the frequency characteristics of the noise contributing to a CEP rms stability. The PSD obtained by the spectrometer fringes measurement is limited to half the sampling frequency. Even considering a fast sampling rate of 1 ms, the $f_{max}$ of the PSD is only 500 Hz. For our system at 100 kHz of repetition rate this is not enough.

### 4.1.2 Fringeezz

Very similar to a spectrometer, a commercial product named *Fringeezz* (Fastlite) is available as a dedicated tool for CEP measurement. This instrument has an integration time low enough to ensure single shot measurement at 100 kHz and a max sampling rate of 10 kHz. This means having PSDs with $f_{max} = 5$ kHz.
For the measurement, the f-2f signal is injected in the Fringezz in the same way than for a standard spectrometer. The processing of the fringes to obtain $\Delta\varphi_{CEP}$ values is done in real time. The software provided by the manufacturer allows to choose the integration time from 1 to 2 pulses at 100 kHz and measure the $\Delta\varphi_{CEP}(t)$. A fast data logging system allows to have long time scale measurements. This tool will be largely used in this manuscript for this kind of measurement.

### 4.1.3 Analog detection: *Beat Interferometry for Rapid Detection* (BIRD)

We can consider that the limit of the spectrometer and Fringeezz sampling rate are related to the digital-to-analog conversion (DAC) speed. A completely analog method can be adopted for high repetition rate detection. The idea is very similar to a spectrometer scheme [Koke *et al.* , 2008]. The f-2f signal is diffracted trough a grating in order to spatially separate the fringes. However, this signal is not detected using a CCD camera or linear detectors, as it is done in spectrometers. A single fringe is selected using a slit. A prism is used to divide the selected fringe signal and reflect it on two photomultiplier tubes (PMTs). The scheme of the setup is shown in figure IV.14 on the right. The signal measured by the two photodetectors is subtracted and measured with an oscilloscope. As for the spectrometer, the position of the fringe is related to the $\varphi_{CEP}$. Assuming a perfectly sinusoidal fringe slope, the CEP phase can be retrieved from the differential voltage using:

$$\Delta\varphi(t) = arcsin\Big(\frac{V(t)}{V_{max}}\Big), \tag{IV.16}$$

where: $V(t)$ is the signal measured by the BIRD and $V_{max}$ is the voltage corresponding to a phase displacement of $\frac{\pi}{2}$.

For matter of clarity, on the right of figure IV.14 is depicted the phase function of the signal measured by the BIRD.

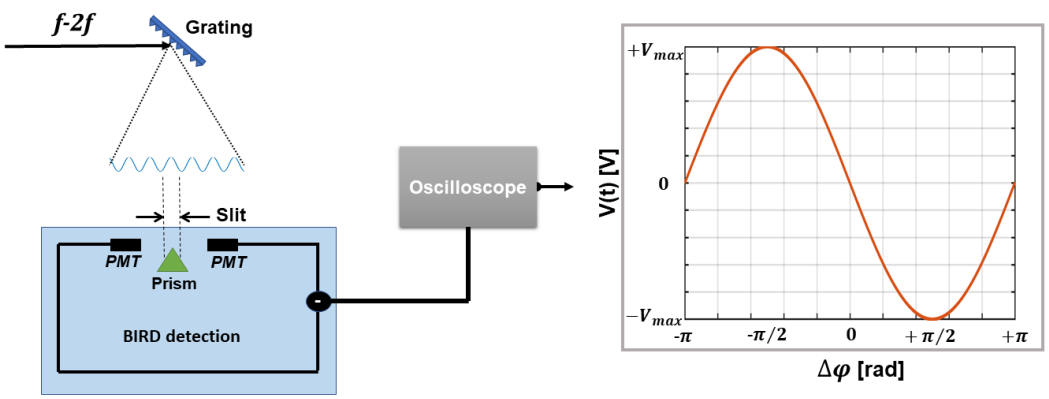


Figure IV.14 – Left: BIRD setup scheme. Right: CEP relationship with photodetectors measured signal

.

Let us consider the phase relation depicted in IV.14. The phase retrieved from a determined

$V(t)$ is unambiguous only on a range of $\pi$. This means that the BIRD measurement is particularly suitable for measuring CEP rms fluctuations that are smaller that 1 rad[1]. In appendix A, a new detection scheme based on BIRD is proposed detecting the CEP fluctuations over a range of $2\pi$.
This completely analogic technique allows to acquire an oscilloscope trace and retrieving the phase via a post-processing. The limitation in terms of PSD BW is the photodetector response. This can be fast enough for 100 MHz repetition rate laser. Indeed, a very similar scheme has been used by Liehl et al. [Liehl *et al.* , 2017] for complete CEP characterization of a 100 MHz laser measuring a PSD with $f_{cut} = 50$ MHz.

### 4.1.4 f-2f setup description

The f-2f setup that we use for all measurements we have realized for CEP characterization of the CEP-stable front-end is shown in figure IV.15. It consists of a YAG crystal for WLG and a BBO, both 3 mm thick, placed in the focal region of the same lens. A half-waveplate and a polarizer cube are used for the f and 2f components polarization re-projection. The *in-line in-focus* configuration is an extremely simple, i.e. stable, version of the f-2f schemes reported in the literature.

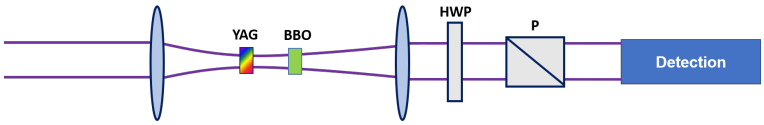


Figure IV.15 – Scheme of the f-2f in-line in-focus setup. HWP: Half-waveplate P: polarizer

The common-path configuration we have adopted reduces the impact of the interferometer on the measurement. The delay between the f and 2f components that is necessary for the spectral fringes generation is linked to the optics in the focus of the lens. We remind that the laser we test is at 1030 nm. The fringes are generated around the SHG of the spectrum at 515nm. The component of the fundamental at 515 nm is generated somewhere in the YAG crystal. The 2f components at 515 nm are generated in the BBO crystal. The delay is determined by the difference between the group velocity at 1030 nm and 515 nm in the YAG. Common-path f-2f have been used in other CEP-related works [Balčiūnas *et al.* , 2014]. The difference with respect to our case is that there is at least another optical components (e.g. lens) between the WLG and the SHG. The available energy of 430 nJ delivered by our CEP-stable FE is barely enough to perform stable WLG in our setup, and make the experiment difficult. All the measurements we will show in the next parts are realized using the full energy.

## 4.2 CEP measurement results

The complete CEP characterization of the OPA output is discussed in this part. The previously discussed three detection techniques are used. The system is always operated at 100 kHz. The pump laser is used with the standard PP (as opposed to synchronously driven), with a non optimized RIN.

### 4.2.1 Integration and down-sampling effects

Let us preliminarily analyze what it means to integrate pulses on the measured value of the CEP shift. In analogy with what we have discussed for the aliasing and filtering, we can approach the CEP case looking at the CEP PSD. If we can measure a value of $\varphi_{CEP}$ from each pulse and with a sampling rate $f_S = f_{rep}$, this means that we are correctly reconstructing the

[1] We have to consider in fact that the phase retrieving is linear only in a small range.

fluctuations of CEP $\varphi_{CEP}$ in the whole BW until $f_{rep}/2$. Look now at the scheme in figure IV.16.

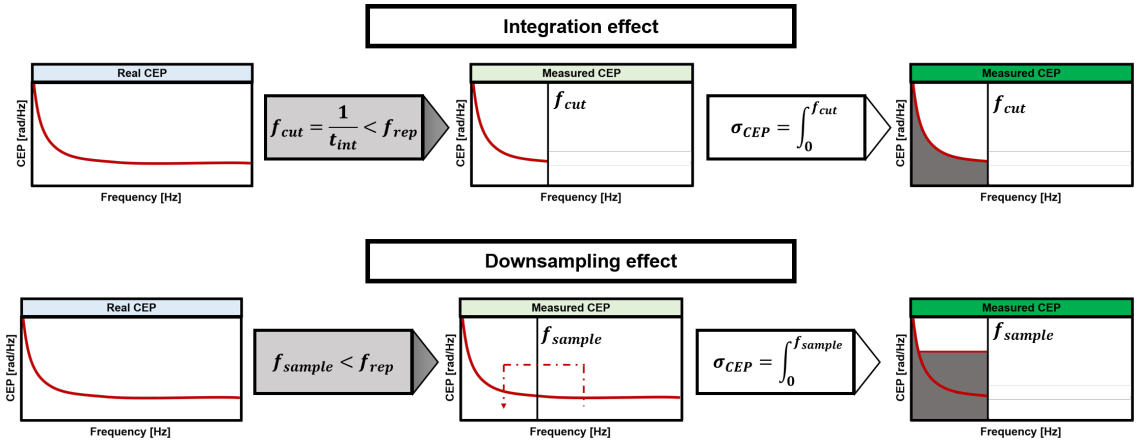


Figure IV.16 – Scheme of the CEP measurement via spectrometer. Top: Effect of integration time on CEP noise measurement. Bottom: Effect of downsampling on CEP noise measurement.

On the top-left is represented the real CEP PSD spanning from 0 to $\frac{f_{rep}}{2}$. Consider an integration time such that $n$ pulses are measured in a single acquisition. This means that the measured CEP BW is filtered with respect to the real CEP on a BW $[0,\ f_{cut} = f_{rep}/n]$. The measured fluctuations CEP rms $\sigma_{CEP}$ are equivalent to the integral in the BW $[0;\ f_{cut}]$. We can easily understand that the measured $\sigma_{CEP}$ is an underestimation of the real one. It is common to say that the underestimation of the CEP noise is proportional to $\sqrt{n}$. This assumption is true only for a white noise. If the CEP PSD presents a peaked structure the underestimation can be more important. Let us consider, now, the down-sampling effect depicted in the bottom line of figure IV.16, where we are sampling with a $f_{sample}$ lower than the $f_{rep}$. We can see that there is no underestimation in the measured $\sigma_{CEP}$ in this case. The spectral components in the BW $[f_{sample}, f_{rep}]$ are aliased in the measurement BW $[0,\ f_{sample}]$. The integral of the measured CEP PSD is equal to the one of the real CEP PSD. Having several aliased components of the CEP PSD means, in contrast, loosing the information about the real frequencies of the noise contributions we want to measure.
These effects are generally applicable to the different detection methods depending on the chosen parameters and properties. Considering the three measurement techniques we will use in this work, only the BIRD allows to acquire a single shot, every shot measurement for acquiring the complete real CEP PSD at 100 kHz.

### 4.2.2 Spectrometer results

As explained above, the f-2f operation is limited by the available pulse energy. This means also that we have a low signal for the detection.

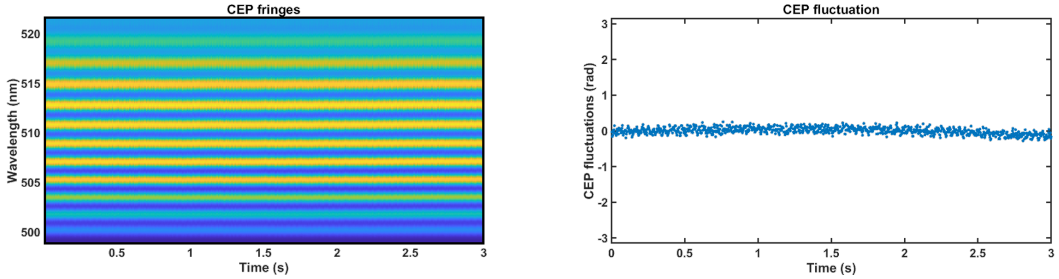


Figure IV.17 – Left: fringe pattern over 3 s . Right: Phase retrieved via FTSI.

We use the spectrometer with 1 ms integration time (corresponding to average over 100 pulses) in order to have enough signal for an optimum SNR. The sampling rate is 330 Hz.

In figure IV.17 the fringes patterns acquisition and the relative calculated phase via FTSI are shown.

The measured $\sigma_{CEP}$ rms is 95 mrad in the interval of measurement of 3 s. It is useful to introduce the concept of contrast or visibility of the fringes. The definition, very common in interferometry, [Hariharan, 2010], is:

$$C = \frac{I_{max} - I_{min}}{I_{max} + I_{min}}, \tag{IV.17}$$

where $I_{max}$ is the intensity in the top of the fringe and $I_{min}$ the minimum intensity measured in the fringes pattern. The value C exists between 0 and 1. Let us analyze what it means for the CEP fringes spectrum we have measured. Taking t=0 acquisition of figure IV.17 we obtain the figure IV.18 We can observe a very high contrast of 0.58. The contrast value changes depending on which fringe is considered. In the case in figure IV.18, the contrast is higher for the central fringes and goes down for the right borders one. The intensity relation between the two arms of the interferometer determines this contrast. The SHG signal and the WLG one in the spectral zone [500 nm; 520 nm] are not uniform and are affecting the contrast behavior. For our scope we consider the maximum contrast as our fringes contrast. We will use this value only for comparative studies where we use always the same measurement criterion ensuring the reliability. For CEP fringes of high repetition rate laser the contrast of fringes is sometimes used to estimate the hidden CEP noise for highly integrated spectrometer measurements. The idea is that high contrast reflects a low contribution of CEP noise hidden by the integration filtering [Lu *et al.* , 2018]. In the case of the above-shown measurement, the high fringe contrast could mean that there are no high frequency CEP noise contributions hidden in the BW [1 kHz; 100 kHz]. In the next chapter we will present a detailed study demonstrating that this criterion is not really faithful for CEP measurements.

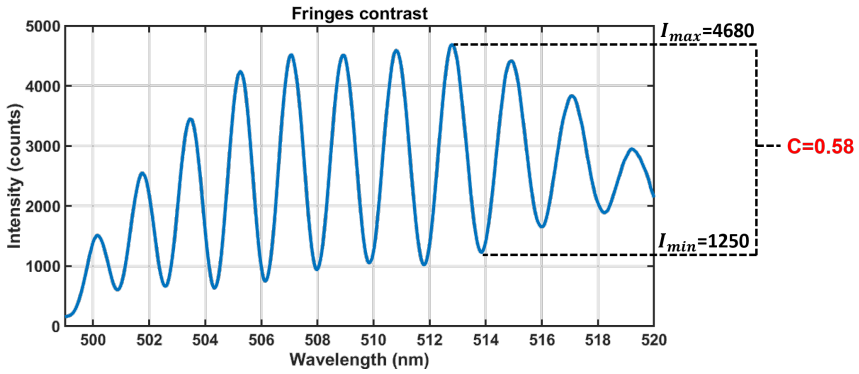


Figure IV.18 – Fringe pattern for contrast of fringes calculation

As we already said we can look at the PSD of the CEP noise for identifying the noise sources. The very low sampling rate translates to a PSD on the BW [0; 160 Hz]. The results in terms of CEP noise PSD and relative integrated noise are depicted in figure IV.19. Similarly to what was done for the IRIN measurement, the integration of the PSD is done from high to low frequency. Obviously, the total integrated CEP corresponds to the 95 mrad measured as rms fluctuation of phase points in figure IV.17. The analysis of the PSD shows that the only visible noise contributions in the CEP noise are a peak at 50 Hz and one at 100 Hz. The one centered at 100 Hz is not well resolved because it is close to the $f_{max}$ of the PSD. In the integrated CEP noise, however, it seems to contribute to a third of the total noise in the bandwidth. The 50 Hz is probably not a real noise but an down-sampling resulting copy of the 100 Hz. Another consideration that can be done is that there is no noise at low frequencies (less than 50 Hz).

This is a confirmation of our OPA mechanical stability. This measurement is interesting as first characterization but at the same time evidences the limits of the measurement concerning the integration time and sampling.

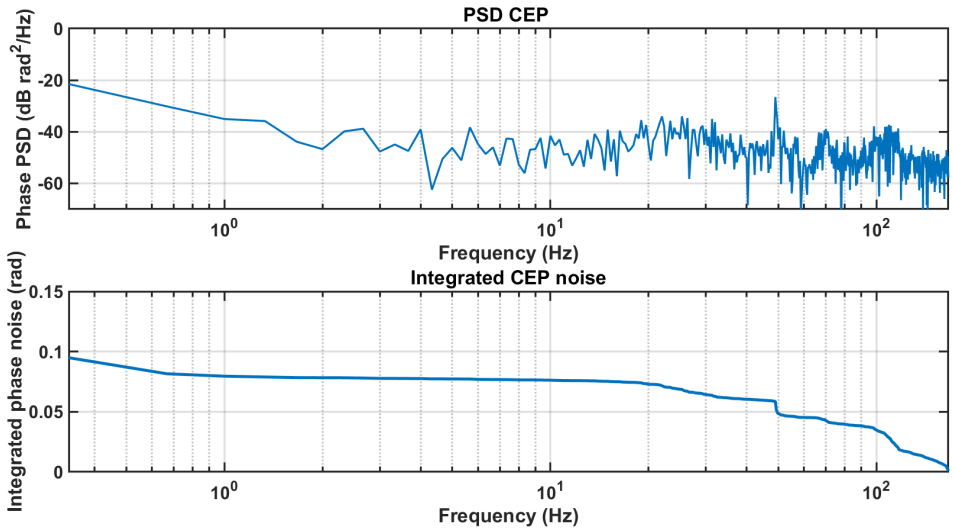


Figure IV.19 – Top: CEP noise PSD from spectrometer measurement Bottom: integrated CEP noise.

### 4.2.3 Fringeezz results

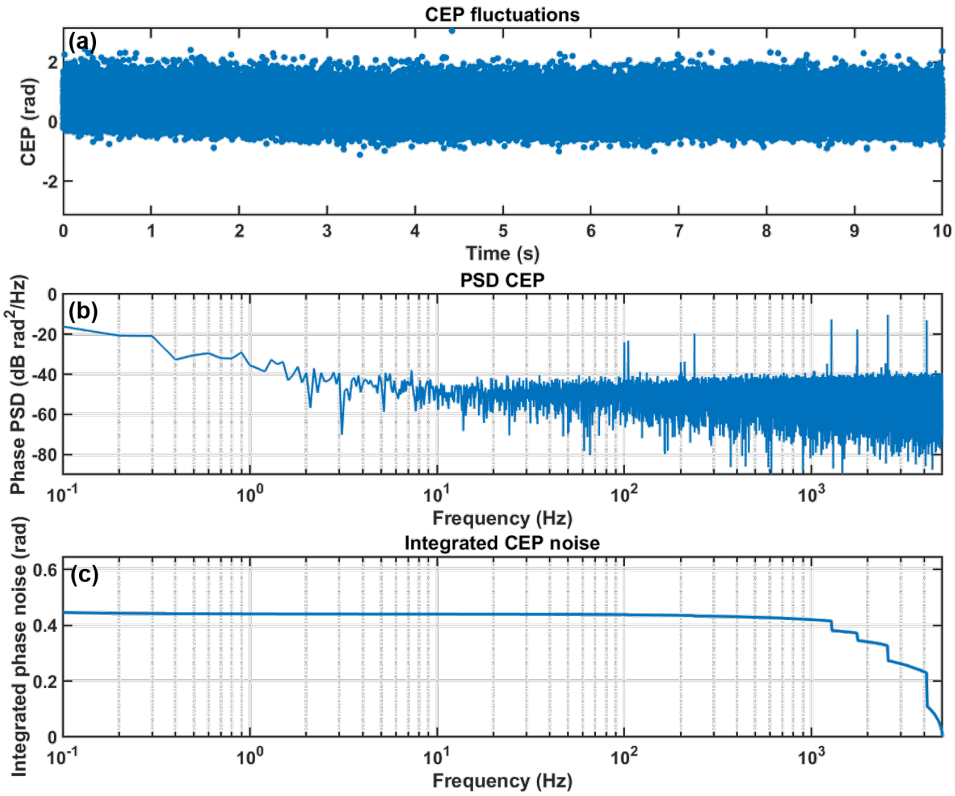


Figure IV.20 – Fringeezz measurement over 10 s. (a) CEP fluctuations, (b) CEP PSD, (c) Integrated CEP noise.

The explained Fringeezz measurement allows to overcome some of the problems of the spectrometer detection. Because of our low signal we cannot exploit completely the instrument features. In particular, we integrate over 2 pulses, using 20 $\mu s$ integration time. The sampling rate in this case is 10 kHz. The Fringeezz is triggered by a clock coming from the laser at 100 kHz divided by 10 in frequency. The results obtained in these conditions are depicted in figure IV.20.

The measurement is realized taking $10^5$ pulses at 10 kHz meaning 10 s measurement interval. The total integrated noise over 10 s is 445 mrad. If we look at figure IV.20 (b) we can compare the PSD of the spectrometer with the one we have measured in the Fringeezz case.
At high frequencies we can see that several peaks are appeared in the kHz range. Once again, these contributions are filtered out in the case of the spectrometer owing to the integration over 100 pulses.
For the low frequencies, we confirm the conclusion obtained with the spectrometer, that there is no large contribution to the noise. This measurement is a stronger validation because of the longer measurement time. If we analyze the integrated noise in figure IV.20 (c), we observe that 90 % of the CEP noise is accumulated between 1kHz and 5 kHz. The already cited peaks have a contribution about half of the total. Considering what we know about the aliasing effect, we cannot state if the position of these noise peaks is real or the result of aliasing. What we can state measuring the central frequency of each pulse, is that the peaks are at $p_1$=1.276 kHz, $p_2$=1.752 kHz and $p_3$ = 4.123 kHz. The remaining peak at 2.553 kHz is, probably a harmonic of $p_1$. In this range of frequency, the noise contributions are due to electronic sources.

### 4.2.4 BIRD results

To complete the CEP characterization of the system we realize a measurement using the BIRD technique. The first step of this measurement is to clearly visualize the fringes spatially diffracted by a grating. A picture of the spatially diffracted fringes is shown in figure IV.21. To the naked eye they look stable in time: our eyes acts as an integrator with a cuoff frequency of 25 Hz. We are sensitive only to very slow fluctuations. This qualitative consideration is again a confirmation of the absence of mechanical contributions in the CEP fluctuations.

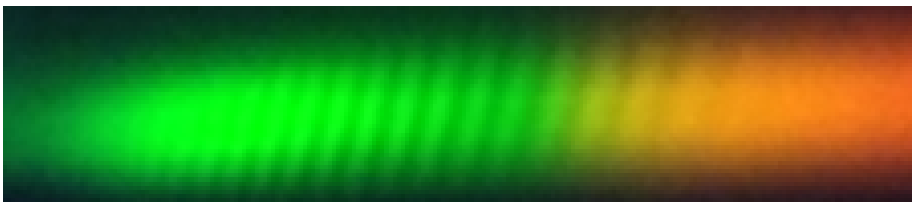

Figure IV.21 – Photo of the spatially separated f-2f fringes.

Only a single fringe is selected using a slit and the position variations are measured using the scheme described before. The obtained PSD and integrated CEP noise are depicted in figure IV.22. The acquisition is done in a measurement interval of 1s. This choice is done to simplify the data processing and considering the fact that we are interested in the measurement of high frequencies (above 1 kHz). Over the whole bandwidth we measure a total rms $\sigma_{CEP}$=470 mrad. The value is slightly higher than the one measured with the Fringeezz where we integrate over 2 pulses. The accuracy of the obtained value is related to the precision of the $V_{max}$ measurement. This voltage is measured on the oscilloscope PMT error signal trace, while sliding a couple of wedges placed just before the f-2f in order to change the CEP. This operation is particularly delicate. As an example an error of 10 mV on a measured $V_{max}$ = 350 mV leads to a difference of 20 mrad in the $\sigma_{CEP}$. The difference with respect to the Fringeezz case can be due to the BIRD accuracy.

The real interest of the BIRD measurement is the complete PSD reconstruction. We can see

that a very peaked noise structure is evidenced. We find a low intensity peak centered at 100 Hz. We can also observe this peak in the spectrometer and in the Fringeezz cases. Looking at the relative integration plot, this peak's contribution is quite weak. The biggest contributions come from high frequencies, confirming what we have measured with the Fringeezz. Five peaks can be distinguished in the BW [1 kHz; 50 kHz]. Considering their central frequencies, we find two fundamental peaks and their harmonics, as follow:

$$p_1 = 2.365 \quad kHz \quad h_{p1} = 4.730 \quad kHz, \tag{IV.18}$$

$$p_2 = 7.118 \quad kHz \quad h1_{p2} = 14.236 \quad kHz \quad h2_{p2} = 21.354 \quad kHz. \tag{IV.19}$$

The two peaks $p_1$ and $p_2$ have probably the same origin as of the ones we have measured with the Fringeezz even if they are not at the same central frequencies. Their frequency range suggests again an electronic noise. To investigate the possible correlations between amplitude noise and CEP noise, we characterize the RIN of the system in the following section.

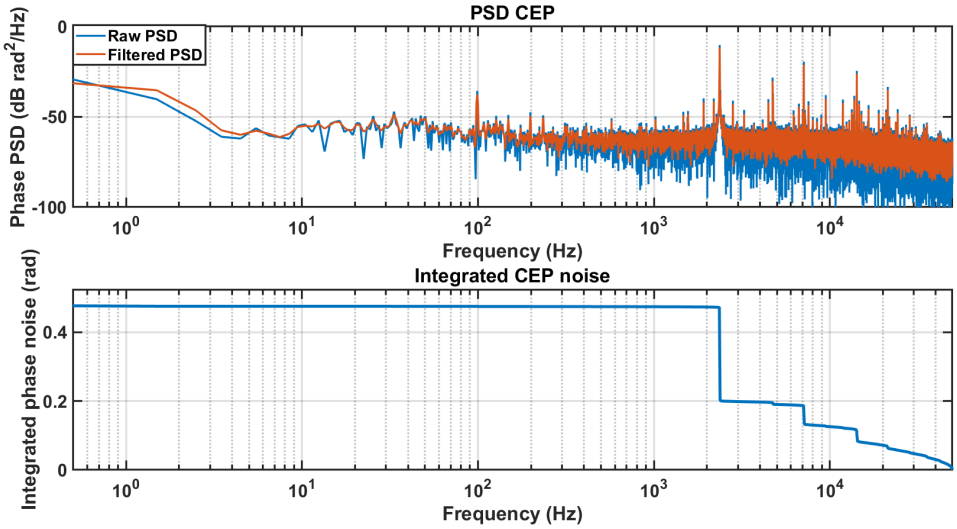


Figure IV.22 – Top: BIRD measured CEP PSD over 1 s measurement time. Bottom: integrated CEP noise over 1 s measurement time.

# 5 RIN characterization

In this section a characterization of the system in terms of RIN is done. In the first section we focus on the relationship between OPA RIN and pump laser RIN. In the second one, the transfer from the RIN of the pump laser to the CEP noise of the CEP-stable output is discussed. Finally, in the last section the improvement on the CEP thanks to the RIN lowering via the PP synchronization is presented.

## 5.1 RIN characterization

The RIN characterization is realized by measuring the RIN at 100 kHz at the output of the pump laser and comparing it with the one measured at the OPA output both taken with ME=80 %. This is the condition we have used for the OPA optimization giving the results presented in this chapter. The measurement setup consists of an amplified PD (PDA36-EC, *Thorlabs*) and a filter at 50 kHz (EF122, *Thorlabs*). The results are depicted in figure IV.23.

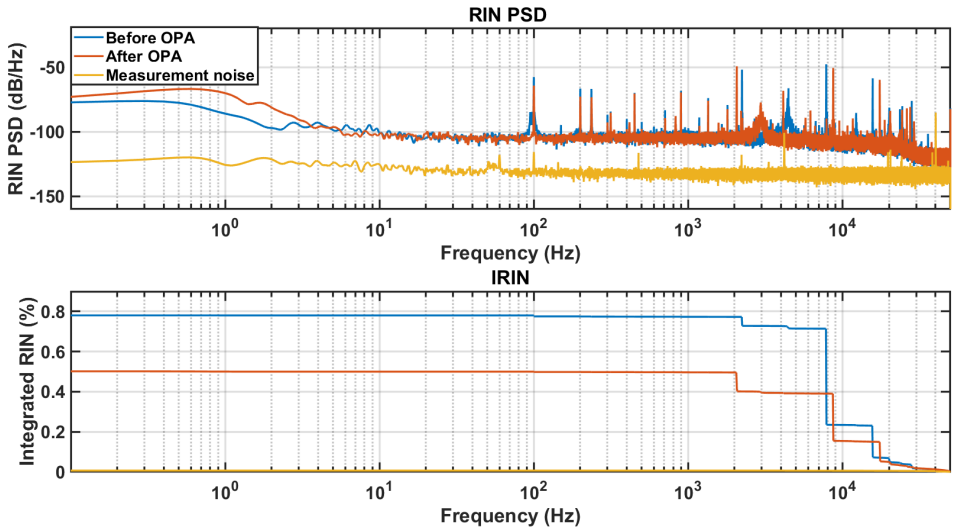


Figure IV.23 – Top: RIN PSD measurement before and after the OPA. Bottom: IRIN measurement before and after OPA.

The OPA RIN output is less than the pump RIN laser one. We can observe that the peaks are reduced and sometimes slightly shifted in frequency. This reduction is probably an effect due to the OPA saturation [Hamm *et al.* , 2000, Inoue & Mukai, 2002]. In our scheme the saturation comes not only from the OPA but also from the SHG stages. In a more general approach, we can ask which part of the scheme acts on the input amplitude noise. In figure IV.24 the nonlinear stages in our setup are summarized.

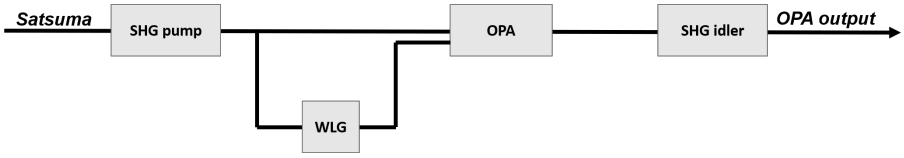


Figure IV.24 – Scheme of the nonlinear stages in the OPA scheme as possible source of the AN alteration.

In particular, we expect that SHGs and OPA in saturation can reduce the AN. The WLG, instead, is the signal generator for the OPA and can add AN. Let us focus our attention only

on the BW around 687 nm. Considering that this spectral part is at the edge of the WLG spectrum, the intensity stability is maintained only if the generation energy is in a specific range. For lower energies we add noise to the input signal because of the WLG instability transferred to the signal. For higher energies the filament in the WLG process breaks up, generating a less stable situation. To demonstrate what we have already said, let us consider a general saturation of the whole setup measuring the power of the frequency doubled idler as a function of the pump laser power, acting on ME efficiency. This parameter, as said before, acts on the transmission of the AOM. It can be directly controlled via the laser software or using an external voltage between 0 V and 5 V. In figure IV.25, it can be seen that the saturation is reached for ME=80 %.

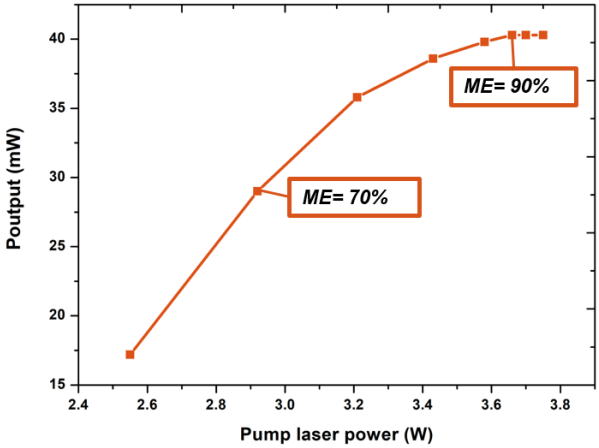


Figure IV.25 – Measured power of the idler in function of the pump laser power, acting on ME efficiency.

We choose two particular situations: ME=70 % and ME= 90 %. The results in terms of RIN before and after the OPA are depicted in figure IV.26.

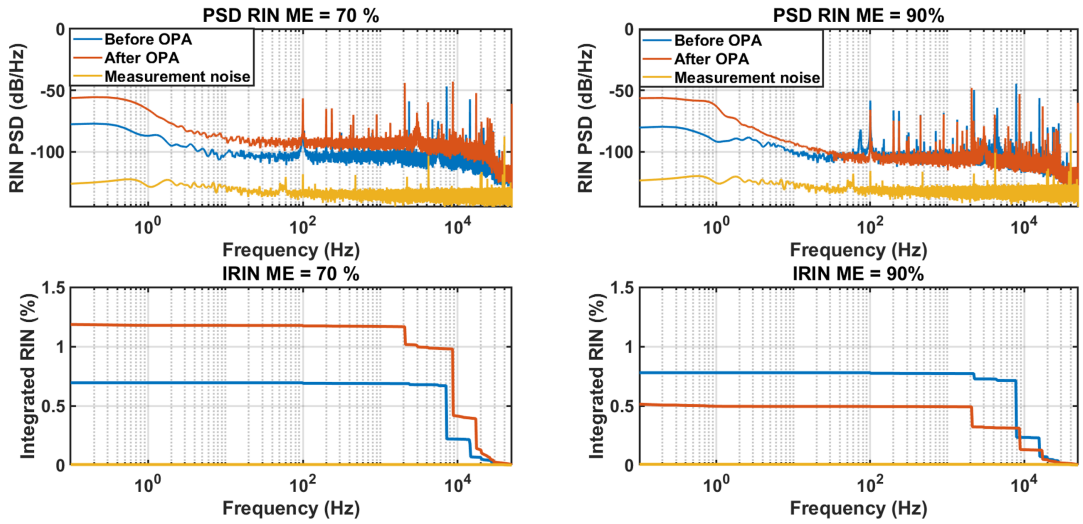


Figure IV.26 – Left: PSD and IRIN of the laser and after the OPA with ME efficiency at 70 %. Right: PSD and IRIN of the laser and after the OPA with ME efficiency at 90 %.

In the case on left, the system adds noise with respect to the pump laser. The OPA and

probably the SHG stages are not saturated. The WLG input energy is very low, probably resulting in an unstable signal for the OPA. In contrast, the case presented on the right corresponds to a situation where the nonlinear stages are well saturated. The output RIN is lower than the input one. The total reduction is around 30 %. Apart from the overall noise reduction we have noticed that the peaks can be shifted in frequency. The effect can come from the OPA system or because of a different source of shift in the pump laser RIN. The measurement here presented for the RIN before and after the OPA are realized during the same day but not simultaneously. To understand better this phenomenon, we decide to introduce a sinusoidal modulation at a specific frequency on the pump laser intensity and we measure the RIN before and after. We choose to have the ME=80% as operation point. We apply a sinus modulation on the ME efficiency input equivalent to 1 % of the laser average power. The central frequency of the modulation is 5 kHz to replicate the behavior of the peaks we have in the laser RIN. The RIN result is plotted in figure IV.27. We can clearly appreciate that the peak is not shifted in frequency.

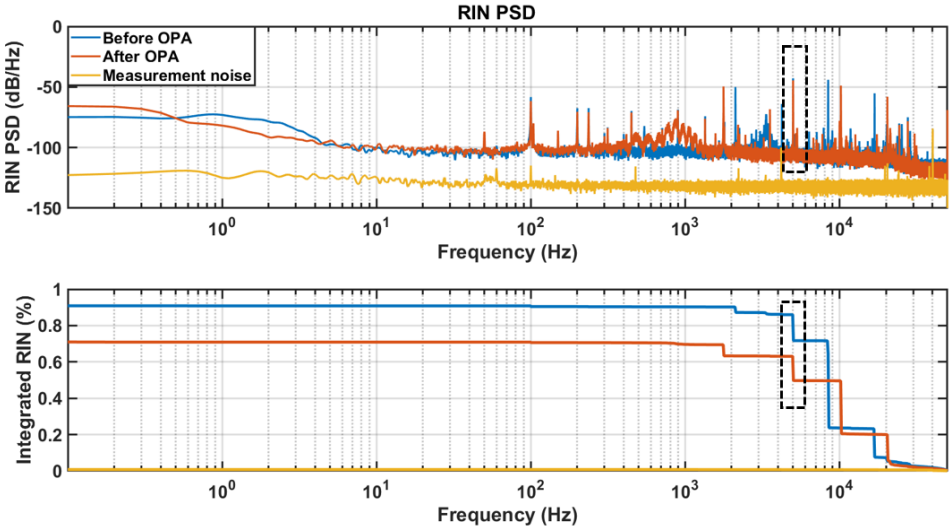


Figure IV.27 – PSD and IRIN of the laser and after the OPA with sinus modulation of 1 % on pump laser average power at f=5 kHz.

This means that the frequency shifting of the peaks is not generated by the OPA but is a shifting proper to the pump laser itself. Analyzing figure IV.27, we can calculated the attenuation of the peak passing through the OPA. Integrating only the BW around the peak [4.995 kHz; 5.005 kHz] in both cases we find a reduction of 25 %. To complete the characterization a *noise transfer function* (NTF) is realized for the system [Mulder *et al.* , 2008]. We want to see how different noise frequencies are transferred through the OPA. For this reason we repeat the measurement done for the 5 kHz case for sinus modulation at $f_{peak}$ = 1 Hz, 5 Hz, 10 Hz, 50 Hz, 95 Hz, 500 Hz, 1 kHz, 5 kHz, 10 kHz. We define as *coefficient of transfer*, $c$, the following ratio:

$$c = \frac{IRIN_{peak}^{pump}}{IRIN_{peak}^{OPA}}, \tag{IV.20}$$

where $IRIN_{peak}^{OPA}$ and $IRIN_{peak}^{pump}$ are the IRIN calculated around the peak(+/- 0.5%) for the RIN before and after the OPA respectively.

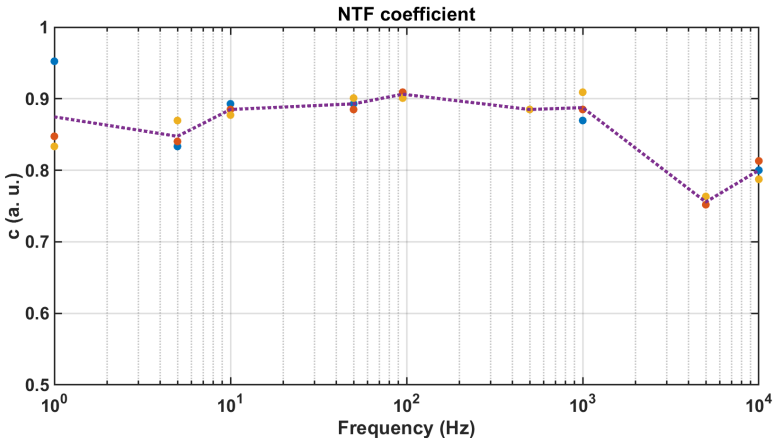


Figure IV.28 – Noise transfer function through the OPA.

In figure IV.28, the results with respect to the frequency are shown. For each modulation applied three RINs have been measured before and after the OPA. The resulting three point for c are represented in blue, red and yellow in the plot. The dotted line is the average value of c. We can conclude that the noise transfer function is almost constant for all the frequencies with a reduction of the noise for the peak between 75 % and 90 %. This behavior is not astonishing if we consider that the saturation processes involved in the OPA are instantaneous.

## 5.2 CEP noise pump laser condition dependency

We can now ask ourselves if the variation in the AN of the pump laser really affects the CEP of our system. Our hypothesis is that in WLG an important amplitude-to-phase noise transfer happens. Baltuska et al. [Baltuska *et al.* , 2003] have shown that the CEP phase is linearly varying for a certain input energy range. This range is a small region between a stable filament generation and the double-filament formation. For our scopes, we decide to have an idea of the stability of the WLG and in particular of the generated signal measuring the pulse-to-pulse rms fluctuations as a function of the WLG input energy.

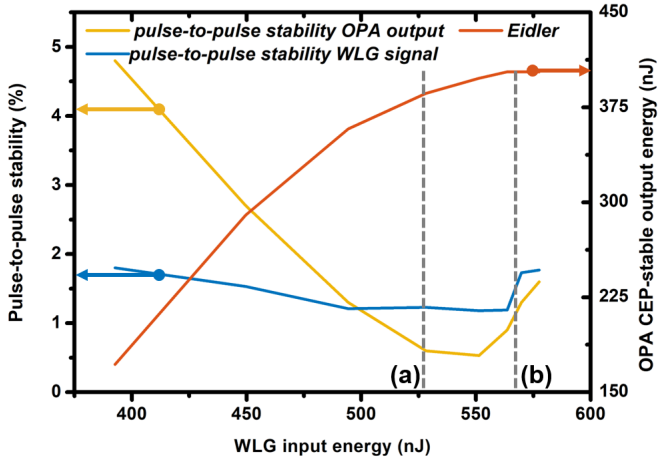


Figure IV.29 – Pulse-to-pulse rms WLG signal fluctuations (blue), Pulse-to-pulse rms OPA output fluctuations (yellow), OPA output energy (red) as a function of the input generation energy.

This measurement is realized filtering the white light with a 10 nm large bandpass filter

centered at 680 nm and detecting with a fast photodiode (DET10A, *Thorlabs*). The results are depicted in blue in figure IV.29.
The pulse-to-pulse stability rms of the signal generated via the WLG in the OPA is used to measure the stability of the WLG process and the relative CEP preservation. In our case, we can see that the pulse-to-pulse rms is minimum in the input WLG energy ranging from 510 nJ to 555 nJ. In the figure we have plotted also two other series of data. In yellow we have the pulse-to-pulse energy stability rms of the OPA output. In red the energy of the OPA output is plotted. The energy of the idler is strictly related to the curve we have shown in figure IV.25 about the saturation of the OPA. The OPA output pulse-to-pulse stability rms is minimum for WLG input energy between 525 nJ and 550 nJ. We choose, now, to measure the CEP in the two situations ($a$) and ($b$) respectively for 520 nJ and 565 nJ. We measure the CEP using the Fringeezz for both cases. The results are shown in figure IV.30. In the case (b) the total integrated noise is almost twice the one of the situation (a). The $\sigma_{CEP}$ rms passes, in fact, from 475 mrad to 880 mrad. Consider the three characterizations in figure IV.29 in the two situations. The saturation in (b) is stronger than in (a) looking at the energy of the OPA output. The pulse-to-pulse rms measured on the OPA output is lower than 1 % in both cases ensuring we are not differently affecting the f-2f CEP measurement because of the AN. The WLG signal pulse-to-pulse fluctuation is higher in (b) than in (a). This is probably the evidence of large amplitude to phase noise coupling in the WLG process for situation (b).

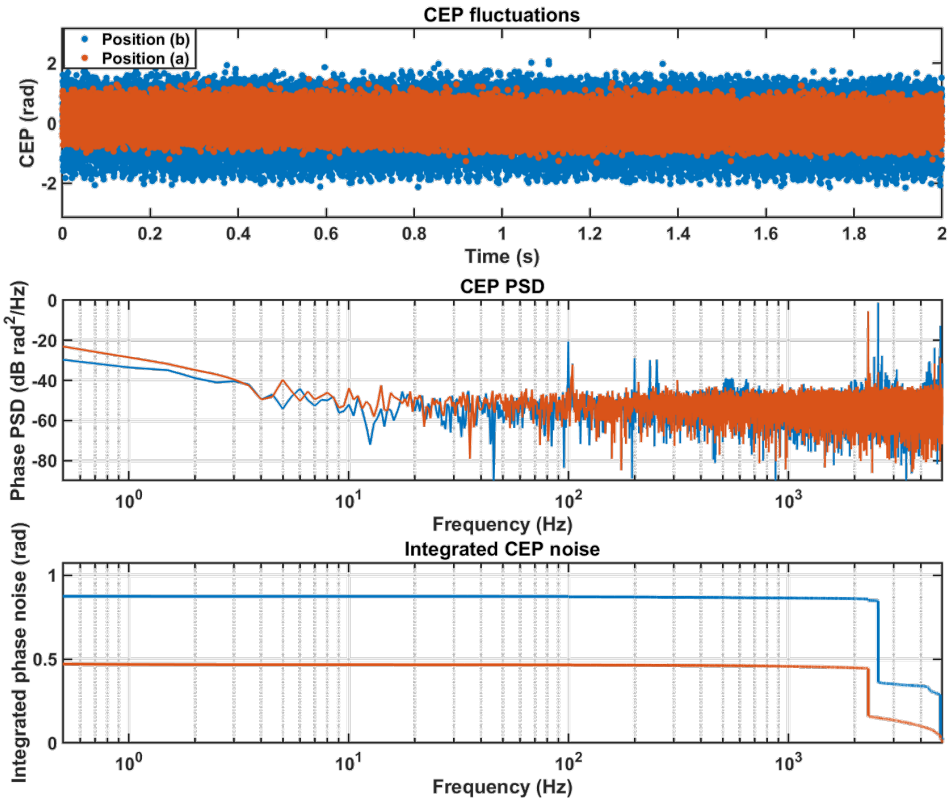


Figure IV.30 – CEP fluctuation, PSD and integrated noise for the cases (a) and (b) evidenced in figure IV.29.

We conclude that WLG optimization is crucial for the CEP performances and this step represents the amplitude to phase transfer mechanism in our system. We choose the WLG condition to have the lowest pulse-to-pulse fluctuations. The best operation conditions for the OPA includes also the lowest possible pulse-to-pulse on the output in order to keep low the AN.

In this optimized condition we still expect a transfer of the pump laser noise to the CEP noise. To demonstrate this, we apply a sinusoidal modulation acting on the ME efficiency as we have already done in the last section. The relative amplitude is of 1 % on the OPA pump laser average power, as before. We verify also that the modulation amplitude on the OPA output is low enough to ensure the CEP preservation in the WLG in the f-2f. Modulations are at frequency f=1 Hz, 10 Hz, 95 Hz, 500 Hz, 1 kHz, 5 kHz, 10 kHz. We realize BIRD measurements for each case in order to obtain the CEP PSD. In figure IV.31 a scheme of the measurement and the PSDs are shown.

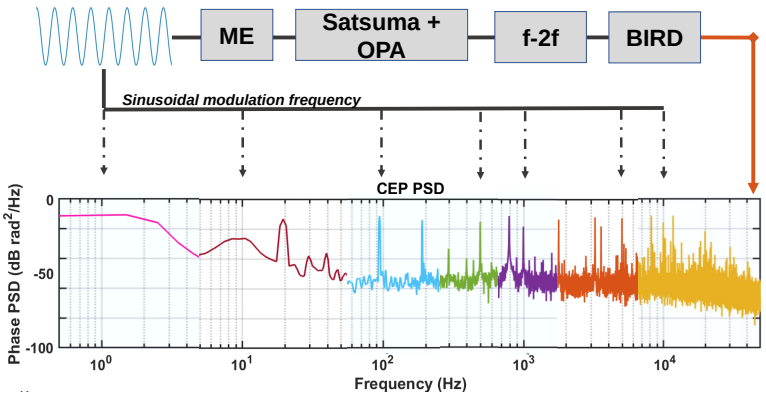


Figure IV.31 – BIRD measured CEP PSD for sinusoidal intensity modulation applied on ME efficiency at f=1 Hz, 10 Hz, 95 Hz, 500 Hz, 1 kHz, 5 kHz, 10 kHz.

The PSD is an overlap of the obtained PSDs plotted in a certain bandwidth around each modulation frequency. The peaks due to the modulations are clearly visible for modulation frequencies higher than 95 Hz. For the cases 1 Hz and 10 Hz, there is still a distinguishable contribution but it is no more the expected peak. This can be explained by the fact that all PSDs are calculated in the same time interval and same sampling rate. This results in a constant frequency step, that is not small enough to resolve peaks at very low frequencies. We can also notice that the peak height is comparable for all the frequencies in the limits of the measurement accuracy. As expected, the transfer is not dependent on the frequency.
We would now like to quantitatively measure the impact of the amplitude modulation on the system CEP stability in our pump laser operation conditions. Because of the low accuracy of the BIRD measurement we decide to use a spectrometer detection for this measurement. The idea is to apply a low frequency modulation on the ME efficiency and measure the fringe patterns with a high integration time. In this way, only the low frequency modulation of the CEP is measured and the higher noise contributions are filtered out. We apply a sinusoidal modulation on ME efficiency corresponding to 1.2 % on the average power at f=50 Hz. We acquire with an integration time of 1 ms and a sampling rate of 3 ms. The resulting fringe pattern acquisitions are depicted in figure IV.32 (a). The calculated CEP phase has a fluctuation 1.67 rad/%, corresponding to a $\sigma_{CEP}$ = 550 mrad rms. This measurement reveals that our pump laser must have the lowest possible AN in order to minimize the CEP fluctuations. We have shown the impact of the AN on CEP stability in passively stabilized WLG seeded system. To our knowledge, no studies have reported on this impact.
We can, also, clearly observe that the phase perfectly replicates the applied sinusoidal function to the ME efficiency looking at IV.31. The ME efficiency can be an actuator of the CEP admitting the variation of the pump laser intensity is linearly transferred to the CEP. To verify this we make two other measurements. First, we apply a sinus with higher amplitude. We decide to have 4.6 % peak-to-peak on the pump laser average power. We change also the frequency reducing it to 25 Hz. The results are shown in figure IV.32 (b). We can see that the sinusoidal behavior is perfectly reproduced in the CEP. The $\sigma_{CEP}$=2.2 rad (equivalent to 1.3

rad/%), demonstrating the consistency with what we have measured in the lower amplitude case in IV.29(a).

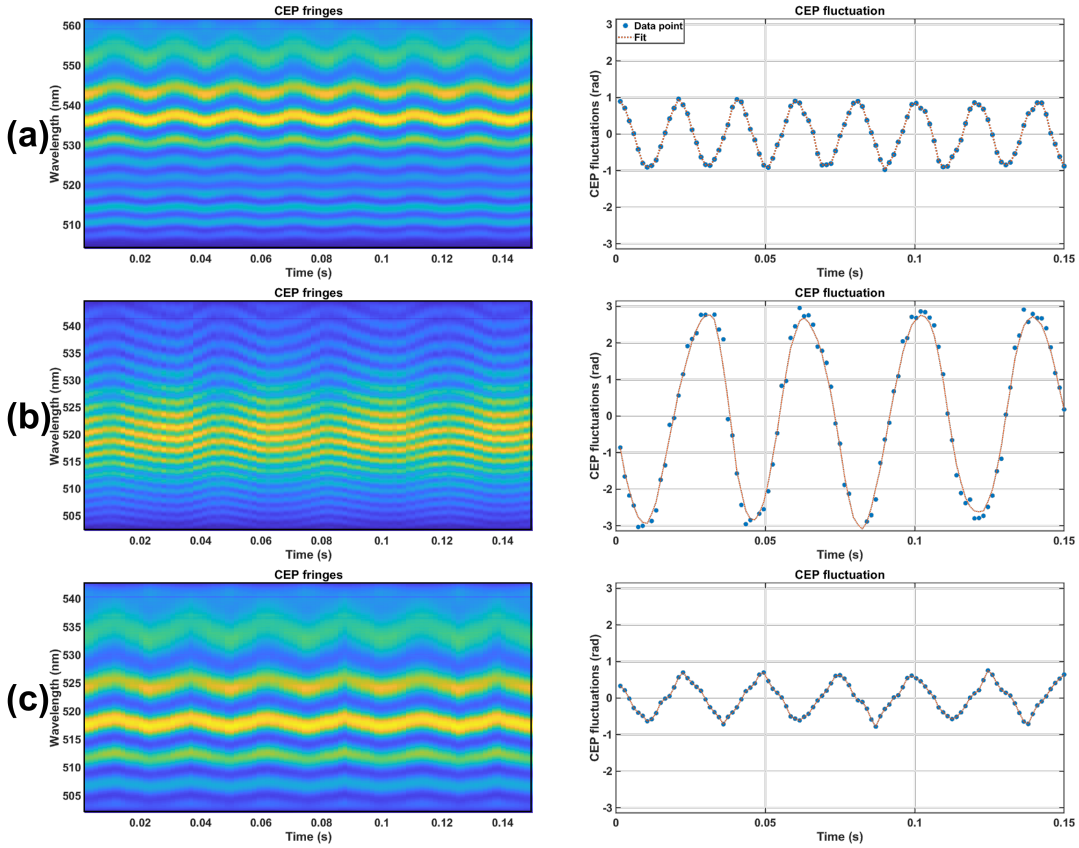


Figure IV.32 – Left: spectrometer acquired fringe patterns over 0.15 s. Right: calculated CEP via FTSI algorithm.

In figure IV.32(c) we finally show the spectrometer CEP measurement when a triangle function with the same amplitude and frequency than the sinus in (a) is applied to the ME efficiency input. Once again the CEP reproduces the intensity variations. The measured $\sigma_{CEP}$ is 450 mrad. We have demonstarted the linearity of the ME efficiency input enabling the use of this component of the pump laser as a CEP controller. It has to be stressed again that the considerations done are true only for the specific operation conditions found for our system.

## 5.3 CEP noise improvement

Let us consider what we have done to improve the pump laser RIN performances in section 4. We want to measure what impact this improvement has on the CEP noise. We therefor modify the pump laser PP from the asynchronous to the synchronous mode described in section 4. We know from the previous analysis that the RIN in the total BW is reduced by 30 %. We expect a CEP noise reduction of the same order of magnitude because of the linearity of the AN-PN transfer demonstrated in the last section. For the CEP measurements we use the Fringeezz as detection method. We realize the measurements with synchronous PP and asynchronous PP in the same day in order to be sure to have the same laser and environmental conditions. We first present in figure IV.33 the results of the Fringeezz detection for the two situations. The measurement is realized integrating over two pulses and sampling at 10 kHz. The $\sigma_{CEP}$ passes from 445 mrad to 300 mrad. This means a reduction of 32 %. We can say that the CEP noise has been linearly reduced with respect to the pump laser RIN as expected.

Analyzing the obtained CEP PSD we can appreciate that in the synchronous case there are

less peaks in the kHz range compared to the asynchronous one. This confirms what we have seen for the RIN measurements and that the improvement is due to an electronic optimization of the system.

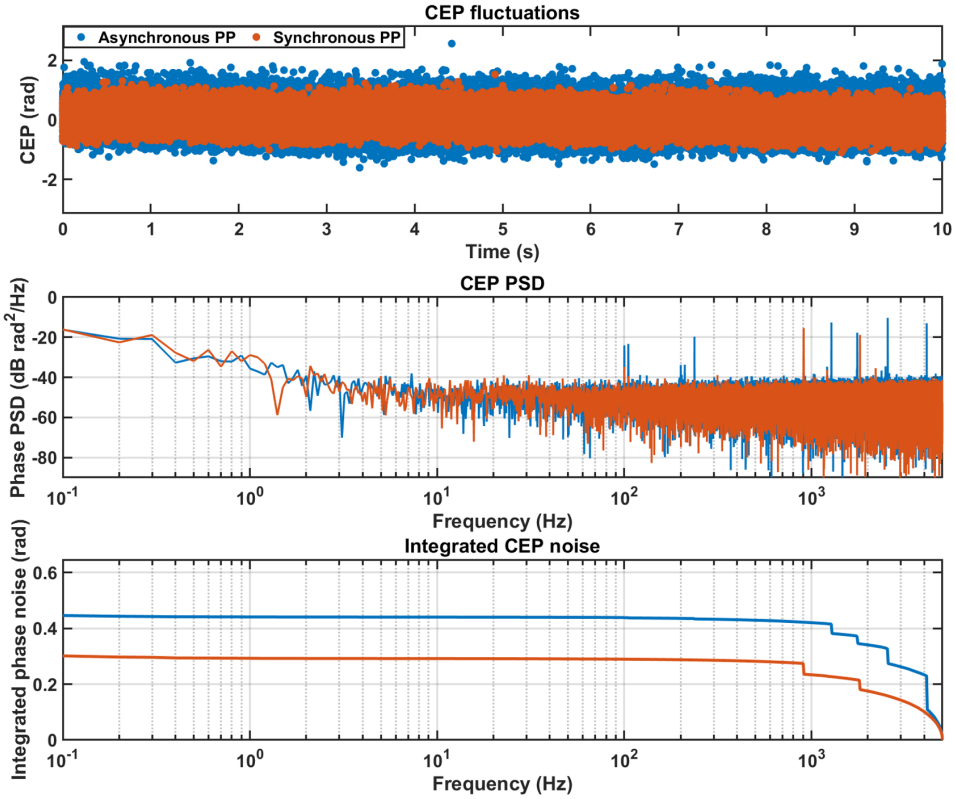


Figure IV.33 – Fringeezz CEP phase measuring, PSD and relative integrated noise for synchronous and asynchronous cases.

# 6 Conclusions

In this chapter we have presented the first part of our laser chain: the CEP-stable front-end. First, we have described theoretically the passive stabilization of the CEP and the difference with respect to the active stabilization for oscillators. We have presented the setup delivering up to 430 nJ at 100 kHz, 200 fs long pulses at 1030 nm. The difficulties of properly measuring the CEP at high repetition rate are depicted. A CEP complete characterization using three different techniques has allowed us to understand that the presented system has less than 470 mrad on short time scale on single shot measurement. This value may appear quite high compared to the low energy laser that are actively CEP stabilized. Two points are interesting in the evaluation of this value in the comparison. First, all the measurements we have realized were limited by the maximum output energy of the OPA. The WLG input energy for the f-2f measurement has to be very carefully chosen in order not to add noises in the measurement. What we measure includes the fluctuation of our f-2f interferometer and constitutes an upper bound of the real source CEP noise. In the future a low energy optimized f-2f with a WLG in a PCF fiber will be realized. Second, in the actively stabilized oscillators the measurement is integrated in a determined BW. For example Koke et al. [Koke *et al.* , 2010] measure 45 mrad on a BW [0.5 Hz; 2.5 MHz] on an oscillator with $f_{rep}$=90 MHz integrating over around 30 pulses. For a larger BW in a 35 minutes measurement they find 570 mrad. These considerations contextualize the presented front-end as suitable as seeder for an application ready source. We have also highlighted the importance of the RIN performances of the pump laser. The AN-PN noise transfer happening in the WLG is shown to be the crucial element for the output CEP. We have shown, that the RIN improvement of the pump laser has lowered linearly the $\sigma_{CEP}$ to 300 mrad.
The optimization of the pump laser AN performances will be one of the strategies for lowering the CEP noise. On the other hand the mechanical stability and robustness of the industrially designed OPA has allowed to show negligible low frequency noise.
We can conclude saying that for this passive CEP-stable system, there are three knobs to be optimized for reaching the best performances: the WLG operation conditions, the pump laser RIN and the mechanical stability of the interferometer. The OPA pumping condition have to be taken into account in order to use the saturation to reduce the pump laser AN.
The described system can be operated at repetition rate ranging from 100 kHz to 500 kHz simply changing the ME operation condition. Our choice to operate at 100 kHz is linked to the difficulty of the CEP single shot measurement at repetition rate higher than 100 kHz.
A CEP-stable seeder at 2$\mu$m emission wavelength can be obtained using the same setup we have described. This is possible eliminating the SHG on the idler of the OPA. Such a CEP-stable seeder can be used for example to seed Tm:based fiber amplifier[Neuhaus *et al.* , 2018]. The CEP-stability rms, before the SHG process, is two times lower than in the presented case.

# Chapter V

# CEP-stable Yb-doped fiber amplification

## Objectifs

In this chapter we make use of the presented CEP-stable front-end, in an Yb-doped fiber CPA scheme. We first introduce the application domain of an high repetition rate amplified source considering the state-of-the art sources. We discuss, in the second section, the difficulties of CEP managing and stabilization in amplified chains. We present in the third section, the realized setup. In the fourth section, we characterize the CEP noise of the system detailing the active feedback loop setup on the CEP. The transfer of the RIN of the seeder through the amplification scheme is finally described in section five.

## Contents

# 1 Context: amplified CEP-stable systems at high repetition rate

In the previous chapter we have introduced CEP-stable low energy lasers saying that one of the most important application domain is strong field physics (SFP). By definition, we talk about of SFP for light-matter interactions involving intensities of $10^{13} - 10^{18}$ $\frac{W}{cm^2}$ [Brabec & Kapteyn, 2008]. The low energy lasers are used as seeder for amplification chains allowing to reach the high energy required. In the last 30 years ultrafast laser technology developments have allowed to shorten the pulse duration to only few-cycles regimes. In these conditions the phase control of the electric field acquires a crucial importance.
The most used laser technology for CEP-stable laser chains for SFP is Ti:S based amplification [Klein & Kafka, 2010, Brabec & Krausz, 2000]. These sources exploit the CPA technique [Strickland & Mourou, 1985] for delivering high peak power short pulses. They can deliver mJ energies at repetition rate ranging from some Hz up to 10 kHz.
Several applications appeared in the last years, pushing this repetition rate limit [Weger *et al.* , 2013, Rothhardt *et al.* , 2016]. In coincidence ion-electrons experiments, for example, higher repetition rates improve the statistics and reduce dramatically the acquisition time [Hädrich *et al.* , 2015]. For repetition rates above 10 kHz high energy Ti:S lasers become extremely costly and complicated. The main reason is that the high average power comes with thermal problems, precluding the realization of the application required sources. The solution for driving high repetition rate SFP experiments is OPCPA [Wolter *et al.* , 2015, Huang *et al.* , 2011, Chalus *et al.* , 2009]. This kind of systems has several advantages such as the very broad emission spectrum in a wide range of central wavelengths [Puppin *et al.* , 2015, Rigaud *et al.* , 2016]. Several CEP-stable OPCPAs have been reported in last years and repetition rate systems up to the MHz range have been demonstrated [Rothhardt *et al.* , 2012]. Despite the advantages, because of the low conversion efficiency (less than 30 %) these systems require very energetic pumping lasers.
Yb-doped fiber lasers are an appealing alternative answering to the applications needs. Laser energy of the order of 1 mJ , with pulses of 260 fs and repetition rate of 1 MHz at 1030 nm have been reported [Müller *et al.* , 2016]. Post-compression techniques applied to this technology has enabled the pulse reduction towards few-cycles pulse regime [Lavenu *et al.* , 2017, Hädrich *et al.* , 2011, Lavenu *et al.* , 2019]. Nevertheless, the CEP stabilization of this kind of sources is the missing feature for opening the road for competing with OPCPAs. Only two works have shown CEP-stable high average power lasers based on Yb technology [Balčiūnas *et al.* , 2014, Saule *et al.* , 2017]. In the first case, Balciunas et al. [Balčiūnas *et al.* , 2014] present a Yb-KGW oscillator amplified in a regenerative amplifier in a CPA scheme. In the second one, an Yb-doped fiber amplifier seeded by a Ti:S oscillator is used. In this chapter we will describe the CEP-stabilization of our CPA YDFA scheme seeded by the front-end presented in the chapter IV. The amplifier is followed by a nonlinear post-compression stage. The revealed CEP-stability performances trace the road for a new generation of laser drivers for high repetition rate SFP.

# 2 Background: stabilization of CEP in amplifiers

In this section we discuss the problems related to CEP-stable pulse amplification. In the first part the CPA scheme issues to manage for a CEP-stability preservation are described. In the second section the feedback loop principles for high repetition rate amplified chains are discussed.

## 2.1 CEP-stability in CPA laser chains

The CPA, as explained in chapter II, consists of a stretcher, an amplifier and a compressor. Each of these three elements can act on CEP-stability adding noises degrading the seeder one. Before discussing in details each of them, it is useful to consider a CEP noise PSD similarly to the ones we have shown in the previous chapter. We can distinguish three different noise classes depending on the frequency. Let us have a look at table V.1.

| **CEP noise sources in CPA** | | |
|---|---|---|
| **Noise class** | **Noise frequency** | **Element affected by the noise** |
| ***Slow fluctuations*** | [0 Hz; 10 Hz] | Environmental changes (temperature drifts, humidity) on the beam pointing in compressor and stretcher pathway . |
| ***Acoustic noises*** | [10 Hz ; 1 kHz] | Vibrations on mechanical mounts in compressor and stretcher. |
| ***Electronic noises*** | [0 Hz; MHz] | Pump laser drivers and electronics elements |

Table V.1 – CEP noise sources and affected elements in CPA.

The CEP noise PSD measured after the amplifier provides a fingerprint of the noises sources introduced in the CPA chain. For each noise class, a different element in the CPA is involved. Different solutions can be adopted for noise reduction depending not only on the frequency range but also on the component causing it.
In a simplified analysis, the slow fluctuations come from the environment generating a beam pointing instability inside stretcher and compressor. The acoustic noises are affecting the large elements managing the dispersion in stretcher and compressor. Finally, the electronic noises can come from the pump laser of the amplifier. Moreover, electronic noise can be already present in the seeding signal as we have seen in the previous chapter. This class of noise can be present at any noise spectrum frequency. Something on the structure of the different noises has to be pointed out as well. The electronic noises and the acoustic ones appear as peaks in the PSD corresponding to a specific frequency as we have seen in the RIN PSD in chapters III and IV. The slow fluctuations normally appear, instead, as a continuous 1/f noise behavior. As we have already mentioned elsewhere, the CEP is sensitive to any change of dispersion. We have to consider that even a slight beam pointing displacement in a long propagation path means a different pathlength in air and in optical elements. For a laser at 1030 nm, only 80 $\mu$m of fused silica added in the optical pathway produce a CEP shift of $\pi$, as we have seen in the last chapter.

### 2.1.1 CEP noise in stretchers and compressors

The CEP noise in stretchers and compressors depends on the type of the configuration chosen. These two steps in the CPA scheme are clearly the ones that influence the most the CEP because they introduce large amounts of geometrically dispersion. Let us focus on the most common case configuration: the grating pair. In particular, a double pass configuration is considered. In figure V.1 we can see respectively in (a), (b) and (c) the fluctuations of the entrance beam pointing, the fluctuation of the grating angle and the fluctuation of distance between gratings.

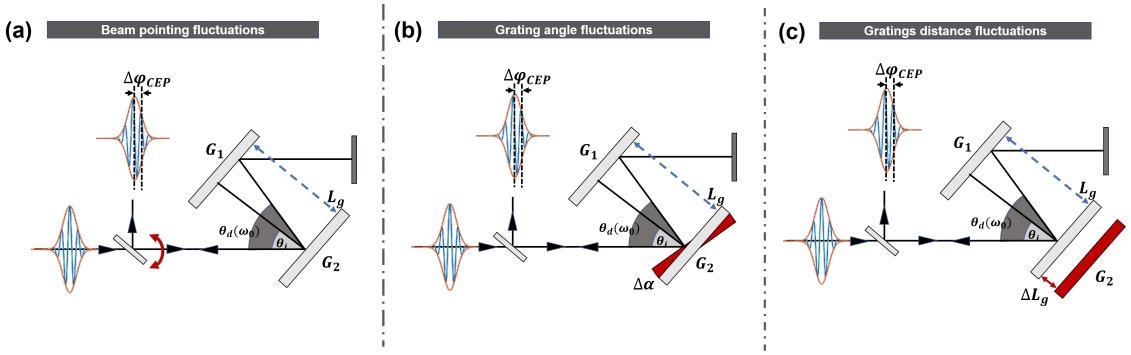


Figure V.1 – Scheme of the CEP impact elements on the grating pair: (a) beam pointing fluctuations; (b) grating angle fluctuations; (c) gratings distance fluctuation.

For each situation depicted in figure V.1 we can see that the output pulse would have experienced a CEP shift $\Delta\varphi_{CEP}$ per passage. For the case in figure V.1(a) [Kakehata *et al.* , 2002]:

$$\Delta\varphi_{CEP} = 2\pi\frac{L_g}{a}\frac{cos(\theta_i)}{cos(\theta_d(\omega_0))}[1 + tan^2(\theta_d(\omega_0))]\boldsymbol{\Delta}\gamma, \tag{V.1}$$

where $L_g$ is the grating distance, $a$ is the grating period, $\theta_i$ is the incidence angle on the grating, $\theta_d(\omega_0)$ is the diffraction angle for an angular frequency $\omega_0$ and $\Delta\gamma$ is the fluctuation of the beam pointing. Let us consider a situation that will be meaningful for the setup we will present in the next section of this chapter. We consider a grating with a=1750 lines/mm, $\theta_i$=66 degree for a central wavelength of 1030 nm, and a distance of 30 cm between the gratings. The $\Delta\varphi_{CEP}$ is about 100 rad for a beam pointing displacement of only 50 $\mu$rad. The CEP noise added is enormous. This is true for a single pass configuration. In the double pass grating pair, the added CEP noise by the displacement of the first pass is corrected by the second one [Kakehata *et al.* , 2002], as can be seen in figure V.2(a) where the added CEP for each pass is shown respectively in blue and red for the first and second pass. Only a very low residual phase shift of 190 mrad to the beam pointing remains at the compressor output for 50 $\mu$rad of entrance beam depointing as can be seen in yellow in the same figure. The input beam displacement, results in a change in the incidence angle and consequently of the diffraction one. The case of grating fluctuation depicted in V.1 (b) is, for this reason, easily comparable to the one of the single pass grating pair with a beam displacement. The added CEP is given by:

$$\Delta\varphi_{CEP} = 4 * 2\pi\frac{L_g}{a}cos(\theta_i)[1 + tan^2(\theta_d(\omega_0))]\boldsymbol{\Delta}\alpha, \tag{V.2}$$

where $\Delta\alpha$ is the fluctuation of grating $G1$ as shown in figure V.1(b). The CEP noise degradation is higher with respect to the above discussed case. The obtained CEP shift per pass are depicted in V.2(b). It can be seen that the CEP shift compensates between first and second pass in the same way it was for the case (a). The order of magnitude of fluctuation is about ten times larger than in the first case. This means that the low residual phase shift is larger proportionally too.

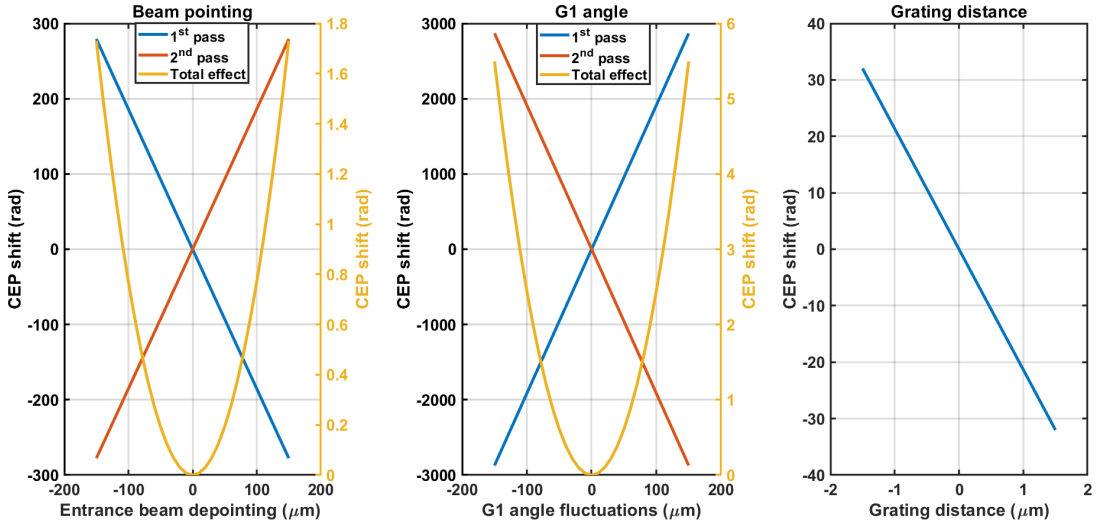


Figure V.2 – Effect of the single pass and double pass grating pair compressor on the CEP noise.

The CEP shift per pass due to a variation of the distance between the gratings is finally calculated as [Chang, 2006]:

$$\Delta\varphi_{CEP} = 2\pi\frac{\mathbf{\Delta L_g}}{a}(tan(\theta_d(\omega_0))), \tag{V.3}$$

where $\Delta L_g$ is the fluctuation between the gratings $G1$ and $G2$ as shown in figure V.1(c). The double pass case is depicted in V.2(c) where the CEP shift of equation (V.3) is multiplied by 2. The change in distance between the gratings is the dominant effect because it is the only one that it is not corrected by the second passage. In particular, if we consider a displacement of one of the grating with respect to the other of the order of the wavelength, a CEP shift of 20 rad occurs. For this reason, we need to reduce as much as possible the impact of vibrations on the gratings. In the next section we will present the CPA setup. We will use a *Chirped Fiber Bragg Grating* (CFBG) as a stretcher and a grating pair free space compressor. We can neglect the impact of the CFBG considering it as a stretcher where the beam displacement due to the environmental conditions is negligible. The compressor, instead, adds noise in the CPA chain as we have presented in this section. We will cover in the following the strategies we have chosen in our setup to reduce and correct the compressor impact on the output CEP noise.

### 2.1.2 Pump intensity noise transfer

Pump intensity noises are transferred to the amplified signal. The situation is strictly linked to what we have discussed in the case of the RIN to CEP noise transfer in the last chapter. Let us assume that our pump laser for the amplifier has a RIN PSD, for example, evidencing a peak at some kHz due to an electronic component. This peak is transferred to the CEP noise if an high AN-PN coupling effect is involved in the amplification. In the previous treatment we have said that in the FE the transfer occurs in the WLG because of the SPM. A nonlinear effect depending on the intensity is involved in the AN-PN coupling. In the case of the amplifier medium we can recall that the B integral accumulated through the medium of length L is $B = \frac{2\pi}{\lambda n_0}\int_0^L n_2 I dz$. In amplifiers, the B integral is usually kept of the order of some radians for fiber amplifier. The propagation length for a CEP shift of $2\pi$ is defined as $L_{2\pi,Kerr} = \frac{1}{\frac{d\Delta n}{d\lambda}} = \frac{1}{\frac{dnI}{d\lambda}}$. For simplicity we consider the intensity $I$ constant along the amplifier medium length $L$. We can write [Kakehata *et al.* , 2002]:

$$\Delta\varphi_{CEP} = \frac{\lambda n_0}{n_2}\frac{dn_2}{d\lambda}B. \tag{V.4}$$

As an example we can take fused silica as material where the refractive index change happens and the $n_2$ and $\frac{dn_2}{d\lambda}$ calculated for the case with $\lambda$=800 nm [Kakehata *et al.* , 2002]. We expect that the values are meaningful also for a rough estimation at $\lambda$=1030 nm. The resulting $\Delta\varphi_{CEP} = -0.49$ rad is for a $\lambda = 1030$ nm and a B=1. Taking, as an example, a pump laser fluctuation of 1 % rms, we obtain that the induced fluctuation of the CEP is less than 5 mrad. If the amplifier is not in a highly non-linear regime, the pump noise added through SPM in the amplifier is negligible with respect to the contributions we have analyzed for the stretcher and compressor. In a more general view, we will see that our setup relies on several amplification stages. Each step can have an impact on the output amplified CEP noise. Moreover we have to stress that the seeder intensity noise can also be transferred to the CEP if a highly nonlinear effect is involved. In the last section of the chapter the RIN to CEP transfer along the amplification chain will be studied for these reasons.

## 2.2 Amplifier CEP-noise feedback loop techniques

We need to correct the CEP noise accumulated in the CPA scheme. In particular we expect to have acoustic and environmental noise to be corrected. This requires the implementation of a feedback loop acting until frequency of around few kHz. In order to do this, we need a sufficiently fast detection and actuator. The different detection techniques for the CEP have been discussed in the last chapter evidencing the pros and cons of each of them. For the actuators in the case of amplified systems, several possibilities can be found in the literature.

### 2.2.1 CEP actuators for CPA chains

As we have already found in the oscillator feedback cases, the first approach is to correct the CEP drifts acting on the elements introducing the CEP noise. In this sense, Li et al. [Li *et al.* , 2008] use a piezoelectric motor on one grating in a compressor to actively change the grating distance. They obtain 230 mrad in-loop measured closed loop CEP noise. The limit of this approach is that the cutoff frequency of the feedback is only 60 Hz. Wang et al. [Wang *et al.* , 2010], instead, make use of a spatial light modulator (SLM) in a 4-f stretcher for directly acting on the phase. They shows 173 mrad of measured CEP noise over some minutes in closed-loop. Also in this case, the feedback actuation frequency is very low. For fast correction of the CEP drift, a dedicated actuator have to be introduced. An excellent example is to use an Acousto-optic programmable dispersive filter (AOPDF) [Tournois, 1997]. This element acts directly on the phase CEP using a feedback dependent RF wave. With this technique feedback loops acting on kHz range have been shown [Lücking, 2014], measuring lower than 100 mrad rms fluctuations over 50 s.

### 2.2.2 *Electro-optic modulator* (EOM) as CEP actuator

We decide to use a different tool to act on the CEP for the feedback loop: an EOM [Feng *et al.* , 2013]. It is interesting to analyze how the CEP is changed passing through this actively driven component. In the simplest description, an EOM is a crystal experiencing a change of the refractive index when we apply a voltage V on it. Considering the EOM we will use we can focus on $LiNbO_3$ crystals and study the Pockels effect for the phase and CEP modulations [Saleh *et al.* , 1991]. Let us consider the transverse case, where a plane wave is transmitted through a crystal of length $L$ and thickness d. A voltage V is applied along d. The refractive index of the material is modified by the applied electric field $E = V\Gamma/d$, where $\Gamma$ is a term taking into account the real voltage passing through the crystal with respect to the

applied one. We can write that the refractive index is modified as follows:

$$n(E) \approx n - \frac{1}{2} r n^3 E, \tag{V.5}$$

where $r$ is a generic coefficient indicating the change due to the Pockels effect in the crystal permeability tensor. In particular, for each polarization axes, we have:

$$n_o(E) \approx n_o - \frac{1}{2} r_{13} n_o^3 E, \tag{V.6}$$

$$n_e(E) \approx n_e - \frac{1}{2} r_{33} n_e^3 E. \tag{V.7}$$

It is common to refer to a voltage value $V_\pi$ such that the phase at the output of the EOM is defined as:

$$\varphi = \varphi_0 - \pi \frac{V(t)}{V_\pi}, \tag{V.8}$$

where $\varphi_0 = \frac{2\pi n L}{\lambda}$ and:

$$V_\pi = \frac{d}{L} \frac{\lambda}{r n^3}. \tag{V.9}$$

The phase shift of $\pi$ does not correspond to a CEP shift of $\pi$. We need to introduce a $V_{\pi,CEP}$ that indicate the voltage required for a CEP shift of $\pi$. The effect is due to the difference between the propagation of the group and phase velocities through the crystal and it has been studied by Gobert et al. [Gobert *et al.* , 2011]:

$$\Delta\varphi_{CEP} \approx 2\pi \left[ \frac{3}{2} n_e^2(\lambda) r_{33}(\lambda) \frac{\partial n_e}{\partial \lambda}(\lambda) + \frac{n_e^2(\lambda)}{2} \frac{\partial r_{33}}{\partial \lambda}(\lambda) \right] LE, \tag{V.10}$$

where $\lambda$ is the laser central wavelength. To find $V_{\pi,CEP}$, we can put $\Delta\varphi_{CEP} = \pi$ in equation (V.10) and considering (V.9), we find:

$$V_{\pi,CEP} = \frac{n_e r_{33}}{\lambda} \frac{1}{\left( r_{33} \frac{\partial n_e}{\partial \lambda}(\lambda) + n_e \frac{\partial r_{33}}{\partial \lambda}(\lambda) \right)} V_\pi. \tag{V.11}$$

It is interesting to make a numerical estimation of the ratio $V_\pi / V_{\pi,CEP}$ in order to have an idea of the difference between the two effects in a quantitative way. We consider a laser centered at 1030 nm. For $r_{33} = 32.2$ pm/V, $\frac{\partial n_e}{\partial \lambda} = -0.0565\ \mu m^{-1}$, $\frac{\partial r_{33}}{\partial \lambda} = -2$ pm/V/$\mu$m, $n_e = 2.1574$, we have:

$$\frac{V_\pi}{V_{\pi,CEP}} = 0.145. \tag{V.12}$$

We have to point out that this is only a rough estimation of the $V_{\pi,CEP}$, because $\frac{\partial r_{33}}{\partial \lambda}$ is known with an high incertitude degree depending on specific measurement conditions. Even though, this result is particularly useful considering our scopes. The $V_\pi$ is indicated in commercial EOM data-sheets. In the following, we will see in detail our setup case where we use a fiber $LiNbO_3$ EOM.

# 3 Setup of the amplification chain

In this section we discuss the setup of our CPA scheme. The setup is composed of three main parts: the amplifier front-end, the YDFA, and the post-compression *multi-pass cell* (MPC).

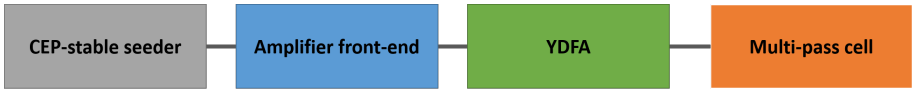


Figure V.3 – Scheme of the elements in the laser chain.

In the next sections, each element of the setup is extensively discussed.

## 3.1 Amplifier Front-End

We define as the amplifier front-end the optical setup just after the CEP-stable seeder. This setup is used for providing the seeder necessary for the YDFA. The setup is depicted in figure V.4.

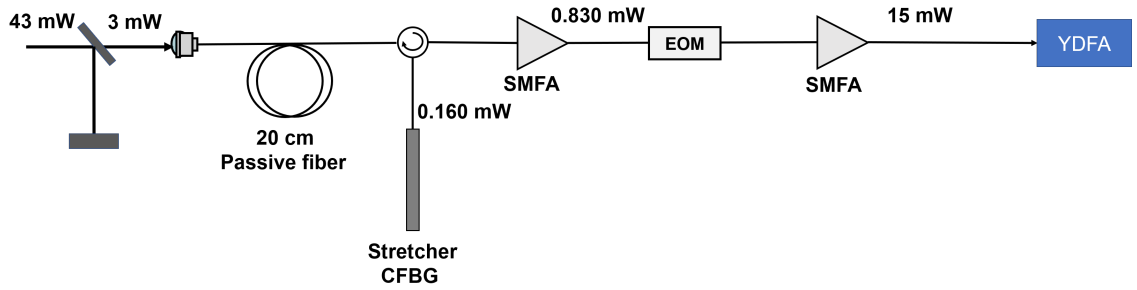


Figure V.4 – Setup of the amplifier front end. CFBG: Chirped Fiber Bragg Grating; SMFA: Single-mode fiber amplifier; EOM: Electro-optic modulator.

A small fraction of the OPA output is injected in the fiber FE to be amplified. The reason is that, as we have seen, the pulses at the OPA output are 200 fs long, with an energy of 400 nJ. The nonlinear effects generated in the fiber are dramatic because of the high intensity corresponding to these parameters. We use only 3 mW average power, at 100 kHz repetition rate. It is important to stress that even in this case, the first part of the front-end before the CFBG can be critically nonlinear because of the high peak power. This means that the CEP-seeder RIN is transferred to the CEP in this part of the FE, as we will see in section 5. The CFBG stretches the original pulse of around 200 fs to 300 ps. The CFBG is designed to match the second and third order dispersion of the compressor. After the fiber stretcher, the pulse is amplified using two step of *single mode fiber amplifiers* (SMFA) providing about 15 mW of amplified signal. Between the two amplifiers an integrated $LiNbO_3$ EOM is placed. It is used as CEP actuator as we already mentioned, and will be described in more details later on.

## 3.2 YDFA

The 15 mW stretched pulses are amplified using a rod-type fiber amplifier. This particular type of fiber has been introduced in chapter II. The signal is amplified to 4.6 W, altough this amplifier can be used for higher output power. The choice we have made here is to have a proof-of-principle system for the analysis of the CEP impact. A free space compressor is used for the compression. A 1750 lines/mm transmission grating is used in a four pass configuration.
As we have seen in the last section, the compressor setup must be designed very carefully to reduce the added CEP noise. We need to avoid mounts vibrations in the acoustic range

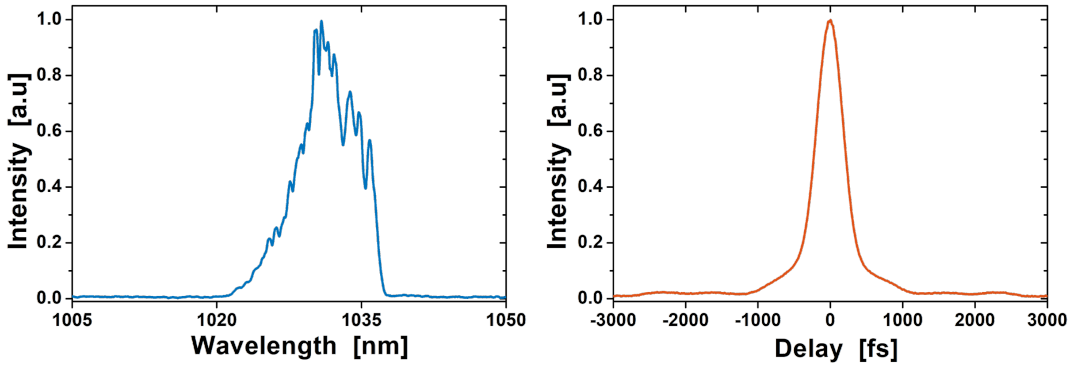


Figure V.5 – Left: spectrum of the compressor output. Right: autocorrelation trace of the compressor output.

and slow fluctuations. The slow frequency vibrations come from the optical table where the compressor stands. To avoid the transfer to the compressor mounts, we place our mounts on a heavy aluminum plate connected to the optical table by Sorbothane feets (*AV4*, Thorlabs) dumping vibrations. To reduce the impact of the acoustic range vibrations on the compressor elements, a double enclosure system is set up.
At the compressor output 3.3 W of average power is available. The spectrum and the autocorrelation trace are shown figure V.5 .

The spectrum is 16 nm-wide at 10 dB width. It is cut on the long wavelength side. This is due to clipping on one of the compressor mount. The corresponding pulse width is measured to be 350 fs at FWHM considering a Gaussian fit as shown in figure V.5

## 3.3 Multi-pass cell (MPC)

We have said that post-compression is a key element for reaching very short pulse durations. Essentially this stage consists in broadening the spectrum at the compressor output via SPM. The problem is that strong SPM effects in free space inevitably leads to beam profile distortion. Several techniques have been proposed to realize this broadening in the last decades. The most used is a gas-filled hollow core fiber [Chen *et al.* , 2011]. The CEP fluctuations induced by this type of post-compression stage have been studied by Lucking et al. [Lücking *et al.* , 2014a, Lücking *et al.* , 2014b].

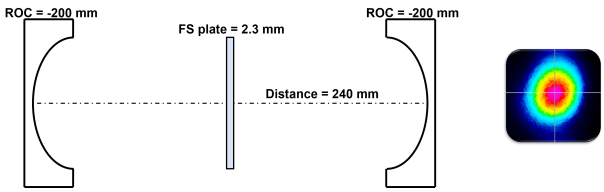


Figure V.6 – Left: scheme of the MPC setup. Right: beam profile at the MPC output.

We decide to use a different post-compression approach: the multi-pass cell [Weitenberg *et al.* , 2017a, Weitenberg *et al.* , 2017b, Schulte *et al.* , 2016]. This choice is due to the relatively low energies of our system. The idea is to make SPM broadening in a bulk transparent medium. If we directly focus the beam in a thick bulk material, SPM comes with the spatial deformation of the beam profile. To avoid this, the beam pass several times in a thin piece of nonlinear responding material (typically fused silica) to make small amounts of B-integral per pass. In this way at the output of the cell, the spectrum is broadened and the beam profile is preserved. The cell has to be designed considering the entrance energy and

the desired spectral broadening at the output. The setup we have used to broaden the about 30 $\mu$J energy pulse is depicted in figure V.6 on the left. We use two concave mirrors with radius of curvature of 200 mm arranged in a Herriott cell configuration. A 2.4 mm thick fused silica plate is placed in the middle of the cell. With this configuration we realize 30 passes in the fused silica plate accumulating a total B-integral of about 4 rad. The beam size of the compressor output is matched to have the stationary beam inside the cell. The beam profile measured using a CCD camera is shown on the right in figure V.6, showing a Gaussian profile without distortion due to the nonlinearity.

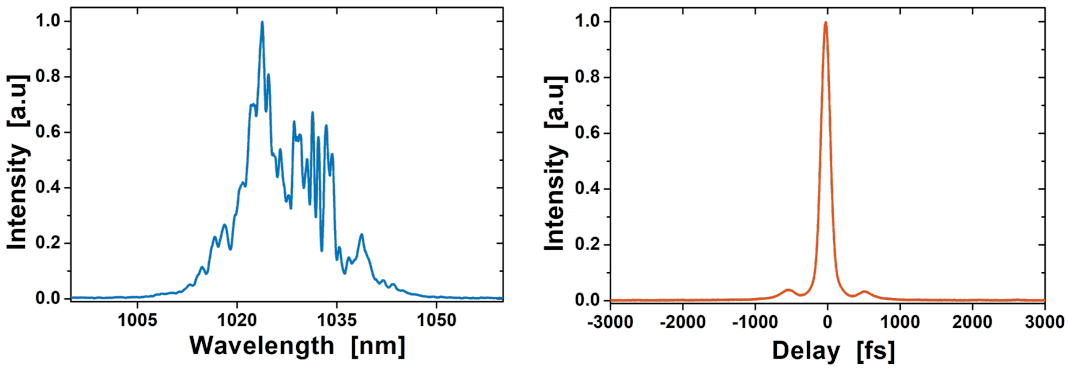


Figure V.7 – Left: spectrum measured at MPC output. Right: autocorrelation trace measured at MPC output.

The broadened spectrum is shown in figure V.7. In comparison with the compressor output, the spectrum width has increased from 16 nm to 45 nm measured at -10 dB width. We use two chirped mirrors to compress the pulse after the MPC spectral broadening. We realize four bounces on -1200 $fs^2$ dispersive mirrors. The obtained autocorrelation trace is shown in figure V.7 on the right. The pulse duration at FWHM considering a Gaussian fit is 95 fs. The transmission of the MPC plus chirped mirrors is 90 %, giving 2.95 W of average power available at the output.
The pulse duration shortening we have realized using the MPC has two main motivations. The first, as already anticipated, is to test the CEP-stable compatibility of such a post-compression system. The second one is linked to the CEP measurement. The WLG coherence is very sensitive to the pulse duration [Calendron *et al.* , 2015] especially in bulk media. For this reason we cannot realize a CEP f-2f measurement directly at the compressed YDFA output.

# 4 CEP characterization and feedback

In this section we present the CEP characterization of the amplified and post-compressed system. We discuss the feedback choices and the CEP characterization made using the three detection techniques. Finally a comparison between two detection techniques on the feedback is analyzed.

## 4.1 Free-running and feedback setup

The CEP measurement and detection techniques are the same as the ones presented in chapter IV. The difference in this case is that we are not limited by the energy we can use for the WLG in the f-2f interferometer. We use about 1 $\mu$J for the WLG in a 3 mm thick YAG and we make the SHG in a 2 mm thick BBO crystal in type I phase matching configuration. As first measurement, we detect the CEP drift in free running using a highly integrating spectrometer in order to see only the very slow fluctuations. For this reason we detect using an integration time of 1 ms. The resulting measured CEP over 3 s is depicted in figure V.8.

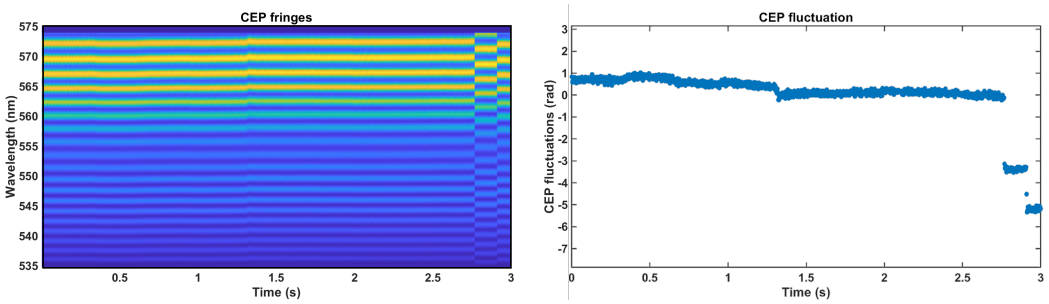


Figure V.8 – Left: Free-running CEP measurement fringe patterns over 3 s. Right: retrieved CEP.

The $\sigma_{CEP}$ is 1.25 rad over the 3 s. Analyzing figure V.8, two tendencies in the CEP behavior have to be pointed out. In the first about 2.5 s of acquisition time, a slow drift can clearly be seen. In the last 0.5 s of acquisition time, two phase jumps occur. These phase jumps are the more problematic for the CEP stability. It is something that we have not seen in the CEP-seeder analysis. This means that it is coming from the amplification chain.
We want to set up a feedback loop able to correct the slow drift and the phase jumps, maintaining the CEP at a constant value. As a first step, we want to verify our actuator. We have calculated in the first section the relation between the manufacturer specified $V_\pi$ and the $V_{\pi,CEP}$. We use an integrated $LiNbO_3$ with a specified $V_\pi = 2$ V. This means considering what we have said a $V_{\pi,CEP}$ of 14.3 V.

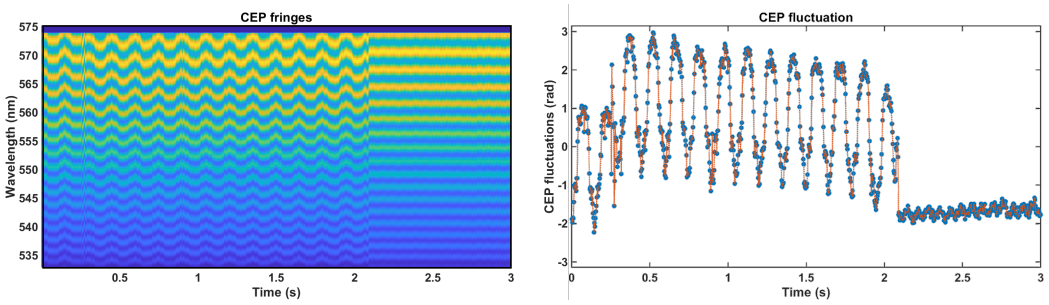


Figure V.9 – Left: Free-running CEP measurement fringe patterns over 3 s with an applied sinus modulated function at f=15 Hz and amplitude of 10V for the first 2 s. Right: retrieved CEP.

To experimentally measure this value, we realize a spectrometer measurement integrating over 100 pulses, and applying to the EOM a sinusoidal modulated voltage at 15 Hz frequency and 10 V peak-peak of amplitude. In figure V.9 the results are depicted. The sinus function is applied to the EOM only for the first 2 s of acquisition. In this way we can observe the difference between the modulated and the free running situation for the measured CEP. The measured peak-peak CEP in the modulated part is 3.64 rad. This means that the measured $V_{\pi,CEP} \approx 9$ V. The estimated and measured values therefore roughly match. It is interesting to see that the sinusoidal behavior is clearly visible in the fringe pattern and in the retrieved phase. This confirms the linear response of the EOM and its suitability as actuator.
For the feedback, we decide to detect the CEP using the Fringeezz. The spectrometer sampling rate is too low considering also the data processing required for the CEP measurement via computer. The Fringeezz, instead, has a dedicated output allowing to have a CEP dependent voltage signal without passing through the computer data processing.
To implement the feedback, we need a proper detection and actuation, as well an electronic support. We use a commercial digital PID (Laselock, *TEM Messtechnik*). Apart for the standard PID functionality, this tool has a particular function for correcting our phase jumps faster than the simple PID does. A "search and relock" functionality allows to automatically relock the error signal of the feedback at the error target when one of the error bounds is reached. In terms of CEP value, this means that each time a phase jump occurs, bringing the CEP value (and the Fringeezz measured error signal) outside the bounds, the search and relock automatically relocks the CEP to the original value. This commercial PID is specified for working at speed higher than our laser repetition rate. The feedback frequency limit will depend on the detection and on the optimization of the PID parameters [Åström & Hägglund, 1995].

## 4.2 Fringeezz feedback action

In figure V.10 the complete scheme of the setup, starting from the CEP-stable seeder to the MPC output and f-2f CEP measuring setup is shown.

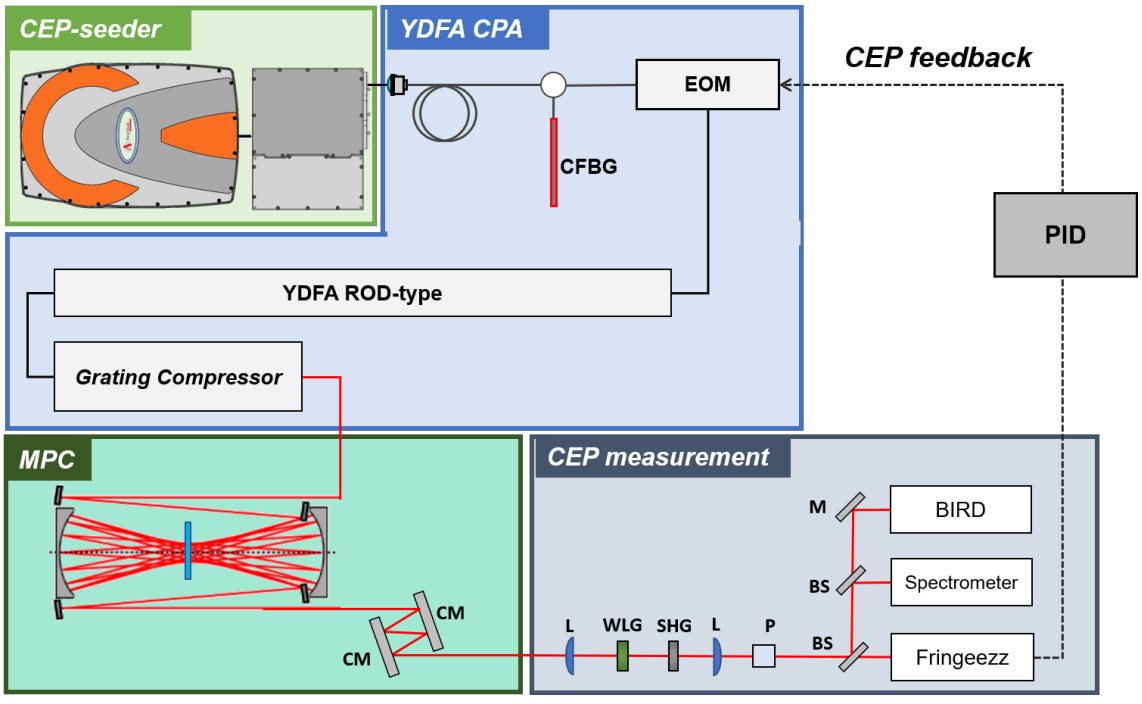


Figure V.10 – General scheme of the laser setup. CM: chirped mirrors; M: mirror; L: lens; BS: beam-splitter; P: polarizer cube.

Let us focus on the detection part. We can see that the in-line in-focus f-2f is used at the MPC output. A series of two beam-splitters allows to use the three detection instruments we have described in chapter IV at the same time. We measure the CEP noise signal for the feedback loop using the Fringeezz. The Fringeezz gives an output we can use as error signal for the feedback loop and at the same time, a measured CEP using the software. We optimize the PID parameters to reduce the rms CEP noise measured. After the optimization, we obtain the result in figure V.11. The CEP noise PSDs of the measurement realized with the Fringeezz in single-shot pulse integration and with 10 kHz repetition rate are shown over 10 s, in open and closed loop operations.

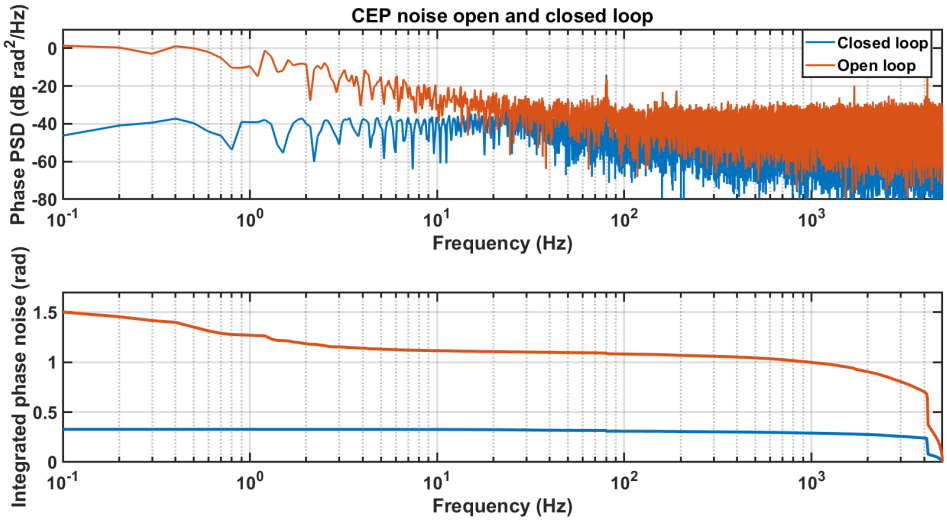


Figure V.11 – Top: Fringeezz measured CEP noise PSD in open (red) and closed loop (blue). Bottom: Fringeezz measured integrated CEP noise in open (red) and closed loop (blue).

The integrated CEP noise passes from 1.5 rad in open loop to 325 mrad in closed loop. Analyzing the open loop PSD and the related integrated behavior, we can refer to the spectrometer measurement shown in figure V.8 showing the CEP drift and the phase jumps. In the bandwidth [0.1 Hz; 1 Hz] we can see the impact of slow fluctuations. These contribute to about 0.4 rad of the total CEP noise. The remaining noise comes from the BW [1 KHz; 5 kHz]. In this frequency area we see a peak contributing to only 0.2 rad and a white noise. It is interesting to compare this result with the closed loop case. In the BW concerning the slow fluctuations, the PSD and the corresponding integrated noise are flat. The fluctuations are corrected by the feedback loop action. In the BW [1 kHz; 5 kHz], the peak is sensibly reduced passing from -5.3 dB to -15.99 dB of amplitude. The white noise is also attenuated. The feedback is acting on the whole detection BW. This is not astonishing if we think that the PID electronics is much faster than 10 kHz and the actuator has a 150 MHz bandwidth. The action of the feedback loop relies only on the parameters chosen for the PID. We can conclude that the feedback is well optimized and limited to the detection speed. In the remaining of this chapter, we will test another feedback loop using the BIRD instead of the Fringeezz as detection method.
It is interesting to evaluate the long-term stability of the feedback loop. For this, we use the Fringeezz on a single-shot integration at 10 kHz acquisition rate. We can save a large number of samples. The measured CEP noise in closed loop, corresponding to $\sigma_{CEP} = 375$ mrad over 66 minutes, is depicted in figure V.12. On the left, a density plot indicates the density of the CEP value calculated for each 1 s. This means that the false colors scale going from blue to red represents respectively from the less to the more recurrent value. On the right of figure V.12 an histogram considering all the counts is depicted. We can conclude that the feedback

loop and the whole system are stable in the long term time scale.

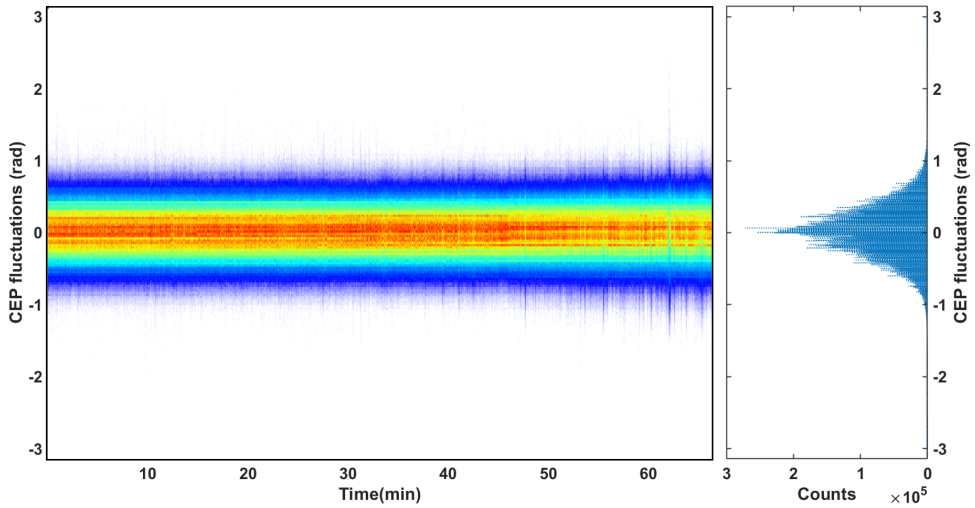


Figure V.12 – Long term CEP noise measurement using Fringeezz.

Let us have a look again at the general scheme depicted in figure V.10. In the feedback loop idea, the spectrometer and BIRD measurements can be considered as two out-of-loop measurements. As already said the BIRD allows to realize single-shot, every shot measurement at 100 kHz. The PSD and the integrated CEP noise over 1s are shown in figure V.13. The measured CEP noise in the BW [1 Hz; 50 kHz] closed loop is 325 mrad. This measurement confirms what we have obtained in the in-loop measurement.

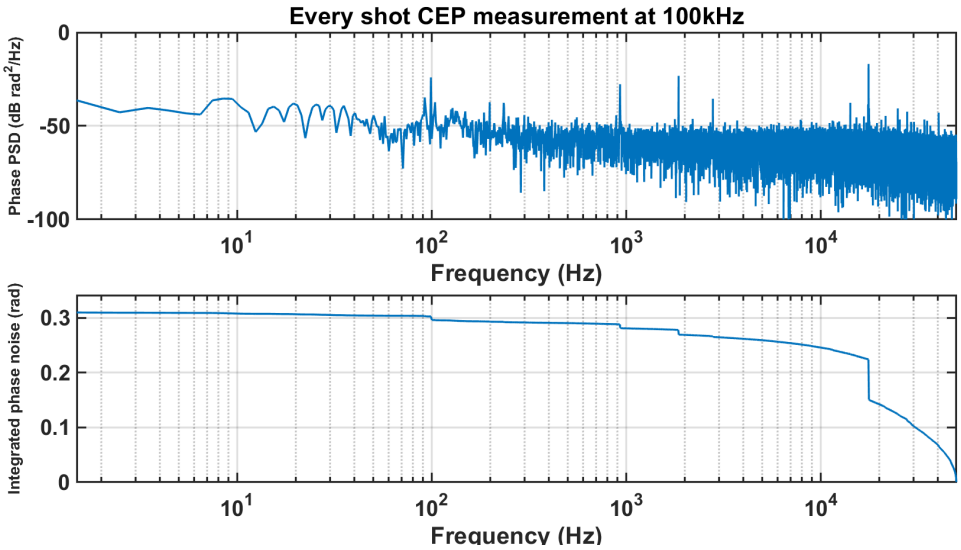


Figure V.13 – Top: PSD CEP measured by BIRD over 1 s. Bottom: integrated CEP noise.

We now use the spectrometer detection to validate further the Fringeezz and BIRD results.

## 4.3 Integration time in high repetition rate CEP measurements

We have discussed in the previous chapter the spectrometer detection issues linked to the sampling and integration time. Considering the stability of our system, it is relevant to systematically analyze the impact of this on the CEP noise measured and on the visibility of the

spectral fringes. We realize three measurements over 3 s using three different integration times: 30 $\mu$s, 100 $\mu$s and 1 ms. In figure V.14 the results are plotted. From the top to the bottom, each line refers to the integration of 100, 10 and 3 pulses. For each case, from left to right a fringe spectrum acquisition, the fringe pattern over 3 s, the retrieved phase and histogram distribution are shown.

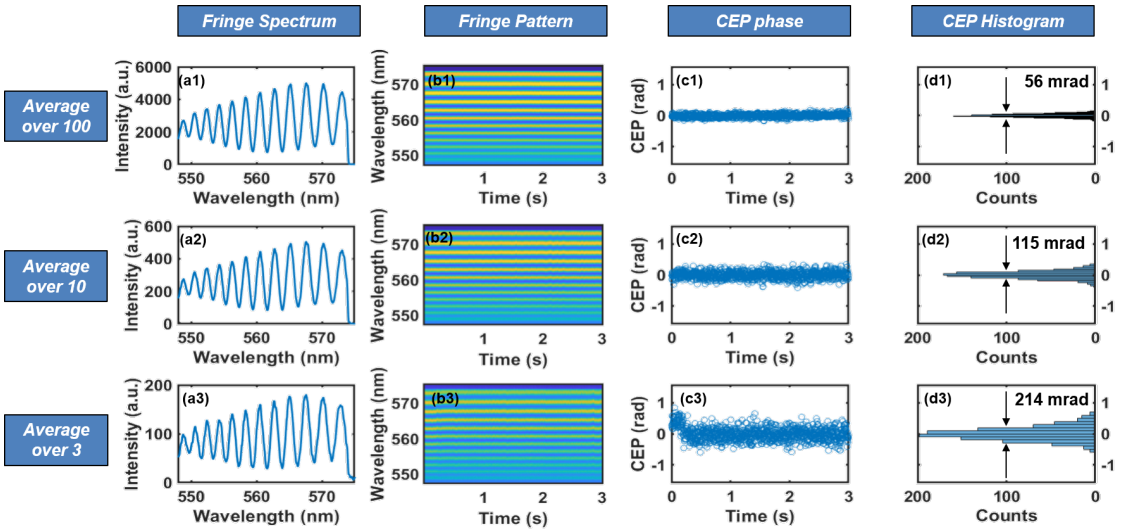


Figure V.14 – Out-of-loop f-2f spectral fringes measurement with a spectrometer. (a1-a3) Single acquisition of spectral fringes with integration times corresponding to 100, 10 and 3 pulses respectively. (b1-b3) Corresponding fringe pattern evolution as a function of time over 3 s. (c1-c3) Corresponding CEP drift as a function of time. (d1-d3) Histograms of CEP fluctuations.

The CEP noise rms is 56 mrad in the BW [0.3 Hz; 1 kHz]. It passes respectively to 115 mrad and 214 mrad in the BW [0.3 Hz; 10 kHz] and in [0.3 Hz; 33.3 kHz]. The noise degradation is clearly visible comparing the plots in (b1), (c1) and (d1) with (b2), (c2), (d2) and (b3), (c3), (d3) in figure V.14. Let us now consider the spectrometer acquisition at t=0 in (a1), (a2) and (a3). We can calculate the contrast in the three cases as we have explained in section 4.2. We obtain 0.68 for all three spectra. The contrast is not changing even though the CEP noise rms is sensibly degraded. This indicates that using the contrast change as analysis of the hidden CEP noise is not a valid method. In the previous section we have shown in figure V.13 the measured complete CEP noise PSD in closed loop using the BIRD. We can see which noise contribution is added passing from the case 1 to 2 and 3. Focusing on the difference between the BW [0.3 Hz; 1 kHz] to [0.3 Hz; 10 kHz] between 1 and 2 cases, we can observe that the added noise is white. The CEP rms ratio between the two situations is 2. We have said that if the hidden noise by integration is white the underestimation of the CEP rms is proportional to the $\sqrt{n}$, where $n$ is 10 in our case. Even in the white noise case, the estimation is not really accurate.
We can conclude that for high repetition rate lasers, integrated CEP spectral measurement are an underestimation of the total noise and contrast cannot be used as indication of the hidden noise.

## 4.4 BIRD feedback loop

We want to validate the result of the feedback loop changing the detection method. We have seen in the case of the feedback loop with the Fringeezz that our action works until 5 kHz. Using the BIRD allows to detect all the shots, meaning a $f_{sample}$= 100 kHz. To test the

feedback we have done with the Fringeezz, we use an electronic filter before the PID controller to have the same conditions. We use the same PID coefficient and we measure the out-of-loop CEP noise using the Fringeezz as it is shown in the scheme in figure V.15(a).

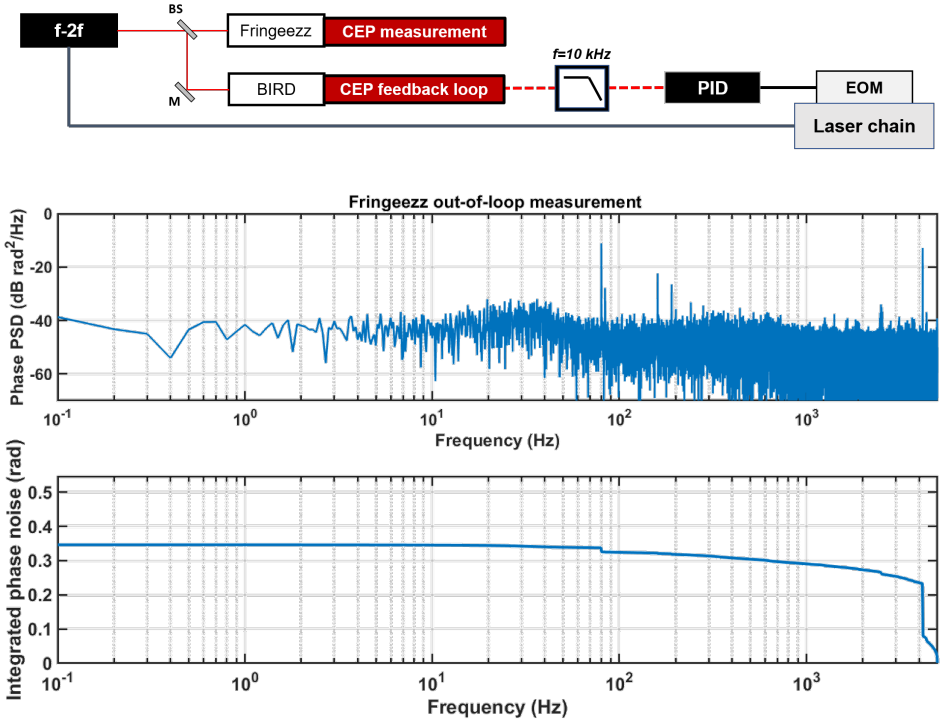


Figure V.15 – scheme of the detection and measurement

We show the results in closed loop for the PSD and integrated CEP noise in figure V.15(b). The Fringeezz measurement is realized over 10 s. The integrated noise obtained is the same we have found for the Fringeezz detection. The CEP PSD presents the same structure in figure V.11. The peak in the high frequency range is contributing to about half of the total CEP noise. It is the same we can see in the Fringeezz feedback loop. The BIRD feedback loop in these conditions has the same effects. This is a confirmation of the fact that the feedback is limited only by the detection speed. As a perspective, the PID parameters re-optimization can be used to obtain an higher bandwith feedback loop, without using the low-pass filter at the PID input.

# 5 RIN characterization

In this section we discuss the RIN characterization of the amplification chain. In the first part the propagation of the RIN from the CEP-seeder to the MPC output is analyzed. In the second part the impact on the CEP is studied.

## 5.1 RIN in the amplification chain

Let us analyze the scheme we have seen in figure V.4 and the general scheme in figure V.10. The RIN of the CEP-seeder is affected from several elements through the laser chain. In the SMFA as well as in the main YDFA the RIN of the signal is transferred to the output following a certain NTF. In our case we show that the signal noise is transferred to the output. One point is interesting in this sense: gain saturation. The RIN saturation effect is different with respect to the OPA case we have studied in section 5 of the chapter IV. The OPA is an instantaneous process meaning that the RIN saturation effect is not frequency dependent. In the case of the amplification in fiber, instead, we will see that this is not true. High power extraction of the amplifier satisfies this condition. In our FE, both SMFAs are well saturated satisfying this requirement. The YDFA operation, instead, not fully satisfies this condition. We measure the RIN of the CEP-seeder (at OPA output) and at the output of the YDFA. In order to really test the transfer of the noise we modulate the CEP-seeder applying a modulation on the ME efficiency corresponding to 1% of the Satsuma average power as we have already done in the section 5 of chapter IV. We study two different cases: an applied sinusoidal modulation centered at f=200 Hz and one centered at f=1 kHz. Moreover, the OPA is operated not in the saturation condition in order to really see the effect of the fiber amplifiers. The measurements are realized during the same day in order to have the same operations conditions. The measurement setup consists of a PD (DET36A/2, *Thorlabs*) and a low-pass filter at f=50 kHz (EF124, *Thorlabs*). The results are shown in figure V.16.

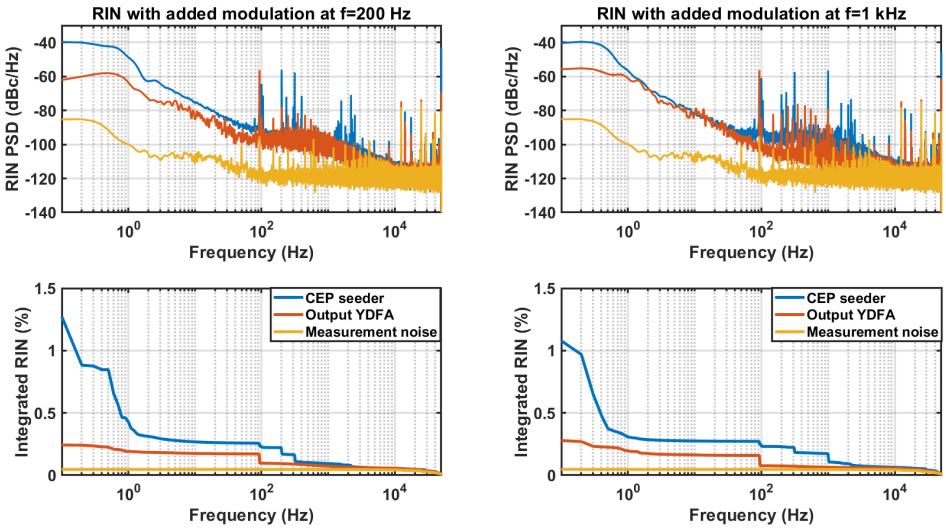


Figure V.16 – Left: RIN PSD and IRIN at the FE output (red) compared to the FE input (blue) with an added sinusoidal modulation on the ME efficiency of the Satsuma centered at f=200 Hz. Right: RIN PSD and IRIN at the FE output (red) compared to the FE input (blue) with an added sinusoidal modulation on the ME efficiency of the Satsuma centered at f=1 kHz.

Let us start analyzing the case of the modulation at f=200 Hz. In blue is the measurement at the OPA output. The IRIN on the BW [0.1 Hz; 50 kHz] is 1.3 % rms. This very high value is due to the low frequency noise and is probably due to the OPA not favorable operation

conditions. The peak at f=200 Hz is clearly visible looking at the PSD and at the corresponding IRIN. If we look, now, at the output of the YDFA, the IRIN in the same BW is of 0.24 % rms. The measured PSD is completely different showing only a peak centered at 100 Hz. The added modulation is not visible at all. Repeating the experiment in the case of the modulation centered at f=1 kHz, we find essentially the same results: the IRIN in the BW [0.1 Hz; 50 kHz] passes from 1.1 % rms to 0.27 % rms, and the peak at 1 kHz (clearly visible before the YDFA) disappears in the output PSD. Analyzing the results we understand that the phenomenon is quite different from the case of the OPA. In that case we observed that the RIN structure of the amplified signal was the same of the one of the signal. The peaks were reduced in amplitude because of the saturation. In this case, we cannot find any of the peaks present in the signal RIN.

The amplitude noise transfers in fiber amplifier has been broadly studied [Gürel *et al.* , 2014, Guiraud *et al.* , 2016]. In particular, a transfer frequency can be estimated to predict how the pump or signal RIN are transferred to the output, as shown in figure V.17.

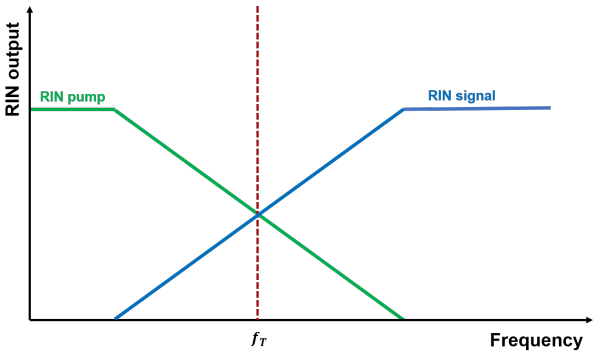


Figure V.17 – Definition of the RIN transfer frequency in amplifier

As a first approximation, we consider our laser in CW operation and follow the calculation made by Guiraud et al. [Guiraud *et al.* , 2016]:

$$f_T = \frac{1}{2\pi} P_s(L)\left(\Gamma_s \frac{\sigma_a + \sigma_e}{A}\right), \tag{V.13}$$

where $P_s(L)$ is the number of photons per second at the output (z=L) of the fiber amplifier, $\Gamma$ is the signal overlap with the fiber doped area, $\sigma_a$ and $\sigma_e$ are respectively the absorption and emission cross section for the signal, $A$ is fiber mode area. We can see that for the same fiber amplifier, the $f_T$ depends linearly to the output power. Considering our three stages amplification scheme, it is interesting to estimate the transfer frequency for the first stage. We can calculate $f_T$ considering that at the output of this amplifier we have 10 mW of average power. We find $f_T \approx 4$ kHz. This means that all the AN noise of the signal lower than 4 kHz is not transferred to the output. Clearly this is just a rough estimation and we can see if we have a deeper look at the PSDs in the two cases in figure V.16, that the peaks of the YDFA output replicate the ones of the signal for $f > 10kHz$. The amplitude of the peaks at the output is reduced with respect to the input ones. Considering what has been predicted by Gurel et al.[Gürel *et al.* , 2014], this is not astonishing. In their more accurate model they show that the transfer for pump and signal in the amplifier are respectively a low-pass and high-pass filter following a Lorentzian shaped behavior.

For our application, it is now important to evaluate what is the impact of the MPC on the RIN. We have seen how non linear effects can be source of a strong degradation of the RIN if not correctly handled. We measure the RIN before and after the MPC in the operation conditions of the CEP characterization shown in this chapter. In order to compare with the results discussed for the fiber amplifier, we consider again the case of a small modulation at f=1 kHz applied to the ME of the Satsuma. The results are depicted in figure V.18.

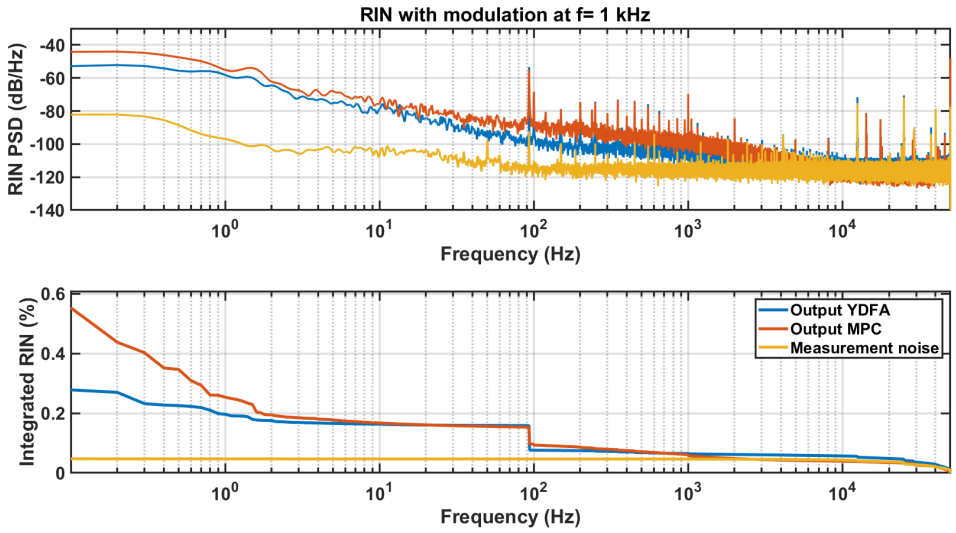


Figure V.18 – RIN PSD and IRIN at the MPC output (red) compared to the MPC input (blue) with an added sinusoidal modulation on the ME efficiency of the Satsuma (pumping the CEP-seeder) centered at f=1 kHz.

We can see that the noise at the output of the MPC is the same of the input except for the low frequencies (less than 10 Hz). This added noise at low frequency can be due to mechanical and environmental instabilities coupled with the MPC geometry. It has to be noticed that this kind of coupling effect is enhanced because of the long beam propagation occurring in the MPC.

## 5.2 RIN transfer to YDFA and feedback action

We have seen in the section 5 of the chapter IV, how an intensity modulation on the pump laser is transferred to the CEP noise and how important is the evaluation of the coupling phenomena in our setup. In the case of the amplification chain, we find, as was observed for the CEP seeder, that the nonlinear stages are responsible for this transfer. The B integral is the parameter measuring the degree of nonlinearity. If we consider the FE scheme in figure V.4, the AN-PN coupling occurs in the very first part of the FE. In the 20 cm of passive fiber, in fact, the pulse has a very high peak power because it has not yet be stretched. The SPM is dominant in this case, producing a spectrum broader than the original one. The broadening process allows to cover the 30 nm width of the CFBG. The B-integral accumulated can be estimated to 14 rad. We have already commented about the relatively small B-integral accumulated in the main YDFA: in our operation conditions we accumulate only 1.5 rad in the main amplifier. The sum of the B-integrals of both SMFAs is about 0.7 rad. We can say that the total accumulated B-integral in the amplification chain is 16 rad. Considering what we have said in section 3, a 1% rms pulse-to-pulse fluctuation produces a CEP noise due to the AN-PN coupling of 80 mrad rms. We understand that even if the front-end is highly nonlinear the dominant part of the CEP noise PSD at the output of the MPC originates in the CEP-seeder and from the noise due to the compressor instabilities.
It is interesting to analyze the measured CEP PSD in the cases of the modulation applied on the ME of the Satsuma presented for the RIN transfer analysis in the previous section. In this way we can see the impact of an intensity modulation on the pump laser of the CEP-seeder on the whole laser chain. In figure V.19 the Fringeezz measurement for a modulation corresponding to 1% peak-to-peak of the pump laser average power centered at f=70 Hz is shown. The measurement are realized in closed loop and compared at the same conditions without the applied modulation.

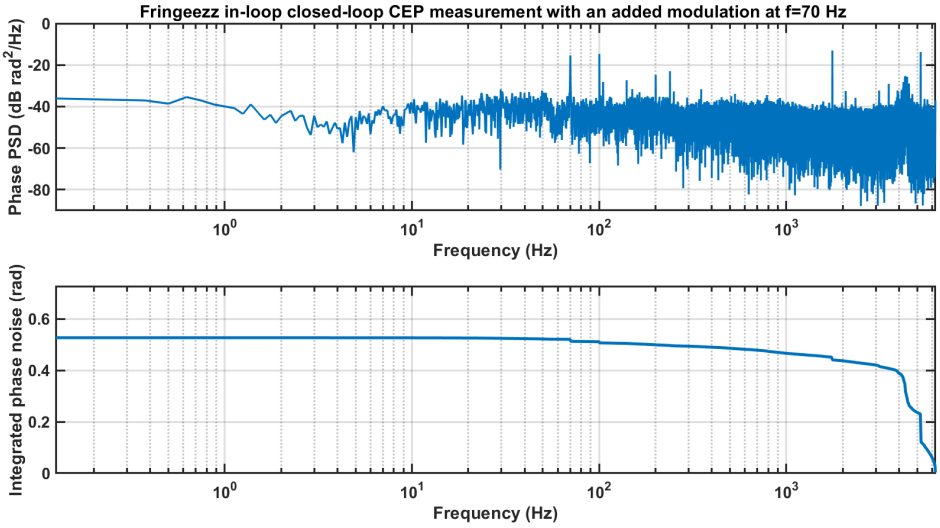


Figure V.19 – CEP PSD and integrated CEP noise Frineezz measurement at the MPC output with a sinusoidal modulation at f=70 Hz applied to the ME efficiency.

Looking at the PSD we can clearly see the peak at 70 Hz. This means that the intensity modulation on the CEP-seeder pump laser is transferred to the amplifier output even in closed loop. The contribution of the modulation looking at the integrated CEP noise is negligible.
In order to better understand the occurring phenomena, we repeat the measurement applying to the ME efficiency a white noise contribution of the same amplitude of the sinusoidal modulation applied before. We repeat the Fringeezz measurement measuring in the same conditions than before. The results are shown in figure V.20. The total CEP noise in the BW [0.1; 5 kHz] passes from 257 mrad to 306 mrad rms in the case of the white noise applied to the ME efficiency of the Satsuma. It can be seen as the relative CEP contribution added is white as well.

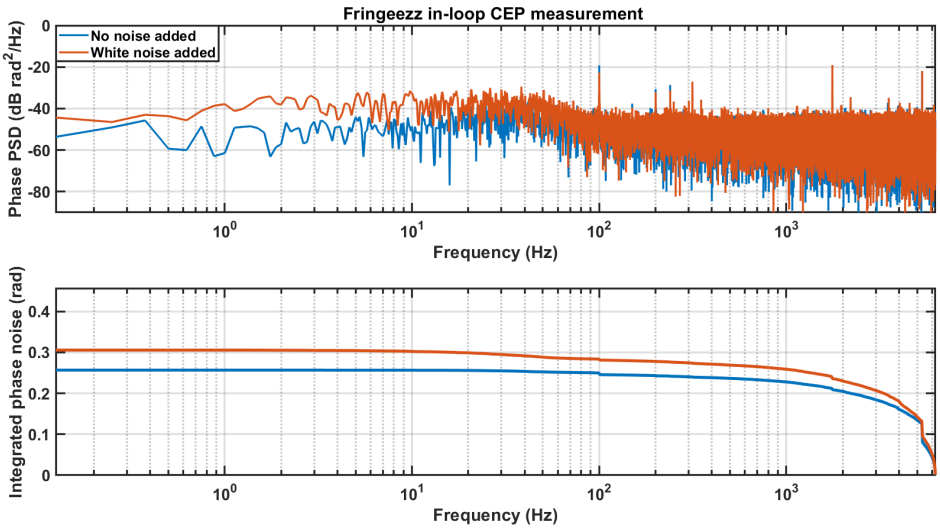


Figure V.20 – CEP PSD and integrated CEP noise Fringeezz measurement at the MPC output with (blue) and without (red) a white noise applied to the ME efficiency.

We can conclude that a transfer of noise is of around 50 mrad for 1 % of noise amplitude applied on the CEP-seeder pump.

We can now, ask what is the action of the feedback loop on noise contributions accumulated in the amplification chain. We have said that the compressor is the most sensitive element for

the CEP noise. We make an experiment adding a vibration on the optical table where the compressor is standing. This vibration is produced by the flowing water through two tubes fed by a chiller. We can see the Fringeezz measurement in this case, in figure V.21.

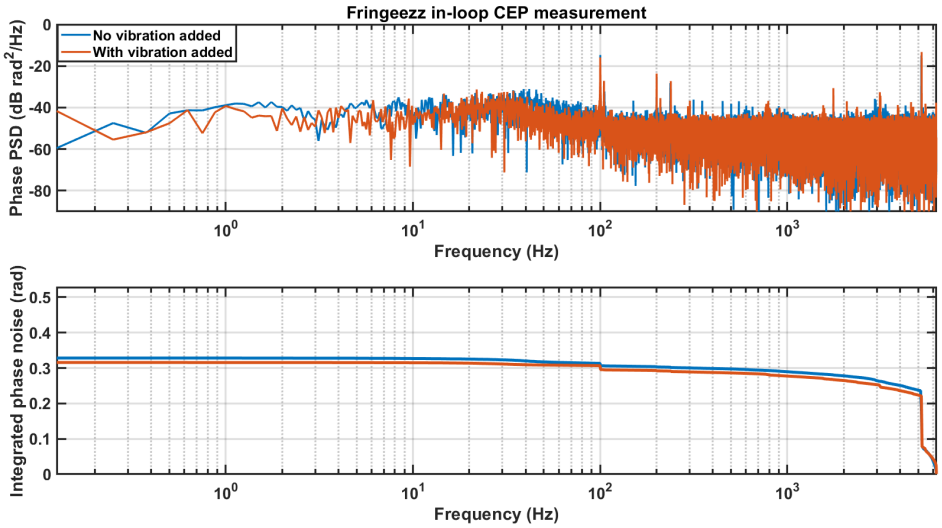


Figure V.21 – CEP PSD and integrated CEP noise Fringeezz measurement at the MPC output with (blue) and without (red) mechanical vibration added to the compressor.

It can be seen, looking at the integrated CEP noises that the total noise is essentially the same with and without vibration. To be more precise, the case with vibration added, is slightly (less than 10 mrad) lower than the one without the vibration. This difference is in the limit of the accuracy of the measurement.
We can conclude that the feedback action corrects the CEP noise generated in the compressor.

## 6 Conclusions

In this chapter we have discussed the seeder CEP stability preservation in the amplification chain. The CEP noise sources are discussed. The compressor has been indicated as the most critical element. We have presented the setup of our proof-of principle system where the already presented CEP-seeder is the starting point for an amplification in a YDFA and the post-compression in a MPC. The strategies for CEP-stabilization along the CPA chain are of two types. First the environmental noises are reduced to the minimum by a solid mechanics and isolation of the compressor setup. Second, a feedback loop is realized to correct the accumulated CEP noise. The feedback relies on a Fringeezz CEP detection, a commercial PID and a fiber EOM as actuator, assuring a fast feedback limited only by the detection at 10 kHz. It has been shown that the feedback correct the CEP noise added in the laser chain. The measured CEP at the output of the system is comparable to the CEP-seeder measured one in the chapter IV. In particular, a long-term single shot CEP measurement has shown 370 mrad over one hour.
RIN transfer analysis from the CEP-seeder to the MPC output has allowed to point out that a careful design for the amplification stages allows to obtain a very low RIN amplified system. In the case of our system, the RIN at the output of the YDFA is lower than the CEP-seeder one. The system delivers at the MPC output 30 $\mu$J pulses, at 100 kHz, with 100 fs duration. It has to be mentioned, considering what have been said about rod-type YDFAs in chapter II, that the system is able to produce pulses with much higher energies. We decide to operate it in low gain conditions in order to make a characterization and validate the CEP-compatibility of the whole system. The system will be upgraded in the future to produce more than 100 $\mu$J pulses. Considering what we have seen in section 5, the contribution of the higher pump regime is still negligible with respect to the CEP noise degradation occurring in the compressor.
As a general conclusion we can say that our system CEP-stability after optimization of the compressor and of the feedback loop, depends completely on the seeder. In this sense, the seeder pump fluctuations impact on the CEP measured at the MPC in closed loop operations has been highlighted.

# Chapter VI

# High repetition rate optimized High Harmonics Generation (HHG) source

## Objectifs

In this chapter the design of a setup for high harmonics generation is presented. The setup is optimized for obtaining the highest performances in terms of cutoff energy and photon flux using a fiber source. First, the context of the setup realization is discussed considering the fiber few-cycle source used as reference. The state-of-the art for high repetition rate HHG sources is described. In the second section, the theory of HHG in gas, including phase matching considerations is explained. In the third part, the technical choices done for the setup are presented.

## Contents

# 1 Context: High repetition rate HHG sources

We have discussed the importance of a phase controlled high repetition rate source for SFP experiments in the previous chapter. One of the most important phenomenon in this area is HHG. We have said in the general introduction that along this thesis, we have pursued two main goals: first, the realization of a CEP-stable fiber ultrafast laser and second, the design of a dedicated HHG line. This second objective is the core of this last chapter. The HHG source will be used for coherent diffraction imaging (CDI) experiments in the future, as explained in the general introduction. The HHG interaction setup is designed and optimized for the parameters of the fiber source and on the requirements of the CDI experiments.
The source we consider for the design of the experiment is not the one presented in the first four chapters of this thesis. As we have said, the presented CEP-stable amplified source is a proof-of-principle scheme demonstrating the compatibility of the fiber laser setup with low noise CEP stabilization. For the HHG design, we use the system described in the article by Lavenu et al. [Lavenu *et al.* , 2019]. The laser delivers 150 $\mu$J at 150 kHz repetition rate, for a pulse time duration of two optical cycles (6.8 fs). In the future, the CEP-stability will be provided on this system.
For the CDI application, instead, the requirements boil down to maximizing the flux of spatially coherent photons at 13 nm. The low wavelength provides high resolution for the imagining [Gardner *et al.* , 2017, Seaberg *et al.* , 2011]. The high repetition rate is a big advantage for this application because it translates to reducing the acquisition time. The CEP control in this case will allow to have a stable and repeatable spectrum for each shot.

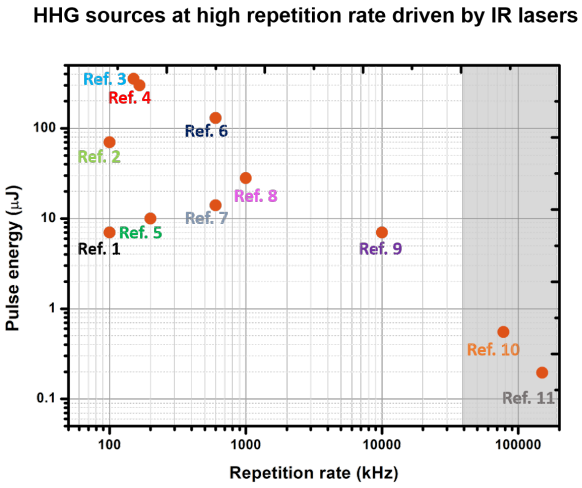


| | Pulse duration | Focal spot diameter | Central wavelength |
|---|---|---|---|
| Ref. 1 | 47 fs | 50 µm | 800 nm |
| Ref. 2 | 16 fs | 40 µm | 1030 nm |
| Ref. 3 | 8 fs | 90 µm | 1030 nm |
| Ref. 4 | 130 fs | 100 µm | 1030 nm |
| Ref. 5 | 8 fs | 90 µm | 890 nm |
| Ref. 6 | 30 fs | 90 µm | 1030 nm |
| Ref. 7 | 7 fs | 35 µm | 918 nm |
| Ref. 8 | 270 fs | 33 µm | 1030 nm |
| Ref. 9 | 30 fs | 22 µm | 1030 nm |
| Ref. 10 | 50 fs | 24 µm | 1040 nm |
| Ref. 11 | 120 fs | 100 µm | 1030 nm |

Figure VI.1 – Left: plot indicating the different published HHG sources driven by high repetition rate ($\geq$ 100 kHz) IR laser respect to the driver laser pulse energy. Ref.1=[Heyl *et al.* , 2012]; Ref.2=[Gonzalez *et al.* , 2018]; Ref.3=[Rothhardt *et al.* , 2014]; Ref.4=[Comby *et al.* , 2018]; Ref.5=[Rudawski *et al.* , 2015]; Ref.6=[Hädrich *et al.* , 2014]; Ref.7=[Krebs *et al.* , 2013]; Ref.8= [Boullet *et al.* , 2009]; Ref.9=[Hädrich *et al.* , 2015]; Ref.10=[Pupeza *et al.* , 2013]; Ref.11=[Cingöz *et al.* , 2012]. Right: table summarizing the pulse duration, the focused spot diameter and the central wavelength, for each case in the plot on the left. The shaded area represents the work using an enhancement cavity for the HHG.

Before discussing the details of the source we have realized for this work, it is interesting to analyze the state of the art of HHG sources driven by high repetition rate lasers. The range of intensity required for HHG is $10^{13} - 10^{15}$ $\frac{W}{cm^2}$. In the literature, mJ-class Ti:S lasers

have been used for HHG experiments up to 10 kHz repetition rate [Hüve *et al.* , 2006]. Let us focus on higher repetition rate cases, where $f_{rep} \geq 100$ kHz, in the IR range. For achieving these high repetition rates, the HHG driver lasers are typically OPCPA systems or fiber based schemes. In figure VI.1(left) we have summarized the driving laser parameters with respect to the repetition rate and pulse energy. In figure VI.1(right), we report the driver laser pulse duration, the diameter of the focused laser spot on the gas interaction medium and the central wavelength.

We can see that the energies used in the shown cases in figure VI.1 are lower with respect to the Ti:S case, with pulse energies ranging from 0.5 $\mu$J to 343 $\mu$J. To obtain the required intensities for an efficient HHG process, the driver laser has to be strongly focused in the gas interaction medium. In the right column in the table in figure VI.1, it can be noticed that the diameter of the spot in the gas is lower than 100 $\mu$m. It is common to refer to this HHG method as *tight-focusing configuration*. The interaction gas method used for all the sources cited in figure VI.1 is a gas jet delivered through a nozzle. The grey-shaded area underlines that a enhancement cavity is used for the HHG [Moll *et al.* , 2006]. This tool allows to obtain efficient HHG even with very low input energy driver laser. The price to pay is the complexity of the system with respect to the single pass HHG found in all the other cited cases.

Considering the driver laser we will use in terms of pulse duration, energy and repetition rate we can conclude that, from the analysis of the high repetition rate sources in figure VI.1, we need to focus in a very small spot diameter in order to reach the high intensities required. Additionally we need to optimize the interaction length in the medium. In the case of the above-mentioned tight-focusing geometries, the interaction length can be limited by the Rayleigh range. Considering that we need to focus a low energy system using a short focal length lens to obtain the HHG intensity range, the resulting short depth of focus will limit the interaction length.

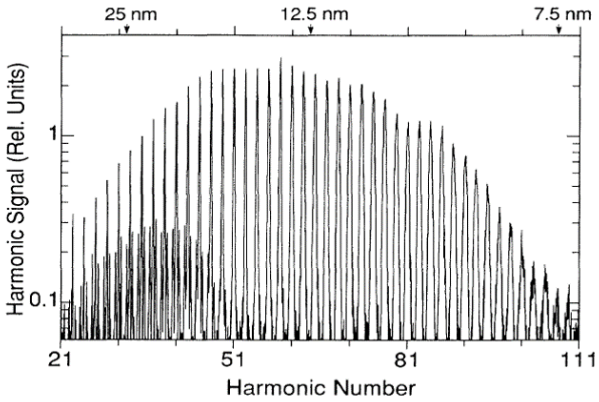


FIG. 4. Harmonic spectrum at $1.3\times10^{15}$ W/cm$^2$, for 13 Torr of Ne in a 2.5-mm tube. The features running through the low harmonics are high harmonics appearing in second order of the monochromator grating. The spectral width of individual harmonics is instrument limited.

Figure VI.2 – HHG spectrum in Ne. Image taken from [Macklin *et al.* , 1993].

In one of the first demonstration of HHG a different configuration was used, focusing the driver laser in a gas filled tube [Macklin *et al.* , 1993]. Macklin et al. measure HHG in Ne extending up to the 109th harmonic of a 15 mJ, 125 fs Ti:S laser at 5 Hz repetition rate, as shown in figure VI.2.

This result is interesting for our scopes because of the wavelength range reached by the HHG process. Although the big difference in terms of repetition rate, pulse duration and energy with respect to our driver laser, it can be seen that the intensities involved are comparable to the tight focusing cases. In the case of figure VI.2 a loose focusing is used to

obtain a long interaction length in a gas-filled tube where the intensity is high enough for HHG process. In this reference the glass tube is used for the purpose of localizing the gas at the interaction point, but it does not provide guiding to the laser beam: the length of the tube is smaller than the Rayleigh range. Another approach that can be helpful for our tight focusing geometry is to use the guiding phenomenon inside a capillary. This helps maintaining a high intensity on a small spot size for lengths longer than the Rayeigh range. This idea has been used in several works involving low repetition rate ($f_{rep} < 10$ kHz) sources in the last two decades [Durfee III *et al.* , 1999, Rundquist *et al.* , 1998, Pfeifer *et al.* , 2005]. A particular optimization is required for the best utilization of this configuration. Particular care have to be taken on the method of gas injection and on gas pressure distribution for an efficient HHG process. Goh et al. use large diameter capillary (500 $\mu$m) with a particular capillary gas injection for HHG using an high energy (several mJ) laser [Goh *et al.* , 2016, Goh *et al.* , 2015, Goh, 2015]. In Kapteyn-Mournane group smaller diameter capillary are structurally modified, modulating the internal profile, for enhancing the HHG process[Bartels *et al.* , 2002, Gibson *et al.* , 2003, Chen *et al.* , 2010].
We decided to apply the capillary for our high repetition rate system. In this chapter we present extensively the advantages of this geometry for our case and the specific implications involved in the efficient HHG process.

# 2 Theory of HHG in gas

In this section we quickly present some key elements of theory for the understanding of the HHG phenomenon. We start discussing the *three steps model* considering a single-atom response and continue with the presentation of macroscopic phase matching condition. The phase matching conditions are first discussed in a gas jet case, then for of a guiding interaction medium.

## 2.1 Single atom response: the three step model

This semi-classical model gives a good explanation of the experimental results [Krause *et al.* , 1992]. Let us consider one atom irradiated by the high intensity electric field. The mechanism leading to HHG is described by three steps: an electron is ionized from the atom [1], the electron is accelerated by the laser field, the electron recombines with the parent ion emitting an XUV photon. The model relies on two main approximations:

- Single active electron (SAE): for the model, we consider the relation between a single electron and the electric field.
- Strong field approximation (SFA): the ionized electron is influenced only by the laser electric field, neglecting the interaction with the parent ion potential.

The scheme in figure VI.3 shows a depiction of the three steps, we explain in the next three subsections.

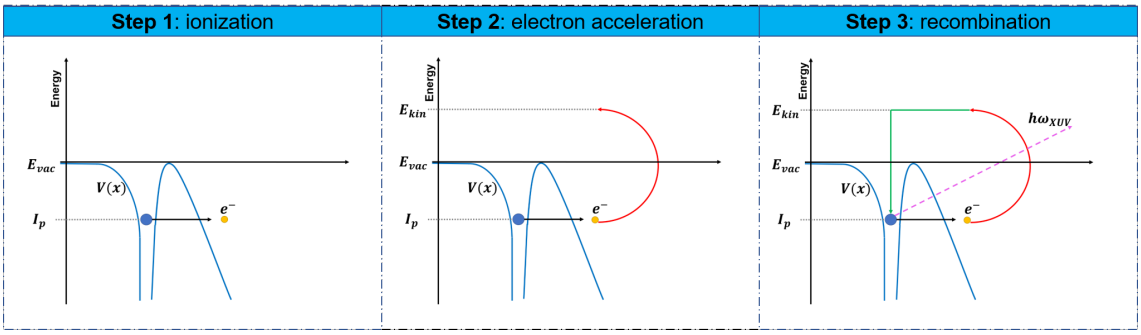


Figure VI.3 – Scheme depicting the three step model. V(x) is the atom potential; $I_p$ is the ionization potential; $e^-$ is the ionized electron; $E_{kin}$ is the kinetic energy accumulated by the electron; $hbar\omega_{XUV}$ is the energy of the emitted photon.

### 2.1.1 Step 1: Ionization

Before the laser interaction, avalanche electron has a Coulomb potential V(x). The ionization of the gas atoms for the HHG process occurs in particular conditions, where the laser field is such that the photon energy is lower the ionization potential $I_p$. Two cases are considered: the multi-photon ionization and the tunneling. We introduce the *Keldysh parameter* as:

$$\gamma = \omega \frac{\sqrt{2mI_p}}{eE}, \tag{VI.1}$$

where $E$ is electric field, $\omega$ is the laser frequency, $m$ is the electron mass, $e$ is the electron charge. The value of this parameter allows to discriminate which process dominates.

- For $\gamma > 1$, multi-photon ionization dominates, meaning that the Coulomb potential is unperturbed and the ionization occurs for the absorption of several photons. This phenomenon is not the prevalent one in the HHG process.

[1] via tunneling ionization effect.

- For $\gamma < 1$, V(X) is deformed as shown on the case in figure VI.3 on the left, forming a finite barrier. The electron can cross the potential barrier through the tunneling effect.

In our case we can calculate, as an example, the Keldysh parameter for a 1030 nm laser with an intensity of $10^{14}$ $\frac{W}{cm^2}$, ionizing an Ar atom having $I_p$=15.76 eV, we obtain $\gamma = 0.28$. We confirm that for our scopes, the ionization process is dominated by tunneling effect.

### 2.1.2 Step 2: Acceleration of the electron

The electron in the continuum is accelerated by the electric field. Let us consider the classical motion equation for the electron. For an electric field given by, $E = E_s cos(\omega t)$, we can write:

$$m\overrightarrow{a} = -eE, \tag{VI.2}$$

where $\overrightarrow{a}$ is the acceleration vector. We can write:

$$m\frac{d\overrightarrow{v}}{dt} = -eEcos(\omega t). \tag{VI.3}$$

This equation can be solved for finding the equation for the speed v(t):

$$\int_0^{v(t)} dv = -\frac{eE}{m}\int_{t'}^{t} cos(\omega t)dt, \tag{VI.4}$$

where we have used for the integration boundaries a generic speed function $v(t)$ and $t'$ is the ionization time. We can integrate once more to obtain the following electron motion equation:

$$x(t) = -\frac{eE}{m\omega^2}[cos(\omega t) - cos(\omega t') + \omega(t-t')sin(\omega t')], \tag{VI.5}$$

It is interesting to have a sketch for understanding the physical meaning of this equation. In figure VI.4, we show the trajectories x(t) of the accelerated electron position for values of $\omega t'$ ranging from $-\frac{\pi}{5}$ to $\frac{\pi}{5}$. The position x=0 is the position of the parent ion. Let us make a qualitative analysis of the trajectories. Looking at steps two and three depicted in figure VI.3, we can see that the electron must come back to the parent ion to trigger the emission of an XUV photon. This means that the electron trajectories have to come back to the x=0 position in order to recombine with the parent ion.

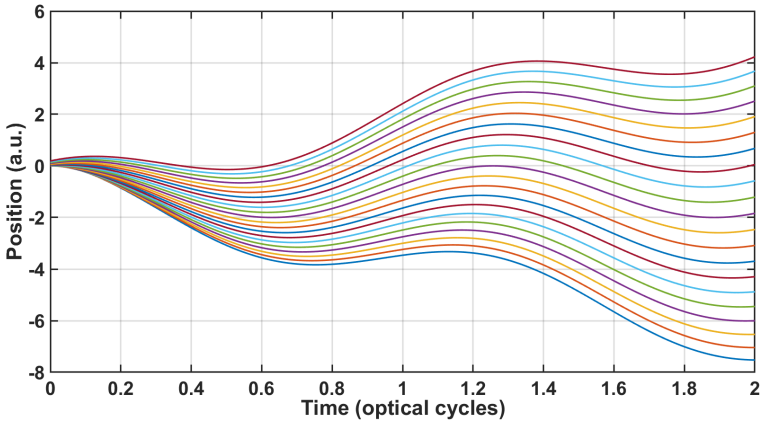


Figure VI.4 – Scheme depicting different electron trajectories in time for different cases of $\omega t'$ from $-\frac{\pi}{5}$ to $\frac{\pi}{5}$.

We can observe that not all the electron trajectories satisfy the $\omega(t')$ conditions for having an intersection with the position 0 other than the origin. Considering an electric field oscillating

at frequency $\omega$, this means that only for some t' the electron can recombine with the parent ion. It can be shown that only for t' such that $\omega t' \in [0; \pi/2] \cup [\pi; \frac{3\pi}{2}]$ an XUV photon can be generated.
When the recombination conditions are satisfied, the electron can spend more or less time before of coming back to the parent ion depending on the trajectories. In general, we can write the kinetic energy as:

$$E_{kin} = \frac{1}{2} m \overrightarrow{v}^2 = \frac{1}{2} \frac{e^2 E^2}{m^2 \omega^2} [sin(\omega t) - sin(\omega t')]^2. \tag{VI.6}$$

The average value of the kinetic energy acquired, $\langle E_{kin} \rangle$:

$$U_p = \frac{1}{4} \frac{e^2 E^2}{m^2 \omega^2}; \tag{VI.7}$$

where $U_p$ stands for *ponderomotive potential*.

### 2.1.3 Step 3: recombination

We have seen in the previous paragraph that the electron is recombined with the parent ion only for determined trajectories and the electron is acquiring more or less kinetic energy in the acceleration step depending on the trajectories. The emitted photon energy is, then:

$$\hbar\omega = I_p + E_{kin}. \tag{VI.8}$$

There is a maximum value of kinetic energy acquired at acceleration step, that can be calculated to be $E_{kin}^{max} = 3.17 U_p$, so that:

$$\hbar\omega_{max} = I_p + (3.17) U_p. \tag{VI.9}$$

Equation (VI.9) is known as the cutoff law and has been experimentally verified for the first time by Krause et al. in 1992 [Krause *et al.* , 1992]. The physical meaning of this equation is that the HHG spectrum is spanning until a maximum energy equivalent to $\hbar\omega_{max}$. In particular, it can be seen that this cutoff scales proportionally to the $U_p$, meaning:

$$\hbar\omega_{max} \propto {\lambda_0}^2 I_L, \tag{VI.10}$$

where $\lambda_0$ is the laser wavelength and $I_L$ is the laser intensity. The described model is very useful for a first rough estimation of the theoretically maximum photon energy that can be reached for a certain laser intensity, central wavelength and gas characteristics. In figure VI.5, a schematic representation of the HHG spectrum obtained from the three step model implications is shown [Salieres & Lewenstein, 2001]. Only odd order harmonics are generated, due to the centro-symmetric nature of the generation medium. Three different emission regions can be evidenced having different conversion efficiency.

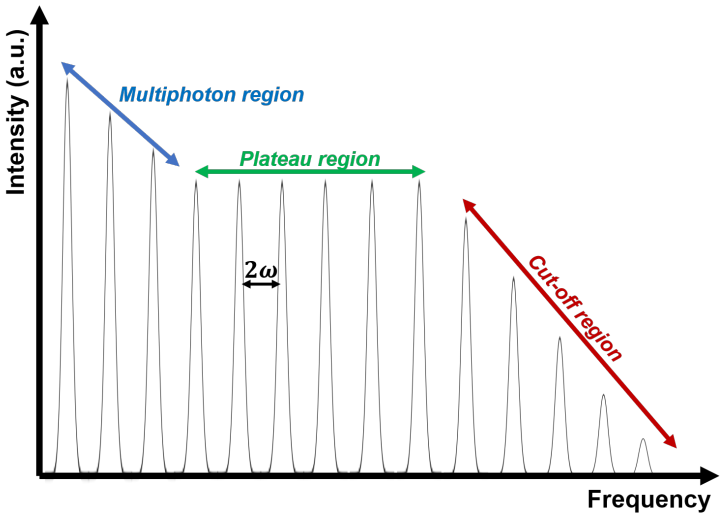


Figure VI.5 – Scheme of the HHG spectrum.

## 2.2 Phase matching

The HHG phenomenon is an highly non linear effect considering the generation of high energy photons due to the interaction of a laser with a gas medium. A macroscopic analysis is also required to understand the emitted XUV spectrum. In particular, like the nonlinear effects we have seen for crystals, it is required to satisfy a phase matching condition such that the XUV photons generated by each single atom interaction along propagation are constructively summed giving rise to the output. Let us consider, as an example, a one-dimension model using the scheme in figure VI.6 where a gas jet of atoms interacts with the waist of a focused laser beam.

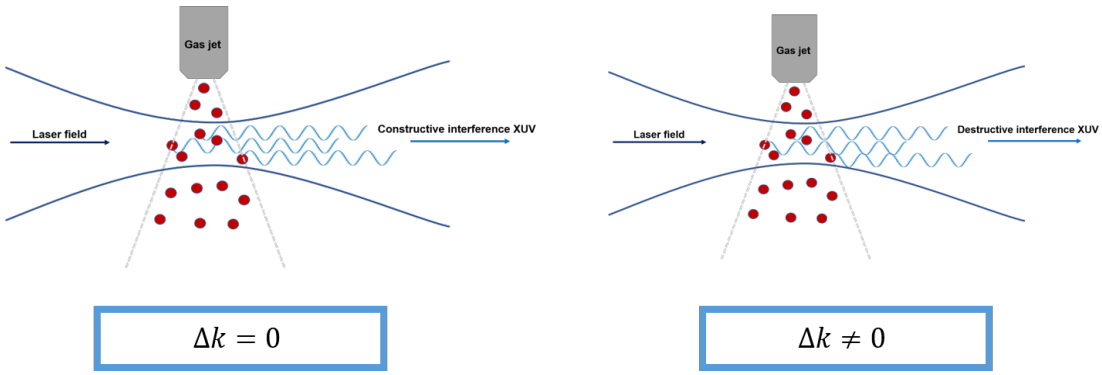


Figure VI.6 – Scheme of the phase matched (left) and not phase matched (right) HHG process in one dimension.

In perfect analogy with what we have discussed in chapter II, there exists a phase term $\Delta k$ to be matched in order to obtain the constructive summing of the XUV photons. The phase matching conditions depend on several parameters of the laser field, the interaction medium geometry and the gas pressure [Constant *et al.* , 1999]. We consider the case of a gas jet and the one of a guiding capillary underlining the differences between these two cases.

### 2.2.1 HHG phase matching: gas jet case

We need to consider a mismatch between the fundamental IR laser beam and harmonic order $q$ as follow:

$$\Delta \overrightarrow{k} = q \overrightarrow{k}_f + \overrightarrow{k}_q, \tag{VI.11}$$

where: $q$ is the harmonic order, $\overrightarrow{k}_f$ is the fundamental wavevector and $\overrightarrow{k}_q$ is the harmonic $q$ wavevector. The mismatch can be decomposed in four terms as follows [Kazamias *et al.* , 2011]:

$$\Delta \overrightarrow{k} = \Delta \overrightarrow{k}_{geom} + \Delta \overrightarrow{k}_{ele} + \Delta \overrightarrow{k}_{atom} + \overrightarrow{k}_{dipole}, \tag{VI.12}$$

where $\Delta \overrightarrow{k}_{geom}$ is a phase term depending on the laser focusing geometry, $\Delta \overrightarrow{k}_{ele}$ is the dispersion term due to the free electron induced through ionization, $\Delta \overrightarrow{k}_{atom}$ is the mismatch generated by the dispersion difference between the fundamental and the $q^{th}$ harmonic, $\overrightarrow{k}_{dipole}$ is the phase shift due to the emitting dipole. Let us analyze in details each term.

- $\Delta \overrightarrow{k}_{geom}$ is the phase term due to the laser focusing conditions. A Gaussian beam experiences a phase shift with respect to a plane wave denoted as the *Gouy phase* $\phi_{Gouy}$ and calculated as:

$$\phi_{Gouy} = -arctan\Big(\frac{z}{z_R}\Big), \tag{VI.13}$$

  where $z_R$ is the Rayleigh distance. In the case of the mismatch in equation (VI.12), we have:

$$\Delta \overrightarrow{k}_{geom} \approx -\frac{1}{z_R}(q-1). \tag{VI.14}$$

- $\Delta \overrightarrow{k}_{ele}$ is the phase term due to the free electrons in the interaction gas. We have said in the three steps model section that not all ionized electrons recombine. To define the dispersion due to the free electrons, it is useful to introduce the plasma frequency $\omega_p$:

$$\omega_p = \sqrt{\frac{e^2 N_e}{m_e \varepsilon_0}}, \tag{VI.15}$$

  where: $e$ is the electron charge, $N_e$ is the free electrons density, $m_e$ is the electron mass. the phase mismatch on the fundamental laser frequency case is:

$$\Delta \overrightarrow{k}_{ele,f} \approx -\frac{1}{2}\frac{{\omega_p}^2}{\omega^2}, \tag{VI.16}$$

  meaning that the phase mismatch in equation (VI.12) is given by:

$$\Delta \overrightarrow{k}_{ele} \approx -q\frac{e^2 N_e}{2 m_e \varepsilon_0 \omega c}, \tag{VI.17}$$

  where c is the speed of light in vacuum.

- $\Delta \overrightarrow{k}_{atom}$ is the phase shift due to the difference between the refractive index of the neutral gas atoms for fundamental and harmonic wavelength, calculated as follow:

$$\Delta \overrightarrow{k}_{atom} = \frac{2\pi q}{\lambda}(n(\omega) - n(\omega_q)), \tag{VI.18}$$

  where $\omega_q$ is the harmonic frequency and $\lambda$ and $\omega$ are the fundamental wavelength and frequency.

- $\overrightarrow{k}_{dipole}$ is the phase mismatch due to the atomic dipole phase. This term depends linearly on the intensity gradient:

$$\overrightarrow{k}_{dipole} = \alpha \overrightarrow{\nabla} I, \tag{VI.19}$$

where $\alpha$ is a coefficient depending on the electron trajectory and laser parameters.

We can comment the obtained relation, observing that the terms $\Delta \overrightarrow{k}_{ele}$ and $\Delta \overrightarrow{k}_{atom}$ depend only on the gas structure. The $\Delta \overrightarrow{k}_{geom}$ depends only on the harmonic order considered and on the laser focusing geometry. The last term depends both on laser and interaction medium conditions.

### 2.2.2 HHG phase matching in a capillary

We consider now what we have to change in the phase matching criteria we have presented above if the interaction medium is a capillary instead of a gas jet. We can say that the terms depending on the gas characteristics such as $\Delta \overrightarrow{k}_{ele}$ and $\Delta \overrightarrow{k}_{atom}$ do not change. The geometrical mismatch term is clearly different and can be shown [Rundquist *et al.* , 1998, Durfee III *et al.* , 1999] to become:

$$\Delta \overrightarrow{k}_{geom} = -q \frac{u_{11}^2 \lambda}{4\pi a^2}, \tag{VI.20}$$

where $a$ is the capillary radius and $u_{11}$ ($u_{11} \approx 2.405$) is the first zero of the Bessel function $J_0$[1]. Another difference can be found in the dipole term. We can see that in the case of the capillary, we can consider the intensity gradient as constant along the propagation axis by definition. For our one dimension model we can neglect this term. The model presented for the gas jet and for the guided case allows to introduce a new parameter indicating the interaction length through which the harmonics are phase matched, called *coherence length* $L_{coh}$ [Constant *et al.* , 1999]:

$$L_{coh} = \frac{\pi}{\Delta \overrightarrow{k}}. \tag{VI.21}$$

We can see that in the perfect phase matching case this length tends to infinity. The number of generated photons is linked to the coherence length. This simple model, indeed, we have not considered the upper limit for the HHG length: the generated harmonics re-absorption in the gas medium. We can introduce an absorption length $L_{abs}$ that indicates the maximum medium interaction length before HHG re-absorption, defined as:

$$L_{abs} = \frac{1}{\sigma \rho}, \tag{VI.22}$$

where $\sigma$ is the ionization cross section and $\rho$ is the density for the interaction gas. A more accurate model with respect to the one we have presented has been established by Constant et al. [Constant *et al.* , 1999] in 1999. The resulting optimum condition for phase matching generation considering absorption length are reached for:

$$L_{med} > 5L_{abs}; L_{coh} > 5L_{abs}, \tag{VI.23}$$

where $L_{med}$ is the length of the interaction medium[2]. We can conclude that both phase matching condition and cutoff law have to be carefully considered for an optimized design of a dedicated HHG line.

[1] We consider that the laser is guided in the capillary in the beam mode $EH_{11}$ [Agrawal, 2000].

[2] In the case of the capillary we will consider this length equivalent to the capillary one.

# 3 HHG line design

In this section we discuss the design of the HHG line optimized for the fiber laser and the CDI requirements as we have already mentioned in the context section. In the first section, we apply the conclusion for optimizing the HHG XUV photons flux we have presented in the theoretical part. In the second section, we present the complete setup explaining the technological choices we have made.

## 3.1 HHG line design at 13 nm: design and simulations

We have anticipated in the context section that we want to use a capillary. We therefor need to estimate the inner diameter and length of the capillary for our laser intensity and to the 13 nm wavelength.

### 3.1.1 Preliminary considerations

We have seen in equation (VI.9) that the maximum energy of the emitted photons can be estimated using the cutoff law. Our goal is to have HHG XUV photons at $\lambda = 13$ nm. Considering our driver laser emits at 1030 nm, we need harmonic 79.
The most common used gases for HHG are Ar, Ne and He. We can calculate as an indication the laser intensities required to obtain a theoretical cutoff at 13 nm for these three cases are respectively $2.85 \times 10^{14}\ W/cm^2$, $2.65 \times 10^{14}\ W/cm^2$, $2.55 \times 10^{14}\ W/cm^2$. Looking at these results, one can conclude that all the gases, with a sufficient high intensity can produce an XUV contribution at 13 nm. This is not true because the *saturation ionization intensity* limits the HHG generation effect. This intensity depends on several factors concerning the laser and the gas characteristics. It is very difficult to estimate precisely this intensity. We can have an idea of what we expect in our case looking at the calculations done by Shiner et al. [Shiner *et al.* , 2013] for different laser central wavelengths and pulse durations as reported in figure VI.7.

Table 1. Calculated saturation intensities for the noble gases using the Yudin–Ivanov nonadiabatic ionization model [24]. At the saturation intensity ($I_{sat}$), 43% of the sample on axis is ionized by the end of the pulse.

| $\lambda$ (nm) | Cycles | $\tau$ (fs) | $I_{sat}$ ($10^{14}$ W cm$^{-2}$) | | | | |
|---|---|---|---|---|---|---|---|
| | | | Xe | Kr | Ar | Ne | He |
| 800 | 2 | 5 | 1.60 | 2.85 | 4.51 | 14.4 | 23.0 |
| 800 | 10 | 27 | 1.01 | 1.81 | 2.86 | 9.10 | 14.5 |
| 800 | 20 | 53 | 0.86 | 1.54 | 2.44 | 7.75 | 12.3 |
| 1400 | 2 | 9 | 1.52 | 2.62 | 4.06 | 12.5 | 19.8 |
| 1400 | 10 | 47 | 1.03 | 1.77 | 2.72 | 8.28 | 13.0 |
| 1400 | 20 | 93 | 0.89 | 1.53 | 2.35 | 7.13 | 11.2 |
| 1800 | 2 | 12 | 1.45 | 2.47 | 3.81 | 11.6 | 18.4 |
| 1800 | 10 | 60 | 1.01 | 1.71 | 2.62 | 7.90 | 12.4 |
| 1800 | 20 | 120 | 0.88 | 1.49 | 2.27 | 6.82 | 10.7 |

Figure VI.7 – Table reporting the saturation intensity for noble gases, taken from [Shiner *et al.* , 2013].

Analyzing the results in figure VI.7 we can see that the saturation intensity increases with shorter laser pulses. At the same time, it decreases drastically when going from the heavier to the lighter noble gas considered. To have a clearer idea of what it means for our laser parameters, we fit the results in figure VI.7 in order to obtain an indication of the saturation intensity useful for our case. In figure VI.8 on the left, we show the resulting fit for Ar, Ne and He as a function of the laser pulse duration (in terms of optical cycles). Let us consider the pulse duration range between 2 and 4 optical cycles, we can see that the lighter is the gas, the more important is the saturation intensity difference. Looking at the curves shown in figure

VI.8 on the right, we can see that the difference between the calculated $I_{sat}$ for 800 nm and 1030 nm is negligible for Ar. It becomes more important for Ne and He case.

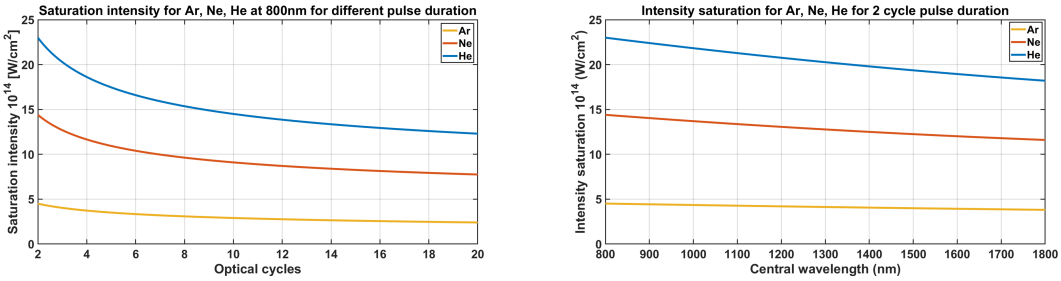


Figure VI.8 – Saturation intensity estimation. Left: $I_{sat}$ calculated at 800 nm depending on driver laser optical cycles. Right: $I_{sat}$ calculated at 2 optical cycle duration for different laser central wavelengths.

The saturation intensity for Ar, Ne and He for a 2 optical cycles pulse centered at 1030 nm are respectively $4.33 \times 10^{14}$ $W/cm^2$, $13.59 \times 10^{14}$ $W/cm^2$, $21.66 \times 10^{14}$ $W/cm^2$. From this rough estimation, we can see that in the Ar case the saturation intensity is close to the estimated required minimum intensity for having the cutoff at 13 nm. From this discussion and considering what can be found in literature for comparable intensity sources we decide to use Ne gas for our setup.
The advantage of using a capillary is having a IR laser intensity constant along the capillary length. To reach a cutoff lower than 13 nm in Ne, we need to have an intensity of $5 \times 10^{14}$ $W/cm^2$ in the capillary core. Considering the laser energy and pulse duration we decide to use for our design twp different capillary diameters respectively of 60 $\mu$m, 80 $\mu$m. In an ideal case[1], we get respectively $I = 2.1 \times 10^{15}$ $W/cm^2$, $I = 1.2 \times 10^{15}$ $W/cm^2$. In all three cases we ensure a high enough intensity.
In the above discussed conclusions we have completely neglected phase matching and absorption problems for HHG. It has to be stressed that the gas pressure is the knob we can turn to obtain phase matching. In the case of Ne, we expect that phase matching is achieved for pressures of some hundreds of mbar considering what can be found for waveguides of comparable inner diameter and laser intensities [Paul *et al.* , 2003, Popmintchev *et al.* , 2009].

### 3.1.2 Capillary design: flowing gas simulations

We use commercially available fused silica capillaries (*Vitrocom*[2]). The geometry of this capillary is such that we have a small inner diameter (as previously mentioned: 60 $\mu$m, 80 $\mu$m) and an outer diameter of 5.5 mm. For our setup we choose a capillary length of 2 cm.
One question to answer is how to inject the gas inside the inner diameter of the capillary. The simplest way we can think about it is to make holes along the capillary diameter for injecting the gas. We have to be careful about two issues considering this approach: optical guiding losses of the laser beam and uniformity of the pressure profile along the capillary length. To reduce the impact of the first problem, we qualitatively can understand that the best solution is to use the lowest possible number of holes with the smallest diameter. To have the most uniform pressure profile along the capillary length, we expect the simplest solution is the exact opposite one: the largest number of largest diameter of holes. We need therefore to reach a trade-off between these two extreme situations. We have realized a simulation in collaboration with O. Sublemontier (NIMBE group, CEA Saclay), to simulate two cases. We focus only on the gas pressure profile along the capillary. The schemes for the two studied situations are

[1] Without considering the coupling losses.
[2] www.vitrocom.com

sketched in figure VI.9(a) and VI.9(b). In the first case we have three holes having a diameter comparable with the capillary inner diameter of 100 $\mu$m. In the second one, only two 1 mm large holes are drilled. The guiding losses are very important in the second case and negligible in the first one. The length of the capillary is also slightly different.

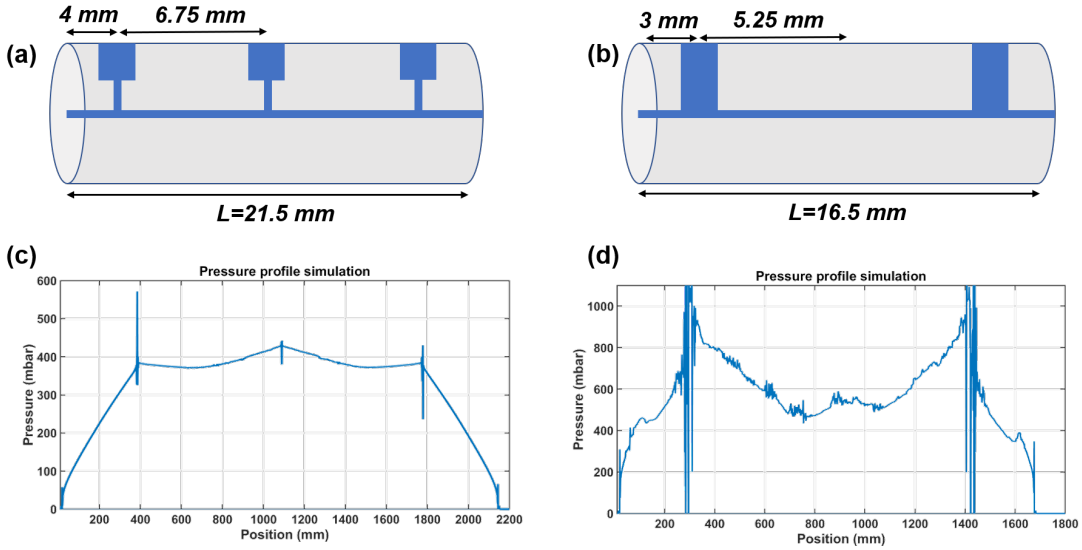


Figure VI.9 – Simulation of gas flowing pressure through the capillary inner diameter in two different case. (a) Scheme of the simulated situation with three holes with hole diameter of 100 $\mu$m and capillary diameter of 100 $\mu$m. (b) Scheme of the simulated situation with two holes with hole diameter of 1 mm and capillary diameter of 100 $\mu$m. (c) Pressure profile in the case (a). (d) Pressure profile in the case (b).

The pressure profile is simulated considering a static pressure accessing to the capillary transverse holes. The simulation is realized by increasing the input static pressure until we reach in the middle of the capillary a pressure of 400 mbar. In figure VI.9(c) we can see the resulting pressure profile. In this case the input pressure reservoir is at 500 mbar. The pressure profile corresponding to the second case is shown in VI.9(d). In this case 1 bar is used as input to reach a comparable pressure in the middle of the capillary length. Moreover, comparing the two cases concerning the pressure uniformity, we can clearly see that design (a) is more favorable with respect to (b). In both cases we can see that the pressure clearly drops off between the outer holes and the capillary edges. The real HHG zone is the one between the two outer holes.
We can conclude from the simulation analysis that a good solution for injecting the gas through the capillary requires that the holes diameter is of the same size as the capillary inner diameter. Three equally distant holes are enough to have a sufficiently uniform pressure for more than 1.5 cm as seen in figure VI.9(c). Considering the very small size of the capillary inner diameter we need to drill holes 2.5 mm long and 100 $\mu$m large. The challenging fabrication of these channels is discussed in the next section.

### 3.1.3 Capillary design: drilling technique

The realization of the holes for the gas injection is realized using the *Femtosecond laser irradiation followed by chemical etching* (FLICE) technique [Osellame *et al.* , 2012]. This technique allows to realize three-dimensional channels in fused silica substrates. The method mainly consists of two steps: laser irradiation and chemical etching.

- First the zone we want to drill is irradiated using a femtosecond laser. The sample is moved in x, y, z direction using a automated nm-precision stage. The laser is fo-

cused using a microscope objective on the substrate in order to have an intensity such that the fused silica is modified. The intensity is lower than the ablation threshold [Hnatovsky *et al.* , 2006]. The substrate is modified and particular structures, called *nano-cracks*, are generated. These nano-cracks are of size comparable to $\frac{\lambda}{2n}$, where $n$ is the fused silica refractive index and $\lambda$ is the laser wavelength. Moreover, these structures are very sensitive to the irradiation laser polarization. Examples scanning-electron microscope images, taken from [Hnatovsky *et al.* , 2006] of the nano-cracks are shown in figure VI.10. In figure VI.10(a) there is the case of structures generated with the laser linear polarization parallel to the movement of the sample stage. In figure VI.10(b), the opposite case considering a polarization perpendicular to the writing direction.

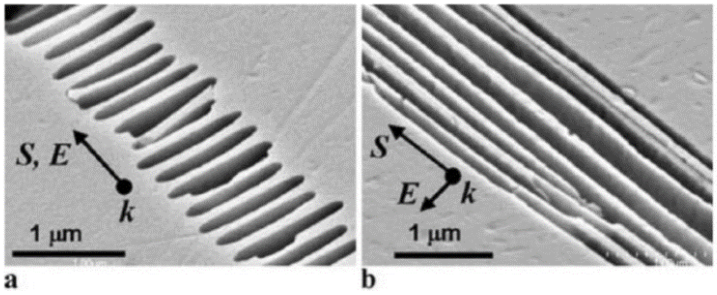


Figure VI.10 – Polarization-selective etching enabled by nanograting formation. E is the laser polarization vector and S is the writing direction. SEM images of xy-sections of modification produced in the transverse writing geometry with linear polarization (a) parallel and (b) perpendicular to the writing direction. Adapted from [Hnatovsky *et al.* , 2006].

- In the second step, the substrate is immersed in an acid solution of HF[1]. The acid has an etching rate several orders of magnitude greater in the irradiated zone with respect to the non-modified fused silica. The case considering a linear polarization perpendicular to the writing direction (like in VI.10(b)) is the most favorable for a fast etching rate. Careful management of the etching times, considering the different etching rate, allows to fabricate channels corresponding to the irradiated zones.

In our case the capillary holes are realized in collaboration with the FemtoFab group at Istituto Italiano di Tecnologia (IIT) [2]. I have spent my master internship in this group working on this technique applications.
For the capillary design we start from what we have used for the simulation in VI.9(a). The holes diameter is the same as the capillary internal diameter. The capillary length is exactly 20 mm. In order to have the longest possible zone where the pressure profile is constant, one hole is placed at the center of the capillary length. The two extreme ones, instead, are at a distance of 2 mm from the edges. In this way, we can expect a constant pressure profile for 1.6 mm.
The FLICE technique is commonly used for plane substrate modification. This is because in the irradiation step, the laser is focused on the sample substrate through an objective. A non-plane substrate results in changing the properties of the irradiation because it changes the focusing geometry. The realization of the 2.5 mm deep and 100 $\mu$m large hole is particularly tricky because of this issue. The curved capillary surface is acting as an added cylindrical lens after the laser focusing objective. To solve this problem, one side of the capillary is polished in order to obtain a plane surface for the laser irradiation. The other element to manage is the internal surface quality of the capillary. During the etching step, we must prevent the HF acid

[1] Hydrofluoric acid
[2] https://www.iit.it/centers/cnst-polimi

to access the inner diameter of the capillary. The HF acid can, in fact, generate a degradation of the internal surface roughness of the capillary. Moreover, if the interaction acid-capillary inner diameter is long, the diameter itself of the capillary can be affected being enlarged by the acid action. The obtained results on a 60 $\mu$m inner diameter capillary are shown in figure VI.11.

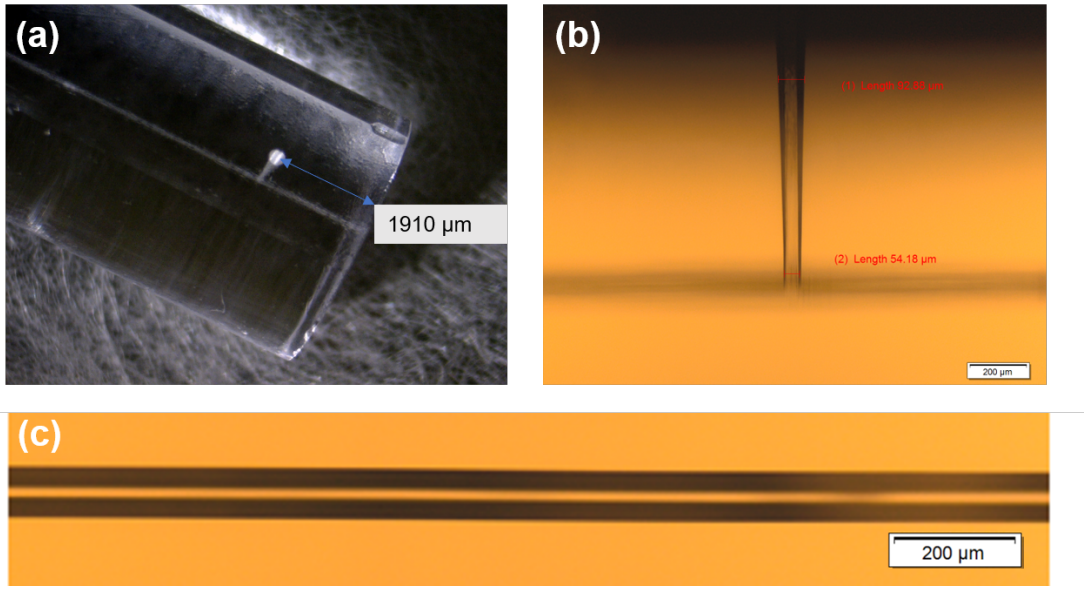


Figure VI.11 – Optical microscope images for a drilled hole though the 60 $\mu$m inner diameter capillary. (a) Image of the hole distance to the capillary edge. (b) Image of the hole, showing that at the inner diameter intersection, the hole diameter is around 60 $\mu$m. (c) Image of the inner diameter of the capillary after the hole fabrication.

We can see in figure VI.11(a) that the hole is perfectly at 2 mm from the edge as we have specified. In figure VI.11(b) we can see that the hole diameter is the same of the capillary inner diameter at the intersection. The injection part of the hole, instead, measures around 93 $\mu$m. The hole has a smoothly conical structure. Finally, in VI.11(c), the inner capillary section is shown. We can observe that the internal surface roughness is not degraded.

## 3.2 HHG line at 13 nm: technical choices

We now discuss the technical choices and the resulting setup realization for the HHG line. The scheme of the complete setup of the HHG line is shown in figure VI.12. It is composed of 3 main parts: HHG interaction chamber, an IR filtering part and the detection part. We discuss in details the three parts considering the issues and the solutions we have adopted for each of them.

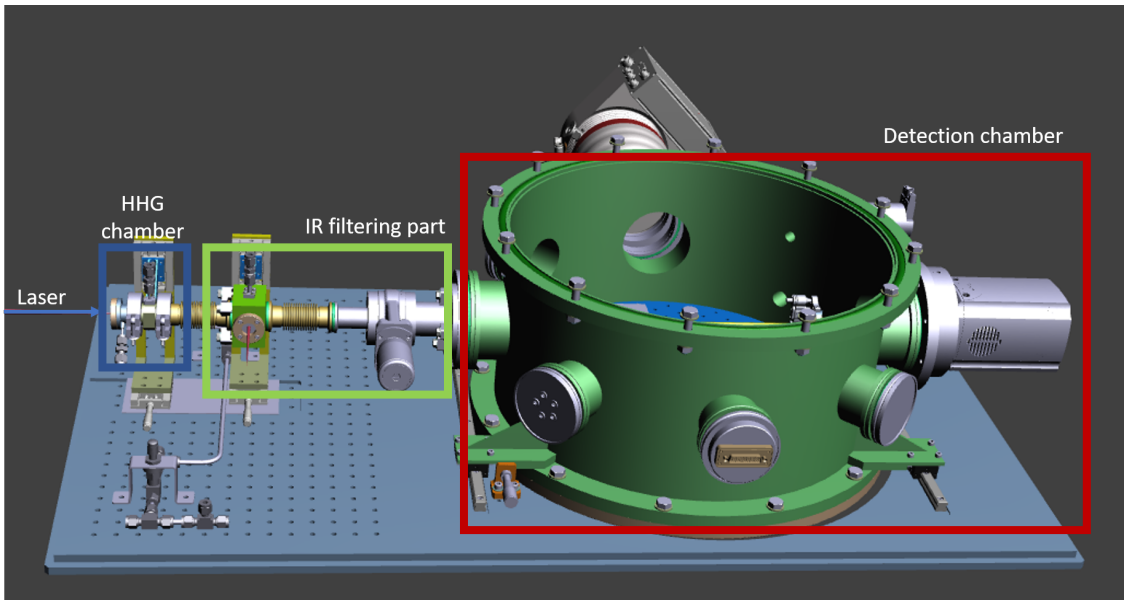


Figure VI.12 – Design of the complete HHG 13 nm line composed by the HHG chamber, the IR filtering part and the detection chamber.

### 3.2.1 HHG chamber

We have discussed how the capillary is designed and how the holes for the gas injection are realized. The capillary is mounted in the HHG chamber we have evidenced in blue in figure VI.12. The transverse section of this chamber is shown in figure VI.13. We can see that the capillary is mounted in a chamber where the gas in injected through the top. The HHG chamber is placed on linear translation stages in the (x,y) directions for the capillary laser coupling alignment. The alignment procedure can be done even when the whole system is under vacuum, considering the translations are external to the chamber.

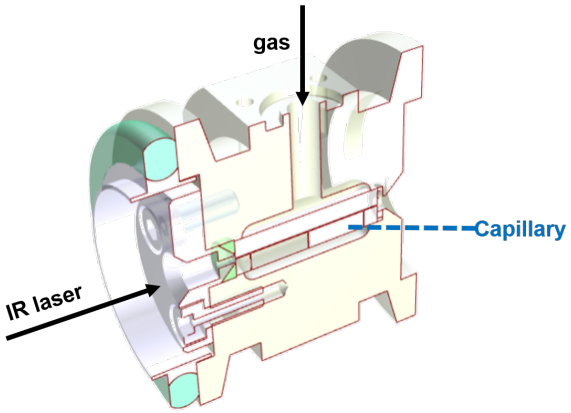


Figure VI.13 – Transverse section of the HHG chamber where the capillary is mounted.

### 3.2.2 IR filtering

For the high repetition rate HHG sources, one of the main problem to manage is the high IR residual beam average power. In our case, we use the system evidenced in green in figure VI.12 to handle this problem. Most of the residual IR beam is reflected out by using a highly reflecting mirror hole at 1030 nm. The mirror is drilled with a 1 mm diameter traversing hole at 45 degree. The idea is to exploit the fact that the XUV beam and the IR one have very

different divergences at the output of the capillary. In particular, the NA scales linearly with the wavelength. This means that the 13 nm beam is diverging about 80 times less than the 1030 nm centered one. The biggest fraction of the IR residual beam is reflected outside by the mirror and the XUV is passing through the hole. A depiction of this part of the system is in figure VI.14.

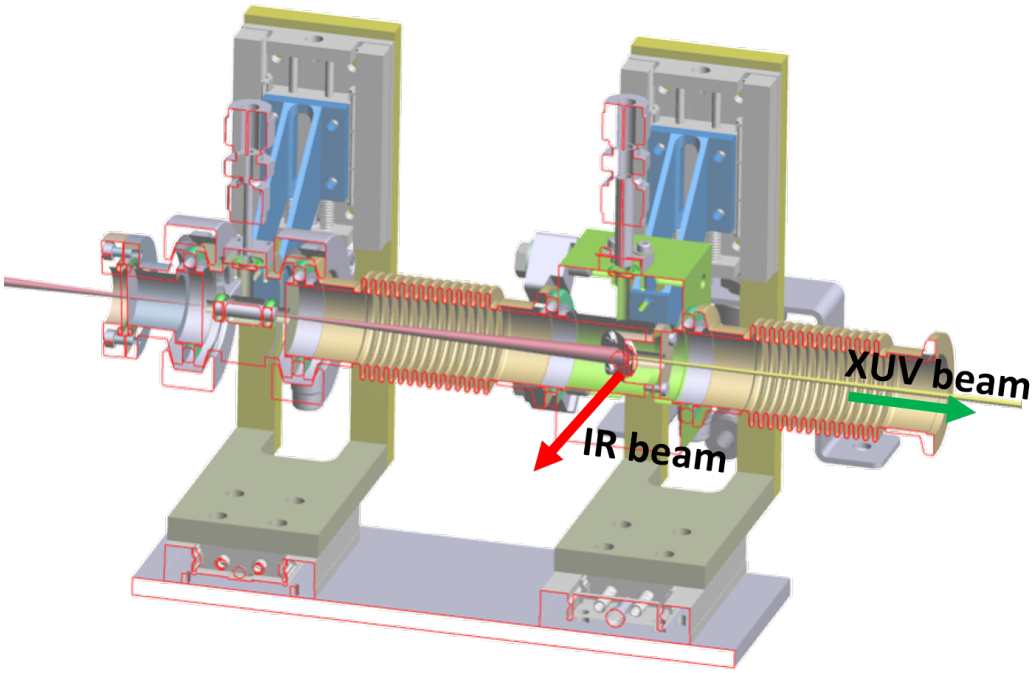


Figure VI.14 – Transverse section of the HHG chamber and the filtering chamber.

Analyzing figure VI.14, we can see that the *filtering chamber*, inside which the holed mirror is placed is mounted on the same translation system as the HHG chamber. In between flexible connections are used to guarantee a separate adjustment of each chamber. The reflected IR beam passes through a fused silica window and can be used as a diagnostic. This beam can be used, for example, to optimize the alignment of the HHG chamber. A fraction of the IR beam is transmitted through the holed mirror together with the XUV beam. We can estimate the transmitted fraction for the three capillaries diameter case. We want to minimize the residual transmitted IR without loosing the XUV part. For this reason, the distance between the capillary end and the hole of the mirror is changed for the different capillary diameters. In table VI.1, the resulting optimized cases for the capillaries of internal diameter of 60 $\mu$m, 80 $\mu$m are shown. In all considered case the XUV beam is completely transmitted through the mirror hole. As can be seen looking at the general scheme in VI.12, before the detection chamber the XUV and the remaining IR fraction passes through a filter. This filter is used for selected part of the harmonics spectrum we want. For the case of the HHG at 13 nm, we will use a Zr 200 nm thick filter. Considering the very small thickness, this filter is very fragile. The impinging average power density must be kept as low as possible. The filter damage threshold is not specified by the manufacturer and it is very difficult to estimate because it can depend on the size of the filter, on the way the filter is mounted in addition to the laser operation conditions. To have an idea of reported case situations, where the filter is not damaged we can refer to the works of Gonzalez et al. [Gonzalez *et al.* , 2018] and Comby et al. [Comby *et al.* , 2018]. In these cases, the driver laser is very similar to the one we consider for the HHG line design. In our case the transmitted IR is low, as we have shown. We can estimate a power density on the filter surface in the two inner diameters capillaries cases. The results are tabulated in the table VI.1, where we have considered 12 W of average input power in the IR and an ideal

transmission of the capillary of 90 %. The power density is calculated considering the beam size on the filter comparable to the filtering hole diameter. The power density is especially low for the 60 $\mu$m capillary case, because of the high divergence of the beam at the capillary output.

| **IR filtering residual percentage** | | |
|---|---|---|
| **Capillary ID [$\mu$m]** | **60** | **80** |
| **Transmitted % IR power [a.u.]** | 4.3 | 4.9 |
| **Distance capillary end - filtering hole [mm]** | 200 | 250 |
| **Power density on Zr filter [$\frac{W}{cm^2}$]** | 59.5 | 67.47 |

Table VI.1 – Results on IR filtering.

### 3.2.3 Detection/imaging chamber

The last part of our HHG line, evidenced in red in figure VI.12, has a double function: HHG detection and chamber for the *Coherent Diffraction Imaging (CDI)* experiment. Let us analyze the two different setups in the next paragraphs.

**HHG detection: XUV spectrometer** In this part, the HHG spectrum is detected. For this scope, we need a diffraction grating and an XUV detector. In our case, we have chosen a commercial customized XUV transmission grating (TG) (*Eulitha*[1]) and an XUV camera (i-kon M, *Andor*[2]) for the XUV spectrometer. The transmission grating is realized on a substrate of 100 nm SiN using a lithographic technique and is coated with a 60 nm thick Cr film. The SiN is engraved to obtain the grating structure. The transmission of the grating is measured by the manufacture to be between 3 % and 4 % around the 13 nm wavalength. Two different groove densities of 5500 lines/mm and 2750 lines/mm are realized in order to offer a certain flexibility. The groove density chosen and the distance between TG and detector is determining the spatial resolution of the detected harmonics. The more harmonic orders we detect on the camera sensor, the less spatially resolved they are.
The XUV camera has a square CCD sensor of 1024 pixels with 13 $\mu$m side. It is mounted on one of the side of the detection chamber. The distance between the grating and the camera sensor and the groove density chosen determines the number of detected harmonics in the bandwidth around 13 nm and the spatial detection resolution. It can be understood by looking at the scheme in figure VI.15(a), a top view of the detection chamber configuration. The XUV camera is plugged slightly off-centered with respect to the HHG axis. In this way, the 1st order of the grating is illuminating the camera. As we have said the bandwidth of harmonics detected by the camera depends on the distance of the transmission grating, the groove density chosen and the range of harmonics we want to detect. The circular chamber has a diameter of 400 mm. This means that several different positions of the TG can be adopted for different HH detection. As an example we can detect the wavelength range 8-20 nm using the 5500 grove density with a distance of 200 mm between the CCD and the grating.

[1] www.eulitha.com
[2] andor.oxinst.com

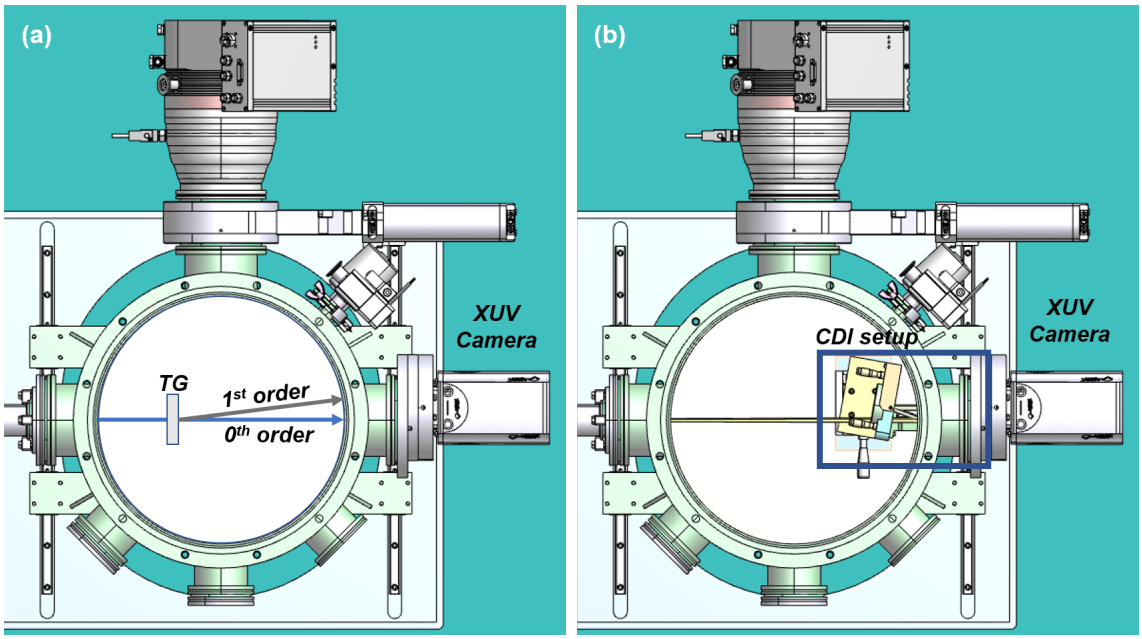


Figure VI.15 – (a) Detection chamber scheme. TG: Transmission Grating. (b) CDI chamber experiment.

**CDI chamber configuration** The detection chamber can be used to perform CDI experiments. The corresponding configuration can be seen in VI.15(b). For the CDI experiment we use the XUV camera as detector. The HHG light in the range around 13 nm is focused on the sample we want to image using an off-axis parabola with an angle of incidence of 20 degree. The parabola is realized via a multi-layered coating allowing to select the wavelength bandwidth we want to use for the imaging experiment. A reflective mirror allows to obtain this grazing angle reflecting the XUV beam. The focal length of the parabola is 100 mm. Considering we need to collect the whole diffracted beam after the focus, we need the sample to be located very close to the XUV camera. To allow this, mechanical mounts are realized allowing to install the sample inside the access where the camera is plugged. The CDI setup is particularly compact as can be seen in figure VI.15(b) in the blue square.
An interesting technical point is that the relative position of the XUV beam axis with respect to the camera has to be different between the detection and CDI experiment chamber configuration. In particular a position difference of about 10 mm is required for passing from one to the other configuration. The whole chamber, where the camera is plugged, is placed, for this reason, on a translation stage.

## 4 Conclusions

In this chapter we have presented the design of an HHG line for CDI experiment at 13 nm. The setup has been optimized on the parameters of the 2-optical cycle fiber source realized in the context of the HELLIX project [Lavenu *et al.* , 2019].
We have recalled some theoretical principles of HHG, in particular the phase matching for a capillary interaction configuration. We have, then, presented the designed setup highlighting the particular features we have studied for the setup. The presented setup is realized with a high degree of versatility in mind. Although we have considered the system only for the wavelength range around the 13 nm, different HHG XUV ranges can be obtained with minimal setup modifications. The complete line is conceived as composed by three blocks: HHG chamber, IR filtering and XUV spectrometer/CDI experiment part. Let us consider as a different example an experiment using HHG around 40 nm instead of 13 nm. To efficiently generate these harmonics we use the same HHG interaction chamber. We can use either Ar or Ne lowering the pressure with respect to the 13 nm case for phase matching the interaction. The IR filtering through the holed mirror is optimized changing the distance between the capillary end and the holed mirror adding or shortening the length of the tubes connecting the two chambers. The spectrometer chamber configuration is changed modifying the distance between the transmission grating and the XUV camera. Finally, for the CDI experiment, only the multi-layer coating of the parabola has to be changed for matching the modified wavelength range. We can conclude that the system is easily adaptable to a large range of XUV wavelengths.
The whole setup measures only (125 cm x 70 cm)[1]. This small size, along with the compactness of the driver laser [Lavenu *et al.* , 2019], will constitute a demonstration of a really table-top XUV experiment.
In the next months the designed source will be tested and optimized for the HHG CDI experiment. In a second time, the CEP-stability of the driver laser will be added as an upgrade for the source. For the CDI experiment, this last improvement will allow to use a stable wavelenth range near the XUV cut-off, improving the image reconstruction quality.
We are working, in collaboration with T. Auguste (LIDYL, CEA-Saclay) to simulate the capillary phase matching specific conditions for HHG for our laser and gas parameters.

[1] Considering the 13 nm optimized configuration.

# Chapter VII

# Conclusions and perspectives

This thesis has been realized around two main research axes: the demonstration of the CEP-stabilization of a high repetition rate all-Yb fiber laser source and the design of a laser parameters-optimized CDI application ready sub-20 nm HHG beamline.

**CEP-stabilization of an Yb-based high repetition rate source** The complete CEP-stability compatibility with a full Yb-doped CPA based source has been shown. In particular the CEP-stable chain has been realized in two main parts: the CEP-stable seeder and the Yb-doped CEP-stable amplifier.

In the first block, the CEP is passively stabilized pumping an OPA setup using a commercial Yb-doped amplifier laser. The CEP-stable seeder delivers 400 nJ, 150 fs long pulses with a repetition rate of 100 kHz. The system can be operated at repetition rate from 100 kHz to 500 kHz changing the operation mode of the pump laser. An unprecedented detailed CEP characterization at this high repetition rate has been realized using three different detection methods. A single shot measured CEP-stability lower than 300 mrad rms over 10 seconds has been shown. The robustness and compactness of the system has proven the negligible impact of slow environmental effects on the CEP. This measurement is probably limited by the measurement setup low input energy. In the future, a dedicated fiber based f-2f will be developed to realize a proper CEP measurement at low energy level of some tens of nJ.

The RIN has been introduced as a key parameter in the characterization of femtosecond laser sources. In particular, it has been shown the strong impact of the pump laser RIN in a passively stabilized setup as the one we have presented. We have shown as implementing an oscillator synchronous pulse-picking scheme in the pump laser, the RIN is reduced of 25 % with respect to the standard, asynchronous case. The improvement is linearly reported to the CEP noise. The lowest measured CEP noise case is for the one where the synchronous PP is implemented.

The CEP-seeder represents a good comparison point with the oscillator class lasers, showing similar performances in terms of CEP-stability.

The Yb-doped fiber CEP amplifier is presented as the combination of a CPA amplification scheme and a nonlinear step of post-compression by a MPC. We have shown that the system delivers pulses at 100 kHz with 100 fs pulse duration and 30 $\mu$J of energy. The configuration represents a test setup including all the CEP-stability critical elements for the few-cycle Yb-doped fiber sources. The compressor has been shown to be the most sensitive element, coupling environmental instabilities to the CEP noise. The highly nonlinear steps where high B-integrals are accumulated are critical as well because the AN is efficiently coupled to the CEP noise. We have implemented a feedback loop to correct the CEP drift accumulated because of these elements. The CEP in-loop and out-of-loop detection has shown that the feedback corrects this added noises contributions. The CEP noise is detected using a Fringeezz, and corrected acting on an integrated EOM. The feedback has been shown to be limited to the Fringeezz detection

speed of 10 kHz. An integrated CEP noise of 325 mrad have been measured in the BW [1 Hz; 50 kHz]. The measurement realized using the BIRD technique measuring every laser shot at 100 kHz is the most complete measurement realized using an f-2f CEP measurement scheme on an amplified system at this repetition rate. The robustness of the system and the slow CEP drift efficient correction has been demonstrated measuring a CEP noise of 375 mrad rms over one hour. In the future, the whole laser system will be upscaled at higher repetition rates complicating even more the precise CEP characterization. For these reasons new detection methods have to be implemented.

We have discussed also the impact of the RIN in the amplified source. As a first result we have shown that the saturation effects, in the OPA and in fiber amplifier, allows a reduction of the RIN of the output of the amplified source with respect to the commercial pump laser. However, we have also shown that the RIN of the pump laser remains critical for the CEP noise of the amplified system. In particular, we have shown that an added white noise corresponding to 1 % peak-to-peak of the pump laser average power produced an added CEP-noise of 50 mrad rms in the output.

**Design of CDI HHG sub-20 nm line** In the last chapter we have presented the design of the sub-20 nm HHG line for the CDI experiment.
To reach efficiently extreme UV part of the spectrum with a high average power system, we have design a HHG system based on a gas-filled capillary. The system is composed by three modules: HHG generation, IR filtering, and detection/CDI chamber. We have simulated the gas injection system, pointing out its importance for the gas pressure uniformity along the capillary length. It has been shown that for a two centimeter long medium, three holes with a diameter size comparable to the inner diameter of the capillary, ensure the requirements of gas pressure. The technical challenging point of drilling 2.5 mm deep and 100 $\mu$m large holes is presented. The FLICE technique is used to overcome this point and realizing the gas injection for the capillary. We have studied the problem of managing and filtering the remaining high average power of the HHG driving IR beam. The high average power proper to the high repetition rate can be the first source of damage for XUV optics. In our configuration this is true for the ultra-thin XUV metallic filters and for the XUV camera detector.
The last part of the designed setup has the double function of XUV spectrometer and CDI experiment. The spectrometer is composed of an XUV commercial transmission grating and an XUV camera. It is set for detection in the range 8-20 nm. A larger analysis detection wavelength range can be reached using the same components with slight modifications in their arrangement. The same experiment chamber, using the same XUV camera, can be used for CDI experiments.
In the next months the designed setup will be used for the first tests of HHG using a fiber high energy, high repetition rate, two optical cycle source [Lavenu *et al.* , 2019].

To conclude, this thesis work opens the way for the a new generation of HHG-based high repetition rate sources in the XUV. In the future the two main axes of this work will be gathered toghether. This will be possible applying the demonstrated CEP-stabilization techniques on the laser setup we have used for the HHG line setup. The industry ready robustness and reduced size of the system will allow real table-top CDI experiments.

In a more general vision, the developed high repetition rate HHG beamline can be used for other application than CDI. As already mentioned in the introduction COLTRIMS requires high repetition rate sources. The source is also suitable for photoemission spectroscopy purposes such as angle resolved photoemission spectroscopy (ARPES). These applications are nowadays moslty realized using sinchrothrones or free-electron laser facilities. The new generation of high repetition rate HHG sources will represent a turn-key, low cost alternative for these experiments.

# Bibliography


[Agrawal, 2000] Agrawal, Govind P. 2000. Nonlinear fiber optics. *Pages 195–211 of: Nonlinear Science at the Dawn of the 21st Century*. Springer.

[Alfano & Shapiro, 1970] Alfano, Robert R, & Shapiro, SL. 1970. Observation of self-phase modulation and small-scale filaments in crystals and glasses. *Physical Review Letters*, **24**(11), 592.

[Aoyama *et al.* , 2003] Aoyama, M, Yamakawa, K, Akahane, Y, Ma, J, Inoue, N, Ueda, H, & Kiriyama, H. 2003. 0.85-PW, 33-fs Ti: sapphire laser. *Optics letters*, **28**(17), 1594–1596.

[Apolonski *et al.* , 2000] Apolonski, A, Poppe, A, Tempea, G, Spielmann, Ch, Udem, Th, Holzwarth, RHTW, Hänsch, Theodor W, & Krausz, Ferenc. 2000. Controlling the phase evolution of few-cycle light pulses. *Physical Review Letters*, **85**(4), 740.

[Arditi & Picqué, 1980] Arditi, M, & Picqué, JL. 1980. A cesium beam atomic clock using laser optical pumping. Preliminary tests. *Journal de Physique Lettres*, **41**(16), 379–381.

[Åström & Hägglund, 1995] Åström, Karl Johan, & Hägglund, Tore. 1995. *PID controllers: theory, design, and tuning*. Vol. 2. Instrument society of America Research Triangle Park, NC.

[Balčiūnas *et al.* , 2014] Balčiūnas, Tadas, Flöry, Tobias, Baltuška, Andrius, Stanislauskas, Tomas, Antipenkov, Roman, Varanavičius, Arūnas, & Steinmeyer, Günter. 2014. Direct carrier-envelope phase control of an amplified laser system. *Optics letters*, **39**(6), 1669–1672.

[Baltuška *et al.* , 2002] Baltuška, Andrius, Fuji, Takao, & Kobayashi, Takayoshi. 2002. Controlling the carrier-envelope phase of ultrashort light pulses with optical parametric amplifiers. *Physical review letters*, **88**(13), 133901.

[Baltuska *et al.* , 2003] Baltuska, Andrius, Uiberacker, Matthias, Goulielmakis, Eleftherios, Kienberger, Reinhard, Yakovlev, Vladislav S, Udem, Thomas, Hansch, Theodor W, & Krausz, Ferenc. 2003. Phase-controlled amplification of few-cycle laser pulses. *IEEE Journal of Selected Topics in Quantum Electronics*, **9**(4), 972–989.

[Bartels *et al.* , 2002] Bartels, Randy A, Paul, Ariel, Green, Hans, Kapteyn, Henry C, Murnane, Margaret M, Backus, Sterling, Christov, Ivan P, Liu, Yanwei, Attwood, David, & Jacobsen, Chris. 2002. Generation of spatially coherent light at extreme ultraviolet wavelengths. *Science*, **297**(5580), 376–378.

[Baudisch *et al.* , 2016] Baudisch, M, Wolter, B, Pullen, M, Hemmer, M, & Biegert, Jens. 2016. High power multi-color OPCPA source with simultaneous femtosecond deep-UV to mid-IR outputs. *Optics letters*, **41**(15), 3583–3586.

[Baumgartner & Byer, 1979] Baumgartner, R, & Byer, R. 1979. Optical parametric amplification. *IEEE Journal of Quantum Electronics*, **15**(6), 432–444.

[Birks *et al.* , 1997] Birks, Tim A, Knight, Jonathan C, & Russell, P St J. 1997. Endlessly single-mode photonic crystal fiber. *Optics letters*, **22**(13), 961–963.

[Borchers *et al.* , 2011] Borchers, B, Koke, S, Husakou, A, Herrmann, J, & Steinmeyer, G. 2011. Carrier-envelope phase stabilization with sub-10 as residual timing jitter. *Optics letters*, **36**(21), 4146–4148.

[Boullet *et al.* , 2009] Boullet, Johan, Zaouter, Yoann, Limpert, Jens, Petit, Stéphane, Mairesse, Yann, Fabre, Baptiste, Higuet, Julien, Mével, Eric, Constant, Eric, & Cormier, Eric. 2009. High-order harmonic generation at a megahertz-level repetition rate directly driven by an ytterbium-doped-fiber chirped-pulse amplification system. *Optics letters*, **34**(9), 1489–1491.

[Brabec & Kapteyn, 2008] Brabec, Thomas, & Kapteyn, Henry. 2008. *Strong field laser physics*. Vol. 1. Springer.

[Brabec & Krausz, 2000] Brabec, Thomas, & Krausz, Ferenc. 2000. Intense few-cycle laser fields: Frontiers of nonlinear optics. *Reviews of Modern Physics*, **72**(2), 545.

[Brodeur & Chin, 1999] Brodeur, A, & Chin, SL. 1999. Ultrafast white-light continuum generation and self-focusing in transparent condensed media. *JOSA B*, **16**(4), 637–650.

[Budriūnas *et al.* , 2015] Budriūnas, Rimantas, Stanislauskas, Tomas, & Varanavičius, Arūnas. 2015. Passively CEP-stabilized frontend for few cycle terawatt OPCPA system. *Journal of Optics*, **17**(9), 094008.

[Budunoğlu *et al.* , 2009] Budunoğlu, Ibrahim Levent, Ülgüdür, Coşkun, Oktem, Bulent, & Ilday, Fatih Ömer. 2009. Intensity noise of mode-locked fiber lasers. *Optics letters*, **34**(16), 2516–2518.

[Butkus *et al.* , 2004] Butkus, R, Danielius, R, Dubietis, A, Piskarskas, A, & Stabinis, A. 2004. Progress in chirped pulse optical parametric amplifiers. *Applied Physics B*, **79**(6), 693–700.

[Calendron *et al.* , 2015] Calendron, Anne-Laure, Çankaya, Hüseyin, Cirmi, Giovanni, & Kärtner, Franz X. 2015. White-light generation with sub-ps pulses. *Optics express*, **23**(11), 13866–13879.

[Cerullo & De Silvestri, 2003] Cerullo, Giulio, & De Silvestri, Sandro. 2003. Ultrafast optical parametric amplifiers. *Review of scientific instruments*, **74**(1), 1–18.

[Cerullo *et al.* , 2011] Cerullo, Giulio, Baltuška, A, Mücke, Oliver D, & Vozzi, Caterina. 2011. Few-optical-cycle light pulses with passive carrier-envelope phase stabilization. *Laser & Photonics Reviews*, **5**(3), 323–351.

[Chalus *et al.* , 2009] Chalus, Olivier, Bates, Philip K, Smolarski, Mathias, & Biegert, Jens. 2009. Mid-IR short-pulse OPCPA with micro-Joule energy at 100kHz. *Optics express*, **17**(5), 3587–3594.

[Chang, 2006] Chang, Zenghu. 2006. Carrier-envelope phase shift caused by grating-based stretchers and compressors. *Applied optics*, **45**(32), 8350–8353.

[Chen *et al.* , 2010] Chen, M-C, Arpin, P, Popmintchev, T, Gerrity, M, Zhang, B, Seaberg, M, Popmintchev, D, Murnane, MM, & Kapteyn, HC. 2010. Bright, coherent, ultrafast soft x-ray harmonics spanning the water window from a tabletop light source. *Physical Review Letters*, **105**(17), 173901.

[Chen *et al.* , 2011] Chen, X, Malvache, A, Ricci, A, Jullien, A, & Lopez-Martens, R. 2011. Efficient hollow fiber compression scheme for generating multi-mJ, carrier-envelope phase stable, sub-5 fs pulses. *Laser Physics*, **21**(1), 198–201.

[Cingöz *et al.* , 2011] Cingöz, A, Yost, DC, Allison, TK, Ruehl, A, Fermann, ME, Hartl, I, & Ye, J. 2011. Broadband phase noise suppression in a Yb-fiber frequency comb. *Optics letters*, **36**(5), 743–745.

[Cingöz *et al.* , 2012] Cingöz, Arman, Yost, Dylan C, Allison, Thomas K, Ruehl, Axel, Fermann, Martin E, Hartl, Ingmar, & Ye, Jun. 2012. Direct frequency comb spectroscopy in the extreme ultraviolet. *Nature*, **482**(7383), 68.

[Coen *et al.* , 2001] Coen, Stephane, Chau, Alvin Hing Lun, Leonhardt, Rainer, Harvey, John D, Knight, Jonathan C, Wadsworth, William J, & Russell, Philip St J. 2001. White-light supercontinuum generation with 60-ps pump pulses in a photonic crystal fiber. *Optics letters*, **26**(17), 1356–1358.

[Comby *et al.* , 2018] Comby, Antoine, Descamps, Dominique, Gonzalez, Aura, Guichard, Florent, Petit, Stephane, Zaouter, Yoann, & Mairesse, Yann. 2018. High-harmonics of harmonics of a fiber laser: a milliwatt XUV ultrashort source. *arXiv preprint arXiv:1811.05178*.

[Constant *et al.* , 1999] Constant, E, Garzella, D, Breger, P, Mével, E, Dorrer, Ch, Le Blanc, C, Salin, F, & Agostini, P. 1999. Optimizing high harmonic generation in absorbing gases: Model and experiment. *Physical Review Letters*, **82**(8), 1668.

[Cruz *et al.* , 1988] Cruz, CH Brito, Becker, PC, Fork, Richard L, & Shank, Charles V. 1988. Phase correction of femtosecond optical pulses using a combination of prisms and gratings. *Optics letters*, **13**(2), 123–125.

[Cundiff, 2002] Cundiff, Steven T. 2002. Phase stabilization of ultrashort optical pulses. *Journal of Physics D: Applied Physics*, **35**(8), R43.

[Davenport *et al.* , 1958] Davenport, Wilbur B, Root, William L, *et al.* . 1958. *An introduction to the theory of random signals and noise*. Vol. 159. McGraw-Hill New York.

[de Vries *et al.* , 2015] de Vries, Oliver, Saule, Tobias, Plötner, Marco, Lücking, Fabian, Eidam, Tino, Hoffmann, Armin, Klenke, Arno, Hädrich, Steffen, Limpert, Jens, Holzberger, Simon, *et al.* . 2015. Acousto-optic pulse picking scheme with carrier-frequency-to-pulse-repetition-rate synchronization. *Optics express*, **23**(15), 19586–19595.

[Dubietis *et al.* , 1992] Dubietis, A, Jonusauskas, G, & Piskarskas, A. 1992. Powerful femtosecond pulse generation by chirped and stretched pulse parametric amplification in BBO crystal. *Optics Communications*, **88**(4-6), 437–440.

[Dubietis *et al.* , 2017] Dubietis, Audrius, TamoÅ¡auskas, G, Å uminas, R, Jukna, Vytautas, & Couairon, Arnaud. 2017. Ultrafast supercontinuum generation in bulk condensed media. *Lithuanian Journal of Physics*, **57**(3), 113–157.

[Durfee III *et al.* , 1999] Durfee III, Charles G, Rundquist, Andy R, Backus, Sterling, Herne, Catherine, Murnane, Margaret M, & Kapteyn, Henry C. 1999. Phase matching of high-order harmonics in hollow waveguides. *Physical Review Letters*, **83**(11), 2187.

[Eisberg & Resnick, 1974] Eisberg, Robert, & Resnick, Robert. 1974. *Quantum physics*. John Wiley New York.

[Feng *et al.* , 2013] Feng, C, Hergott, J-F, Paul, P-M, Chen, X, Tcherbakoff, O, Comte, M, Gobert, O, Reduzzi, M, Calegari, F, Manzoni, C, *et al.* . 2013. Complete analog control of the carrier-envelope-phase of a high-power laser amplifier. *Optics express*, **21**(21), 25248–25256.

[Ferray *et al.* , 1988] Ferray, M, L'Huillier, Anne, Li, XF, Lompre, LA, Mainfray, G, & Manus, C. 1988. Multiple-harmonic conversion of 1064 nm radiation in rare gases. *Journal of Physics B: Atomic, Molecular and Optical Physics*, **21**(3), L31.

[Fuji *et al.* , 2004] Fuji, Takao, Apolonski, Alexander, & Krausz, Ferenc. 2004. Self-stabilization of carrier-envelope offset phase by use of difference-frequency generation. *Optics letters*, **29**(6), 632–634.

[Fuji *et al.* , 2005] Fuji, Takao, Rauschenberger, Jens, Apolonski, Alexander, Yakovlev, Vladislav S, Tempea, Gabriel, Udem, Thomas, Gohle, Christoph, Hänsch, Theodor W, Lehnert, Walter, Scherer, Michael, *et al.* . 2005. Monolithic carrier-envelope phase-stabilization scheme. *Optics letters*, **30**(3), 332–334.

[Fuji *et al.* , 2006] Fuji, Takao, Ishii, Nobuhisa, Teisset, Catherine Y, Gu, Xun, Metzger, Th, Baltuska, Andrius, Forget, N, Kaplan, D, Galvanauskas, A, & Krausz, Ferenc. 2006. Parametric amplification of few-cycle carrier-envelope phase-stable pulses at 2.1 $\mu$m. *Optics letters*, **31**(8), 1103–1105.

[Gardner *et al.* , 2017] Gardner, Dennis F, Tanksalvala, Michael, Shanblatt, Elisabeth R, Zhang, Xiaoshi, Galloway, Benjamin R, Porter, Christina L, Karl Jr, Robert, Bevis, Charles, Adams, Daniel E, Kapteyn, Henry C, *et al.* . 2017. Subwavelength coherent imaging of periodic samples using a 13.5 nm tabletop high-harmonic light source. *Nature Photonics*, **11**(4), 259.

[Gibson *et al.* , 2003] Gibson, Emily A, Paul, Ariel, Wagner, Nick, Gaudiosi, David, Backus, Sterling, Christov, Ivan P, Aquila, Andy, Gullikson, Eric M, Attwood, David T, Murnane, Margaret M, *et al.* . 2003. Coherent soft x-ray generation in the water window with quasi-phase matching. *Science*, **302**(5642), 95–98.

[Gobert *et al.* , 2011] Gobert, O, Paul, PM, Hergott, JF, Tcherbakoff, O, Lepetit, F, D'Oliveira, P, Viala, F, & Comte, M. 2011. Carrier-envelope phase control using linear electro-optic effect. *Optics express*, **19**(6), 5410–5418.

[Goh, 2015] Goh, Siew Jean. 2015. Toward spatial and spectral control of waveguided high-harmonic generation.

[Goh *et al.* , 2015] Goh, SJ, Tao, Y, van der Slot, Petrus JM, Bastiaens, HJM, Herek, J, Biedron, SG, Danailov, MB, Milton, SV, & Boller, K-J. 2015. Single-shot fluctuations in waveguided high-harmonic generation. *Optics express*, **23**(19), 24888–24902.

[Goh *et al.* , 2016] Goh, SJ, Reinink, Johan, Tao, Y, van der Slot, Petrus JM, Bastiaens, HJM, Herek, Jennifer Lynn, Biedron, SG, Milton, SV, & Boller, K-J. 2016. Spectral control of high-harmonic generation via drive laser pulse shaping in a wide-diameter capillary. *Optics express*, **24**(2), 1604–1615.

[Golinelli *et al.* , 2017] Golinelli, A, Chen, X, Gontier, E, Bussière, B, Tcherbakoff, O, Natile, M, dâOliveira, P, Paul, P-M, & Hergott, J-F. 2017. Original Ti: Sa 10 kHz front-end design delivering 17 fs, 170 mrad CEP stabilized pulses up to 5 W. *Optics letters*, **42**(12), 2326–2329.

[Gonzalez *et al.* , 2018] Gonzalez, Aura Inés, Jargot, Gaëtan, Rigaud, Philippe, Lavenu, Loic, Guichard, Florent, Comby, Antoine, Auguste, Thierry, Sublemontier, Olivier, Bougeard,

Michel, Zaouter, Yoann, *et al.* . 2018. Spatio-spectral structures in high harmonic generation driven by tightly focused high repetition rate lasers. *JOSA B*, **35**(4), A6–A14.

[Gu *et al.* , 2009] Gu, Xun, Marcus, Gilad, Deng, Yunpei, Metzger, Thomas, Teisset, Catherine, Ishii, Nobuhisa, Fuji, Takao, Baltuska, Andrius, Butkus, Rytis, Pervak, Volodymyr, *et al.* . 2009. Generation of carrier-envelope-phase-stable 2-cycle 740-$\mu$J pulses at 2.1-$\mu$m carrier wavelength. *Optics express*, **17**(1), 62–69.

[Guiraud *et al.* , 2016] Guiraud, Germain, Traynor, Nicholas, & Santarelli, Giorgio. 2016. High-power and low-intensity noise laser at 1064 nm. *Optics letters*, **41**(17), 4040–4043.

[Gürel *et al.* , 2014] Gürel, K, Elahi, P, Budunoğlu, L, Şenel, Ç, Paltani, P, & Ilday, FÖ. 2014. Prediction of pulse-to-pulse intensity fluctuation characteristics of high power ultrafast fiber amplifiers. *Applied Physics Letters*, **105**(1), 011111.

[Hädrich *et al.* , 2011] Hädrich, S, Carstens, H, Rothhardt, J, Limpert, J, & Tünnermann, A. 2011. Multi-gigawatt ultrashort pulses at high repetition rate and average power from two-stage nonlinear compression. *Optics express*, **19**(8), 7546–7552.

[Hädrich *et al.* , 2013] Hädrich, Steffen, Klenke, Arno, Hoffmann, Armin, Eidam, Tino, Gottschall, Thomas, Rothhardt, Jan, Limpert, Jens, & Tünnermann, Andreas. 2013. Nonlinear compression to sub-30-fs, 0.5 mJ pulses at 135 W of average power. *Optics letters*, **38**(19), 3866–3869.

[Hädrich *et al.* , 2014] Hädrich, Steffen, Klenke, Arno, Rothhardt, Jan, Krebs, Manuel, Hoffmann, Armin, Pronin, Oleg, Pervak, Vladimir, Limpert, Jens, & Tünnermann, Andreas. 2014. High photon flux table-top coherent extreme-ultraviolet source. *Nature Photonics*, **8**(10), 779.

[Hädrich *et al.* , 2015] Hädrich, Steffen, Krebs, Manuel, Hoffmann, Armin, Klenke, Arno, Rothhardt, Jan, Limpert, Jens, & Tünnermann, Andreas. 2015. Exploring new avenues in high repetition rate table-top coherent extreme ultraviolet sources. *Light: Science & Applications*, **4**(8), e320.

[Hädrich *et al.* , 2016] Hädrich, Steffen, Rothhardt, Jan, Krebs, Manuel, Demmler, Stefan, Klenke, Arno, Tünnermann, Andreas, & Limpert, Jens. 2016. Single-pass high harmonic generation at high repetition rate and photon flux. *Journal of Physics B: Atomic, Molecular and Optical Physics*, **49**(17), 172002.

[Hamm *et al.* , 2000] Hamm, Peter, Kaindl, Robert A, & Stenger, Jens. 2000. Noise suppression in femtosecond mid-infrared light sources. *Optics letters*, **25**(24), 1798–1800.

[Hamstra & Wendland, 1972] Hamstra, Robert H, & Wendland, Paul. 1972. Noise and frequency response of silicon photodiode operational amplifier combination. *Applied optics*, **11**(7), 1539–1547.

[Hänsch, 1972] Hänsch, Theodor W. 1972. Repetitively pulsed tunable dye laser for high resolution spectroscopy. *Applied Optics*, **11**(4), 895–898.

[Hänsch, 2006] Hänsch, Theodor W. 2006. Passion for precision (Nobel lecture). *ChemPhysChem*, **7**(6), 1170–1187.

[Hariharan, 2010] Hariharan, Parameswaran. 2010. *Basics of interferometry*. Elsevier.

[Haworth *et al.* , 2007] Haworth, CA, Chipperfield, LE, Robinson, JS, Knight, PL, Marangos, JP, & Tisch, JWG. 2007. Half-cycle cutoffs in harmonic spectra and robust carrier-envelope phase retrieval. *Nature Physics*, **3**(1), 52.

[Heyl *et al.* , 2012] Heyl, CM, Güdde, J, LâHuillier, Anne, & Höfer, U. 2012. High-order harmonic generation with $\mu$J laser pulses at high repetition rates. *Journal of Physics B: Atomic, Molecular and Optical Physics*, **45**(7), 074020.

[Hnatovsky *et al.* , 2006] Hnatovsky, C, Taylor, RS, Simova, E, Rajeev, PP, Rayner, DM, Bhardwaj, VR, & Corkum, PB. 2006. Fabrication of microchannels in glass using focused femtosecond laser radiation and selective chemical etching. *Applied Physics A*, **84**(1-2), 47–61.

[Holst, 1998] Holst, Gerald C. 1998. *Sampling, aliasing, and data fidelity for electronic imaging systems, communications and data acquisition.*

[Huang *et al.* , 2011] Huang, Shu-Wei, Cirmi, Giovanni, Moses, Jeffrey, Hong, Kyung-Han, Bhardwaj, Siddharth, Birge, Jonathan R, Chen, Li-Jin, Li, Enbang, Eggleton, Benjamin J, Cerullo, Giulio, *et al.* . 2011. High-energy pulse synthesis with sub-cycle waveform control for strong-field physics. *Nature photonics*, **5**(8), 475.

[Huber *et al.* , 2017] Huber, Marinus, Schweinberger, Wolfgang, Stutzki, Fabian, Limpert, Jens, Pupeza, Ioachim, & Pronin, Oleg. 2017. Active intensity noise suppression for a broadband mid-infrared laser source. *Optics express*, **25**(19), 22499–22509.

[Hutley, 1982] Hutley, Michael C. 1982. Diffraction gratings. *Techniques of Physics, London: Academic Press, 1982.*

[Hüve *et al.* , 2006] Hüve, J, Haarlammert, T, Steinbrück, T, Kutzner, J, Tsilimis, G, & Zacharias, H. 2006. High-flux high harmonic soft X-ray generation up to 10 kHz repetition rate. *Optics communications*, **266**(1), 261–265.

[Inoue & Mukai, 2002] Inoue, Kyo, & Mukai, Takaaki. 2002. Experimental Study on Noise Characteristics of a Gain-Saturated Fiber Optical Parametric Amplifier. *J. Lightwave Technol.*, **20**(6), 969.

[ISO 11554:2017, 2017] ISO 11554:2017. 2017 (Mar.). *Optics and photonics-Lasers and laser-related equipment â Test methods for laser beam power, energy and temporal characteristics.* Standard. International Organization for Standardization, Geneva, CH.

[Jahnke *et al.* , 2004] Jahnke, T, Weber, Th, Osipov, T, Landers, AL, Jagutzki, O, Schmidt, L Ph H, Cocke, CL, Prior, MH, Schmidt-Böcking, H, & Dörner, R. 2004. Multicoincidence studies of photo and Auger electrons from fixed-in-space molecules using the COLTRIMS technique. *Journal of Electron Spectroscopy and Related Phenomena*, **141**(2-3), 229–238.

[Jones *et al.* , 2000] Jones, David J, Diddams, Scott A, Ranka, Jinendra K, Stentz, Andrew, Windeler, Robert S, Hall, John L, & Cundiff, Steven T. 2000. Carrier-envelope phase control of femtosecond mode-locked lasers and direct optical frequency synthesis. *Science*, **288**(5466), 635–639.

[Jullien *et al.* , 2011] Jullien, Aurélie, Chen, X, Ricci, A, Rousseau, J-P, Lopez-Martens, R, Ramirez, LP, Papadopoulos, D, Pellegrina, A, Druon, Frédéric, & Georges, Patrick. 2011. High-fidelity front-end for high-power, high temporal quality few-cycle lasers. *Applied Physics B*, **102**(4), 769–774.

[Kafka & Baer, 1987] Kafka, JD, & Baer, T. 1987. Prism-pair dispersive delay lines in optical pulse compression. *Optics letters*, **12**(6), 401–403.

[Kakehata *et al.* , 2002] Kakehata, M, Fujihira, Y, Takada, H, Kobayashi, Y, Torizuka, K, Homma, T, & Takahashi, H. 2002. Measurements of carrier-envelope phase changes of 100-Hz amplified laser pulses. *Applied Physics B*, **74**(1), s43–s50.

[Kazamias *et al.* , 2011] Kazamias, S, Daboussi, S, Guilbaud, O, Cassou, K, Ros, D, Cros, B, & Maynard, G. 2011. Pressure-induced phase matching in high-order harmonic generation. *Physical Review A*, **83**(6), 063405.

[Kim & Song, 2016] Kim, Jungwon, & Song, Youjian. 2016. Ultralow-noise mode-locked fiber lasers and frequency combs: principles, status, and applications. *Advances in Optics and Photonics*, **8**(3), 465–540.

[Klein & Kafka, 2010] Klein, Julien, & Kafka, James D. 2010. The Ti: Sapphire laser: the flexible research tool. *Nature Photonics*, **4**(5), 289.

[Klenner *et al.* , 2013] Klenner, Alexander, Emaury, Florian, Schriber, Cinia, Diebold, Andreas, Saraceno, Clara J, Schilt, Stéphane, Keller, Ursula, & Südmeyer, Thomas. 2013. Phase-stabilization of the carrier-envelope-offset frequency of a SESAM modelocked thin disk laser. *Optics express*, **21**(21), 24770–24780.

[Koke *et al.* , 2008] Koke, Sebastian, Grebing, Christian, Manschwetus, Bastian, & Steinmeyer, Günter. 2008. Fast f-to-2f interferometer for a direct measurement of the carrier-envelope phase drift of ultrashort amplified laser pulses. *Optics letters*, **33**(21), 2545–2547.

[Koke *et al.* , 2010] Koke, Sebastian, Grebing, Christian, Frei, Harald, Anderson, Alexandria, Assion, Andreas, & Steinmeyer, Günter. 2010. Direct frequency comb synthesis with arbitrary offset and shot-noise-limited phase noise. *Nature Photonics*, **4**(7), 462.

[Koplow *et al.* , 2000] Koplow, Jeffrey P, Kliner, Dahv AV, & Goldberg, Lew. 2000. Single-mode operation of a coiled multimode fiber amplifier. *Optics letters*, **25**(7), 442–444.

[Krause *et al.* , 1992] Krause, Jeffrey L, Schafer, Kenneth J, & Kulander, Kenneth C. 1992. High-order harmonic generation from atoms and ions in the high intensity regime. *Physical Review Letters*, **68**(24), 3535.

[Krausz, 2016] Krausz, Ferenc. 2016. The birth of attosecond physics and its coming of age. *Physica Scripta*, **91**(6), 063011.

[Krebs *et al.* , 2013] Krebs, Manuel, Hädrich, Steffen, Demmler, Stefan, Rothhardt, Jan, Zaïr, Amelle, Chipperfield, Luke, Limpert, Jens, & Tünnermann, Andreas. 2013. Towards isolated attosecond pulses at megahertz repetition rates. *Nature photonics*, **7**(7), 555.

[Lavenu *et al.* , 2017] Lavenu, L, Natile, M, Guichard, Florent, Zaouter, Y, Hanna, Marc, Mottay, E, & Georges, P. 2017. High-energy few-cycle Yb-doped fiber amplifier source based on a single nonlinear compression stage. *Optics express*, **25**(7), 7530–7537.

[Lavenu *et al.* , 2019] Lavenu, L, Natile, M, Guichard, F, Délen, X, Hanna, M, Zaouter, Y, & Georges, P. 2019. High-power two-cycle ultrafast source based on hybrid nonlinear compression. *Optics express*, **27**(3), 1958–1967.

[Li *et al.* , 2008] Li, Chengquan, Mashiko, Hiroki, Wang, He, Moon, Eric, Gilbertson, Steve, & Chang, Zenghu. 2008. Carrier-envelope phase stabilization by controlling compressor grating separation. *Applied Physics Letters*, **92**(19), 191114.

[Li *et al.* , 2018] Li, Wenqi, Gan, Zebiao, Yu, Lianghong, Wang, Cheng, Liu, Yanqi, Guo, Zhen, Xu, Lu, Xu, Min, Hang, Yin, Xu, Yi, *et al.* . 2018. 339 J high-energy Ti: sapphire chirped-pulse amplifier for 10 PW laser facility. *Optics letters*, **43**(22), 5681–5684.

[Liehl *et al.* , 2017] Liehl, Andreas, Fehrenbacher, David, Sulzer, Philipp, Leitenstorfer, Alfred, & Seletskiy, Denis V. 2017. Ultrabroadband out-of-loop characterization of the carrier-envelope phase noise of an offset-free Er: fiber frequency comb. *Optics letters*, **42**(10), 2050–2053.

[Limpert *et al.* , 2004] Limpert, J, Liem, A, Reich, M, Schreiber, T, Nolte, S, Zellmer, H, Tünnermann, A, Broeng, J, Petersson, A, & Jakobsen, C. 2004. Low-nonlinearity single-transverse-mode ytterbium-doped photonic crystal fiber amplifier. *Optics Express*, **12**(7), 1313–1319.

[Limpert *et al.* , 2005] Limpert, J, Deguil-Robin, N, Manek-Hönninger, I, Salin, F, Röser, F, Liem, A, Schreiber, T, Nolte, S, Zellmer, H, Tünnermann, A, & others. 2005. High-power rod-type photonic crystal fiber laser. *Optics Express*, **13**(4), 1055–1058.

[Limpert *et al.* , 2012] Limpert, Jens, Stutzki, Fabian, Jansen, Florian, Otto, Hans-JÃ¼rgen, Eidam, Tino, Jauregui, Cesar, & TÃ¼nnermann, Andreas. 2012. Yb-doped large-pitch fibres: effective single-mode operation based on higher-order mode delocalisation. *Light: Science & Applications*, **1**(4), e8.

[Lu *et al.* , 2018] Lu, Chih-Hsuan, Witting, Tobias, Husakou, Anton, Vrakking, Marc JJ, Kung, AH, & Furch, Federico J. 2018. Sub-4 fs laser pulses at high average power and high repetition rate from an all-solid-state setup. *Optics express*, **26**(7), 8941–8956.

[Lücking, 2014] Lücking, Fabian. 2014. *Carrier-envelope phase control for the advancement of attosecond pulse generation.* Ph.D. thesis, lmu.

[Lücking *et al.* , 2012] Lücking, Fabian, Assion, Andreas, Apolonski, Alexander, Krausz, Ferenc, & Steinmeyer, Günter. 2012. Long-term carrier-envelope-phase-stable few-cycle pulses by use of the feed-forward method. *Optics letters*, **37**(11), 2076–2078.

[Lücking *et al.* , 2014a] Lücking, Fabian, Trabattoni, Andrea, Anumula, Sunilkumar, Sansone, Giuseppe, Calegari, Francesca, Nisoli, Mauro, Oksenhendler, Thomas, & Tempea, Gabriel. 2014a. Direct measurement of nonlinear carrier-envelope phase changes in hollow fiber compression. *Pages SW1E–2 of: CLEO: Science and Innovations.* Optical Society of America.

[Lücking *et al.* , 2014b] Lücking, Fabian, Trabattoni, Andrea, Anumula, Sunilkumar, Sansone, Giuseppe, Calegari, Francesca, Nisoli, Mauro, Oksenhendler, Thomas, & Tempea, Gabriel. 2014b. In-Situ Measurement of Intensity-Dependent Carrier-Envelope Phase Changes in Hollow Fiber Compression. *Pages 08–Tue of: International Conference on Ultrafast Phenomena.* Optical Society of America.

[Ma *et al.* , 2014] Ma, Xiuquan, Zhu, Cheng, Hu, I-Ning, Kaplan, Alex, & Galvanauskas, Almantas. 2014. Single-mode chirally-coupled-core fibers with larger than 50$\mu$m diameter cores. *Optics express*, **22**(8), 9206–9219.

[Macklin *et al.* , 1993] Macklin, J _ J, Kmetec, JD, & Gordon III, CL. 1993. High-order harmonic generation using intense femtosecond pulses. *Physical review letters*, **70**(6), 766.

[Mackowiak *et al.* , 2015] Mackowiak, Verena, Peupelmann, Jens, Ma, Yi, & Gorges, Anthony. 2015. Nep–noise equivalent power. *Thorlabs, Inc., Newton, NJ, USA, White Paper.*

[Martinez, 1987] Martinez, O. 1987. 3000 times grating compressor with positive group velocity dispersion: Application to fiber compensation in 1.3-1.6 $\mu mregion. IEEE Journal of Quantum Electronics, \mathbf{23}(1), 59 - -64.$

[Martinez *et al.* , 1984] Martinez, OE, Gordon, JP, & Fork, RL. 1984. Negative group-velocity dispersion using refraction. *JOSA A*, **1**(10), 1003–1006.

[Matos *et al.* , 2006] Matos, Lia, Mücke, Oliver D, Chen, Jian, & Kärtner, Franz X. 2006. Carrier-envelope phase dynamics and noise analysis in octave-spanning Ti: sapphire lasers. *Optics express*, **14**(6), 2497–2511.

[Mayer *et al.* , 2014] Mayer, Benedikt W, Phillips, Christopher R, Gallmann, Lukas, & Keller, Ursula. 2014. Mid-infrared pulse generation via achromatic quasi-phase-matched OPCPA. *Optics express*, **22**(17), 20798–20808.

[McCumber, 1966] McCumber, DE. 1966. Intensity fluctuations in the output of cw laser oscillators. I. *Physical Review*, **141**(1), 306.

[McPherson *et al.* , 1987] McPherson, A, Gibson, G, Jara, H, Johann, U, Luk, Ting S, McIntyre, IA, Boyer, Keith, & Rhodes, Charles K. 1987. Studies of multiphoton production of vacuum-ultraviolet radiation in the rare gases. *JOSA B*, **4**(4), 595–601.

[Minck *et al.* , 1966] Minck, RW, Terhune, RW, & Wang, CC. 1966. Nonlinear optics. *Applied optics*, **5**(10), 1595–1612.

[Moll *et al.* , 2006] Moll, Kevin D, Jones, R Jason, & Ye, Jun. 2006. Output coupling methods for cavity-based high-harmonic generation. *Optics express*, **14**(18), 8189–8197.

[Moses *et al.* , 2009] Moses, J, Huang, S-W, Hong, K-H, Mücke, OD, Falcão-Filho, EL, Benedick, A, Ilday, FÖ, Dergachev, A, Bolger, JA, Eggleton, BJ, *et al.* . 2009. Highly stable ultrabroadband mid-IR optical parametric chirped-pulse amplifier optimized for superfluorescence suppression. *Optics letters*, **34**(11), 1639–1641.

[Mulder *et al.* , 2008] Mulder, Theresa D, Scott, Ryan P, & Kolner, Brian H. 2008. Amplitude and envelope phase noise of a modelocked laser predicted from its noise transfer function and the pump noise power spectrum. *Optics express*, **16**(18), 14186–14191.

[Müller *et al.* , 2016] Müller, Michael, Kienel, Marco, Klenke, Arno, Gottschall, Thomas, Shestaev, Evgeny, Plötner, Marco, Limpert, Jens, & Tünnermann, Andreas. 2016. 1 kW 1 mJ eight-channel ultrafast fiber laser. *Optics letters*, **41**(15), 3439–3442.

[Neuhaus *et al.* , 2018] Neuhaus, M, Fuest, Harald, Seeger, M, Schötz, Johannes, Trubetskov, M, Russbueldt, P, Hoffmann, HD, Riedle, E, Major, Zs, Pervak, V, *et al.* . 2018. 10 W CEP-stable few-cycle source at 2 $\mu$m with 100 kHz repetition rate. *Optics express*, **26**(13), 16074–16085.

[Nicholson *et al.* , 2007] Nicholson, JW, Fini, JM, Yablon, AD, Westbrook, PS, Feder, K, & Headley, C. 2007. Demonstration of bend-induced nonlinearities in large-mode-area fibers. *Optics letters*, **32**(17), 2562–2564.

[Nisoli, 1997] Nisoli, M. 1997. M. Nisoli et al., Opt. Lett. 22, 522 (1997). *Opt. Lett.*, **22**, 522.

[Osellame *et al.* , 2012] Osellame, Roberto, Cerullo, Giulio, & Ramponi, Roberta. 2012. *Femtosecond laser micromachining: photonic and microfluidic devices in transparent materials*. Vol. 123. Springer Science & Business Media.

[Paschotta, 2004] Paschotta, R. 2004. Noise of mode-locked lasers (Part I): numerical model. *Applied Physics B*, **79**(2), 153–162.

[Paul *et al.* , 2003] Paul, Ariel, Bartels, RA, Tobey, R, Green, H, Weiman, S, Christov, IP, Murnane, MM, Kapteyn, HC, & Backus, S. 2003. Quasi-phase-matched generation of coherent extreme-ultraviolet light. *Nature*, **421**(6918), 51.

[Petermann, 1991] Petermann, Klaus. 1991. *Laser Diode Modulation and Noise*. Vol. 3. Springer Science & Business Media.

[Pfeifer *et al.* , 2005] Pfeifer, Thomas, Kemmer, Ron, Spitzenpfeil, Robert, Walter, Dominik, Winterfeldt, Carsten, Gerber, Gustav, & Spielmann, Christian. 2005. Spatial control of high-harmonic generation in hollow fibers. *Optics letters*, **30**(12), 1497–1499.

[Popmintchev *et al.* , 2009] Popmintchev, Tenio, Chen, Ming-Chang, Bahabad, Alon, Gerrity, Michael, Sidorenko, Pavel, Cohen, Oren, Christov, Ivan P, Murnane, Margaret M, & Kapteyn, Henry C. 2009. Phase matching of high harmonic generation in the soft and hard X-ray regions of the spectrum. *Proceedings of the National Academy of Sciences*, **106**(26), 10516–10521.

[Poppe *et al.* , 2001] Poppe, Andreas, Holzwarth, Ronald, Apolonski, Alexander, Tempea, Gabriel, Spielmann, Ch, Hänsch, Theodor W, & Krausz, Ferenc. 2001. Few-cycle optical waveform synthesis. *Applied Physics B*, **72**(3), 373–376.

[Pupeza *et al.* , 2013] Pupeza, Ioachim, Holzberger, Simon, Eidam, T, Carstens, Henning, Esser, D, Weitenberg, J, Rußbüldt, P, Rauschenberger, Jens, Limpert, J, Udem, Th, *et al.* . 2013. Compact high-repetition-rate source of coherent 100 eV radiation. *Nature Photonics*, **7**(8), 608.

[Puppin *et al.* , 2015] Puppin, Michele, Deng, Yunpei, Prochnow, Oliver, Ahrens, Jan, Binhammer, Thomas, Morgner, Uwe, Krenz, Marcel, Wolf, Martin, & Ernstorfer, Ralph. 2015. 500 kHz OPCPA delivering tunable sub-20 fs pulses with 15 W average power based on an all-ytterbium laser. *Optics express*, **23**(2), 1491–1497.

[Quimby, 2006] Quimby, Richard S. 2006. *Photonics and lasers: an introduction.* John Wiley & Sons.

[Quinlan *et al.* , 2013] Quinlan, Franklyn, Fortier, Tara M, Jiang, Haifeng, & Diddams, Scott A. 2013. Analysis of shot noise in the detection of ultrashort optical pulse trains. *JOSA B*, **30**(6), 1775–1785.

[Rausch *et al.* , 2009] Rausch, Stefan, Binhammer, Thomas, Harth, Anne, Schulz, Emilia, Siegel, Martin, & Morgner, Uwe. 2009. Few-cycle oscillator pulse train with constant carrier-envelope-phase and 65 as jitter. *Optics express*, **17**(22), 20282–20290.

[Ravasio *et al.* , 2009] Ravasio, A, Gauthier, D, Maia, FRNC, Billon, M, Caumes, JP, Garzella, D, Géléoc, M, Gobert, O, Hergott, Jean-François, Pena, AM, *et al.* . 2009. Single-shot diffractive imaging with a table-top femtosecond soft x-ray laser-harmonics source. *Physical review letters*, **103**(2), 028104.

[Reduzzi *et al.* , 2015] Reduzzi, Maurizio, Carpeggiani, Paolo, Kühn, Sergei, Calegari, Francesca, Nisoli, Mauro, Stagira, Salvatore, Vozzi, Caterina, Dombi, Peter, Kahaly, Subhendu, Tzallas, Paris, *et al.* . 2015. Advances in high-order harmonic generation sources for time-resolved investigations. *Journal of Electron Spectroscopy and Related Phenomena*, **204**, 257–268.

[Reichert *et al.* , 1999] Reichert, J, Holzwarth, R, Udem, Th, & Haensch, T W_. 1999. Measuring the frequency of light with mode-locked lasers. *Optics communications*, **172**(1-6), 59–68.

[Rigaud *et al.* , 2016] Rigaud, Philippe, Van de Walle, Aymeric, Hanna, Marc, Forget, Nicolas, Guichard, Florent, Zaouter, Yoann, Guesmi, Khmaies, Druon, Frédéric, & Georges, Patrick. 2016. Supercontinuum-seeded few-cycle mid-infrared OPCPA system. *Optics express*, **24**(23), 26494–26502.

[Robinson & Harder, 2009] Robinson, Ian, & Harder, Ross. 2009. Coherent X-ray diffraction imaging of strain at the nanoscale. *Nature materials*, **8**(4), 291.

[Rothhardt *et al.* , 2012] Rothhardt, Jan, Demmler, Stefan, Hädrich, Steffen, Limpert, Jens, & Tünnermann, Andreas. 2012. Octave-spanning OPCPA system delivering CEP-stable few-cycle pulses and 22 W of average power at 1 MHz repetition rate. *Optics express*, **20**(10), 10870–10878.

[Rothhardt *et al.* , 2014] Rothhardt, Jan, Hädrich, Steffen, Klenke, Arno, Demmler, Stefan, Hoffmann, Armin, Gotschall, Thomas, Eidam, Tino, Krebs, Manuel, Limpert, Jens, & Tünnermann, Andreas. 2014. 53 W average power few-cycle fiber laser system generating soft x rays up to the water window. *Optics letters*, **39**(17), 5224–5227.

[Rothhardt *et al.* , 2016] Rothhardt, Jan, Hädrich, Steffen, Shamir, Yariv, Tschnernajew, Maxim, Klas, Robert, Hoffmann, Armin, Tadesse, Getnet K, Klenke, Arno, Gottschall, Thomas, Eidam, Tino, *et al.* . 2016. High-repetition-rate and high-photon-flux 70 eV high-harmonic source for coincidence ion imaging of gas-phase molecules. *Optics express*, **24**(16), 18133–18147.

[Rudawski *et al.* , 2015] Rudawski, Piotr, Harth, Anne, Guo, Chen, Lorek, Eleonora, Miranda, Miguel, Heyl, Christoph M, Larsen, Esben W, Ahrens, Jan, Prochnow, Oliver, Binhammer, Thomas, *et al.* . 2015. Carrier-envelope phase dependent high-order harmonic generation with a high-repetition rate OPCPA-system. *The European Physical Journal D*, **69**(3), 70.

[Rulliere, 2005] Rulliere, Claude. 2005. *Femtosecond laser pulses*. Springer.

[Rundquist *et al.* , 1998] Rundquist, Andy, Durfee, Charles G, Chang, Zenghu, Herne, Catherine, Backus, Sterling, Murnane, Margaret M, & Kapteyn, Henry C. 1998. Phase-matched generation of coherent soft X-rays. *Science*, **280**(5368), 1412–1415.

[Saleh *et al.* , 1991] Saleh, Bahaa EA, Teich, Malvin Carl, & Saleh, Bahaa E. 1991. *Fundamentals of photonics*. Vol. 22. Wiley New York.

[Salieres & Lewenstein, 2001] Salieres, Pascal, & Lewenstein, Maciej. 2001. Generation of ultrashort coherent XUV pulses by harmonic conversion of intense laser pulses in gases: towards attosecond pulses. *Measurement Science and Technology*, **12**(11), 1818.

[Saule *et al.* , 2017] Saule, Tobias, Holzberger, Simon, De Vries, O, Plötner, M, Limpert, J, Tünnermann, A, & Pupeza, Ioachim. 2017. Phase-stable, multi-$\mu$J femtosecond pulses from a repetition-rate tunable Ti: Sa-oscillator-seeded Yb-fiber amplifier. *Applied Physics B*, **123**(1), 17.

[Scherz, 2006] Scherz, Paul. 2006. *Practical electronics for inventors*. McGraw-Hill, Inc.

[Schulte *et al.* , 2016] Schulte, Jan, Sartorius, Thomas, Weitenberg, Johannes, Vernaleken, Andreas, & Russbueldt, Peter. 2016. Nonlinear pulse compression in a multi-pass cell. *Optics letters*, **41**(19), 4511–4514.

[Scott *et al.* , 2001] Scott, Ryan P, Langrock, Carsten, & Kolner, Brian H. 2001. High-dynamic-range laser amplitude and phase noise measurement techniques. *IEEE Journal of selected topics in quantum electronics*, **7**(4), 641–655.

[Seaberg *et al.* , 2011] Seaberg, Matthew D, Adams, Daniel E, Townsend, Ethan L, Raymondson, Daisy A, Schlotter, William F, Liu, Yanwei, Menoni, Carmen S, Rong, Lu, Chen, Chien-Chun, Miao, Jianwei, *et al.* . 2011. Ultrahigh 22 nm resolution coherent diffractive imaging using a desktop 13 nm high harmonic source. *Optics express*, **19**(23), 22470–22479.

[Shannon, 1948] Shannon, Claude Elwood. 1948. A mathematical theory of communication. *Bell system technical journal*, **27**(3), 379–423.

[Shiner *et al.* , 2013] Shiner, AD, Trallero-Herrero, C, Kajumba, Nathaniel, Schmidt, BE, Bertrand, JB, Kim, Kyung Taec, Bandulet, H-C, Comtois, D, Kieffer, J-C, Rayner, DM, *et al.* . 2013. High harmonic cutoff energy scaling and laser intensity measurement with a 1.8 $\mu$m laser source. *Journal of Modern Optics*, **60**(17), 1458–1465.

[Shirakawa *et al.* , 1999] Shirakawa, A, Sakane, I, Takasaka, M, & Kobayashi, T. 1999. Sub-5-fs visible pulse generation by pulse-front-matched noncollinear optical parametric amplification. *Applied physics letters*, **74**(16), 2268–2270.

[Steinmeyer *et al.* , 1999] Steinmeyer, G, Sutter, DH, Gallmann, L, Matuschek, N, & Keller, U. 1999. Frontiers in ultrashort pulse generation: pushing the limits in linear and nonlinear optics. *Science*, **286**(5444), 1507–1512.

[Steinmeyer *et al.* , 2013] Steinmeyer, Günter, Borchers, Bastian, & Lücking, Fabian. 2013. Carrier-envelope phase stabilization. *Pages 89–110 of: Progress in Ultrafast Intense Laser Science*. Springer.

[Stolen & Ashkin, 1973] Stolen, RH, & Ashkin, A. 1973. Optical Kerr effect in glass waveguide. *Applied Physics Letters*, **22**(6), 294–296.

[Strickland & Mourou, 1985] Strickland, Donna, & Mourou, Gerard. 1985. Compression of amplified chirped optical pulses. *Optics communications*, **55**(6), 447–449.

[Stuik & Bijkerk, 2002] Stuik, Remko, & Bijkerk, Fred. 2002. Linearity of P–N junction photodiodes under pulsed irradiation. *Nuclear Instruments and Methods in Physics Research Section A: Accelerators, Spectrometers, Detectors and Associated Equipment*, **489**(1-3), 370–378.

[Swan *et al.* , 2008] Swan, Michael Craig, Liu, Chi-Hung, Guertin, Doug, Jacobsen, Nick, Tankala, Kanishka, & Galvanauskas, Almantas. 2008. 33m Core Effectively Single-Mode Chirally-Coupled-Core Fiber Laser at 1064-nm. *Page OWU2 of: Optical Fiber Communication Conference*. Optical Society of America.

[Szipöcs *et al.* , 1994] Szipöcs, Robert, Ferencz, KÃ¡rpÃ¡t, Spielmann, Christian, & Krausz, Ferenc. 1994. Chirped multilayer coatings for broadband dispersion control in femtosecond lasers. *Optics letters*, **19**(3), 201–203.

[Takeda *et al.* , 1982] Takeda, Mitsuo, Ina, Hideki, & Kobayashi, Seiji. 1982. Fourier-transform method of fringe-pattern analysis for computer-based topography and interferometry. *JosA*, **72**(1), 156–160.

[Tawfieq *et al.* , 2018] Tawfieq, Mahmoud, Hansen, Anders Kragh, Jensen, Ole Bjarlin, Marti, Dominik, Sumpf, Bernd, & Andersen, Peter E. 2018. Intensity Noise Transfer Through a Diode-pumped Titanium Sapphire Laser System. *IEEE Journal of Quantum Electronics*, **54**(1), 1–9.

[Telle *et al.* , 1999] Telle, Harald R, Steinmeyer, G, Dunlop, AE, Stenger, J, Sutter, DH, & Keller, U. 1999. Carrier-envelope offset phase control: A novel concept for absolute optical frequency measurement and ultrashort pulse generation. *Applied Physics B*, **69**(4), 327–332.

[Thai *et al.* , 2011] Thai, A, Hemmer, M, Bates, PK, Chalus, O, & Biegert, J. 2011. Sub-250-mrad, passively carrier–envelope-phase-stable mid-infrared OPCPA source at high repetition rate. *Optics letters*, **36**(19), 3918–3920.

[Tournois, 1997] Tournois, Pierre. 1997. Acousto-optic programmable dispersive filter for adaptive compensation of group delay time dispersion in laser systems. *Optics communications*, **140**(4-6), 245–249.

[Treacy, 1969] Treacy, Edmond. 1969. Optical pulse compression with diffraction gratings. *IEEE Journal of quantum Electronics*, **5**(9), 454–458.

[Vernaleken *et al.* , 2012] Vernaleken, Andreas, Schmidt, Bernhard, Wolferstetter, Martin, Hänsch, Theodor W, Holzwarth, Ronald, & Hommelhoff, Peter. 2012. Carrier-envelope frequency stabilization of a Ti: sapphire oscillator using different pump lasers. *Optics Express*, **20**(16), 18387–18396.

[Von der Linde, 1986] Von der Linde, D. 1986. Characterization of the noise in continuously operating mode-locked lasers. *Applied Physics B*, **39**(4), 201–217.

[Wang *et al.* , 2010] Wang, H, Chini, M, Wu, Y, Moon, E, Mashiko, H, & Chang, Z. 2010. Carrier–envelope phase stabilization of 5-fs, 0.5-mJ pulses from adaptive phase modulator. *Applied Physics B*, **98**(2-3), 291–294.

[Waxer *et al.* , 2003] Waxer, LJ, Bagnoud, V, Begishev, IA, Guardalben, MJ, Puth, J, & Zuegel, JD. 2003. High-conversion-efficiency optical parametric chirped-pulse amplification system using spatiotemporally shaped pump pulses. *Optics letters*, **28**(14), 1245–1247.

[Weger *et al.* , 2013] Weger, Matthias, Maurer, Jochen, Ludwig, André, Gallmann, Lukas, & Keller, Ursula. 2013. Transferring the attoclock technique to velocity map imaging. *Optics express*, **21**(19), 21981–21990.

[Weiner, 2011] Weiner, Andrew. 2011. *Ultrafast optics*. Vol. 72. John Wiley & Sons.

[Weitenberg *et al.* , 2017a] Weitenberg, Johannes, Vernaleken, Andreas, Schulte, Jan, Ozawa, Akira, Sartorius, Thomas, Pervak, Vladimir, Hoffmann, Hans-Dieter, Udem, Thomas, Russbüldt, Peter, & Hänsch, Theodor W. 2017a. Multi-pass-cell-based nonlinear pulse compression to 115 fs at 7.5 $\mu$J pulse energy and 300 W average power. *Optics express*, **25**(17), 20502–20510.

[Weitenberg *et al.* , 2017b] Weitenberg, Johannes, Saule, Tobias, Schulte, Jan, & Rußbüldt, Peter. 2017b. Nonlinear Pulse Compression to Sub-40 fs at 4.5\mu $JPulseEnergybyMulti-Pass-CellSpectralBroadening.IEEEJournalofQuantumElectronics$, **53**(6), 1 − −4.

[Welch, 1967] Welch, Peter. 1967. The use of fast Fourier transform for the estimation of power spectra: a method based on time averaging over short, modified periodograms. *IEEE Transactions on audio and electroacoustics*, **15**(2), 70–73.

[Wnuk *et al.* , 2010] Wnuk, Pawel, Stepanenko, Yuriy, & Radzewicz, Czeslaw. 2010. High gain broadband amplification of ultraviolet pulses in optical parametric chirped pulse amplifier. *Optics express*, **18**(8), 7911–7916.

[Wolter *et al.* , 2015] Wolter, Benjamin, Pullen, Michael G, Baudisch, Matthias, Sclafani, Michele, Hemmer, Michaël, Senftleben, Arne, Schröter, Claus Dieter, Ullrich, Joachim, Moshammer, Robert, & Biegert, Jens. 2015. Strong-field physics with mid-IR fields. *Physical Review X*, **5**(2), 021034.

[Xu *et al.* , 1996] Xu, Lin, Spielmann, Ch, Poppe, A, Brabec, T, Krausz, Ferenc, & Hänsch, TW. 1996. Route to phase control of ultrashort light pulses. *Optics letters*, **21**(24), 2008–2010.

[Yu *et al.* , 2007] Yu, Tae Jun, Hong, Kyung-Han, Choi, Hyung-Gyu, Sung, Jae Hee, Choi, Il Woo, Ko, Do-Kyeong, Lee, Jongmin, Kim, Junwon, Kim, Dong Eon, & Nam, Chang Hee. 2007. Precise and long-term stabilization of the carrier-envelope phase of femtosecond laser pulses using an enhanced direct locking technique. *Optics express*, **15**(13), 8203–8211.

université PARIS-SACLAY

ÉCOLE DOCTORALE
Ondes et Matière (EDOM)

**Titre :** Stabilisation en CEP d'un amplificateur à fibre dopée Yb à haute cadence pour la génération d'harmoniques d'ordre élevé

**Mots clés :** Laser ultra-rapide, Stabilisation de la CEP, haute cadence, courte durée d'impulsion, HHG.

**Résumé :**
Depuis une vingtaine d'années, la physique attoseconde, via le phénomène de génération d'harmoniques d'ordres élevés (HHG), a permis de nombreuses avancées dans la compréhension des phénomènes de dynamique ultra-rapide. Les lasers femtoseconde émettant des impulsions de fortes énergies et de durées de quelques cycles optiques sont les outils indispensables à cette physique. De plus, la phase entre la porteuse et l'enveloppe (CEP) des impulsions doit être contrôlée. Récemment les lasers basés sur les fibres dopées ytterbium ont permis de transposer les expériences d'HHG à haute cadence. La stabilisation de la CEP pour ce type de systèmes constitue la brique manquante au développement de sources à haute cadence pleinement compatibles avec ces applications. Cette thèse a été consacrée à la stabilisation CEP d'un laser à fibre dopée ytterbium pour une application à la génération de rayonnement cohérent dans l'XUV à fort flux de photon.
Dans la première partie nous présentons l'architecture d'une source à un taux de répétition de 100 kHz stable en CEP émettant des impulsions de 30 $\mu$J et 96 fs. Ce système constitue une preuve de principe pour les futures sources haute énergie. La stabilisation de CEP est assurée par une architecture hybride composée d'un injecteur stabilisé passivement suivi d'un amplificateur de puissance stabilisé activement. Un bruit résiduel de CEP inférieur à 400 mrad est obtenu dans différentes configurations, de la mesure courte durée (1 s) tir à tir jusqu'à la mesure sur une heure de fonctionnement.
Dans la seconde partie nous présentons la mise au point d'une ligne HHG XUV optimisée à 13 nm sur les paramètres d'un laser à fibre, pour des applications à l'imagerie par diffraction cohérente.

**Title :** High-repetition rate CEP-stable Yb-doped fiber amplifier for high harmonic generation

**Keywords :** Ultrafast lasers, CEP stabilization, high repetition rate, few-cycle pulse duration, HHG.

**Abstract :** In the last two decades, attosecond physics, based on the high harmonic generation (HHG) phenomenon, has allowed a better understanding of ultrafast dynamics in the microcosm. High-energy few-cycles carrier-envelope phase (CEP) stabilized sources are the main enabling tools for this physics. Recently, temporally compressed Ytterbium-doped fiber amplifiers have been successfully used as high XUV photon flux HHG drivers. CEP stabilization of these sources would ensure their full compatibility with attoscience. The thesis is devoted to the CEP stabilization of a high repetition rate Yb-doped fiber femtosecond source, for high XUV photon flux beamline applications.
In the first part, we present the architecture of such a source at 100 kHz repetition rate delivering 30 $\mu$J 96 fs CEP-stable pulses. It constitutes a test bench for future energy-scaled few-cycle sources. The CEP stabilization is ensured in a hybrid architecture including a passively stabilized frontend followed by an actively stabilized power amplifier. A residual CEP noise lower than 400 mrad is measured using various setups, including a shot-to-shot measurement over 1 s and a long-term stability over 1 h.
In the second part, we discuss the design of a high flux HHG beamline optimized for a future generation of fiber-based driver at 13 nm for applications to coherent diffraction imaging.

**Université Paris-Saclay**
Espace Technologique / Immeuble Discovery
Route de l'Orme aux Merisiers RD 128 / 91190 Saint-Aubin, France